

UNIVERSITAT POLITÈCNICA DE VALÈNCIA

**INSTITUTO INTERUNIVERSITARIO DE INVESTIGACIÓN DE
RECONOCIMIENTO MOLECULAR Y DESARROLLO TECNOLÓGICO**



**Novel probes, carriers and prodrugs to target
senescent cells *in vivo***

PhD. THESIS

Submitted by

Beatriz Lozano Torres

PhD. Supervisors:

Prof. Ramón Martínez Máñez

Prof. Félix Sancenón Galarza

València, September 2021



UNIVERSITAT
POLITÈCNICA
DE VALÈNCIA

RAMÓN MARTÍNEZ MÁÑEZ, PhD in Chemistry and Professor at the *Universitat Politècnica de València* and FÉLIX SANCENÓN GALARZA, PhD in Chemistry and Professor at the *Universitat Politècnica de València*

CERTIFY:

That the work "***Novel probes, carriers and prodrugs to target senescent cells in vivo***" has been developed by Beatriz Lozano Torres under their supervision at the Instituto Interuniversitario de Investigación de Reconocimiento Molecular y Desarrollo Tecnológico (IDM) of the *Universitat Politècnica de València*, and at the Unidad Mixta UPV-CIPF de Investigación en Mecanismos de Enfermedades y Nanomedicina, as a Thesis Project to obtain the degree of PhD in Chemistry at the *Universitat Politècnica de València*.

Valencia, September XX 2021

Prof. Ramón Martínez Máñez

Prof. Félix Sancenón Galarza

*Detrás de los sueños,
siempre hay esfuerzos que la gente no ve*

A mis padres, hermano y marido.

***“Science is not only a disciple of reason,
but, also, one of romance and passion”.***

Stephen Hawking

***“Most people say that it is the intellect which makes a
great scientist. They are wrong: it is character.”***

Albert Einstein

***“A man who dares to waste one hour of time
has not discovered the value of life.”***

Charles Darwin

Índice

Acknowledgements	1-5
Resumen	7-11
Resum	13-17
Abstract	19-22
Publications	23-28
Abbreviations and Acronyms	29-34

Chapter 1 | General introduction **37-80**

1.1 Molecular recognition	37
1.1.1 <i>Molecular probes</i>	38-39
1.1.2 <i>Nanotechnology</i>	40-41
1.2 Cellular senescence	42-62
1.2.1 <i>Senescence in health and disease</i>	45-49
1.2.2 <i>Senescence induction methods</i>	49-53
1.2.3 <i>Senescence markers</i>	53-58
1.2.4 <i>Senolytics</i>	58-60
1.2.5 <i>Senomorphics</i>	60
1.2.6 <i>The importance of targeting senescent cells</i>	60-62
1.3 Chemical probes for the detection of senescent cells	63-74
1.3.1 <i>SA-β-Gal-dependent chromo-fluorogenic probes</i>	63-69
1.3.2 <i>Other hydrolases probes</i>	70-71
1.3.3 <i>Lipofuscin detection</i>	71-72
1.3.4 <i>Other approaches for the detection of senescent cells using chemical probes</i>	72-74
1.4 Nanodevices targeting senescent cells	75-80

Chapter 2 | Objectives **83**

Chapter 3 | An OFF-ON two-photon fluorescent probe for tracking cell senescence in vivo. **87-113**

3.1 Abstract	88
3.2 Introduction	88-90
3.3 Results and discussion	90-96
3.4 Conclusions	96-97
3.5 Acknowledgments	97
3.6 References	97-99

3.7 Supporting Information	100-113
3.7.1 <i>Materials and methods</i>	100
3.7.2 <i>Synthesis of AH</i>	101-103
3.7.3 <i>Synthesis of AHGa</i>	103-105
3.7.4 <i>Optical studies of AH and AHGa</i>	107-109
3.7.4.1 <i>UV, excitation and fluorescence spectra of AH and AHGa</i>	107-108
3.7.4.2 <i>AH fluorescence changes with pH</i>	108
3.7.4.3 <i>AH and AHGa quantum yield measurements</i>	108-109
3.7.5 <i>In vitro experiments</i>	109-110
3.7.5.1 <i>Cell lines</i>	109
3.7.5.2 <i>Cell viability assays</i>	109-110
3.7.6 <i>In vivo experiments</i>	110-112
3.7.6.1 <i>Mice</i>	110
3.7.6.2 <i>Xenograft assays</i>	111
3.7.6.3 <i>Ex vivo imaging of different sections of fresh organs after AHGa treatment</i>	111-112
3.7.7 <i>References</i>	112-113

Chapter 4 | A two-photon probe based on naphthalimide-styrene fluorophore for the in vivo tracking of cellular senescence

117-156

4.1 Abstract	118
4.2 Introduction	118-121
4.3 Experimental section	122-125
4.3.1 <i>Materials</i>	122
4.3.2 <i>Hydrolysis reaction</i>	122-123
4.3.3 <i>Cell lines</i>	123
4.3.4 <i>In vitro viability assays.</i>	123
4.3.5 <i>Mouse models.</i>	124-125
4.3.6 <i>Preparation of mouse tumour slices for imaging experiments</i>	125
4.4 Results and discussion	125-135
4.4.1 <i>Synthesis, Characterization, Spectroscopic Features, and Mechanism.</i>	125-127
4.4.2 <i>In Vitro Validation of HeckGal probe.</i>	128-131
4.4.3 <i>In Vivo Validation of HeckGal probe</i>	131-135
4.5 Conclusions	135-136
4.6 Associated content	136
4.7 Acknowledgments	137

4.8 Author contribution	137-138
4.9 References	138-140
4.10 Supporting information	141-156
4.10.1 <i>Table S1. Recently published fluorogenic molecular probes for cellular senescence detection</i>	141
4.10.2 <i>Synthesis of Heck and HeckGal</i>	142-152
4.10.3 <i>Heck fluorescence emission not depends on pH</i>	152
4.10.4 <i>Hydrolysis reaction of Heck-Gal into Heck fluorophore</i>	153
4.10.5 <i>Heck and HeckGal quantum yield measurements</i>	153
4.10.6 <i>In vitro viability assays</i>	154
4.10.7 <i>Emission spectrum of Heck after two-photon excitation</i>	155
4.10.8 <i>Co-staining does not affect to Heck signal</i>	156

Chapter 5 | A renal clearable fluorogenic probe for in vivo detection of cellular senescence **159-198**

5.1 Abstract	160
5.2 Introduction	160-162
5.3 Results and discussion	162-175
5.3.1 <i>Synthesis, spectroscopic characterization, and mechanism studies</i>	162-164
5.3.2 <i>Cy7Gal monitors senescence induction in mouse mammary tumour cells in vitro</i>	164-167
5.3.3 <i>Renal clearance of Cy7 fluorophore allows cell senescence burden evaluation in vivo in a 4T1 breast cancer model treated with senescence-inducing chemotherapy</i>	167-170
5.3.4 <i>In vivo cell senescence burden evaluation in naturally aged BALB/cByJ mice</i>	171-173
5.3.5 <i>In vivo senescence burden evaluation in a senescence-accelerated mouse model</i>	173-175
5.3.6 <i>Cy7Gal is a sensitive and specific probe for senescence burden evaluation regardless of the murine model</i>	175
5.4 Conclusions	175-176
5.5 Acknowledgments	176
5.6 Author Contributions	177
5.7 Competing Interest Statement	177
5.8 Data availability statement	178
5.9 References	178-181
5.10 Supporting information	182-198
5.10.1 <i>Materials</i>	182

5.10.2 Synthesis and characterization of Cy7Gal	182-183
5.10.3 Synthesis and characterization of Cy7	183-184
5.10.4 Synthesis and characterization of WOS-Cy7Gal	185-186
5.10.5 Characterization	186
5.10.6 Hydrolysis of Cy7Gal by human- β Gal	186
5.10.7 Interferents	187
5.10.8 Cell culture	187
5.10.9 Confocal in vitro experiments	187
5.10.10 Competition experiments with D-Galactose	187
5.10.11 Downregulation experiments	188
5.10.12 Western blot analysis of β -galactosidase expression	188
5.10.13 In vitro cytotoxicity studies.	189
5.10.14 Animals	189
5.10.15 In vivo 4T1 breast cancer model treated with senescence-inducing chemotherapy	189
5.10.16 Renal clearance of Cy7Gal	190
5.10.17 Experiments with WOS-Cy7Gal	190-191
5.10.18 Ex vivo IVIS studies	191
5.10.19 Ki67 immunohistochemistry	191
5.10.20 Statistical analyses	191-192
5.10.21 Cy7 and Cy7Gal quantum yield measurements	192
5.10.22 Cy7 fluorescence emission at different pH	192
5.10.23 Hydrolysis of Cy7Gal by human β -Galactosidase and interferents	193
5.10.24 Silencing and western blotting experiments of β -galactosidase	194
5.10.25 X-Gal staining of kidney, liver and tumors from BALB/cByJ female mice carrying orthotopic 4T1 mammary tumors with or without palbociclib treatment	195
5.10.26 Images of BALB/cByJ female mice bearing 4T1 mammary tumors treated with palbociclib and i.p. injected with Cy7Gal	196
5.10.27 Fluorophore biodistribution in BALB/cByJ mice bearing 4T1 mammary tumours treated with palbociclib and in the animal model of accelerated aging SAMP8 and its control SAMR1, after i.p. injection with Cy7Gal or WOS-Cy7Gal	197
5.10.28 Images of 2 and 14 months old BALB/cByJ female mice i.p. injected with Cy7Gal	198

Chapter 6 | Real time in vivo detection of cellular senescence through the controlled release of the NIR fluorescent dye Nile Blue **201-229**

6.1 Abstract	202
6.2 Introduction	202-205
6.3 Results and discussion	205-211
6.3.1 <i>Synthesis, Characterization, Spectroscopic Features and Mechanism</i>	205
6.3.2 <i>In vitro validation</i>	207-208
6.3.3 <i>In vivo validation</i>	208-211
6.4 Conclusions	211-212
6.5 Acknowledgements	212
6.6 References	213-214
6.7 Supporting information	215-229
6.7.1 <i>Materials and methods</i>	215-216
6.7.2 <i>Synthesis of materials</i>	216-217
6.7.3 <i>Materials characterization</i>	218-223
6.7.4 <i>Calculations of loaded and released NB</i>	223-224
6.7.5 <i>Cargo release experiments</i>	224
6.7.6 <i>In vitro studies</i>	224-226
6.7.7 <i>In vivo studies</i>	226-227
6.7.8 <i>Immunohistochemistry protocol</i>	227
6.7.9 <i>Biodistribution experimental protocol</i>	228
6.7.10 <i>Toxicity and pro-inflammatory factors in vivo evaluation of S3</i>	229

Chapter 7 | Galacto-conjugation of Navitoclax as an efficient strategy to increase senolytic specificity and reduce platelet toxicity **233-281**

7.1 Abstract	234
7.2 Introduction	235-238
7.3 Results	239-254
7.3.1 <i>Synthesis, characterisation and hydrolysis reaction studies</i>	239-240
7.3.2 <i>Nav-gal is a prodrug with effective wide-ranging senolytic activity that depends on GLB1 activity</i>	240-245
7.3.3 <i>Nav-gal induces apoptosis of senescent cells while preserving viability of nonsenescent cells</i>	245-246

7.3.4 Cisplatin and Nav-gal have additive antitumour effects when used concurrently and sequentially	246-249
7.3.5 Therapeutic activity of Nav-gal in xenografts and orthotopic models of NSCLC	249-251
7.3.6 Nav-gal has reduced platelet toxicity when compared with Navitoclax	252-255
7.4 Discussion	255-259
7.5 Experimental procedures	260-269
7.5.1 Synthesis, characterisation and hydrolysis reaction studies	260
7.5.2 Characterisation of Nav-gal prodrug	260-261
7.5.3 Hydrolysis reaction of Nav-gal studies	261
7.5.4 Cells and reagents	261-262
7.5.5 GLB1 downregulation	262
7.5.6 Cell viability and apoptosis analysis	263
7.5.7 Clonogenic assay	264-265
7.5.8 Immunoblotting	265
7.5.9 Mouse experiments	265-266
7.5.10 Histology	267
7.5.11 Platelet apoptosis analysis	268
7.5.12 Statistical analysis	268-269
7.6 Acknowledgments	269
7.7 Conflict of interests	270
7.8 Author contributions	270-271
7.9 Data availability statement	271
7.10 References	271-273
7.11 Supporting Information	274-281
<i>Figure S1. Molecular characterisation of pro-drug Nav-gal.</i>	274-275
<i>Figure S2. Assessment of the induction of cellular senescence in cell lines used for in vitro experiments</i>	276
<i>Figure S3. The galacto-conjugated pro-drug Nav-gal shows a lower induction of apoptosis of nonsenescent melanoma SK-Mel-103 cells and lung cancer A549 cells, and significantly decreases clonogenic potential in combination with cisplatin</i>	277-278
<i>Figure S4. Sequential Nav-gal treatment after chemotherapy Decreases tumour volume and platelet toxicity compared to Navitoclax.</i>	279
<i>Figure S5. Concomitant treatment of lung tumours with pro-drug Nav-Gal and cisplatin significantly decreases tumour burden in an orthotopic lung cancer mouse model.</i>	280-281

Figure S6. Gating strategy for the analysis of Annexin V-positive platelets (apoptotic platelets) in samples from human and mouse blood.

281

Chapter 8 | Conclusions and Perspectives

285-288

Acknowledgements

Agradecimientos

Ahora que me encuentro en la recta final de esta etapa quisiera dedicarles unas líneas a las personas que me han ayudado y han estado en mi camino en todos estos años.

En primer lugar, me gustaría dar las gracias a mis directores de tesis Ramón y Félix. A Ramón por acogerme en su grupo de investigación, por sus consejos y por ser tan exigente conmigo haciendo que explote y exprima mis capacidades al máximo. Siempre has confiado en mí y me has dejado trabajar y desarrollar los proyectos con gran libertad. Esto me ha permitido conseguir una formación súper versátil, ampliando mi conocimiento químico y aprendiendo muchísimo del mundo bio y del trabajo con animales que me apasiona (un gran descubrimiento para mí 😊). También me gustaría agradecerte la posibilidad que has brindado de colaborar con tan diversos grupos de investigación, en especial en los proyectos de senescencia que han resultado ser muy fructíferos para mi carrera investigadora y por dejarme exponer mis trabajos en tantos congresos. Y por último y no menos importante por la comprensión que has demostrado siempre ante imprevistos y problemas personales, sobre todo en el último año... Vivir lejos de la familia y tener un bebé intentando mantener a flote una carrera investigadora es un trabajo arduo complicado y siempre has sabido cómo ayudarnos tanto a Juanfran como a mí a conciliar vida profesional y personal. Por todo ello GRACIAS de nuevo. Y qué decirle a Félix que no sepa... desde el primer momento que pisé el laboratorio 2.6 has sido mi apoyo continuo. Más que un director de tesis, siempre me has parecido un amigo, una persona con la que poder contar en cualquier momento. Por nuestra formación, hemos conectado en la manera de ver las cosas en el trabajo y he aprendido taaanto de ti que nunca podré agradecértelo suficiente. Cada vez que había que analizar a fondo un RMN,

Agradecimientos

enfrentarse a una reacción nueva, hacer papeleos (sabes que lo odio) o escribir un artículo te sentabas conmigo hasta que se solucionaba. Durante estos siete años me has apoyado y ayudado tanto en el área profesional como en la personal y a pesar de que últimamente hayamos dejado un poco de lado las “cervecitas de después”, y las comilonas en “Los Hechizos de Morgana” las recuerdo con mucho cariño y espero que de vez en cuando sigamos con esta bonita costumbre☺. GRACIAS Félix, por todo y por ser así de bueno con la gente.

Además de mis directores de tesis, quiero hacer mención especial a Manuel Serrano por acogerme en su laboratorio del CNIO cuando no sabía ni lo que era un pase de células y a Dani por abrirme las puertas del mundo bio, recuerdo esos días interminables con Irene y contigo en el CNIO cuando no sabíamos coger una pipeta de cultivos, parece mentira que haya pasado tanto tiempo. Me alegro mucho de toda tu evolución ¡y de que ahora seas el Jefe! Te deseo todos los éxitos del mundo y aunque no hayamos conseguido esa ansiada Marie Curie, espero que algún día podamos volver a trabajar juntos. Gracias también a Mar por hacerme sentir una más en tu laboratorio estos últimos años, siempre tan comprensiva y regalándonos tu tiempo para resolver dudas y diseñar experimentos. Has sido un apoyo muy grande en esta última etapa. A Elena, aunque no nos hayamos cruzado mucho en los proyectos siempre has estado dispuesta para organizar las cosas y resolver las dudas de papeleos, contratos etc. y por ser “la mami” del laboratorio, eres un pilar muy importante en el grupo, gracias. A Mari Carmen, ¡hay que ver lo que sabe esta mujer de RMN, PLS Y PCAs eh!. He aprendido mucho de ti, cosas que me parecían extraterrestres y complejísimas, pero con tu paciencia y buen humor conseguiste que mi cabeza dura lo entendiese. Y por último a Andrea, por acompañarnos a Irene y a mí en nuestros inicios senescentes y por los buenos (y malos) ratos en el CNIO, en el IRB y en las reuniones de PringaSen. Las risas que nos hemos echado con los viajes a

Mozambique y con las contaminaciones no tienen precio. Eres el alma de la fiesta y siempre encuentras palabras de ánimo para todos nosotros.

También quiero dar las gracias a todas las personas que han pasado por el grupo durante todo este tiempo por los momentos compartidos: Edgar, Cris T, Carol, Cris M, Lluís, María Ruíz, Adrián, Lorena, Xente, Àngela, Marta, Amelia, Santi, Elisa, Tania, Eva, María, Paula, Andrea Escudero, Serena, Angy, Bea, Alejandra, Gema, Mónica, Elena, Araceli, Blanca. A Andy, por estar siempre dispuesto a bailarse una salsita conmigo en mitad del lab y por su alegría que contagia. Y a la nueva generación que acaba de entrar al grupo y he tenido la suerte de conocer aun sin ir al labo por la baja de maternidad: Giovanni, Guillermo y Laura, y a Marcia, una magnífica persona, transparente, que aprende rapidísimo y muy trabajadora.

Quisiera, además dedicarles unas líneas a Juan Carlos, Andrea y Cris, del 2.5, que me dejaron acompañarles en los tiempos de “menjador” que han sido el fruto de una gran amistad. Gracias por los momentos vividos y por ser tan excelentes personas. Sois también un apoyo muy grande para Juanfran y para mí.

Por otra parte, quiero agradecer su apoyo y su compañía a los que ahora puedo llamar con orgullo amigos, que a pesar de la separación del grupo por laboratorios hemos conseguido mantener el contacto como si nada hubiera pasado. A Luis, por simplificar las cosas y ser tan práctico, hablar contigo siempre me ha transmitido mucha tranquilidad. ¡Parece mentira que siempre hayamos ido tan a la par con las bodas y los bebés! Tenemos formas de pensar y vivir bastante parecidas y eso se traduce en lo que te admiro y el cariño que te tengo. A Alba, por dejarme cuidarla y ser su segunda mami, por ser mi confidente y yo la suya, por los tintos de verano compartidos, por los cabreos y por volver a ser las mismas después, y por ser taaaan trabajadora y ayudarme con su esfuerzo en la última etapa. A Iris por ser sinónimo de felicidad, chica, es que mira que cuesta verte

decaída o enfadada... Eres un chute de energía y cada vez que apareces por el 2.6 se me alegra el día. A Toni, siempre tan aplicado y dispuesto a ayudar. Admiro muchísimo tu forma de ser, tranquilo y amable y con las cosas tan claras. Y por último a Irene, por tantos momentos buenos y malos, me pongo a recordar y me vienen a la mente un sinfín de imágenes: sintetizando nanopartículas, la primera vez trabajando con navitoclax disfrazadas hasta la nariz, volviendo de comidas de navidad a parar reacciones, saltando la valla del CNIO a las 12 de la noche como buenas delincuentes y yéndonos después a la Tagliatella a comernos una pizza y bebernos una botella de Lambrusco para celebrarlo, en el animalario aprendiendo a sondar y recogiendo el pipi de nuestras pobres niñas... Me has enseñado taaaanto que no sé ni cómo darte las gracias. Y, por supuesto, siempre compartiendo el mundo del baile, aunque hayamos tirado por estilos diferentes. Y gracias a ti y a Vicente por los primeros zapatitos de baile de Triana, ¡pronto los desgastará! ¡No podía ser de otra forma!! ☺

Finalmente, quiero dar las gracias a las personas más importantes de mi vida, mi familia. Gracias mamá, papá y Toño ya que sin vosotros no estaría donde estoy ni sería la persona que soy. Siempre me habéis apoyado en TODO, vuestra ayuda incondicional es el motor más importante de mi vida. Siempre alegres, aún en los peores momentos, siempre animándome a ser mejor, a superarme. Habéis confiado en mí desde pequeña, me enseñasteis lo que significa el trabajo duro, nunca me habéis puesto obstáculos y siempre os habéis mostrado orgullosos de vuestra niña. No podría imaginar mejores padres, formáis un gran equipo. Deseo que Juanfran y yo seamos, al menos la mitad de buenos padres que sois vosotros. Y si hablo de buenos padres, no os digo cómo sois de buenos abuelos, Triana tiene mucha suerte de teneros, aunque aún no sepa hablar, sé que os adora. Los otros abuelos no se quedan atrás... Gracias Paqui y Blandez por aceptarme como otra hija más y ser siempre tan buenos conmigo. Triana tiene mucha suerte de contar

también con los mejores abuelos sevillanos. Y a los titos Raquel e Isra, gracias también por esas partidas de Parchís que nos hacen desconectar un rato ¡menudo vicio! Os adoro family.

Por último, GRACIAS a mi mitad, a mi corchito que siempre me saca a flote, compañero de aventuras, mi marido y el padre de mi hija y también el mejor compañero de trabajo, Juanfran. Hemos crecido tanto juntos que parece increíble que sólo hayan pasado 6 años desde que nos cruzamos en los pasillos del departamento y de aquel viaje a Japón. Me cuidas, me consientes, me haces especial y me has dado el mejor regalo que podía esperar. A tu lado no me da miedo nada porque podemos con lo que nos echen, demostrado está. Triana y yo te queremos más que a nada.

Resumen

La presente tesis doctoral titulada “**Nuevas sondas, portadores y profármacos dirigidos a células senescentes *in vivo***” se centra en el diseño, preparación, caracterización y evaluación de sondas basadas en fluoróforos funcionalizados o en nanopartículas, así como en el desarrollo de profármacos, aplicadas al campo de la senescencia celular.

En el primer capítulo se introducen, a nivel general, los diferentes conceptos relacionados con el reconocimiento molecular y la detección de biomarcadores. Seguidamente se introducen conceptos básicos de senescencia celular y envejecimiento, así como el papel que juegan las células senescentes a nivel fisiológico, en enfermedades asociadas al envejecimiento celular y en el cáncer. Por último, se aborda también la creciente necesidad de desarrollar nuevas herramientas de diagnóstico y terapias centradas en la detección y tratamiento de dichas enfermedades.

En el segundo capítulo se exponen los objetivos generales de la presente tesis doctoral, así como los objetivos concretos que son abordados en los diferentes capítulos experimentales.

En el tercer capítulo se describe una nueva sonda molecular para la detección de senescencia *in vivo*. En concreto, se describe el diseño de una sonda de dos fotones basada en un fluoróforo de naftalimida conectada, mediante un éster metílico de L-histidina, con una galactosa acetilada que esta unida a uno de los átomos de nitrógeno aromático de la L-histidina a través de un enlace *N*-glicosídico hidrolizable (**AHGa**). La sonda inicial presenta una baja emisión pero en células senescentes se transforma en un fluoróforo con alto rendimiento cuántico que permite visualizar estas células debido a la hidrólisis del enlace *N*-glicosídico por la enzima β -galactosidasa sobreexpresada en este tipo de células. La sonda es capaz de detectar *in vitro* células de melanoma humano SK-Mel-103 tratadas con

quimioterapia inductora de senescencia frente a células control. Adicionalmente, se validó la detección *in vivo* de senescencia en ratones con xenoinjertos tumorales tratados con quimioterapia inductora de senescencia.

Basándonos en los resultados obtenidos en el capítulo tres, en el capítulo cuatro se describe un sistema similar cuyas características confieren al fluoróforo una mayor longitud de onda de excitación (**HeckGal**). La nueva sonda es capaz de detectar células senescentes debido a la sobreexpresión de la enzima β -galactosidasa asociada a senescencia en gran variedad de líneas celulares con diversos métodos de inducción de senescencia. Esta sonda se validó también *in vivo* en un modelo ortotópico de cáncer de mama de ratón tratado con quimioterapia inductora de senescencia, y en un modelo de ratón de fibrosis renal.

Seguidamente, el capítulo cinco, se centra en un nuevo concepto de sondas moleculares no invasivas, que proporcionan una señal fácilmente legible a través de simples medidas de fluorescencia de la orina. Esta idea se llevó a cabo mediante la funcionalización de una sonda con grupos que le confieren características diuréticas (rápida eliminación renal) y el concepto se aplicó al diseño de una sonda para a la detección en orina de la carga senescente en diversos modelos. La sonda (**Cy7Gal**) está basada en la cianina-7 que es hidrolizada por la enzima β -galactosidasa en un fluoróforo altamente emisivo **Cy7**. **Cy7Gal** y **Cy7** contienen restos de ácido sulfónico que aumentan su solubilidad en agua y desencadenan su rápida excreción por el sistema urinario. El grado de senescencia se cuantificó por medición directa de fluorescencia en orina en tres modelos de senescencia en ratones: (i) un modelo ortotópico de cáncer de mama en ratones BALB/cByJ con senescencia inducida por quimioterapia; (ii) ratones BALB / cByJ envejecidos de forma natural; y (iii) ratones con senescencia acelerada (SAMP8, del inglés *Senescence Accelerated Mouse-Prone 8*). Además,

las imágenes IVIS *ex vivo* permiten la evaluación de senescencia en diversos órganos. La sonda **Cy7Gal** es el primer ejemplo para la detección y cuantificación no invasiva en orina de la presencia *in vivo* de células senescentes y puede servir como base en el desarrollo de nuevas sondas moleculares para el diagnóstico rápido en orina de diferentes enfermedades, así como para el seguimiento de tratamientos terapéuticos.

Por último, en lo que a detección de senescencia celular se refiere, se presenta en el capítulo seis la detección óptica *in vivo* de senescencia celular mediante el uso de nanopartículas de sílice mesoporosas (**S3**) cargadas con el fluoróforo Nile Blue (**NB**) y funcionalizadas en su superficie externa con un galactohexasacárido. El **NB** está aprobado por la FDA para su uso en humanos y presenta emisión en el infrarrojo cercano (NIR). La emisión a 672 nm de **NB** se encuentra prácticamente desactivada dentro de los poros de las nanopartículas **S3**, debido a la planaridad de la molécula y su capacidad para dar interacciones de apilamiento- π . Las nanopartículas **S3** están funcionalizadas con un galactohexasacárido que les confiere una selectividad específica hacia células senescentes. En presencia de estas células y de β -galactosidasa, el galactosacárido es hidrolizado, produciéndose la liberación de **NB** que vuelve a emitir fluorescencia. La eficacia de la sonda para detectar ópticamente senescencia celular se validó *in vivo* en células senescentes SK-Mel-103 y 4T1, y en ratones BALB/cByJ con tumores ortotópicos de cáncer de mama tratados con quimioterapia *in vivo*.

Una vez alcanzados los objetivos planificados en lo referente al diagnóstico, en el capítulo siete se abordó la mejora de uno de los senolíticos más potentes y ampliamente conocido en el campo de la senescencia celular que existe a día de hoy en el mercado: el Navitoclax, también conocido como ABT-263. Muchas potenciales terapias senolíticas a humanos se ven obstaculizadas por la

especificidad subóptima de los fármacos senolíticos para las células senescentes y las altas toxicidades que reducen sus ventanas terapéuticas. El senolítico Navitoclax es un inhibidor selectivo de las proteínas antiapoptóticas BCL-2, BCL-XL y BCL-W, y su principal efecto secundario en humanos es que induce la muerte apoptótica de las plaquetas (trombocitopenia) al depender éstas de BCL-XL para su supervivencia. El efecto senolítico de este compuesto proviene de la sobreexpresión de proteínas de la familia BCL-2 en células senescentes. Teniendo en cuenta lo anterior, se diseñó y preparó un pro-fármaco a través de la funcionalización de Navitoclax con un residuo galactosídico (**Nav-gal**), con el fin de que éste no fuese capaz de inhibir las proteínas antiapoptóticas de la familia BCL-2 cuando está unido al azúcar, evitando así la muerte de células no senescentes. Al entrar en el lisosoma de células senescentes, el enlace glicosídico se hidroliza por acción de la enzima β -galactosidasa (SA β Gal), obteniendo Navitoclax libre que mata a la célula. La pro-droga **Nav-gal** se validó en células senescentes de cáncer de pulmón humanas (A549) y de ratón (L1475 (luc)); líneas celulares de cáncer de melanoma humano (SK-Mel-103) y glándula mamaria de ratón (4T1); células de carcinoma colorrectal (HCT116); fibroblastos de pulmón de ratón (células MLg) y fibroblastos de pulmón humano (ER: células Mek IMR90) observando un IC₅₀ similar a el Navitoclax en células senescentes, pero protegiendo a las células no senescentes. Además, los estudios *in vivo* tras el tratamiento con un inductor quimioterapéutico de senescencia y **Nav-gal** produjeron la reducción de células senescentes en un modelo ortotópico de cáncer de pulmón y la disminución del tamaño tumoral en ratones xenoinjertados con células de cáncer de pulmón humanas. Por otra parte, se reduce significativamente la trombocitopenia a las dosis de tratamiento, consiguiéndose así una mejora en el perfil terapéutico del fármaco.

Por último, en el capítulo ocho, se presentan las conclusiones principales extraídas de los estudios con los diferentes sistemas desarrollados, así como las conclusiones generales extraídas de esta tesis doctoral. El desarrollo de sondas, nanomateriales y profármacos para detectar y eliminar selectivamente células senescentes *in vivo* se presenta como una nueva estrategia con gran potencial en el campo de las enfermedades relacionadas con el envejecimiento. Se espera que los resultados obtenidos en esta tesis puedan servir como base para el desarrollo de nuevas sondas moleculares y senolíticos para el diagnóstico y tratamiento temprano de diferentes enfermedades, así como para el seguimiento en pacientes de tratamientos senoterapéuticos.

Resum

La present tesi doctoral titulada “**Noves sondes, portadors i pro-fàrmacs dirigits a cèl·lules senescentes *in vivo***” es centra en el disseny, preparació, caracterització i avaluació de sondes basades en fluoróforos funcionalitzats o nanopartícules, així com en el desenvolupament de profàrmacs, aplicades a el camp de la senescència cel·lular.

En el primer capítol s'introdueixen, a nivell general, els diferents conceptes relacionats amb el reconeixement molecular i la detecció de biomarcadors. Seguidament s'introdueixen conceptes bàsics de senescència cel·lular i envelliment, així com el paper que juguen les cèl·lules senescentes a nivell fisiològic, en les malalties associades a l'envelliment cel·lular i en el càncer. Finalment, s'aborda la creixent necessitat de desenvolupar noves eines de diagnòstic i teràpies centrades en la detecció i tractament d'aquestes malalties.

En el segon capítol, s'exposen els objectius generals de la present tesi doctoral així com els objectius concrets que són abordats en els diferents capítols experimentals.

En el tercer capítol es descriu una nova sonda molecular per a la detecció de senescència *in vivo*. En concret, es descriu el disseny d'una sonda de dos fotons basada en un fluorófor de naftalimida connectat, mitjançant un èster metílic de L-histidina, amb una galactosa acetilada que està unida a un dels àtoms de nitrogen aromàtic de la L-histidina a través d'un enllaç N-glicosídic hidrolitzable (**AHGa**). La sonda inicial presenta una baixa emsió però en cèl·lules senescentes es transforma en un fluorófor amb alt rendiment quantinc que permet visualitzar aquestes cèl·lules a causa de la hidròlisi de l'enllaç N-glicosídic per l'enzim β -galactosidasa sobreexpressada en aquest tipus de cèl·lules. La sonda és capaç de detectar *in vitro* cèl·lules de melanoma humà SK-Mel-103 tractades amb quimioteràpia inductora de senescència enfront de cèl·lules control.

Adicionalment, es va validar la detecció *in vivo* de senescència en ratolins amb xenoinjerts tumorals tractats amb quimioteràpia inductora de senescència.

Basant-nos en els resultats obtinguts en el capítol tres, en el capítol quatre es descriu un sistema similar però en aquest cas amb un fluoròfor amb una major longitud d'ona d'excitació i d'emissió (**HeckGal**).

La nova sonda és capaç de detectar cèl·lules senescentes causa de la sobreexpressió de l'enzim β -galactosidasa associada a senescència en gran varietat de línies cel·lulars amb diversos mètodes d'inducció de senescència. Aquesta sonda es va validar també *in vivo* en un model ortotòpic de càncer de mama de ratolí tractat amb quimioteràpia inductora de senescència, i en un model de ratolí de fibrosi renal.

Seguidament, en el capítol cinc, ens centrem en un nou concepte de sondes moleculars no invasives, que proporcionen un senyal fàcilment llegible a través de simples mesures de fluorescència de l'orina pel fet que existeix una creixent necessitat de mètodes de diagnòstic no invasius, barats i versàtils. Aquesta idea es va dur a terme mitjançant la funcionalització d'un fluoròfore comú amb grups que li confereixen característiques diürètiques (ràpida eliminació renal) i el concepte es va aplicar a el disseny d'una sonda per a la detecció en orina de la càrrega senescente en diversos models. La sonda (**Cy7Gal**) està basada en la cianina-7 que és hidrolitzada per l'enzim β -galactosidasa en un fluoròfor altament emissiu **Cy7**. **Cy7Gal** i **Cy7** contenen restes d'àcid sulfònic que augmenten la seua solubilitat en aigua i desencadenen la seua ràpida excreció pel sistema urinari. El grau de senescència es va quantificar per mesurament directe de fluorescència en orina en tres models de senescència en ratolins: (i) un model ortotòpic de càncer de mama de ratolí en ratolins BALB/cByJ amb senescència induïda per quimioteràpia; (ii) ratolins BALB/cByJ envellits de manera natural; i (iii) ratolins amb senescència accelerada (SAMP8, de l'anglès Senescence Accelerated Mouse-Prone 8). A més, les imatges IVIS *ex vivo* permeten l'avaluació de senescència en diversos òrgans. La

sonda **Cy7Gal** és el primer exemple per a la detecció i quantificació no invasiva en orina de la presència *in vivo* de cèl·lules senescentes i pot servir com a base en el desenvolupament de noves sondes moleculars per al diagnòstic ràpid en orina de diferents malalties, així com per al seguiment de tractaments terapèutics.

Finalment en el que a detecció de senescència cel·lular es refereix, es presenta en el capítol sis la detecció òptica *in vivo* de senescència cel·lular mitjançant l'ús de nanopartícules de sílice mesoporoses (**S3**) carregades amb el fluorófor Nile Blue (**NB**) i funcionalitzades en la seua superfície externa amb un galactohexasacàrido. El **NB** està aprovat per la FDA i presenta emissió en l'infraroig pròxim (NIR). L'emissió a 672 nm de **NB** es troba pràcticament desactivada dins dels porus de les nanopartícules **S3**, degut a la planaritat de la molècula i la seua capacitat per a donar interaccions d'apilament- π . Les nanopartícules **S3** estan cobertes amb un galactohexasacàrid que els confereix una selectivitat específica per les cèl·lules senescentes. En presència de aquestes cèl·lules i de β -galactosidasa, el galactohexasacàrid és hidrolitzat, produint-se l'alliberament de **NB** que torna a emetre fluorescència. L'eficàcia de la sonda per a detectar òpticament la senescència cel·lular es va validar *in vitro* en cèl·lules senescentes SK-Mel-103 i 4T1, i en ratolins BALB/cByJ amb tumors ortotòpics de càncer de mama tractats amb quimioteràpia *in vivo*.

Una vegada aconseguits els objectius planificats referent al diagnòstic, en el capítol set, es va abordar la millora d'un dels senolítics més potents i àmpliament conegut en el camp de la senescència cel·lular que existeix hui dia en el mercat: el Navitoclax, també conegut com ABT-263. Moltes potencials teràpies senolítiques a humans es veuen obstaculitzades per l'especificitat subòptima dels fàrmacs senolítics per a les cèl·lules senescentes i les altes toxicitats que redueixen les seues finestres terapèutiques. El senolític Navitoclax és un inhibidor selectiu de les proteïnes antiapoptotiques BCL-2, BCL-XL i BCL-W, i el seu principal efecte secundari en humans és que indueix la mort apoptòtica de les plaquetes

(trombocitopenia) en dependre aquestes de BCL-XL per a la seua supervivència. L'efecte senolítico d'aquest compost prové de la sobreexpressió de proteïnes de la família BCL-2 en cèl·lules senescentes. Tenint en compte l'anterior, es dissenya i va preparar un pro-fàrmac a través de la funcionalització de Navitoclax amb un residu galactosídico (**Nav-gal**), amb la finalitat que aquest no fóra capaç d'inhibir les proteïnes antiapoptóticas de la família BCL-2 quan està unit al sucre, evitant així la mort de cèl·lules no senescentes. En entrar en el lisosoma de cèl·lules senescentes, l'enllaç glicosídic s'hidrolitza per acció de l'enzim β -galactosidasa (SA β Gal), obtenint Navitoclax lliure que mata a la cèl·lula. La pro-droga **Nav-gal** es va validar en cèl·lules senescentes de càncer de pulmó humanes (A549) i de ratolí (L1475 (luc)); línies cel·lulars de càncer de melanoma humà (SK-Mel-103) i glàndula mamària de ratolí (4T1); cèl·lules de carcinoma colorectal (HCT116); fibroblastos de pulmó de ratolí (cèl·lules MLg) i fibroblastos de pulmó humà (ER: cèl·lules Mek IMR90) observant un IC50 similar al Navitoclax en cèl·lules senescentes però protegint a les cèl·lules no senescentes. A més els estudis *in vivo* després del tractament amb un inductor quimioterapèutic de senescència i **Nav-gal** van produir la reducció de cèl·lules senescentes en un model ortotòpic de càncer de pulmó i la disminució de la grandària tumoral en ratolins xenoinjertados amb cèl·lules de càncer de pulmó humanes. A més es redueix significativament la trombocitopenia a les dosis de tractament, aconseguint-se així una millora en el perfil terapèutic del fàrmac.

Finalment, en el capítol huit, es presenten les conclusions principals extretes dels estudis amb els diferents sistemes desenvolupats així com les conclusions generals extretes d'aquesta tesi doctoral. El desenvolupament de sondes, nanomaterials i profàrmacos per a detectar i eliminar selectivament cèl·lules senescentes *in vivo* es presenta com una nova estratègia amb gran potencial en el camp de les malalties relacionades amb l'envelliment. S'espera que els resultats obtinguts en aquesta tesi puguin servir com a base per al desenvolupament de

noves sondes moleculars i senolítiques per al diagnòstic i tractament primerenc de diferents malalties, així com per al seguiment en pacients de tractaments

Abstract

This PhD thesis entitled "**New probes, carriers and pro-drugs to target senescent cells *in vivo***" focuses on the design, preparation, characterization and validation of probes based on functionalized fluorophores or nanoparticles coated with biomolecules, as well as on the development of prodrugs, applied to the field of cellular senescence. The first chapter introduces, at a general level, the different concepts related to molecular recognition and the detection of biomarkers. Next, basic concepts of cellular senescence and aging are introduced, as well as the role that senescent cells play at a physiological level, in diseases associated with cellular aging and in cancer. Finally, the growing need to develop new diagnostic tools and therapies focused on the detection and treatment of these diseases is also addressed.

The second chapter sets out the general objectives of this doctoral thesis as well as the specific objectives that are addressed in the different experimental chapters.

The third chapter describes a new molecular probe for the detection of senescence *in vivo*. Specifically, the design of a two-photon probe based on a naphthalimide fluorophore connected, by means of a methyl ester of L-histidine, with an acetylated galactose that is attached to one of the aromatic nitrogen atoms of L-histidine through a hydrolyzable N-glycosidic bond (**AHGa**) is described. The initial probe has a low emission but it is transformed in senescent cells into a fluorophore with high quantum yield due to the hydrolysis of the N-glycosidic bond by the enzyme β -galactosidase overexpressed in senescent cells. The probe is capable of detecting SK-Mel-103 human melanoma cells treated with senescence-inducing chemotherapy *in vitro* against control cells. Additionally, the *in vivo* detection of senescence was validated in mice with tumor xenografts treated with senescence-inducing chemotherapy.

Based on the results obtained in chapter three, chapter four describes a similar fluorophore with a longer excitation wavelength (**HeckGal**). The new probe was capable of detecting senescent cells due to the overexpression of the enzyme β -galactosidase associated with senescence in a wide variety of cell lines and using various methods of inducing senescence. This probe was also validated *in vivo* in a mouse orthotopic model of breast cancer treated with senescence-inducing chemotherapy, and in a mouse model of renal fibrosis.

Chapter five focuses on a new concept of molecular probes, which provide an easily readable signal through simple measurements of fluorescence in urine. This idea was carried out by functionalizing a probe with groups that confer diuretic characteristics (rapid renal clearance) and the concept was applied to the design of a probe to detect cellular senescence burden in various senescence models. The probe (**Cy7Gal**) is based on cyanine-7 which is hydrolyzed by the enzyme β -galactosidase into a highly emissive **Cy7** fluorophore. **Cy7Gal** and **Cy7** contain sulfonic acid residues that increase their solubility in water and trigger their rapid excretion through the urinary system. The degree of senescence was quantified by direct measurement of fluorescence in urine in three models of senescence in mice: (i) an orthotopic model of breast cancer in BALB / cByJ mice with chemotherapy-induced senescence; (ii) naturally aged BALB / cByJ mice; and (iii) mice with accelerated senescence (SAMP8, Senescence Accelerated Mouse-Prone 8). In addition, IVIS *ex vivo* images allow the assessment of senescence in various organs. Our findings demonstrate that renal clearable fluorogenic probes are a versatile modular tool that opens new opportunities to develop simple diagnoses in urine for a variety of diseases where the abnormal enzymatic activity is a biomarker.

Finally, regarding the detection of cellular senescence, chapter six reports the *in vivo* optical detection of cellular senescence through the use of mesoporous silica nanoparticles (**S3**) loaded with the Nile Blue (**NB**) fluorophore and

functionalized on the outer surface with a galactohexasaccharide. **NB** is FDA approved for use in humans and displays a Near Infrared (NIR) emission. The emission at 672 nm of NB is practically deactivated within the pores of the **S3** nanoparticles, due to the planarity of the molecule and its ability to give stacking- π interactions. **S3** nanoparticles are functionalized with a galactohexasaccharide that gives them a specific selectivity towards senescent cells. In the presence of these cells, β -galactosidase hydrolyzes the capping galactosaccharide resulting in the release of the **NB** fluorophore. The efficacy of the probe to optically detect cellular senescence was validated *in vitro* in senescent SK-Mel-103 and 4T1 cells, and *in vivo* in BALB / cByJ mice with orthotopic breast cancer tumors treated with chemotherapy.

Once the planned objectives related with diagnosis were achieved, chapter seven addressed the chemical modification and uses of a powerful and widely known senolytic: Navitoclax, also known as ABT-263. Many potential human senolytic therapies are hampered by the suboptimal specificity of senolytic drugs for senescent cells and the high toxicities that reduce their therapeutic windows. The senolytic Navitoclax is a selective inhibitor of the antiapoptotic proteins BCL-2, BCL-XL and BCL-W, and its main side effect in humans is that it induces apoptotic death of platelets (thrombocytopenia). The senolytic effect of navitoclax comes from the overexpression of proteins of the BCL-2 family in senescent cells. Taking into account the above, a pro-drug was designed and prepared through the functionalization of Navitoclax with a galactosidic residue (**Nav-gal**). Upon entering the lysosome of senescent cells, the glycosidic bond is hydrolyzed by the action of the enzyme β -galactosidase, obtaining free Navitoclax that kills the cell. The prodrug **Nav-gal** was validated in human (A549) and mouse (L1475 (luc)) lung cancer senescent cells; human melanoma cancer cell lines (SK-Mel-103) and mouse mammary gland (4T1); colorectal carcinoma cells (HCT116); mouse lung fibroblasts (MLg cells) and human lung fibroblasts (ER: Mek IMR90

cells) observing an IC50 similar to Navitoclax in senescent cells but protecting non-senescent cells. Furthermore, *in vivo* studies after treatment with a chemotherapeutic senescence inducer and **Nav-gal** produced a reduction of senescent cells in an orthotopic model of lung cancer and a decrease in tumor size in xenografted mice with human lung cancer cells. In addition, thrombocytopenia was significantly reduced at treatment doses, thus achieving an improvement in the therapeutic profile of the drug.

Finally, in chapter eight, the main conclusions obtained from the studies with the different systems developed are presented, as well as the general conclusions drawn from this doctoral thesis. The development of probes, nanomaterials and prodrugs to selectively detect and eliminate senescent cells *in vivo* is presented as a new strategy with great potential in the field of diseases related to aging. It is expected that the results obtained in this thesis can serve as the basis for the development of new molecular and senolytic probes for the early diagnosis and treatment of different diseases, as well as for the follow-up in patients with senotherapeutic treatments.

Publications

Results of this PhD Thesis and other contributions have resulted in the following scientific publications.

Total number of Journal Publications	18
Total number of conference proceeding	32
Journal Publications as 1 st Author	13
Total of number Citations	287
Total number of Patents (1 License)	3
Number of Book Chapters Published	1

Journal Publications:

1. Lozano-Torres, B. et al. (2016). Selective and Sensitive Chromogenic Detection of Trivalent Metal Cations in Water. *Bull. Chem. Soc. Jpn.* 89, 498-500. [IF: 4.488, Citation: 8]
2. Lozano-Torres, B. et al. (2017). Pseudorotaxane capped mesoporous silica nanoparticles for 3,4-methylenedioxymethamphetamine (MDMA) detection in water. *Chem. Commun.* 53, 3559-3562. [IF: 5.996, Citation: 13] UPV website cover and disseminated in national newspapers.
3. Llopis-Lorente, A.,[†] Lozano-Torres, B.,[†] et al. (2017). Mesoporous silica materials for controlled delivery based on enzymes. *J. Mater. Chem. B*, 5, 3069-3083. [IF: 5.344, Citation: 46]. [†]These author contributed equally in this word
4. Lozano-Torres, B. et al. (2017). An OFF-ON Two-Photon Fluorescent Probe for Tracking Cell Senescence in Vivo. *J. Am. Chem. Soc.* 139, 8808-8811. [IF: 14.612, Citation: 67] UPV website cover and disseminated in national newspapers.
5. Lozano-Torres, B. et al. (2018). Anilinopyridine–metal complexes for the selective chromogenic sensing of cyanide anion. *J. Coord. Chem.* 71, 786-796. [IF: 0.665, Citation: 3]
6. Garrido, E., et al. (2018). Chromogenic and Fluorogenic Probes for the Detection of Illicit Drugs. *ChemistryOpen*, 7, 401-428. [IF: 2.370, Citation: 7]

7. Muñoz-Espin, D. et al. (2018). A versatile drug delivery system targeting senescent cells. *EMBO Mol. Med.* 10, e9355. [IF: 10.624, Citation: 75] UPV website cover and disseminated in national newspapers.
8. Pla, L.,[†] Lozano-Torres, B.,[†] et al. (2019). Overview of the Evolution of Silica-Based Chromo-Fluorogenic Nanosensors. *Sensors.* 19, 1-23. [IF: 3.275, Citation: 4].[†]These author contributed equally in this word
9. Lozano-Torres, B., et al. (2019). The Chemistry of Senescence. *Nat. Rev. Chem.* 3, 426–441. [IF: 34.953, Citation: 22]
10. Garrido, E. et al. (2020). Nanosensor for Sensitive Detection of the New Psychedelic Drug 25I-NBOMe. *Chem. Eur. J.* 26, 2813-2816. [IF: 4.857, Citation: 4]
11. González-Gualda, E.,[†] Pàez-Ribes M.,[†] Lozano-Torres, B.[†] et al. (2020). Galacto-conjugation of Navitoclax as an efficient strategy to increase senolytic specificity and reduce platelet toxicity. *Aging Cell.* 19, e13142. [IF: 7.346, Citation: 23] UPV website cover and disseminated in national newspapers. [†]These author contributed equally in this word
12. Lozano-Torres et al. (2020). Real time in vivo detection of cellular senescence through the controlled release of NIR fluorescent dye Nile Blue. *Angew Chem Int Ed.* 9(35), 15152-15156. [IF: 12.257, Citation: 5]
13. García-Fernández, A.,[†] Lozano-Torres, B.[†] et al. (2020). Electro-responsive films based on voltage-gated mesoporous silica nanoparticles grafted onto PEDOT-based conducting polymer. *J Control Release.* 323, 421-430. [IF: 7.877, Citation: 1].[†]These author contributed equally in this word
14. Galiana, I., Lozano-Torres, B. et al. (2020). Preclinical Antitumor Efficacy of Senescence-inducing Chemotherapy Combined with a NanoSenolytic. *J Control Release.* 323, 624-634. [IF: 7.877, Citation: 8]
15. Dominguez, M., Blandez, JF., et al. (2021). A Nanoprobe Based on Gated Mesoporous Silica Nanoparticles for The Selective and Sensitive Detection of Benzene Metabolite t,t-Muconic Acid in Urine. *Chemistry-A European Journal.*, 27 1306-1310. [IF: 4.857]
16. Lozano-Torres, B., et al. (2021) A two-photon probe based on naphthalimide-styrene fluorophore for the in vivo tracking of cellular senescence. *Anal. Chem.* 413, 2361-2388 [IF: 6.350]

17. Lozano-Torres, B., et al. (2021) Chromo-fluorogenic probes for beta-galactosidase detection. *Anal. Bioanal. Chem.* 2361-2388, 413 . [IF: 3.286, Citation: 1]
18. Lozano-Torres, B., et al. (2021). A renal clearable fluorogenic probe for in vivo detection of cellular senescence. *Submitted*

Books:

1. Lozano-Torres, B. et al. (2020). Chapter: Novel Probes and Carriers to target senescent cells. *Senolytics in Disease, Ageing and Longevity. Springer Nature.* Online ISBN: 978-3-030-44903-2. Print ISBN: 978-3-030-44902-5. [Downloads: 137]

International Conferences:

Oral presentations:

1. Lipofuscin labelling through biorthogonal strain-promoted azide-alkyne cycloaddition for the detection of senescent cells in tissues. IX Mediterranean Organic Chemistry Meeting (IX REQOMED). Murcia, Spain, 25/10/2019.
2. Exploring new avenues for detection and clearance of cell senescence. Annual Conference. CIBER-BBN 2019. Tarragona, Spain, 22/10/2019.
3. Lipofuscin labelling through biorthogonal strain-promoted azide-alkyne cycloaddition for the detection of senescent cells in tissues. International Symposium on Dyes & Pigments. Seville, Spain, 11/09/2019.
4. A new two-photon fluorescent probe for in vivo senescent cells detection. International Symposium on Dyes & Pigments. Seville, Spain, 11/09/2019.
5. Novel OFF-ON two photon probes for senescence detection. 2nd Annual Meeting of the Spanish Network of Cellular Senescence: Senescence and Cancer. Madrid, Spain, 25/11/2016.
6. New gated-nanoparticles and molecular probes to detect and remove senescent cells. Tercera Reunión Annual of the Network of Excellence "Cellular Senescence: From mechanisms to therapies". Senestherapy. Madrid, Spain, 24/11/2017.
7. An OFF-ON two photon fluorescent probe for tracking cell senescence in vivo. XII Annual Conference CIBER-BBN 2018. Valladolid, Spain, 13/11/2018.

Publications

- 8.** Novel diagnostic tools for lung cancer early detection. International Cell Senescence Association Conference (ICSA 2017). The Ins and Outs of Cellular Senescence: Understanding the Biology to Foster Healthy Aging and Suppression of Disease. Paris, France, 19/05/2017.
- 9.** Senescence-associated nanoparticles as selective drug delivery system. BIT's 7th Annual International Symposium of Drug Delivery Systems 2017. Prague, Czech Republic, 14/07/2017.
- 10.** New Nile Blue-loaded mesoporous silica nanoparticles for in vivo and real time senescent cells detection. XIII International Workshop on Sensors and Molecular Recognition (IWOSMOR 2019). Valencia, Spain, 05/07/2019.

Poster presentations:

- 1.** In search of vascular senescent cells. Reunión Anual Red de Terapia Celular (TERCEL 2019). Santiago de Compostela, Spain, 29/11/2019.
- 2.** In search of vascular senescent cells. VII International Congress on Research and Innovation in Neurodegenerative. Diseases (CIIEN 2019). 20/09/2019.
- 3.** In search of vascular senescence. XIII International Workshop on Sensors and Molecular Recognition (IWOSMOR 2019). Valencia, Spain, 05/07/2019.
- 4.** New two-photon fluorescent probe for senescent cells detection in an in vivo breast cancer model. XIII International Workshop on Sensors and Molecular Recognition (IWOSMOR 2019). Valencia, Spain, 05/07/2019.
- 5.** Biorthogonal strain-promoted azide-alkyne cycloaddition for the fluorescent detection of senescent cells through lipofuscin labelling. XII International Workshop on Sensors and Molecular Recognition (IWOSMOR 2018). Burjassot, Spain, 06/07/2018
- 6.** In vivo synthesis of a senolytic drug using a biorthogonal reaction catalyzed with heterogeneous copper nanoparticles. XII International Workshop on Sensors and Molecular Recognition (IWOSMOR 2018). Burjassot, Spain, 06/07/2018.
- 7.** Targeting senescent cells: a novel strategy to selectively kill senescent cells. III Encuentro de Investigadores en Cáncer de la Comunidad Valenciana Ciutat D'Alcoi. Alcoi, Spain, 20/04/2018

- 8.** Targeting senescent cells: a novel strategy to selectively kill senescent cellsII National Congress of Young Researchers in Biomedicine. IV Congress of Biomedicine PhD students Valencia. Valencia Spain, 24/11/2017.
- 9.** Senescent-associated nanoparticles as therapeutic derivatives. NanoBio&Med2017. Barcelona, Spain, 24/11/2017.
- 10.** An OFF-ON two-photon fluorescent probe for tracking cell senescence in vivo. XI International Workshop on Sensors and Molecular Recognition. Valencia, Spain, 07/07/2017.
- 11.** Chemical design of novel anthracycline derivatives as potencial senolytic pro-drugs. XI International Workshop on Sensors and Molecular Recognition. Valencia, Spain, 07/07/2017.
- 12.** Targeting senescent cells: a novel strategy to selectively kill senescent cells. XI International Workshop on Sensors and Molecular Recognition. Valencia, Spain, 07/07/2017.
- 13.** 3,4-methylenedioxymethamphetamine (mdma) detection in water with pseudo-rotaxane capped mesoporous silica nanoparticles. XI International Workshop on Sensors and Molecular Recognition. Valencia, Spain, 07/07/2017.
- 14.** Senescent-associated nanoparticles as drug delivery system. 13th Italian Conference on Supramolecular Chemistry. Santa Margherita di Pula (CA), Italy, 21/06/2017.
- 15.** Controlled drug delivery system in senescent cells using galactoligosaccharide-capped nanoparticles. X Annual Conference. CIBER-BBN 2016. Seville, Spain, 29/11/2016.
- 16.** Azo molecular gate in magnetic silica mesoporous material MCM-41 aiming colon epithelial delivery to treat Inflammatory Bowel Diseases. IX International Workshop on Sensors and Molecular Recognition. Valencia, Spain, 07/07/2015
- 17.** Pseudo-rotaxane capped mesoporous silica nanoparticles for melamine detection. IX International Workshop on Sensors and Molecular Recognition. Valencia, Spain, 07/07/2015.
- 18.** Selective and sensitive chromogenic detection of trivalent metal cations in water. IX International Workshop on Sensors and Molecular Recognition. Valencia, Spain, 07/07/2015.

Publications

- 19.** Controlled delivery in senescent cells: galactoligosaccharide-capped nanoparticles as selective drug delivery system. X International Workshop on Sensors and Molecular Recognition. Valencia, Spain, 08/07/2016.
- 20.** Electrochemically stimulated molecules release from new hybrid MCM-41 materials. X International Workshop on Sensors and Molecular Recognition. Valencia, Spain, 08/07/2016.
- 21.** Gated mesoporous silica nanoparticles functionalised PEDOT:PSS as a chemical bidirectional system of communication with neurons. X International Workshop on Sensors and Molecular Recognition. Valencia, Spain, 08/07/2016.
- 22.** Pseudo-rotaxane capped mesoporous silica nanoparticles for electron rich molecules detection X International Workshop on Sensors and Molecular Recognition. Valencia, Spain, 08/07/2016.

Patents, Industrial and Intellectual Property:

- 1.** 2019: Compound for the Detection of Senescent Cells and its Use. P201930893.
- 2.** 2017: Therapeutic Nanoparticles. EP17382901.1
- 3.** 2017: Therapeutic Derivatives. PCT/IB2017/000222

Awards:

- 1. Young Researchers Award.** CIBER-BBN. 12th- 13th Valladolid, Spain. 2018.400 €
- 2. Research Fellow** for FPU's mobility. Ministry of Education, Culture and Sports. Spain. 2012. 4.290 €

Abbreviations and Acronyms

4-OHT	4-hydroxytamoxifen
4T1	Breast cancer cell line
A1155463	Selective inhibitor of BCL-XL
A1331852	Selective inhibitor of BCL-XL
A549	Adenocarcinomic human alveolar basal epithelial cells
ABT-263	Senolytic known as Navitoclax. 4-(4-[[2-(4-Chlorophenyl)-5,5-dimethyl-1-cyclohexen-1-yl]methyl]-1-piperazinyl)-N-[[4-[[{(2R)-4-(4-morpholinyl)-1-(phenylsulfanyl)-2-butanyl]amino}-3-[[trifluoromethyl)sulfonyl]phenyl)sulfonyl]benzamide
ABT-737	Senolytic known as Venetoclax. 4-{4-[(4'-Chloro-2-biphenyl)methyl]-1-piperazinyl}-N-[[4-[[{(2R)-4-(dimethylamino)-1-(phenylsulfanyl)-2-butanyl]amino}-3-nitrophenyl)sulfonyl]benzamide
ACN	Acetonitrile
AcOEt	Ethylacetate
AD	Adipose tissue
AHGa	Two-photon probe presented in this PhD thesis which is hydrolyzed into AH
AKP	Alkaline phosphatase
AKT	Also known as PKB, protein kinase B
ALB	Albumin
APTES	3-aminopropyltriethoxysilane
ATCC	American Type Culture Collection
ATM/ ATR	Ataxia–telangiectasia mutated/ Ataxia telangiectasia and Rad3-related protein
ATP	Adenosine 5'-triphosphate
ATR	Attenuated total reflection (ATR-FTIR)
B2MG	β 2-microglobulin
BCL	Anti-apoptotic B cell lymphoma
BCL-2	B cell Lymphoma
BCL-XL	B cell lymphoma-extra large
BET	Brunauer-Emmet-Teller
BIBR1532	Non-nucleosidic inhibitor of the native and recombinant human telomerase
BIL	Bilirubin
BJ	Human fibroblasts

Abbreviations

BJH	Barret-Joyner-Halenda
BM	Bone marrow
BMVC4	3,6-bis(4-methyl-2-vinylpyrazinium iodine) carbazole
CaCO₃	Calcium carbonate
CCL20	Chemokine (C-C motif) ligand 20
CD4+ T	T helper cells
CD8+ T	T helper cells cluster of differentiation,
CD-9	A cell surface glycoprotein
CDCI₃	Deuterium chloroform
CDDP	Cisplatin
CDIs	Coefficients of drug interactions
CDK	Cyclin-dependent kinases
COSY	Correlated spectroscopy
CQDs	Carbon Quantum dots
CTAB	Cetyltrimethylammonium bromide
CTP	Cytidine triphosphate
CyBC9	Probe for cellular senescence detection based on membrane potential of mitochondria
DC1787	Cells from patients suffering congenital dyskeratosis
DLS	Dynamic light scattering
DMEM	Dulbecco's Modified Eagle Medium
DMSO	Dimethyl sulfoxide
DNA	Deoxyribonucleic acid
Dox/Doxo	Doxorubicin
E2F	Transcription factors involved in cell proliferation, differentiation, and apoptosis
EA	Elemental analysis
EDC/NHS	1-ethyl-3-(3-dimethylaminopropyl)carbodiimide/ <i>N</i> -hydroxysuccinimide
EDX	Energy dispersive x-ray spectroscopy
EJ	Bladder cancer cells
Et₂O	Diethylether
FA	Folic acid
FACS	Fluorescence-Activated Cell Sorting
FBS	Fetal Bovine Serum
FDA	Food and Drug Administration
FDG	Fluorescein-di-(β -D-galactopyranoside
FITC	Fluorescein isothiocyanate

FL118	4R)-4-Ethyl-4-hydroxy-8,9-methylenedioxy-1H-pyrano[3',4':6,7]indolizino[1,2-b]quinoline-3,14(4H,12H)-dione
FT-IR	Fourier-transform infrared spectroscopy
GalNP	MSN capped with galactoligosaccharide
GalNP(Dox)	MSN capped with galactoligosaccharide loaded with doxorubicin
GalNP(Nav)	MSN capped with galactoligosaccharide loaded with navitoclax
Gal-Pro	Also named NIR-BG, probe for senescent cells detection.
GLB1	Galactosidase beta 1
GOT	Aspartate transaminase
GPT	Glutamic pyruvic transaminase
GROα	Growth-regulated oncogene α
H2O2	Hydrogen peroxide
H460	A human large-cell lung carcinoma line
HAT	Histone acetyltransferase
HCT116	Human colon cancer cell line
HDAC	Histone deacetylase
HDF	Human dermal fibroblasts
HeckGal	Two-photon probe presented in this PhD thesis which is hydrolyzed into Heck fluorophore
HEK	Human embryonic kidney
HeLa	Henrietta Lacks, immortal cells
heMSCs	human early mesenchymal stromal cells
HGF	Hepatocyte growth factor
HIF1α	Hypoxia-inducible factor 1
HPLC	High-performance liquid chromatography
HRas	Harvey Rat Sarcoma
HR-TEM	High-resolution transmission electron microscopy
HSP90	Heat shock protein
HT1080	Fibrosarcoma cells
HUVEC	Human umbilical vein endothelial cells
I.V.	Intravenous
IC50	Half maximal inhibitory concentration
ICG	Indocyanine green
ICP-MS	Inductively coupled plasma mass spectrometry
IGFBPs	Insulin-like growth factor-binding proteins

IHC	Immunohistochemistry
IL-1 β	Interleukin-1 β
IL-6	Interleukin-6
IUPAC	Union of Pure and Applied Chemistry
IVIS	<i>In vivo</i> imaging system
Ki67	Nuclear protein that is associated with and may be necessary for cellular proliferation.
LacZ	Lactose operon
MCF7	Michigan Cancer Foundation-7 breast cancer cell
MCM	Mobil Composition of Matter
MDM2	Murine double minute 2
MeOH	Methanol
MRE11	Double-strand repair protein
MSNs	Mesoporous silica nanoparticles
mTOR	Mammalian Target of Rapamycin
MTT	3-(4,5-dimethylthiazol-2-yl)-2,5-diphenyltetrazolium bromide. Assay for cell viability
MUF	4-Methylumbelliferyl α -L-Fucopyranoside
MUG	4-Methylumbelliferyl β -D-galactopyranoside
NanoMIPs	Molecularly imprinted polymer nanoparticles
Nav-gal	Potent senolytic prodrug developed in this thesis
NB	Nile Blue A perchlorate
NIR	Near-infrared
nm	Nanometers
NMR	Nuclear magnetic resonance
NPs	Nanoparticles
NSCLC	Non-small cell lung cancer
ONPG	ortho-nitrophenyl- β -galactoside
OVCAR3	Human ovarian carcinoma cell line with androgen and estrogen receptors
OVCAR4	Human ovarian carcinoma cell line
OVCAR5	Human ovarian carcinoma cell line
OVCAR8	Human ovarian carcinoma cell line
OVK18	Human cell line derived from ovarian cancer
p15	Cyclin-dependent kinase 4 inhibitor B
p16	Cyclin-dependent kinase 2 inhibitor A
p21	Cyclin-dependent kinase 1 inhibitor
p27	Cyclin-dependent kinase 1 inhibitor B

p53	Cellular tumor antigen p53, the Guardian of the Genome.
PBS	Phosphate buffer saline
PEG	Polyethyleneglycol
PET	Positron-emission tomography
PFA	Paraformaldehyde
PI3K	Phosphatidylinositol-4,5-bisphosphate 3-kinase
PKC,	Protein kinase C
pRb	Phosphorilated retinoblastoma
PTFE	Polytetrafluoroethylene
PXRD	Powder x-ray diffraction
Rb	Retinoblastoma protein
RhB	Rhodamine B
RNA	Ribonucleic acid
ROS	Reactive oxygen species
Rpe	Retinal pigment epithelial cell line
RPMI	Roswell Park Memorial Institute
SAHF	Senescence- associated heterochromatin foci
SASP	Senescence-associated secretory phenotype
SAβGal	Senescence Associated β -Galactosidase
SBB	Sudan Black B
SCAPs	Senescent-cell antiapoptotic pathways
SCID	Severe combined immunodeficient
SD	Standard deviation
SEM	Standard error of the mean
SG1	A two-photon ratiometric probe for senescent cells detection
SHIN3	Human ovarian serous cystadenocarcinoma
shRNA	Short hairpin RNA
SIPS	Stress-induced premature senescence
siRNA	small interfering RNA
SK-Mel-103	Human melanoma cell line
SKOV3	Ovarian serous cystadenocarcinoma
Spider-Gal	<i>E</i> -2-[2-(6-hydroxy-2,3-dihydro-1 <i>H</i> -xanthen-4-yl)vinyl]-3,3-dimethyl-1-propyl-3 <i>H</i> -indole-1-ium
SRP	Senescence-responsive fluorescent probe
SYUIQ-5	<i>N'</i> -(10 <i>H</i> -Indolo [3,2- <i>b</i>]quinolin-11-yl)- <i>N</i> , <i>N</i> -dimethyl-propane-1,3-diamine
TBDPSCI	tert-butylchlorodiphenylsilane
^tBuOOH	tert-Butyl hydroperoxide

Abbreviations

TEM	Transmission electron microscopy
TEM	Transmission electron microscopy
TEM-EDX	Transmission electron microscopy-Energy-dispersive X-ray spectroscopy
TEOS	Tetraethyl orthosilicate
TGA	Thermogravmetric analysis
TIF	Telomere-dysfunction-induced foci
TMAH	Tetramethylammonium hydroxide
TMS	Tetramethylsilane
TUNEL	Terminal deoxinucleotidil transferasa
UBX101	A senolytic for osteoarthritis treatment
UC	Wharton's Jelly tissue
UV-Vis	Ultraviolet-Visible
α-Fuc	α -L-fucosidase
β-CD-CQDs	β -cyclodextrin-functionalized carbon quantum dots
β-Gal	Beta-galactosidase
γH2AX	H2A histone family member X

Chapter 1 | General Introduction

1.1 Molecular recognition

The term “*molecular recognition*” can be defined as the specific interaction between two or more molecules through non-covalent bonds (hydrogen bonds, metal coordination, hydrophobic forces, van der Waals forces, π - π , halogen, electrostatic and/or electromagnetic interactions, etc).¹ The guest and the host involved in molecular recognition exhibit molecular complementarity in terms of geometric and electronic features. Molecular recognition plays an important role in biological systems and is observed between receptor-ligand, antigen-antibody, DNA-protein, sugar-lectin, RNA-ribosome interactions.²

In 1894 Dr. Emil Fisher proposed the first model of molecular recognition: the lock and key principle, a concept closely related with host-guest interactions, applied to enzymes and substrates.³ In this case, enzymes are “*the lock*” and their substrates are “*the key*” that should present a complementary size and shape as shown in Figure 1. Although the “*lock-key*” principle simplifies the mechanism of action of most biological systems, it can explain their high selectivity and specificity. Selectivity is the ability of the host to distinguish among different guests, while specificity is related to the precision of the molecular recognition.⁴

1 J. M. Lehn, “Supramolecular Chemistry – Scope and Perspectives”. *Nobel Lecture*, **1987**

2 a) M. R. Lockett, H. Lange, B. Breiten, A. Heroux, W. Sherman, D. Rappoport, P. O. Yau, P. W. Snyder and G. M. Whitesides, “The Binding of Benzoarylsulfonamide Ligands to Human Carbonic Anhydrase is Insensitive to Formal Fluorination of the Ligand”. *Angew. Chem. Int. Ed.* **2003**, 52, 7714–7717 b) B. Breiten, M. R. Lockett, W. Sherman, S. Fujita, M. Al-Sayah, H. Lange, C. M. Bowers, A. Heroux, G. Krilov and G. M. Whitesides, “Water Networks Contribute to Enthalpy/Entropy Compensation in Protein–Ligand Binding”. *J. Am. Chem. Soc.* **2013**, 135, 15579–15584

3 H. E. Fischer, “Chemistry”. *Nobel Lecture*, **1966**

4 G. Bergmann, B. Von and O. P. Zinn, “Improvement in the definitions of sensitivity and selectivity”. *Anal. Chem.* **1987**, 59, 2522-2526

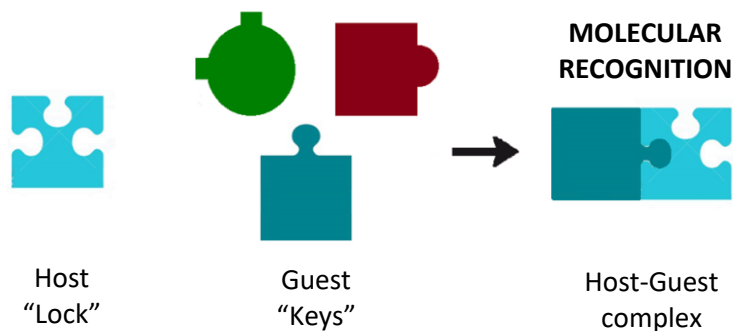


Figure 1. Schematic representation of the "lock-key" principle, which governs molecular recognition.

1.1.1 Molecular probes

Molecular recognition has been widely applied in the development of molecular sensors, also known as probes, chemical sensors or chemosensors. The IUPAC defines a chemosensor as "a device that transforms chemical information ranging from the concentration of a specific sample component to total composition analysis into an analytically useful signal".⁵

Molecular probes are -normally- organic molecules which, when interacting with target (bio)molecules, change one or more of their physicochemical features. These molecular probes have been extensively used in many research fields, such as molecular or chemical biology, drugs detection, monitoring of diseases, etc. Molecular probes are mainly formed by two subunits: the "signaling subunit" and the "binding site" (Figure 2). The binding site is responsible of the selective interaction with one specific guest. This selective recognition of one molecule among different analytes can be achieved by an accurate design of the binding site in order to introduce a high degree of complementarity (matching size, shape, charge, etc.) with the target analyte. On the other hand, the signaling subunit is a

5 a) A. Hulanicki, S. Geab and F. Ingman, "Chemical sensors definitions and classification". *Pure. Appl. Chem.* **1991**, 63, 1247-1250; b) U. E. Spichiger-Keller, "Chemical Sensors for Medical and Biological Applications". Wiley-VCH, **1998**.

molecular entity able to transduce the molecular interaction of the target analyte with the binding site into a measurable macroscopic signal generally related with the concentration of the former. Traditionally, changes in the optical properties (color or fluorescence) or a modification in the electrochemical features (redox potential) has been used as signal outputs.⁶

The design of molecular probes for the chromo-fluorogenic detection of different biomarkers or analytes is an alternative to traditional analytical techniques with advantages such as their chemical simplicity, ease of use, rapid response suitable for real time on-site detection, easy detection to the naked eye, etc. In spite of these remarkable features, the development of chromo-fluorogenic sensors for the selective and sensitive detection of certain analytes, especially biomolecules, is still poorly explored.⁷

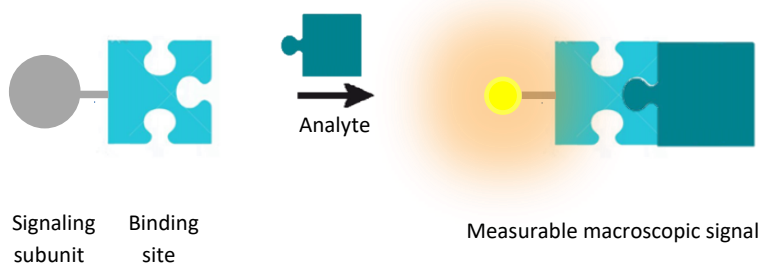


Figure 2. Schematic representation of a molecular probe.

6 a) R. Martínez-Máñez and F. Sancenón, "Fluorogenic and Chromogenic Chemosensors and Reagents for Anions". *Chem. Rev.* **2003**, 103, 4419-4476; b) L. E. Santos-Figueroa, M. E. Moragues, E. Climent, A. Agostini, R. Martínez-Máñez and F. Sancenón, "Chromogenic and fluorogenic chemosensors and reagents for anions. A comprehensive review of the years 2010–2011". *Chem. Soc. Rev.* **2013**, 42, 3489-3613.

7 E. Garrido, L. Pla, B. Lozano-Torres, S. El Sayed, R. Martínez-Máñez and F. Sancenón, "Chromogenic and fluorogenic probes for the detection of illicit drugs". *ChemistryOpen*. **2018**, 7, 401–428.

1.1.2 Nanotechnology

The functionalization of inorganic materials with molecular or supramolecular assemblies has led, in the recent years, to the preparation of hybrid materials, within the nanoscale range, with advanced functionalities.⁸ The grafting of organic (bio)molecules or supramolecules onto selected inorganic solids (with different natures, sizes and shapes) promotes the development of smart nanodevices with applications in several scientific fields.⁹ Inside the realm of smart nanodevices, one appealing concept is related with the design of gated materials. These materials are constructed for the purpose of finely tuning the delivery of (bio)chemical species from the voids of porous supports to a solution in response to an external stimulus.¹⁰ These nanodevices are generally composed by two subunits: (i) a porous inorganic support in which a cargo is entrapped and (ii) selected molecular and/or supramolecular entities, grafted onto the external surface, which control mass transport from the pores (Figure 3). Dealing with both components, one of the most used inorganic supports are mesoporous solids (mainly silica-based in the form of micro- or nanoparticles)¹¹ whereas the gating mechanisms takes advantage of electrostatic

8 a) L. Nicole, C. Laberty-Robert, L. Rozes and C. Sanchez, "Hybrid materials science: a promised land for the integrative design of multifunctional materials". *Nanoscale*. **2014**, 6, 6267-6292. b) A. B. Descalzo, R. Martínez-Máñez, F. Sancenón, K. Hoffmann and K. Rurack, "The supramolecular chemistry of organic-inorganic hybrid materials." *Angew. Chem. Int. Ed.* **2006**, 45, 5924-5948.

9 a) Q. Zhang, E. Uchaker, S. L. Candelariaza and G. Gao, "Nanomaterials for energy conversion and storage". *Chem. Soc. Rev.* **2013**, 42, 3127-3171. b) N. Linares, A. M. Silvestre-Albero E. Serrano, J. Silvestre-Albero and J. García-Martínez, "Mesoporous materials for clean energy technologies". *Chem. Soc. Rev.* **2014**, 43, 7681-7717. c) T. Wagner, S. Haffer, C. Weinberger, D. Klaus, M. Tiemann, "Mesoporous materials as gas sensors". *Chem. Soc. Rev.* **2013**, 42, 4036-4053. d) C. Perogo, R. Millini, *Chem. Soc. Rev.*, 2013, 42, 3956-3976. d) A. E. Garcia-Bennett, "Synthesis, toxicology and potential of ordered mesoporous materials in nanomedicine". *Nanomedicine*. **2011**, 6, 867-877.

10 E. Aznar, M. Oroval, Ll. Pascual, J. R. Murguía, R. Martínez-Máñez and F. Sancenón, "Gated Materials for On-Command Release of Guest Molecules". *Chem. Rev.* **2016**, 116, 561-718.

11 a) A. Stein, "Advances in Microporous and Mesoporous Solids—Highlights of Recent Progress". *Adv. Mater.* **2003**, 15, 763-775. b) G. J. A. A. Soler-Illia and O. Azzaroni, "Multifunctional hybrids by combining ordered mesoporous materials and macromolecular building blocks". *Chem. Soc. Rev.* **2011**, 40, 1107-1150. c) A. P. Wight and M. E. Davis, "Design and Preparation of Organic-Inorganic Hybrid Catalysts". *Chem. Rev.* **2002**, 102, 3589-3614. d) G. Kickelbick, "Hybrid inorganic-organic mesoporous materials". *Angew. Chem. Int. Ed.* **2004**, 43, 3102-3104.

or supramolecular interactions, the rupture/formation of covalent bonds, or changes in the physical properties of molecules or macromolecules.¹² These gated materials presented high potential applications in the field of controlled release and in the development of new sensing/recognition protocols.¹³

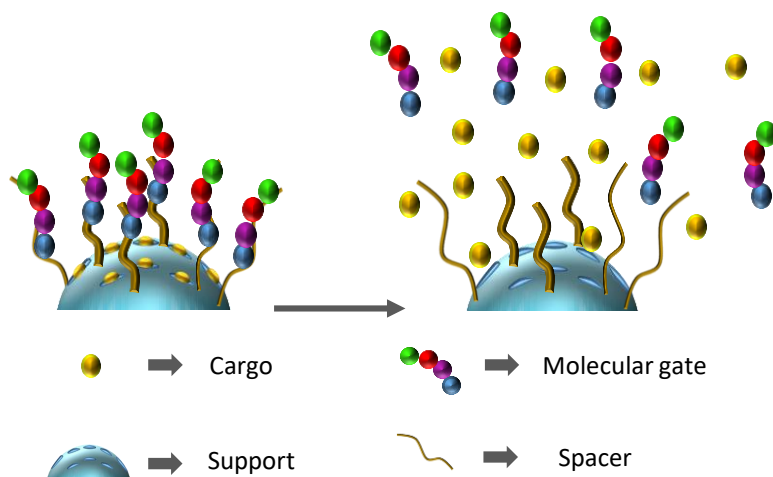


Figure 3. Schematic representation of a molecular gate for on-command controlled release.

One of the most interesting triggers used in the development of gated materials are enzymes.^{10,13} Using enzymes for uncapping gated materials is appealing if we take into account the large amount of different tailor-made specific compounds that can be selectively hydrolysed using enzymes. This technology may provide exquisite selectivity in the design of advanced gated devices for on-command delivery of drugs, biomolecules, or fluorophores in realistic biological environments.

12 a) E. Aznar, R. Martínez-Máñez and F. Sancenón, "Controlled release using mesoporous materials containing gate-like scaffolds", *Expert Opin. Drug Deliv.* **2009**, 6, 643-655. b) Y. -W. Yang, "Towards biocompatible nanovalves based on mesoporous silicananoparticles". *Med. Chem. Commun.* **2011**, 2, 1033-1049.

13 F. Sancenón, Ll. Pascual, M. Oroval, E. Aznar and R. Martínez-Máñez, "Gated silica mesoporous materials in sensing applications". *ChemOpen*, **2015**, 4, 418-437.

1.2 Cellular senescence

Senescence is a state of permanent cell cycle arrest. This state was noticed by Hayflick and co-workers in 1961 while studying the serial cultivation of human diploid cells,¹⁴ which, rather than being immortal, ceased to replicate after a finite number of passages, ('Hayflick's limit'). The cells, including their nuclei, also experienced changes in morphology. Nowadays, we refer to this type of senescence as replicative senescence, which is associated with the shortening of the chromosomal termini, termed telomeres (Figure 4).¹⁵

Other factors, including the activation of oncogenes, inhibition of tumour suppressor genes, accumulation of DNA damage, presence of reactive oxygen species (ROS), metabolic and epigenetic changes, and spindle or nucleolar stress, contribute to another type of senescence known as stress-induced premature senescence (SIPS).¹⁵ SIPS is a way to protect the body from cells that accumulate damage and proliferative defects but cannot undergo apoptosis. A third type of senescence is programmed senescence, which occurs during development.

Intensive research efforts have led to our present understanding of the molecular mechanisms involved in triggering senescence. The mammalian cell cycle consists of two main phases — one involving DNA synthesis (S phase) and another involving cell division (mitosis; M phase). These phases are separated by two gaps (G1 and G2), and passage through the different phases is controlled by cyclin-dependent kinases (CDKs).^{16,17,18} Depending on what the trigger of

14 L. Hayflick, and P. S. Moorhead, "The serial cultivation of human diploid cell strains". *Exp. Cell Res.* **1961**, 25, 585–621

15 a) A. G. Bodnar, et al. "Extension of life-span by introduction of telomerase into normal human cells". *Science*. **1998**, 279, 349–352. b) C. B. Harley, A. B. Futcher and C. W., "GreiderTelomeres shorten during ageing of human fibroblasts". *Nature*. **1990**, 345, 458–460. c) A. M. Olovnikov, "Telomeres, telomerase, and aging: origin of the theory". *Exp. Gerontol.* **1996**, 31, 443–448. d) G.-L. Yu, J. D. Bradley, L. D. Attardi and E. H. Blackburn, "In vivo alteration of telomere sequences and senescence caused by mutated Tetrahymena telomerase RNAs". *Nature*. **1990**, 344, 126–132.

16 J. Bloom and F. R. Cross, "Multiple levels of cyclin specificity in cell-cycle control". *Nat. Rev. Mol. Cell Biol.* **2007**, 8, 149–160.

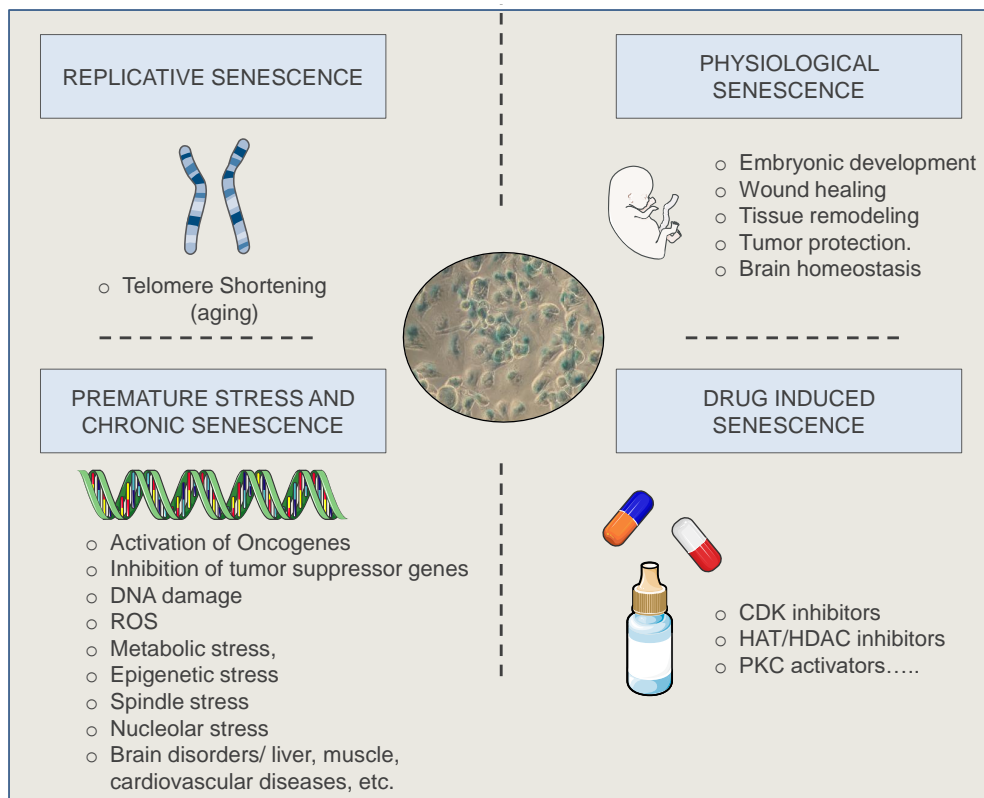


Figure 4. Different types of cellular senescence. Depending on how senescence is triggered, it can be classified as either replicative senescence, stress-induced premature senescence (SIPS) or physiological senescence. Senescence, in particular SIPS, can also be triggered by natural or synthetic drugs. CDK, cyclin-dependent kinases; HAT, histone acetyltransferase; HDAC, histone deacetylase; PKC, protein kinase C; ROS, reactive oxygen species.

senescence is, certain molecular pathways that result in the overexpression of CDK inhibitor proteins, such as p16, p21, p15 or p27, will be activated (Figure 5).

Inhibited CDKs cannot phosphorylate retinoblastoma protein (Rb), which permanently sequesters the transcription factor E2F, a protein that controls the expression of genes that are needed for cell cycle progression. Arrested cells face

17 D. S. Peeper, et al. "A- and B-type cyclins differentially modulate substrate specificity of 534 cyclin-cdk complexes". *EMBO J.* **1993**, *12*, 1947–1954.

18 M. Malumbres and M. Barbacid, "Cell cycle, CDKs and cancer: a changing paradigm". *Nat. Rev. Cancer.* **2009**, *9*, 153–166.

one of three fates: (i) undergo apoptosis; (ii) repair the damage and re-enter the cell cycle; or (iii) remain permanently arrested and become senescent (Figure 5).

Cellular senescence has physiological roles in tissue remodelling during development and after injury.^{19,20,21} However, the chronic accumulation of senescent cells can negatively affect tissue regeneration and function, rendering the tissue more vulnerable to inflammation and aging-related diseases.¹⁷ This introduction describes the fundamental characteristics of senescent cells and how these can be exploited for therapeutic targeting. For example, the induction of senescence via small molecules could constitute the basis of new antitumor treatments.^{22,23} Alternatively, it is possible to decrease the number of senescent cells by using a senolytic drug to kill them or a senomorphic drug to reduce the senescence-associated secretory phenotype (SASP). These approaches are promising strategies to treat aging-related diseases^{24,25} but developments on this front require us to be able to identify senescent cells *in vitro* and *in vivo*. This will allow us to better understand the characteristics of senescence and evaluate medicinal treatments aimed at inducing or eliminating cellular senescence.

19 X. Kong, et al. "Interleukin-22 induces hepatic stellate cell senescence and restricts liver fibrosis in mice". *Hepatology*. **2012**, 56, 1150–1159.

20 B. Ritschka, et al. The senescence-associated secretory phenotype induces cellular plasticity and tissue regeneration". *Genes Dev*. **2017**, 31, 172–183.

21 L. Mosteiro, C. Pantoja, A. de Martino and M. Serrano, "Senescence promotes *in vivo* reprogramming through p16INK4a and IL-6". *Aging Cell* **2018**, 17, 12711–12722.

22 A. Hernandez- Segura, J. Nehme, and M. Demaria, "Hallmarks of cellular senescence". *Trends Cell Biol.* **2018**, 28, 436–453.

23 R. L. Sutherland and E. A. Musgrove, "CDK inhibitors as potential breast cancer therapeutics: new evidence for enhanced efficacy in ER+ disease". *Breast Cancer Res.* **2009**, 11, 112–113.

24 J. L. Kirkland, T. Tchkonja, Y. Zhu, L. J. Niedernhofer and P. D. Robbins, "The clinical potential of senolytic drugs". *J. Am. Geriatr. Soc.* **2017**, 65, 2297–2301.

25 V. Myrianthopoulos, "The emerging field of senotherapeutic drugs". *Future Med. Chem.* **2018**, 10, 2369–2372.

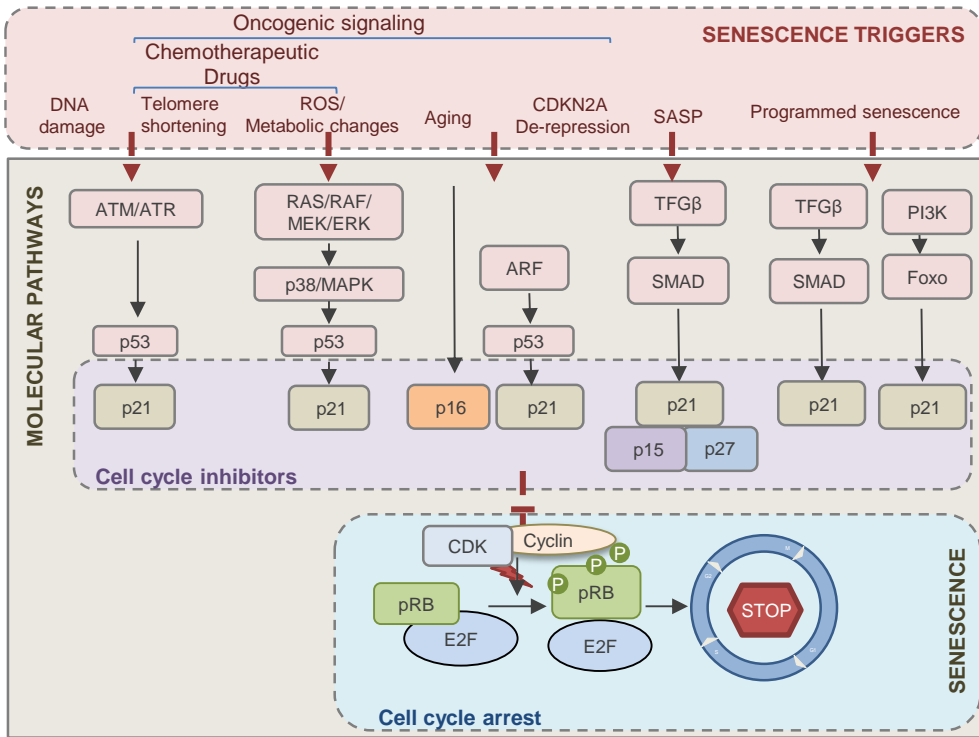


Figure 5. The molecular pathways involved in senescence cell cycle arrest. Various senescence triggers can gate signalling pathways that converge in the overexpression of cell cycle inhibitors, such as p21 and p16^{Ink4a}. These proteins stop cyclin-dependent kinases (CDK)–cyclin complexes from phosphorylating the retinoblastoma protein (Rb). As a result, the transcription factor E2F, which is normally responsible for the expression of the genes needed for cell cycle progression, is sequestered by Rb. The ensuing cell cycle arrest can be transient if cell damage is repaired, or can lead to cell death by apoptosis or to permanent arrest, known as senescence. ATM, ataxia–telangiectasia mutated; ATR, ATM and Rad3-related homologue; ROS, reactive oxygen species; SASP, senescence-associated secretory phenotype.

1.2.1 Senescence in health and disease

Senescent cells differ from other cells in terms of their chemistry and morphology. Moreover, senescent cells have a characteristic SASP, which sees them produce high concentrations of signalling molecules that cause changes in the tissue microenvironment.²⁶ The secretome of senescent cells activates the

26 F. Rodier et al. “Persistent DNA damage signaling triggers senescence-associated inflammatory cytokine

innate and adaptive immune systems by recruiting cells such as natural killer cells, macrophages, neutrophils, CD4⁺ T lymphocytes, CD8⁺ T lymphocytes and B lymphocytes. Under normal conditions, these cells perform immune clearance and eliminate senescent cells from the body.^{27,28} Indeed, preventing damaged or stressed cells from proliferating is the main biological role of cellular senescence.²⁹ Senescence is responsible for maintaining the tissue homeostasis that is necessary for embryonic development, wound healing or tissue remodeling,^{19-21,30,31,32,33} for example, senescence regulates skeletal bone growth during puberty, after which the growth rate eventually decreases.³¹ Further examples of senescence function include the development of the kidneys, the endolymphatic sac in the inner ear^{32,34} and the placenta.³⁵ Although senescence is important in tissue repair and remodelling, inefficient elimination of senescent cells can occur if there is continuous damage or ageing. Thus, senescent cells tend to accumulate in tissues by promoting local inflammation, tissue ageing and destruction.²⁴ Cellular senescence is related to multiple degenerative and hyperplastic pathologies of ageing, and the accumulation of senescent cells is involved in the pathophysiology of many diseases, such as metabolic disorders,³⁶

Secretion". *Nat. Cell Biol.* **2009**, 11, 973–979.

27 A. Sagiv, et al. "NKG2D ligands mediate immunosurveillance of senescent cells". *Ageing.* **2016**, 8, 328–344.

28 T.-W. Kang et al. "Senescence surveillance of pre-malignant hepatocytes limits liver cancer development". *Nature.* **2011**, 479, 547–551.

29 D. Muñoz- Espín and M. Serrano. "Cellular senescence: from physiology to pathology". *Nat. Rev. Mol. Cell Biol.* 2014, 15, 482–496.

30 M. Demaria et al. An essential role for senescent cells in optimal wound healing through secretion of PDGF-AA. *Dev. Cell* 31, 722–733 (2014).

31 C. Li et al. "Programmed cell senescence in skeleton during late puberty". *Nat. Commun.* **2017**, 8, 1312.

32 Storer, M. et al. "Senescence is a developmental mechanism that contributes to embryonic growth and patterning". *Cell* **2013**, 155, 1119–1130.

33W. O'Brien, G. Stenman and R. Sager. "Suppression of tumor growth by senescence in virally transformed human fibroblasts". *Proc. Natl Acad. Sci. USA* **1986**, 83, 8659–8663.

34 D. Muñoz- Espín, et al. "Programmed cell senescence during mammalian embryonic development". *Cell* **2013**, 155, 1104–1118.

35 Z. Sultana, K. Maiti, L. Dedman and R. Smith. "Is there a role for placental senescence in the genesis of obstetric complications and fetal growth restriction?". *Am. J. Obstet. Gynecol.* **2018**, 218, S762–S773.

36 M. J.Schafer, J. D. Miller and N. K. LeBrasseur, "Cellular senescence: implications for metabolic disease". *Mol. Cell. Endocrinol.* **2017**, 455, 93–102.

osteoporosis,^{37,38} pulmonary³⁹ and liver fibrosis,⁴⁰ cardiac⁴¹ and brain disorders,⁴² and kidney disease.^{43,44}

Senescence gives rise to dual and sometimes contradictory consequences, a property it has in common with other physiological processes, such as inflammation. Senescence is necessary for tissue and organ homeostasis but its de-regulation causes diseases.⁴⁵ For example, senescent activated stellate cells facilitate the resolution of liver fibrosis⁴⁶ but also cause age-dependent steatosis.⁴⁷

With respect to diabetes, senescence acts as a balance. On one hand, the increase in the expression of p16^{Ink4} in insulin-producing pancreatic β -cells leads to a decrease in cellular replication, thus lowering the number of cells that produce insulin, which results in the increased risk of type 2 diabetes due to the global decrease in insulin production.^{48,49} On the other hand, it has been shown that, in mice affected by diabetes, the increase in p16^{Ink4} leads to an improved glucose homeostasis and to a consequent improvement in insulin secretion from each single cell; this unexpected functional benefit can be seen as a way to

37 S. Khosla, J. N. Farr and J. L. Kirkland, "Inhibiting cellular senescence: a new therapeutic paradigm for age-related osteoporosis". *J. Clin. Endocrinol. Metab.* **2018**, 103, 1282–1290.

38 J. N. Farr, et al. "Targeting cellular senescence prevents age-related bone loss in mice". *Nat. Med.* **2017**, 23, 1072–1079.

39 M. J. Schafer, et al. "Cellular senescence mediates fibrotic pulmonary disease". *Nat. Commun.* **2017**, 8, 14532.

40 F. Wandrer, et al. "Senescence mirrors the extent of liver fibrosis in chronic hepatitis C virus infection". *Aliment. Pharmacol. Ther.* **2018**, 48, 270–280.

41 R. Sun, et al. "Senescence as a novel mechanism involved in β -adrenergic receptor mediated cardiac hypertrophy". *PLoS One* **2017**, 12, e0182668.

42 D. J. Baker and R. C. Petersen, "Cellular senescence in brain aging and neurodegenerative diseases: evidence and perspectives". *J. Clin. Invest.* **2018**, 128, 1208–1216.

43 H. Yang and A. B. Fogo, "Cell senescence in the aging kidney". *J. Am. Soc. Nephrol.* **2010**, 21, 1436–1439.

44 R. Jimenez, et al. "Replicative senescence in patients with chronic kidney failure". *Kidney Int.* **2005**, 68, S11–S15.

45 S. He and N. E. Sharpless, "Senescence in health and disease". *Cell.* **2017**, 169, 1000–1011.

46 V. Krizhanovsky et al. "Senescence of activated stellate cells limits liver fibrosis". *Cell* **2008**, 134, 657–667.

47 M. Ogrodnik et al. "Cellular senescence drives age-dependent hepatic steatosis". *Nat. Commun.* **2017**, 8, 15691.

48 O. Tavana and C. Zhu. "Too many breaks (brakes): pancreatic β -cell senescence leads to diabetes". *Cell Cycle.* **2011**, 10, 2471–2484.

49 J. Krishnamurthy et al. "p16^{Ink4a} induces an agedependent decline in islet regenerative potential". *Nature.* **2006**, 443, 453–457.

compensate for the loss of regenerative capacity.⁵⁰ Senescence in the placenta is a normal physiological process³⁵ but aberrant senescence can lead to preeclampsia or pre-term birth.^{51,52} Similarly, the role of senescence in tumorigenesis is complex and inducing senescence in tumour cells is an opportunity to alert and activate the immune system to detect and eliminate them.^{53,54,55,56} These observations have led to the development of pro-senescence therapies, one of which uses palbociclib, an inhibitor of CDK4 and CDK6 (Figure 6), to treat advanced breast cancer.^{23,24} Again, the accumulation of senescent cells shows their ‘dark side’ by promoting tumour progression and metastasis. Cancer stemness is promoted by senescence induction⁵⁷ and senescent endothelial cells facilitate tumour cell migration and metastasis.⁵⁸ These pro-tumourigenic effects have further stimulated research interest in killing senescent cells.^{58,59,60} The selective induction of cell death in senescent cells, known as senolysis, has emerged as a new strategy to manage the adverse effects of senescent cells. Senolytic drugs have attracted great interest as a means to fight cancer as well as the many ageing related diseases that are associated with the accumulation of

50 A. Helman et al. “p16Ink4a- induced senescence of pancreatic beta cells enhances insulin secretion. *Nat. Med.* **2016**, *22*, 412–420.

51 T. D. Cindrova, N. M. E. Fogarty, C. J. P. Jones, J. Kingdom and G. J. Burton. “Evidence of oxidative stress-induced senescence in mature, post- mature and pathological human placentas”. *Placenta*. **2018**, *68*, 15–22.

52 L. S. Cox and C. Redman. “The role of cellular senescence in ageing of the placenta”. *Placenta* **2017**, *52*, 139–145.

53 M. Collado et al. “Senescence in premalignant tumours”. *Nature*. **2005**, *436*, 642.

54 Z. Chen et al. “Crucial role of p53-dependent cellular senescence in suppression of Pten-deficient tumorigenesis”. *Nature* **2005**, *436*, 725–730.

55 C. Michaloglou et al. “BRAF^{E600}-associated senescence like cell cycle arrest of human naevi”. *Nature* **2005**, *436*, 720–724.

56 M. Braig et al. “Oncogene- induced senescence as an initial barrier in lymphoma development”. *Nature*. **2005**, *436*, 660–665.

57 M. Schosserer, J. Grillari and M. Breitenbach. “The dual role of cellular senescence in developing tumors and their response to cancer therapy”. *Front. Oncol.* **2017**, *7*, 2781–2793.

58 E. Wieland et al. “Endothelial Notch1 activity facilitates metastasis”. *Cancer Cell*. **2017**, *31*, 355–367

59 M. Milanovic et al. “Senescence- associated reprogramming promotes cancer stemness”. *Nature*. **2017**, *553*, 96–100

60 S. Parrinello, J.-P. Coppe, A. Krtolica and J. Campisi. “Stromal–epithelial interactions in aging and cancer: senescent fibroblasts alter epithelial cell differentiation”. *J. Cell Sci.* **2005**, *118*, 485–496.

senescent cells.^{49,61} In landmark studies, it was shown that eliminating cells that express high levels of the CDK inhibitor p16^{Ink4a} ameliorated ageing related disorders in mice. Because p16^{Ink4a} is also a senescence marker, we can infer that selectively removing senescent cells would also have beneficial effects, further motivating the search for new senolytics.^{62,63}

1.2.2 Senescence induction methods

The approaches to induce SIPS using drugs are described below. Senescent phenotypes are dynamic and can change depending on how senescence was induced (chemical or natural stimuli) and what cell type is involved (normal or tumour cells, different cell lines). Furthermore, individual senescent cells can be heterogeneous in their gene expression signatures even though the cellular population appears homogeneous.^{64,65}

The use of low molecular weight compounds to induce senescence has been reviewed previously,⁶⁶ and the treatments typically involve prolonged exposure to the drug(s), which can be classified into eight groups (Figure 6). One common method to trigger senescence is to use DNA replication stress inducers, such as aphidicolin (a DNA polymerase- α inhibitor),⁶⁷ hydroxyurea (a ribonucleotide

61 C. López- Otín, M. A. Blasco, L. Partridge, M. Serrano and G. Kroemer. "The hallmarks of aging". *Cell*. **2013**, 153, 1194–1217.

62 D. J. Baker et al. "Clearance of p16Ink4a- positive senescent cells delays ageing- associated disorders". *Nature*. **2011**, 479, 232–236.

63 D. J. Baker et al. "Naturally occurring p16Ink4a-positive cells shorten healthy lifespan". *Nature*. **2016**, 530, 184–189.

64 A. Hernandez- Segura et al. "Unmasking transcriptional heterogeneity in senescent cells". *Curr. Biol*. **2017**, 27, 2652–2660

65 C. D. Wiley et al. "Analysis of individual cells identifies cell- to-cell variability following induction of cellular senescence". *Aging Cell*. **2017**, 16, 1043–1050.

66 N. V. Petrova, A. K. Velichko, S. V. Razin and O. L. Kantidze. "Small molecule compounds that induce cellular senescence". *Aging Cell*. **2016**, 15, 999–1017.

67 A. Marusyk, L. J. Wheeler, C. K. Mathews and J. DeGregori. "p53 mediates senescence- like arrest induced by chronic replicational stress". *Mol. Cell. Biol*. **2007**, 27, 5336–5351.

reductase inhibitor),⁶⁸ thymidine (a compound that attenuates deoxycytidine triphosphate synthesis),⁶⁹ bromodeoxyuridine (a DNA replication suppressor),⁷⁰ difluorodeoxycytidine (also known as gemcitabine, a ribonucleotide reductase and CTP synthetase inhibitor)⁷¹ and cyclopentenyl cytosine (a CTP synthetase inhibitor).⁷² Senescence can also be triggered by damaging DNA with doxorubicin,⁷³ etoposide,⁷⁴ daunorubicin,⁷⁵ mitoxantrone,⁷⁶ camptothecin,⁷⁷ cisplatin,⁷⁸ actinomycin D,⁷⁹ bleomycin or temozolomide⁸⁰. As we have noted, telomere shortening and dysfunction elicit a senescence response. This response can be triggered by inhibiting telomerase, an enzyme that maintains the length of

68 E. J. Yeo et al. "Senescence- like changes induced by hydroxyurea in human diploid fibroblasts". *Exp. Gerontol.* **2000**, 35, 553–571.

69 E. Sumikawa, Y. Matsumoto, R. Sakemura, M. Fujii and D. Ayusawa. "Prolonged unbalanced growth induces cellular senescence markers linked with mechano transduction in normal and tumor cells". *Biochem. Biophys. Res. Commun.* **2005**, 335, 558–565.

70 E. Michishita et al. "5-Bromodeoxyuridine induces senescence- like phenomena in mammalian cells regardless of cell type or species". *J. Biochem.* **1999**, 126, 1052–1059.

71 D. E. Modrak, E. Leon, D. M. Goldenberg and D. V. Gold. "Ceramide regulates gemcitabine- induced senescence and apoptosis in human pancreatic cancer cell lines". *Mol. Cancer Res.* **2009**, 7, 890–896.

72 M. Huang, P. Whang, P. Lewicki and B. S. Mitchell. "Cyclopentenyl cytosine induces senescence in breast cancer cells through the nucleolar stress response and activation of p53". *Mol. Pharmacol.* **2011**, 80, 40–48.

73 B. D. Chang et al. "A senescence- like phenotype distinguishes tumor cells that undergo terminal proliferation arrest after exposure to anticancer agents". *Cancer Res.* **1999**, 59, 3761–3767.

74 R. H. te Poele, A. L. Okorokov, L. Jardine, J. Cummings and S. P. Joel. "DNA damage is able to induce senescence in tumor cells *in vitro* and *in vivo*". *Cancer Res.* **2002**, 62, 1876–1883.

75 S. Mansilla, B. Piña and J. Portugal. "Daunorubicin-induced variations in gene transcription: commitment to proliferation arrest, senescence and apoptosis". *Biochem. J.* **2003**, 372, 703–711.

76 J.-P. Coppé et al. "Senescence- associated secretory phenotypes reveal cell- nonautonomous functions of oncogenic RAS and the p53 tumor suppressor". *PLoS Biol.* **2008**, 6, e301.

77 Z. Han et al. "Role of p21 in apoptosis and senescence of human colon cancer cells treated with camptothecin". *J. Biol. Chem.* **2002**, 277, 17154–17160.

78 X. Wang et al. "Evidence of cisplatin- induced senescent-like growth arrest in nasopharyngeal carcinoma cells". *Cancer Res.* **1998**, 58, 5019–5022.

79 S. J. Robles and G. R. Adami. "Agents that cause DNA double strand breaks lead to p16INK4a enrichment and the premature senescence of normal fibroblasts". *Oncogene.* **1998**, 16, 1113–1123.

80 Y. Hirose, M. S. Berger and R. O. Pieper. "p53 effects both the duration of G2/M arrest and the fate of temozolomide- treated human glioblastoma cells". *Cancer Res.* **2001**, 61, 1957–1963.

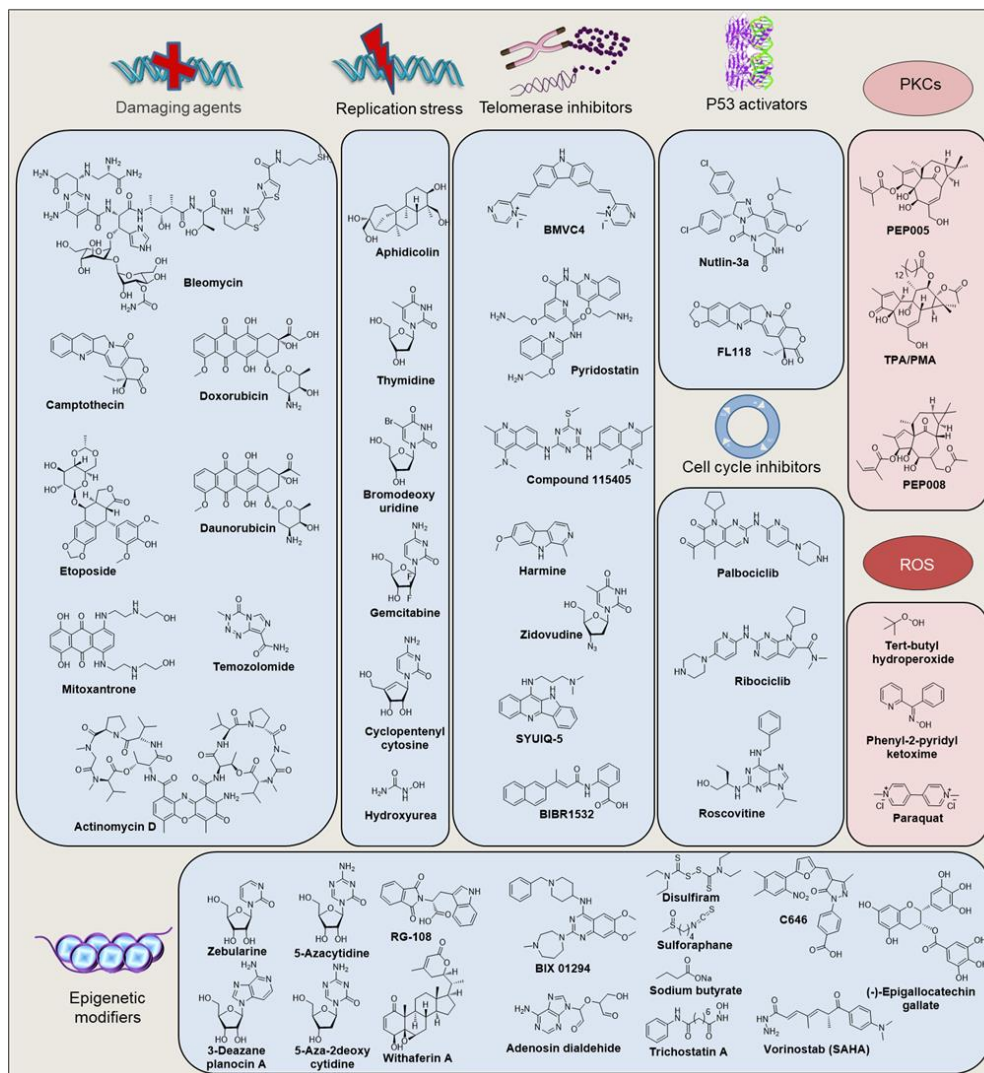


Figure 6. There are many ways to induce senescence. The representative senescence-inducing species are classified according to their mechanism of action. The compounds that act in cell nuclei are presented in blue boxes, while those that are active in the cytosol are shown in an orange box. ROS, reactive oxygen species.

these DNA regions. Telomerase inhibitors developed for this purpose include SYUIQ-5,⁸¹ BMVC4,⁸² pyridostatin,⁸³ compound 115405,⁸⁴ perylene and indole derivatives,⁸⁵ harmine,⁸⁶ BIBR1532 and azidothymidine. Beyond just DNA, we can also consider how the phenotype of senescent cells differs from that of normal cells in terms of chromatin organization and the epigenome. Thus, inhibitors of DNA methyltransferases, histone deacetylases, histone acetyltransferases, and histone methyltransferases are frequently used to induce senescence.⁸⁷ Drugs that cause overexpression of the genes encoding p53, Rb, p21 or p16^{Ink4a} or activate these proteins can induce senescence by activating the p53–p21 and/or p16^{Ink4a}–Rb tumour suppressor pathways. The tumour suppressor p53, referred to as the guardian of the genome, is key to cell cycle arrest, DNA repair and apoptosis.⁸⁸

Activators of p53, such as nutlin-3a (an MDM2 antagonist), can induce senescence. Similarly, FL118 also induces p53-dependent senescence by promoting proteasomal degradation of MDM2,⁸⁹ although senescence might

81 J.-M. Zhou, et al. "Senescence and telomere shortening induced by novel potent G- quadruplex interactive agents, quindoline derivatives, in human cancer cell lines". *Oncogene*. **2006**, 25, 503–511.

82 F.-C. Huang, C.-C. Chang, J.-M. Wang, T.-C. Chang and J.-J. Lin. "Induction of senescence in cancer cells by the G- quadruplex stabilizer, BMVC4, is independent of its telomerase inhibitory activity". *Br. J. Pharmacol.* **2012**, 167, 393–406.

83 S. Müller et al. "Pyridostatin analogues promote telomere dysfunction and long- term growth inhibition in human cancer cells". *Org. Biomol. Chem.* **2012**, 10, 6537–6546.

84 J. F. Riou et al. "Cell senescence and telomere shortening induced by a new series of specific G-quadruplex DNA ligands". *Proc. Natl Acad. Sci. USA.* **2002**, 99, 2672–2677.

85 C. N. Marconett et al. "Indole-3-carbinol downregulation of telomerase gene expression requires the inhibition of estrogen receptor- alpha and Sp1 transcription factor interactions within the hTERT promoter and mediates the G1 cell cycle arrest of human breast cancer cells". *Carcinogenesis* **2011**, 32, 1315–1323.

86 L. Zhao and M. Wink. "The β - carboline alkaloid harmine inhibits telomerase activity of MCF-7 cells by downregulating hTERT mRNA expression accompanied by an accelerated senescent phenotype". *PeerJ.* **2013**, 1, e174 ().

87 M. Vogt, C. Haggblom, J. Yeargin, T. Christiansen-Weber and M. Haas. "Independent induction of senescence by p16^{Ink4a} and p21^{CIP1} in spontaneously immortalized human fibroblasts". *Cell Growth Differ.* **1998**, 9, 139–146.

88 E. R. Kasthuber and S. W. Lowe. "Putting p53 in context". *Cell.* **2017**, 170, 1062–1078.

89 A. Efeyan et al. "Induction of p53-dependent senescence by the mdm2 antagonist nutlin-3a in mouse cells of fibroblast origin". *Cancer Res.* **2007**, 67, 7350–7357.

instead be a result of FL118 inhibiting topoisomerase I.⁹⁰ The cell cycle is mainly regulated by cyclins and CDKs, such that inhibiting these enzymes induces senescence. For example, the CDK4 and CDK6 inhibitors palbociclib, ribociclib and abemaciclib,⁹¹ as well as the non-selective CDK inhibitor roscovitine, can induce premature senescence.⁹² The final class of small molecules that can induce senescence are those that give rise to ROS. ROS production leads to oxidative stress and macromolecular damage in cells.⁹³ For example, molecules such as H₂O₂, *t*-BuOOH, phenyl 2-pyridyl ketoxime, phenylaminonaphthoquinones and paraquat, through either cleavage or redox activity, can give rise to ROS and trigger cellular senescence.

1.2.3 Senescence markers

Given the important role that senescent cells have in ageing and disease, it is no surprising that detecting and eliminating these cells can improve the condition of patients suffering from some diseases.⁹⁴ Most methods aim to detect common senescence markers that are expressed regardless of whether growth arrest arose from a chemical agent or replicative induction.⁹⁵ However, we have yet to identify a single universal senescence marker such that, in general, the presence of senescent cells can only be confirmed by detecting multiple markers. The most noticeable macroscopic sign of senescence are changes in cell morphology (Figure

90 X. Ling, et al. "FL118 Induces p53-dependent senescence in colorectal cancer cells by promoting degradation of MdmX". *Cancer Res.* **2014**, 74, 7487–7497.

91 O. V. Leontieva and M. V. Blagosklonny. "CDK4/6- inhibiting drug substitutes for p21 and p16 in senescence: duration of cell cycle arrest and MTOR activity determine geroconversion". *Cell Cycle.* **2013**, 12, 3063–3069.

92 J.-Y. Park, S.-H. Park and R. H. Weiss. "Disparate effects of roscovitine on renal tubular epithelial cell apoptosis and senescence: implications for autosomal dominant polycystic kidney disease". *Am. J. Nephrol.* **2009**, 29, 509–515.

93 P. D. Ray, B.-W. Huang and Y. Tsuji. "Reactive oxygen species (ROS) homeostasis and redox regulation in cellular signaling". *Cell. Signal.* **2012**, 24, 981–990.

94 Naylor, R. M., Baker, D. J. & van Deursen, J. M. Senescent cells: a novel therapeutic target for aging and age-related diseases. *Clin. Pharmacol. Ther.* **2013**, 93, 105–116.

95 E. Sikora, G. Mosieniak and M. A. Sliwinski. "Morphological and functional characteristic of senescent cancer cells". *Curr. Drug Targets.* **2016**, 17, 377–387.

7).²⁹ Relative to healthy cells, senescent cells *in vitro* have a characteristically flattened appearance and an irregular shape, with enlarged nuclei, increased nucleolar size and accumulated cytoplasmic granules. Additionally, the cells contain many vacuoles, as well as enlarged lysosomes and Golgi apparatus. Moreover, in some cell types, foci of condensed chromatin, termed senescence-associated heterochromatin foci (SAHF), are observed.^{96,97} On the molecular level, although senescent cells are not proliferative, they are metabolically active and

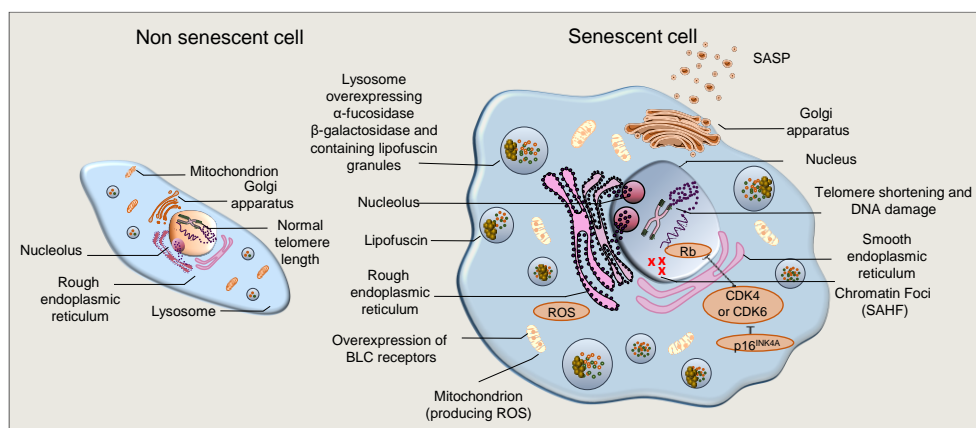


Figure 7. Senescence biomarkers. Compared with a non-senescent cell (left), a senescent cell (right) is larger and flatter. The nucleus of senescent cells is larger than in proliferating cells and may contain chromosomes with shortened telomeres and senescence-associated heterochromatin foci (SAHF). The levels of β -galactosidase, α -fucosidase and many other hydrolases, as well as lipofuscins, are higher in the lysosomes of senescent cells than they are in proliferating cells. The mitochondria in senescent cells produce reactive oxygen species (ROS) and have high concentrations of anti-apoptotic proteins of the BCL-2 family. The Golgi apparatus secretes vesicles containing cytokines and chemokines (senescence-associated secretory phenotype, SASP) that cause changes in the tissue microenvironment and disturb surrounding cells. p16^{INK4A}, a tumour suppressor protein and cyclin-dependent kinase (CDK) inhibitor, is located in the cytoplasm. Inhibition of CDKs prevents the phosphorylation of the nuclear retinoblastoma protein (Rb). Note that the figure is not to scale and the size of each cell depends on the cell line.

96 R. Funayama and F. Ishikawa. "Cellular senescence and chromatin structure". *Chromosoma*. **2007**, 116, 431–440.

97 R. Zhang and P. D. Adams. "Heterochromatin and its relationship to cell senescence and cancer therapy". *Cell Cycle*. **2007**, 6, 784–789.

have ATP levels similar to confluent cells.⁹⁸ Moreover, some types of senescent cells exhibit enhanced glycolysis.^{99,100}

Senescent cells survive by expressing anti-apoptotic B cell lymphoma (BCL) proteins such as BCL-XL, which makes the outer mitochondrial membrane less permeable and, thus, less likely to release apoptosis inducing proteins, such as cytochrome C.¹⁰¹ The absence of the proliferation marker Ki67 and lower phosphorylated Rb (pRb) levels in tumours are indicative of senescence.^{102,103}

Cells that are in the state of replicative senescence typically have short telomeres.^{104,105,106} Human primary somatic cells cannot add telomeric repeats to the ends of their chromosomes if their telomerase enzymes are inhibited. In this case, there is deprotection of chromosomes, DNA becomes damaged and there is limited cell proliferation.^{15,107,108} However, it is possible to keep chromosomes intact by forcing telomerase expression;¹⁵ reactivating these enzymes in mice prematurely aged by telomeric shortening can counter this degeneration.¹⁰⁹

Moreover, depending on the way in which senescence is triggered, telomere shortening can be present or absent, and it is important to determine whether

98 S. Goldstein, S. R. Ballantyne, A. L. Robson and E. J. Moerman. "Energy metabolism in cultured human fibroblasts during aging *in vitro*". *J. Cell. Physiol.* **1982**, 112, 419–424.

99 A. H. Bittles and N. Harper. "Increased glycolysis in ageing cultured human diploid fibroblasts". *Biosci. Rep.* **1984**, 4, 751–756.

100 A. L. Muggleton-Harris and R. Defuria. "Age-dependent metabolic changes in cultured human fibroblasts". *In vitro Cell. Dev. Biol.* **1985**, 21, 271–276.

101 B. G. Childs, D. J. Baker, J. L., Kirkland, J. Campisi and J. M. van Deursen. "Senescence and apoptosis: dueling or complementary cell fates?". *EMBO Rep* **2014**, 15, 1139–1153.

102 D. Muñoz- Espín et al. "A versatile drug delivery system targeting senescent cells". *EMBO Mol. Med.* 2018, **10**, e9355.

103 A. Takahashi, N. Ohtani and E. Hara. "Irreversibility of cellular senescence: dual roles of p16INK4a/Rb-pathway in cell cycle control". *Cell Div.* **2007**, 2, 10–15.

104 K. A. Mather, A. F. Jorm, R. A. Parslow and H. Christensen. "Is telomere length a biomarker of aging? A review". *J. Gerontol. A.* **2011**, 66, 202–213.

105 A. Zietzer and P. Hillmeister. "Leucocyte telomere length as marker for cardiovascular ageing". *Acta Physiol.* **2014**, 211, 251–256.

106 S. Bekaert, T. De Meyer and P. Van Oostveldt. "Telomere attrition as ageing biomarker". *Anticancer Res.* **2005**, 25, 3011–3021.

107 M. A. Blasco et al. "Telomere shortening and tumor formation by mouse cells lacking telomerase RNA". *Cell.* **1997**, 91, 25–34.

108 E. H. Blackburn. "Structure and function of telomeres". *Nature.* **1991**, 350, 569–573.

109 M. Jaskelioff et al. "Telomerase reactivation reverses tissue degeneration in aged telomerase-deficient mice". *Nature.* **2011**, 469, 102–106.

DNA repair and/or maintenance proteins, such as γ H2AX, ataxia–telangiectasia mutated (ATM) and MRE11, are also present at telomeres. Thus, instead of simply measuring telomere length, looking for telomere-dysfunction-induced foci (TIF) could be a less ambiguous means to identify senescence.¹¹⁰ The SASP includes secretion of different cytokines, chemokines and proteases — proteins that change the environment around a cell.^{60,111,112,113,114} These secreted proteins include cleaved cell-surface molecules, extracellular matrix components, inflammatory mediators (IL-6, GRO α and CCL20) and growth factors (hepatocyte growth factor, HGF, and insulin-like growth factor-binding proteins, IGFbps), among others. Taken together, the SASP and its associated molecules are powerful markers of senescence.¹¹⁵

Lipofuscin is a non-degradable aggregate of oxidized proteins, lipids and oligosaccharides that accumulates progressively in the lysosomes of non-proliferative cells. This aggregate is more prominent in senescent cells and it can be visualized by fluorescence microscopy.¹¹⁶ Intracellular lipofuscin accumulation is correlated with senescence¹¹⁷ owing to its colocalization with senescence-associated β -galactosidase (SA- β -Gal) activity, another common biomarker of

110 T. Brugat, F. Nguyen- Khac, A. Grelier, H. Merle- Béral and J. Delic. “Telomere dysfunction- induced foci arise with the onset of telomeric deletions and complex chromosomal aberrations in resistant chronic lymphocytic leukemia cells”. *Blood*. **2010**, 116, 239–249.

111 A. Krtolica, S. Parrinello, S. Lockett, P. Y. Desprez and J. Campisi. “Senescent fibroblasts promote epithelial cell growth and tumorigenesis: a link between cancer and aging. *Proc. Natl Acad. Sci. USA*. **2001**, 98, 12072–12077.

112 T. Kuilman et al. Oncogene- induced senescence relayed by an interleukin- dependent inflammatory network. *Cell* **133**, 1019–1031 (2008).

113 J. C. Acosta et al. “Chemokine signaling via the CXCR2 receptor reinforces senescence”. *Cell*. **2008**, 133, 1006–1018.

114 J. Campisi, J. K. Andersen, P. Kapahi and S. Melov. “Cellular senescence: a link between cancer and aged-related degenerative disease?” *Semin. Cancer Biol.* **2011**, 21, 354–359.

115 J. C. Acosta et al. “A complex secretory program orchestrated by the inflammasome controls paracrine senescence”. *Nat. Cell Biol.* **2013**, 15, 978–990.

116 T. Jung, N. Bader and T. Grune. “Lipofuscin: formation, distribution, and metabolic consequences”. *Ann. NY Acad. Sci.* **2007**, 1119, 97–111.

117 M. L. Katz, W. G. Robinson, R. K. Herrmann, A. B. Groome and J. G. Bieri. Lipofuscin accumulation resulting from senescence and vitamin E deficiency: spectral properties and tissue distribution. *Mech. Ageing Dev.* **1984**, 25, 149–159.

senescence in lysosomes (see below).¹¹⁸ This activity can be detected both *in vitro* and *in situ* by histochemical methods, including staining with the lipophilic diazo dye Sudan Black B (SBB).^{119,120,121}

Acid β -galactosidase (β -Gal, encoded by GLB1) accumulates in the lysosomes of senescent cells and is the origin of SA- β -Gal activity.^{122,123} SA- β -Gal activity is conveniently measured using chromogenic or fluorogenic probes. SA- β -Gal hydrolyses galactosides and this activity has served as the basis of a number of fluorogenic probes, most of which feature a fluorophore covalently linked to the anomeric carbon of a β -galactose. Apart from β -Gal, there are other lysosomal hydrolases that are overexpressed in senescent cells.^{124,125}

Whereas healthy cells respond to mitogens by proliferating (growing and dividing), growth arrest is permanent in senescent cells; that is, they do not re-enter the cell cycle in response to mitogen stimulation.¹²⁶ The proteins responsible for cell proliferation are suitable markers for identifying senescent cells. For example, the tumour suppressors p53, p16^{Ink4a} and p21 are overexpressed during growth arrest.^{127,128,129,130} In particular, the cell cycle inhibitor p16^{Ink4a} has been a

118 E. Georgakopoulou et al. "Specific lipofuscin staining as a novel biomarker to detect replicative and stress-induced senescence. A method applicable in cryo-preserved and archival tissues". *Aging*. **2012**, 5, 37–50.

119 J. B. Gatenby and T. A. Moussa. "The sudan black B technique in cytology". *J. Microsc. Soc.* **1949**, 69, 72–75.

120 G. L. Rasmussen. "A method of staining the statoacoustic nerve in bulk with Sudan black B". *Anat. Rec.* **1961**, 139, 465–469.

121 T. Jung, A. Höhn and T. Grune. "Lipofuscin: detection and quantification by microscope techniques". *Methods Mol. Biol.* **2010**, 594, 173–193.

122 G. P. Dimri et al. "A biomarker that identifies senescent human cells in culture and in aging skin *in vivo*". *Proc. Natl Acad. Sci. USA* **1995**, 92, 9363–9367.

123 A. Biran et al. "Quantitative identification of senescent cells in aging and disease". *Aging Cell* **2017**, 16, 661–671.

124 M. Knas et al. "The profile of lysosomal exoglycosidases in replicative and stress-induced senescence in early passage human fibroblasts". *Folia Histochem. Cytobiol.* **2012**, 50, 220–227.

125 D. Hildebrand et al. " α -Fucosidase as a novel convenient biomarker for cellular senescence". *Cell Cycle*. **2013**, 12, 1922–1927.

126 C. Gey and K. Seeger. "Metabolic changes during cellular senescence investigated by proton NMR-spectroscopy". *Mech. Ageing Dev.* **2013**, 134, 130–138.

127 J. Campisi. "Senescent cells, tumor suppression, and organismal aging: good citizens, bad neighbors". *Cell*. **2005**, 120, 513–522.

128 J. Campisi and F. d'Adda di Fagagna. "Cellular senescence: when bad things happen to good cells". *Nat. Rev. Mol. Cell. Biol.* **2007**, 8, 729–740.

129 J. Krishnamurthy et al. "*Ink4a/Arf* expression is a biomarker of aging". *J. Clin. Invest.* **2004**, 114, 1299–1307.

key tool used to identify senescent cells^{131,132} and, although it has some limitations as an *in vivo* biomarker of senescence, its use is still commonplace.^{133,134,135}

1.2.4 Senolytics

The elimination of senescent cells by selectively inducing apoptosis alleviates several aging-related diseases, reverts long-term degenerative processes and extends both health span and lifespan.¹³⁶ Senolysis — the selective elimination of senescent cells — ameliorates symptoms in mouse models of atherosclerosis, osteoarthritis, cataracts, cardiac hypertrophy, renal dysfunction, lipodystrophy and sarcopenia.^{62,63,137,138,139} Notably, there is a lack of a senolytic drug that is effective in eliminating all types of senescent cells. Furthermore, as we noted above, the diverse causes of senescence can lead to differences in their sensitivity to various aging senolytic drugs. A selective and universal method for the elimination of senescent cells would be a potentially useful therapy, but no such senolytic drugs have been approved yet. Senolytics such as the combination of dasatinib plus

130 B. Vandenberg, B. Brouwers, S. Hatse and H. Wildiers. “p16INK4a: a central player in cellular senescence and promising aging biomarker in elderly cancer patients”. *J. Geriatr. Oncol.* **2011**, 2, 259–269.

131 Serrano, M., Hannon, G. J. & Beach, D. A new regulatory motif in cell- cycle control causing specific inhibition of cyclin D/CDK4. *Nature* **366**, 704–707 (1993).

132 M. Serrano, A. W. Lin, M. E. McCurrach, D. Beach and S. W. Lowe. “Oncogenic *ras* provokes premature cell senescence associated with accumulation of p53 and p16INK4a”. *Cell.* **1997**, 88, 593–602.

133 C. M. Beauséjour et al. “Reversal of human cellular senescence: roles of the p53 and p16 pathways”. *EMBO J.* **2003**, 22, 4212–4222.

134 J. G. Rheinwald et al. “A two- stage, p16INK4A- and p53- dependent keratinocyte senescence mechanism that limits replicative potential independent of telomere status”. *Mol. Cell. Biol.* **2002**, 22, 5157–5172.

135 U. Herbig, W. A. Jobling, B. P. C. Chen, D. J. Chen and J. M. Sedivy. “Telomere shortening triggers senescence of human cells through a pathway involving ATM, p53, and p21CIP1, but not p16INK4a”. *Mol. Cell.* **2004**, 14, 501–513.

136 A. Soto- Gamez and M. Demaria. “Therapeutic interventions for aging: the case of cellular senescence”. *Drug Discov. Today.* **2017**, 22, 786–795.

137 O. H. Jeon et al. “Local clearance of senescent cells attenuates the development of post- traumatic osteoarthritis and creates a pro- regenerative environment”. *Nat. Med.* **2017**, 23, 775–781.

138 D. J. Baker et al. “Opposing roles for p16Ink4a and p19Arf in senescence and ageing caused by BubR1 insufficiency”. *Nat. Cell Biol.* **2008**, 10, 825–836.

139 B. G. Childs et al. “Senescent intimal foam cells are deleterious at all stages of atherosclerosis”. *Science.* **2016**, 354, 472–477.

quercetin are in clinical trials for idiopathic pulmonary fibrosis and chronic kidney disease¹⁴⁰ and, also, UBX101 for osteoarthritis in the knee is in phase I trials.¹⁴¹

Because no single drug can remove all senescent cells, treatments instead must use several drugs, including combinations of small molecules, antibodies and peptides. The first hypothesis-driven approach to senolytic discovery exploited the resistance of senescent cells to apoptosis (recall that they release pro-apoptotic factors to the medium as part of the SASP).¹⁴² This was thought to lead senescent cells to rely on pro-survival pathways to defend against their own pro-apoptotic factors. Using bioinformatics and small interfering RNA (siRNA) technology, different senescent-cell antiapoptotic pathways (SCAPs) have been identified as senolytic targets, including the anti-apoptotic proteins BCL-2, BCL-W and BCL-XL, the transcription factors p53 and p21, hypoxia-inducible factor 1 (HIF1 α), phosphatidylinositol-4,5-bisphosphate 3-kinase (PI3K) and protein kinase B (PKB; also known as AKT), the serine protein inhibitors (serpins) and the heat shock protein HSP90.^{142,143} With knowledge of these SCAPs, it then becomes possible to rationally design drugs. For example, navitoclax (ABT-263) is a specific inhibitor of BCL-2, BCL-XL and BCL-W (also known as BCL-2L2). Other BCL-2 family inhibitors, such as ABT-737 (an inhibitor of BCL-2, BCL-W and BCL-XL) or A1331852 and A1155463 (selective inhibitors of BCL-XL), also display effectiveness *in vitro*^{144,145} and *in vivo*.¹⁴⁶

140 J. N. Justice et al. "Senolytics in idiopathic pulmonary fibrosis: results from a first- in-human, open- label, pilot study". *EBioMedicine*. **2019**, 40, 554–563.

141 US National Library of Medicine. *ClinicalTrials.gov* <https://clinicaltrials.gov/ct2/show/NCT03513016>, **2019**.

142 Y. Zhu et al. "The Achilles' heel of senescent cells: from transcriptome to senolytic drugs". *Aging Cell*. **2015**, 14, 644–658.

143 H. Fuhrmann- Stroissnigg et al. "Identification of HSP90 inhibitors as a novel class of senolytics". *Nat. Commun*. **2017**, 8, 422.

144 R. Yosef et al. "Directed elimination of senescent cells by inhibition of BCL- W and BCL- XL". *Nat. Commun*. **2016**, 7, 11190–11201 ().

145 Y. Zhu et al. "New agents that target senescent cells: the flavone, fisetin, and the BCL- XL inhibitors, A1331852 and A1155463". *Aging*. **2017**, 9, 1–9.

146 R. Yosef et al. "Directed elimination of senescent cells by inhibition of BCL- W and BCL- XL". *Nat. Commun*. **2016**, 7, 11190–11201.

This section concludes by noting that senolytics need not be small molecules. Indeed, nanoparticles can be effective carriers that selectively kill senescent cells. For example, MSNs, loaded with either doxorubicin or navitoclax and capped with a β -1,4-galactose hexamer, can selectively release their cargo in senescent cells because of their characteristically high β -Gal activity.^{147,148} These loaded nanoparticles were used to treat idiopathic pulmonary fibrosis (induced with bleomycin) and in combination with palbociclib to reduce tumours in xenografted mice.¹⁰² It is not only the small-molecule drugs but also their delivery that is important. Thus, mice treated with bleomycin recovered their pulmonary capacity after treatment with doxorubicin-loaded nanoparticles but not with free doxorubicin. The encapsulation of the drug inside the carrier reduces doxorubicin's overall toxicity by increasing its selectivity. Moreover, palbociclib treatment followed with doxorubicin-loaded or navitoclax-loaded nanoparticles leads to tumour regression in xenografted mice.

1.2.5 Senomorphics

Senomorphics are chemical species that inhibit the SASP without killing the senescent cell or reversing its proliferative arrest.¹⁴³ Instead, the molecules used thus far for this purpose interfere with and delay the ageing process, thereby providing a senotherapeutic effect by a mechanism different to that of senolytics.¹⁴⁹ In some cases, attenuating the SASP is accompanied by a lower lysosomal expansion and, thus, lower SA- β -Gal activity. The past decade has seen the emergence of several compounds with senomorphic activity.

147 A. Bernardos et al. "Enzyme- responsive controlled release using mesoporous silica supports capped with lactose". *Angew. Chem. Int. Ed.* **2009**, 48, 5884–5887.

148 A. Agostini et al. "Targeted cargo delivery in senescent cells using capped mesoporous silica nanoparticles". *Angew. Chem. Int. Ed.* **2012**, 51, 10556–10560.

149 L. J. Niedernhofer and P. D. Robbins. "Senotherapeutics for healthy ageing". *Nat. Rev. Drug Discov.* **2018**, 17, 377.

1.2.6 The importance of targeting senescent cells

Overcoming the gradual ageing of the world population remains a formidable challenge for health professionals. As life expectancy increases, the vulnerability to suffer from some type of chronic disease or pathology increases exponentially. In recent years, the scientific community has made a great effort to understand the molecular mechanisms that lead to ageing. A pioneering work, in which the mice were genetically modified to produce high levels of p53 (a tumor suppressor protein), revealed that the mice had almost non-existent cancer rates, but their half-life was significantly shorter and had aging symptoms at an early age.¹⁵⁰ In contrast, “super p53” mice (carrying p53-tg alleles in addition to the two endogenous alleles) presented the same rate of cancer resistance but normal lifespan, probably because p53 is normally regulated in this model.¹⁵¹ It was concluded that there is a strong relationship between cellular senescence and ageing.

As stated above, the main biological role of cellular senescence is to prevent the proliferation of damaged or stressed cells.²⁹ In addition, tissue damage and cellular senescence provide critical signals for cellular reprogramming and it has been reported to be beneficial in various tissue repair settings.^{21,152} However, upon persistent damage or during ageing, the process of tissue repair becomes inefficient and senescent cells tend to accumulate in tissues promoting local inflammation, tissue ageing, dysfunction and destruction, and potentially,

150 S. D. Tyner, S. Venkatachalam, J. Choi, S. Jones, N. Ghebraniouk, H. Igelmann, X. Lu et al. “p53 mutant mice that display early ageing-associated phenotypes”. *Nature*. **2002**, 415, 45-53.

151 I. García-Cao, M. García-Cao, J. Martín-Caballero, L. M. Criado, P. Klatt, J. M. Flores, J. C. Weill et al. “Super p53’ mice exhibit enhanced DNA damage response, are tumor resistant and age normally”. *The EMBO J.* **2002**, 21, 6225-35

152 B. Ritschka, M. Storer, A. Mas, F. Heinzmann, M. C. Ortells, J. P. Morton et al. “The Senescence-Associated Secretory Phenotype induces cellular plasticity and tissue regeneration”. *Genes Dev.* **2017**, 31, 172-83.

tumorigenesis and metastasis.^{29,153} Besides, it has been demonstrated that the selective elimination of senescent cells in genetic models amends a variety of ageing-associated symptoms, ameliorate long-term degenerative processes and extends both healthspan and lifespan.^{63,154} In fact, senotherapy has been shown to ameliorate and even revert certain diseases in mouse models. As we have seen above, a number of these pharmacologically active small compounds or senolytics have been reported to have remarkable therapeutic effects on multiple diseases in mice in association with the elimination of senescent cells.¹⁵⁵ In fact, the elimination of senescent cells is considered today as a promising strategy to treat ageing-related diseases and delay ageing.^{155,156,157}

A related key issue in the senescence field is the design of methods to easily identify cellular senescence.¹⁵⁸ As stated above, a first tool to detect senescent cells came from the discovery that senescent cells show high levels of lysosomal β -Gal activity.¹²² This is known as SA- β -Gal and it has served as the basis for the design of a number of chromo-fluorogenic probes (*vide infra*).¹² Some other markers for senescence, related to the expression of cell cycle inhibitors and/or tumour suppressors, have been reported (*vide ante*).

153 D. McHugh and J. Gil. "Senescence and aging: Causes, consequences, and therapeutic avenues". *J Cell Biol.* **2018**,217, 65-77.

154 D. J. Baker, T. Wijshake, T. Tchkonja, N. K. LeBrasseur, B. G. Childs, B. van de Sluis et al. "Clearance of p16Ink4a-positive senescent cells delays ageing-associated disorders". *Nature.* **2011**, 479, 232-36.

155 M. Paez-Ribes, E. González-Gualda, G. J. Doherty and D. Muñoz-Espín. "Targeting senescent cells in translational medicine". *EMBO Mol Med.* **2019**, 11, e10234.

156 B. G. Childs, M. Gluscevic, D. J. Baker, R. M. Laberge, D. Marquess, J. Dananberg, et al. "Senescent cells: an emerging target for diseases of ageing". *Nat Rev Drug Discov.* **2017**, 16, 718-735.

157 M. Xu, T. Pirtskhalava, J. N. Farr, B. M. Weigand, A. K. Palmer, M. M. Weivoda, et al. "Senolytics improve physical function and increase lifespan in old age". *Nat Med.* **2018**, 24, 1246-1256.

158 B. Lozano-Torres, A. Estepa-Fernández, M. Rovira, M. Orzáez, M. Serrano, R. Martínez-Mañé et al. "The Chemistry of Senescence". *Nat Rev Chem.* **2019**, 3, 426-441.

1.3 Chemical probes for the detection of senescent cells

1.3.1 SA- β -Gal-dependent chromo-fluorogenic probes

Proliferating cells express β -Gal encoded by the GLB1 gene that shows normal activity at pH 4. Since in 1995 Dimri and collaborators reported the overexpression of β -Gal enzyme activity at suboptimal pH (pH 6), due to the expansion of the lysosomal compartment of senescent cells,¹⁵⁹ this enzymatic activity, known as SA- β -Gal, is one of the most commonly used markers for the detection of cellular senescence.¹²¹ This marker is easy to detect and reliable both *in vivo* and *in vitro*.^{160,161} SA- β -Gal activity is conveniently measured using chromogenic or fluorogenic probes taking advantage of the fact that the enzyme hydrolyses galactosidic bonds.¹⁴⁸ In this context, most reported molecular probes able to detect SA- β -Gal are composed by two subunits, i.e. (i) a β -galactose residue as reactive fragment and (ii) a chromophore or fluorophore as a signalling moiety. In most cases both subunits are linked through *O*-glycosidic or *N*-glycosidic covalent bonds or through self-immolative fragments containing one glycosidic linkage.¹⁶² In these probes, the colour or emission of the fluorophore at a certain wavelength is drastically reduced or shifted when galactose is linked to the selected signalling unit. However, in the presence of SA- β -Gal, the glycosidic bond is hydrolysed and the fluorophore or chromophore is released, restoring its emission wavelength or its colour.¹²

159 B. Y. Lee, J. A. Han, J. S. Im, A. Morrone, K. Johung, E. C. Goodwin, et al. "Senescence-Associated β -Galactosidase is lysosomal β -Galactosidase". *Aging Cell*. **2006**, 5, 187-195.

160 H. W. Lee, C. H. Heo, D. Sen, H. O. Byun, I. H. Kwak, G. Yoon, et al. "Ratiometric two-photon fluorescent probe for quantitative detection of β -Galactosidase activity in senescent cells". *Anal Chem*. **2014**, 86, 10001-10005.

161 J. Zhang, C. Li, C. Dutta, M. Fang, S. Zhang, A. Tiwari, et al. "A novel near-infrared fluorescent probe for sensitive detection of β -Galactosidase in living cells". *Anal Chim Acta*. **2017**, 97–104.

162 B. Lozano-Torres, I. Galiana, M. Rovira, E. Garrido, S. Chaib, A. Bernardos, et al. "An OFF–ON two-photon fluorescent probe for tracking cell senescence *in vivo*". *J Am Chem Soc*. **2017**, 139, 8808-8811.

The first chromogenic probe for β -Gal, an *ortho*-nitrophenyl- β -galactoside (**ONPG**, Figure 8), was reported by Aizawa in 1939.¹⁶³ This compound is colourless; however, in presence of β -Gal, the *O*-glycosidic bond is hydrolysed yielding galactose and *ortho*-nitrophenol, which is yellow. A further colorimetric probe for β -Gal detection was synthesized by Horwitz and collaborators in 1964, named **X-Gal**. It consisted of a galactose linked to a substituted indole and it is a well-known colorimetric probe for the detection of β -Gal.¹⁶⁴ In presence of the enzyme, the galactosyl moiety in **X-Gal** is removed giving a 5-bromo-4-chloro-3-indolyl residue, which dimerizes spontaneously and is oxidized into the insoluble intensely blue product 5,5'-dibromo-4,4'-dichloro-indigo following the mechanism shown in Figure 8. Since **X-Gal** was reported, many variants have been synthesized with slight modifications giving final compounds that display different colours in the presence of β -Gal (Figure 8). All these derivatives are usually commercialized as β -Gal activity senescence detection kits. It is important to remark that **ONPG** and **X-Gal** are not permeable to the cell membrane and they can only be used in lysed cells.

In a pioneering work, Rotman et al described in 1961 the first fluorescent probe for measuring β -Gal activity, (fluorescein-di-(β -D-galactopyranoside),^{165,166} (**FDG** in Figure 8). In this study the authors reported that PBS solutions (pH 7.2) of **FDG** were non-emissive ($\lambda_{\text{exc}} = 400 \text{ nm}$) but a remarkable emission band at 490 nm was developed in the presence of β -Gal, due to the hydrolysis of glycosidic bonds and the subsequent release of fluorescein. These optical changes were also used

163 K. Aizawa. "Studien über carbohydrasen II. die fermentative hydrolyse des *p*-Nitrophenol- β -Galactoside". *Enzymologia*. **1939**, 6, 321-324.

164 J. P. Horwitz, J. Chua, R. J. Curby, A. J. Tomson, M. A. Da Rooge, B. E. Fisher, et al. "Substrates for cytochemical demonstration of enzyme activity. I. Some substituted 3-Indolyl- β -D-Glycopyranosides". *J Med Chem*. **1964**, 7, 574-575.

165 B. Rotman. "Measurement of activity of single molecules of β -D-Galactosidase". *Proc Natl Acad Sci U.S.A.* **1961**, 47, 1981-1991.

166 B. Rotman, J. A. Zderic and M. Edelstein. "Fluorogenic substrates for β -D-Galactosidases and phosphatases derived from fluorescein (3,6-dihydroxyfluoran) and its monomethylether". *PNAS U.S.A.* **1963**, 50, 1-6.

to detect β -Gal activity in droplets of silicone oil containing **FDG** and the enzyme. Following a similar approach Hirschmann and co-workers prepared in 1962 a compound named **MUG**¹⁶⁷ for the detection of β -Gal activity (Figure 8). Glycine buffer solutions of **MUG** (pH 7) did not show any emission ($\lambda_{\text{exc}} = 365 \text{ nm}$) whereas in presence of the enzyme, the galactoside residue was removed yielding the highly fluorescent 4-methylumbelliferone fluorophore ($\lambda_{\text{em}} = 455 \text{ nm}$), resulting in an overall OFF-ON response. Unfortunately, **MUG** is also impermeable to the cell

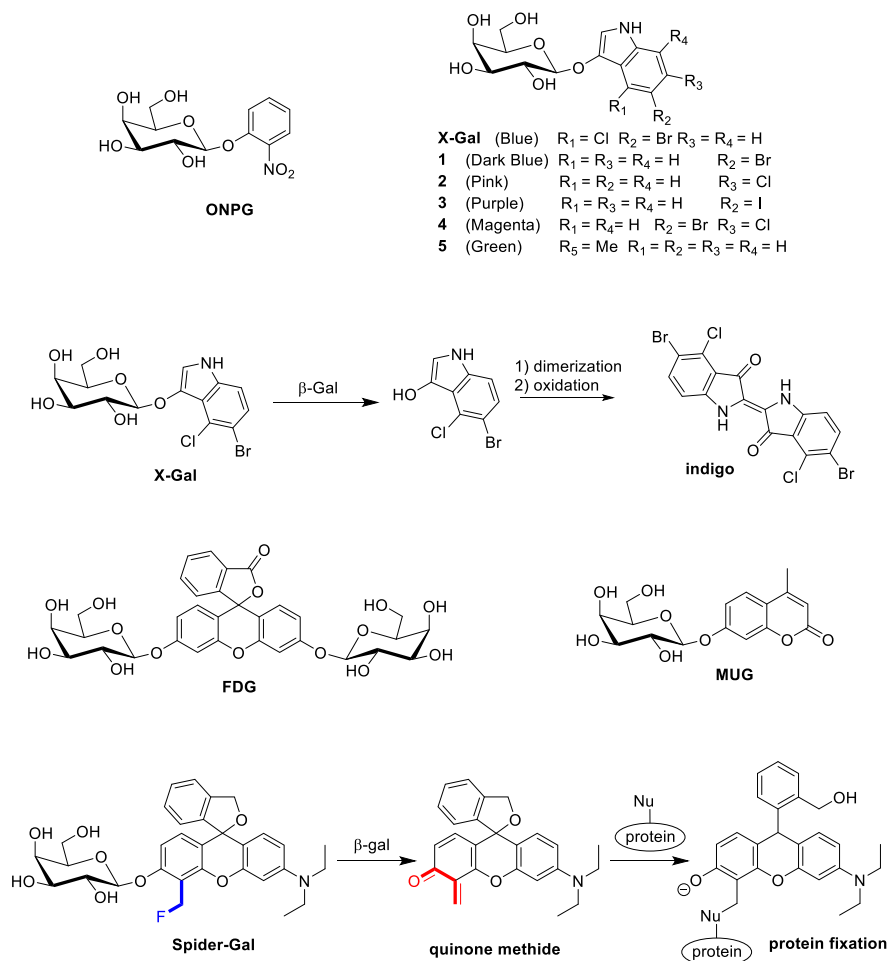


Figure 8. Most commonly and commercially available probes for cellular senescence detection.

167 L. L. Woods and J. Sapp. "A New one-step synthesis of substituted coumarins". *J Org Chem.* **1962**, 27, 3703-3705.

membrane. A great number of other coumarin-based fluorophores for β -Gal activity detection were later described.¹⁶⁸

A recent commercially available probe was developed by Urano and co-workers, who described a fluorogenic hemicyanin probe for labelling living senescent cells in culture and in living tissues. The prepared probe, (E)-2-[2-(6-hydroxy-2,3-dihydro-1*H*-xanthen-4-yl)vinyl]-3,3-dimethyl-1-propyl-3*H*-indole-1-ium, is commonly known as **Spider-Gal** (Figure 8).¹⁶⁹ PBS (pH 7.4) solutions of **Spider-Gal** present an absorption band at 525 nm and are almost non-emissive. However, addition of β -Gal enzyme induces the appearance of a highly fluorescent band at 560 nm (excitation at 525 nm). The observed emission enhancement was ascribed to the β -Gal-induced hydrolysis of **Spider-Gal** that yielded the **quinone methide** derivative shown in Figure 8. In the original research, the response of **Spider-Gal** was tested in HEK cells transfected or not with *LacZ* gene and the probe was able to distinguish between different levels of β -Gal by confocal microscopy, flow cytometry and *ex vivo* fixed tissues. In the last years, **Spider-Gal** has become in a widely used tool by researchers in the field of cellular senescence due to its high sensitivity and its high retentivity inside cells.

Although only a few probes based on the hydrolysis of *O*-glycosidic, *N*-glycosidic covalent bonds by SA- β -Gal enzyme activity are marketed; many probes based on this same idea of β -binding a monosaccharide to a fluorophore have been described.¹² Some of these probes for SA- β -Gal detection have been validated in *lacZ* transfection models which are not exactly realistic senescence models. In fact, in *lacZ* transfection models the transfected cells highly

168 K. R. Gee, W. C. Sun, M. K. Bhalgat, R. H. Upson, D. H. Klaubert, K. A. Latham et al. "Fluorogenic substrates based on fluorinated umbelliferones for continuous assays of phosphatases and β -Galactosidases". *Anal Biochem.* **1999**, 273, 41-48.

169 T. Doura, M. Kamiya, F. Obata, Y. Yamaguchi, T. Y. Hiyama, T. Matsuda et al. "Detection of *LacZ* -positive cells in living tissue with single-cell resolution". *Angew Chem Int Ed.* **2016**, 55, 9620-9624.

overexpress *lacZ* (with excessively high concomitant activity of β -Gal), and the bacterial enzyme is cytosolic and not localized in lysosomes (the usual subcellular location of SA- β -Gal activity) which could lead to failures in the detection of senescence.^{12,162} Moreover, many probes have been validated in *in vivo-lacZ* models according to two approaches: (i) transfecting tumour cells with the pCMV-*lacZ* plasmid and injected them in the animal; or (ii) labelling tumours overexpressing with avidin- β -Gal.^{170,171} A more realistic approach to validate SA- β -Gal probes used cell lines with high lysosomal β -Gal activity *per se*, such as cells from congenital dyskeratosis patients, SHIN3, SKOV3, OVK18, OVCAR3, OVCAR4, OVCAR5, OVCAR8 or HUVEC.^{164,172,173,174,175}

Certain probes have also been tested to detect replicative senescence; senescence induced by reactive oxygen species or chemically induced senescence. Kim et al. reported the ratiometric two-photon fluorescent probe (**SG1**) composed of the fluorophore 6-(benzo[d]thiazol-2'-yl)-2-(methylamino)-naphthalene, a self immolative carbamate as linker, a polyether as solubilizing group and galactose as hydrolytic moiety (Figure 9).¹⁶⁰ The authors found that the maximum of the emission spectra of **SG1** changed from 461 to 540 nm in the presence of β -Gal. β -Gal enzyme induced the hydrolysis of galactose in the anomeric carbon with the subsequent rupture of the self immolative linker that released the polyether-

170 M. Kamiya, H. Kobayashi, Y. Hama, Y. Koyama, M. Bernardo, T. Nagano et al. "An enzymatically activated fluorescence probe for targeted tumor imaging". *J Am Chem Soc.* **2007**, 129, 3918-3929.

171 K. Gu, Y. Xu, H. Li, Z. Guo, S. S. Zhu, S. S. Zhu et al. "Real-time tracking and *in vivo* visualization of β -Galactosidase activity in colorectal tumor with a ratiometric near-infrared fluorescent probe". *J Am Chem Soc.* **2016**, 138, 5334-5340.

172 S. Imai, Y. Kiyozuka, H. Maeda, T. Noda and H. L. Hosick. "Establishment and characterization of a human ovarian serous cystadenocarcinoma cell line that produces the tumor markers CA-125 and tissue polypeptide antigen". *Oncology.* **1990**, 47, 177-184.

173 M. C. Hung, X. Zhang, D. H. Yan, H. Z. Zhang, G. P. He, T. Q. Zhang et al. "Aberrant expression of the C-ErbB-2/Neu protooncogene in ovarian cancer". *Cancer lett.* **1992**, 61, 95-103.

174 T. C. Hamilton, R. C. Young, W. M. McKoy, K. R. Grotzinger, J. A. Green, E. W. Chu et al. "Characterization of a human ovarian carcinoma cell line (NIH:OVCAR-3) with androgen and estrogen receptors". *Cancer Res.* **1983**, 43, 5379-5389.

175 Y. Yuan; W. H. Kim; H. S. Han; J. H. Lee; H. S. Park; J. K. Chung; S. B. Kang and J. G. Park, "Establishment and characterization of human ovarian carcinoma cell lines". *Gynecol Oncol.* **1997**, 66, 378-387.

functionalized 6-(benzo[d]thiazol-2'-yl)-2-(methylamino)-naphthalene fluorophore. Probe **SG1** was tested in human diploid fibroblasts (HDF) in a replicative model of senescence. By treating the cells with **SG1**, the authors observed that the ratio $F_{\text{yellow}}/F_{\text{blue}}$ increased from 0.30 to 1.13 when cells accumulated passages and were excited at a wavelength of 750 nm. Finally, the authors used the probe for staining 7-month-old and 26-month-old Sprague–Dawley rat skin tissues, showing an enhancement of the $F_{\text{yellow}}/F_{\text{blue}}$ ratio.

A new senescence-specific fluorescent probe based in a rhodol core linked to galactose (**SRP**) was studied in vascular endothelial HUVEC cells, where senescence was induced with H_2O_2 (Figure 9). The **SRP** probe showed a high chemoselectivity in the presence of β -Gal versus other enzymes. Senescent cultured HUVEC cells exhibited high fluorescent signal after treatment with the probe, in sharp contrast with non-senescent HUVEC cells.¹⁷⁶ Recently, Zhang and co-workers, prepared a near-infrared fluorescent probe based on hemicyanine skeleton ((E)-2-(2-(6-hydroxy-2,3-dihydro-1H-xanthen-4-yl)vinyl)-3,3-dimethyl-1-propyl-3H-indol-1-ium) conjugated with a D-galactose moiety (**Gal-Pro** in Figure 9). The absorption spectra of **Gal-Pro** in PBS presented an intense band at 596 nm and two weaker absorptions at 560 nm and 643 nm. Moreover, the emission spectra of the probe showed a weak band at 665 nm. In the presence of β -Gal, a new emission band at 703 nm appeared (12.8-fold enhancement). The authors tested the probe response in a premature senescence model of HDF cells induced by H_2O_2 .¹⁶⁴ No signal was observed for control cells, whereas in senescent cells clear turn-on NIR fluorescent images were captured. This molecule, (Figure 9) was also tested in cells with knocked-in *LacZ* and HeLa and MCF7 senescent cells where senescence was induced with camptothecin or radiation therapy. The

176 E. J. Kim, A. Podder, M. Maiti, J. M. Lee, B. G. Chung and S. Bhuniya. "Selective monitoring of vascular cell senescence via β -Galactosidase detection with a fluorescent chemosensor". *Sens Actuator B-Chem.* **2018**, 274, 194-00.

probe was validated *in vivo* in mice bearing *LacZ*(+) tumour and camptothecin drug treated HeLa xenograft models in order to corroborate the applicability of **NIR-BG** in genetically or drug-induced expressed β -Gal.¹⁷⁷

As it is apparent from the literature, only very few reports exist, in which senescence probes have been validated in more realistic *in vivo* models of senescence. An example is the probe **AHGa** (anhydride–histidine–galactose), which contains an *N*-glycosidic bond (Figure 9).¹⁶² **AHGa** probe was tested in SK-MEL-103 xenografted mice in which senescence was induced by oral administration of palbociclib. The tumours in palbociclib-treated mice intravenously injected with the probe showed strong fluorescence relative to non-senescent tumours. Moreover, confocal microscopy images of fresh sections obtained from different organs (such as the liver, spleen, kidneys, lungs and heart) showed non-significant changes in fluorescence.

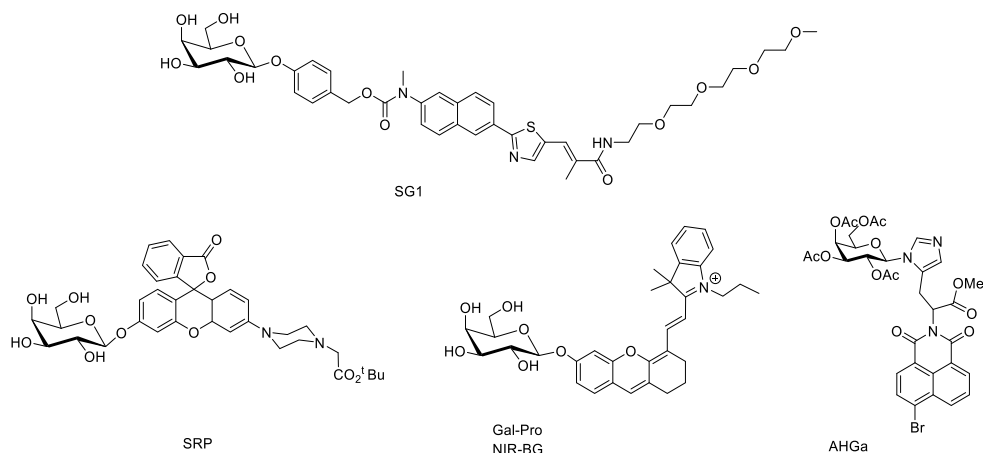


Figure 9. Some other fluorogenic probes for senescence detection.

177 Y. Wang, J. Liu, X. Ma, C. Cui, P. R. Deenik, P. K. P. Henderson et al. "Real-time imaging of senescence in tumors with DNA damage". *Sci Rep.* **2019**, 9, 2102-2013.

1.3.2 Other hydrolases probes

Apart from β -Gal, the overexpression of other lysosomal hydrolases¹²⁴ such as α -L-fucosidase (α -Fuc), has been also employed for the detection of cellular senescence.¹²⁵ The overexpression of α -Fuc was deduced from measurements of the activity of hydrolases in various cell lines using different senescence models. From these studies it was apparent that α -Fuc activity was higher or, at least, comparable with SA- β -Gal in senescent cells. Based on the above, molecular probes containing selected chromophores or fluorophores linked with α -fucose have been developed (**X-Fuc**¹⁷⁸ and **MUF**¹⁷⁹ in Figure 10) and used to measure α -Fuc activity. Other enzymes, such as β -glucuronidase,¹⁸⁰ acid phosphatase, β -hexosaminidase,¹⁸¹ α -mannosidase and *N*-acetyl- β -glucosaminidase,¹⁸² have also been reported to be overexpressed in senescent cells, but in lower levels than those found for β -Gal and α -Fuc. In this context, *p*-nitrophenyl- α -D-mannopyranoside, 4-nitrophenyl *N*-acetyl- β -D-glucosaminide and 4-nitrophenyl- β -D-glucuronide have been employed for activity measurement of α -mannosidase, *N*-acetyl- β -glucosaminidase and β -glucuronidase, respectively, in lysed cells (Figure 10).¹²⁴ Detection of these enzymes using chromo-fluorogenic probes could be an alternative for effective senescence detection.

178 J. R. Esterly, A. C. Standen and B. Pearson. "The histochemical demonstration of intestinal β -D-fucosidase with 5-bromo-4-chloroindole-3-yl- β -d-fucopyranoside". *J Histochem Cytochem.* **1967**, 15, 470-474.

179 A. R. Rushton and G. Dawson. "Glycosphingolipid β -Galactosidases of cultured mammalian cells: characterization of the enzymes from mouse cell line LMTK and human Lesch-Nyhan fibroblasts". *Biochim Biophys Acta Lipids Lipid Metab.* **1975**, 388, 92-105.

180 W. Grabowska, G. Mosieniak, N. Achatowska, R. Czochara, G. Litwinienko, A. Bojko et al. "Curcumin induces multiple signaling pathways leading to vascular smooth muscle cell senescence". *Biogerontol.* **2019**, 20, 783-798.

181 L. Urbanell, A. Magini, L. Ercolani, K. Sagini, A. Polchi, B. Tancini et al. "Oncogenic H-Ras up-regulates acid β -hexosaminidase by a mechanism dependent on the autophagy regulator TFEB". *PLoS ONE.* **2014**, 9, e89485.

182 M. Agirbasli, B. Radhakrishnamurthy, X. Jiang, W. Bao and G. S. Berenson. "Urinary n-acetyl- β -D-Glucosaminidase changes in relation to age, sex, race, and diastolic and systolic blood pressure in a young adult biracial population: The Bogalusa heart study". *Am J Hypertens.* **1996**, 9, 157-161.

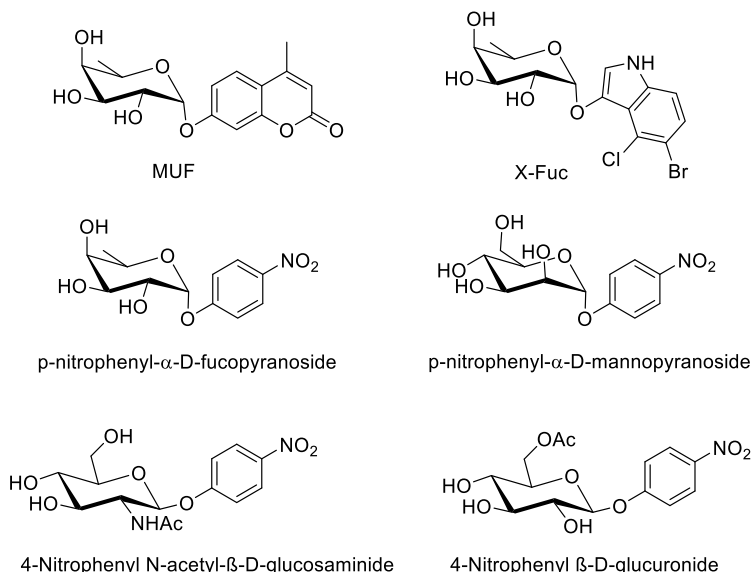


Figure 10. Chromo-fluorogenic probes for the detection of other lysosomal hydrolases.

1.3.3 Lipofuscin detection

Another proposed marker of senescence is lipofuscin. Lipofuscin is a non-degradable aggregate of oxidized proteins, lipids and oligosaccharides that accumulates progressively mostly in aged post mitotic cells.¹¹⁶ Intracellular lipofuscin accumulation appears to be a universal correlate of animal senescence.¹¹⁷ Lipofuscin is an emissive aggregate that can be visualized using fluorescent microscopy. Moreover, histochemical methods, such as staining with Sudan Black B (**SBB**), are commonly used for lipofuscin detection. Lipofuscin stained with **SBB** is applicable for *in vitro* measurements.^{119,120,183} Studies demonstrated that **SBB**-stained lipofuscin is present in cells that expressed SA-β-Gal activity and is absent in SA-β-Gal-negative cells.¹¹⁸ In a modification of this basic procedure, Gorgoulis, Bartek and co-workers recently developed a two-step staining procedure based on a biotin-antibiotin antibody-peroxidase-conjugated

183 T. Jung, A. Höhn and T. Grune. "Lipofuscin: detection and quantification by microscopic techniques". *Methods Mol Biol.* **2010**, 594, 173-193.

reaction, in order to improve the *in vitro* and *ex vivo* lipofuscin detection achieved with commercially available **SBB** staining (Figure 11). In their work, the authors used **SBB-biotin** conjugate to target lipofuscin.¹⁸⁴ After binding of lipofuscin with **SBB-biotin** the staining of senescent cells is carried out upon addition of an anti-biotin antibody functionalized with a peroxidase-conjugated polymeric backbone. Finally, addition of 3,3'-diaminobenzidine (DAB) induced the appearance of a dark blue-black colour (due to the peroxidase-catalysed oxidation of DAB) which indicated the presence of lipofuscin.¹¹⁸

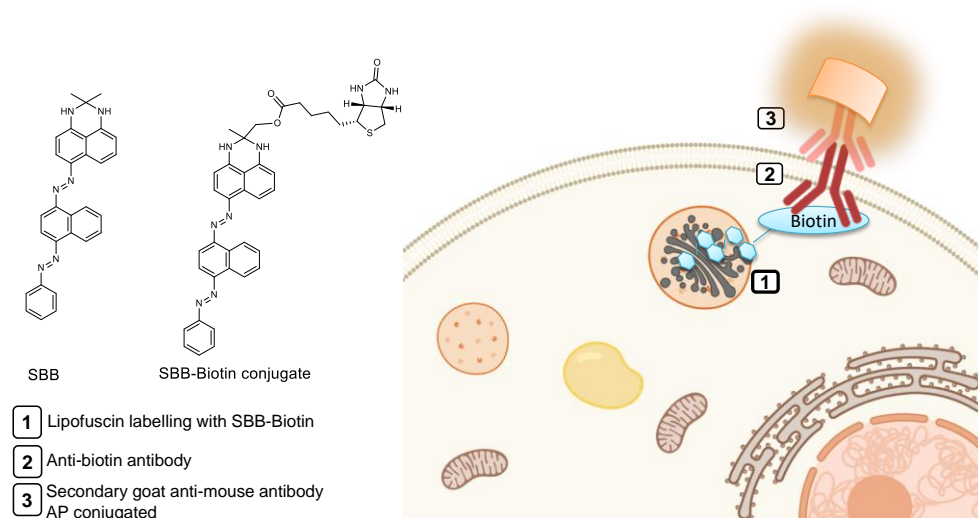


Figure 11. Chemical structures of **SBB** and **SBB-biotin** conjugate developed by Gorgoulis, Bartek and co-workers to detect lipofuscin.

1.3.4 Other approaches for the detection of senescent cells using chemical probes

Based on the facts cited above, it seems clear that most of the described methods for the detection of cellular senescence are based on chromo-

184 K. Evangelou, N. Lougiakis, S. V. Rizou, A. Kotsinas, D. Kletsas, D. Muñoz-Espín et al. "Robust, universal biomarker assay to detect senescent cells in biological specimens". *Aging cell*. **2017**, 16, 192-197.

fluorogenic probes that evaluate SA- β -Gal activity. In spite of this fact, in recent years, other innovative methods for the detection of senescent cells have been proposed which do not rely on the presence of lysosomal β -Gal or do not display a final chromo-fluorogenic signal.

The **CyBC9** probe has been recently developed based on a Cy7 skeleton (Figure 12) that was used for the detection of senescence using proliferative (young) and senescent (old) cells.¹⁸⁵ The probe is a nontoxic membrane-permeable fluorescent molecule. The probe was tested in human early mesenchymal stromal cells (heMSCs) (young and old) from different tissues, such as bone marrow (BM) Wharton's Jelly (UC) and adipose tissue (AD). The authors demonstrated that **CyBC9** probe is accumulated in the mitochondria of senescent cells. The selectivity of the probe is based in the membrane potential of mitochondria. In senescence cells, there is an increase in ROS species that induced the depolarization of the mitochondria membrane allowing the accumulation of the probe **CyBC9**.

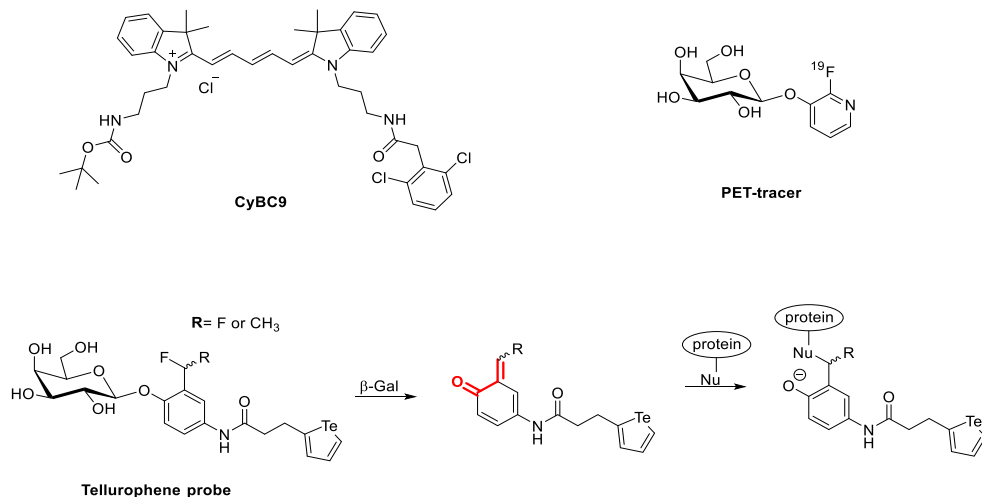


Figure 12. Probes for detection of cellular senescence, measuring SA- β -Gal activity, which are not functionalized with chromo-fluorophores.

185 J. Ang, Y. Lee, D. Raghothaman, P. Jayaraman, K. L. Teo, F. J. Khan et al. "Rapid detection of senescent mesenchymal stromal cells by a fluorescent probe". *Biotechnol J.* **2019**, 14, e1800691.

Lumba et al. reported a probe for lysosomal β -Gal activity capable of detecting cellular senescence in cultured cells by mass cytometry.¹⁸⁶ Mass cytometry is a similar technique to flow cytometry but equipped with an inductively coupled plasma mass spectrometry (ICP-MS) detector. The **tellurophene probe** contains a tellurene moiety as a reporter group which generates a quinone alkide when hydrolysed (Figure 12). The quinone alkide is a reactive alkylating agent that forms covalent tellurophene-bearing conjugates with protein nucleophiles, allowing the quantification of lysosomal β -Gal activity in individual cells by mass cytometry. The authors used a retinal pigment epithelial (Rpe) cell line known to undergo senescence upon H₂O₂ treatment. Upon addition of **tellurophene probe**, they authors observed a higher labelling (ca. 1.75-fold) in senescent Rpe cells compared to control cells by mass cytometry analysis.

Another technique recently used in the detection of senescent cells is positron-emission tomography (PET), for which radioactive molecules linked to β -galactosides are used (**PET-tracer** in Figure 12).¹⁸⁷ **PET-tracer** was tested in two different *in vitro* models: (i) HCT1-16 cells with doxorubicin-induced senescence and (ii) HRas driven liver progenitor cells with a doxycycline regulatable p53-specific shRNA. For this purpose both control and senescent cells of each cell line were treated with the **PET-tracer**, washed and measured in a gamma counter. Senescent cells from both lines incorporated more **PET-tracer** than control ones (ca. 3-fold higher accumulation). Besides, *in vivo* experiments showed higher uptake for senescent HCT1-16 tumours (1.54-fold) compared to control ones whereas the observed value for HRas driven liver progenitor cells was 1.66-fold higher.

186 M. A. Lumba, L. M. Willis, S. Santra, R. Rana, L. Schito, S. Rey et al. "A β -Galactosidase probe for the detection of cellular senescence by mass cytometry". *Org Biomol Chem.* **2017**, 15, 6388-6392.

187 J. Schwenck, J. Cotton, B. Zhou, K. Wolter, A. Kuehn, K. Fuchs et al. "In vivo imaging of tumor senescence with a novel beta-Galactosidase specific PET tracer". *Nuklearmedizin*, **2019**, 58, 106.

1.4 Nanodevices targeting senescent cells

Additionally to molecular-based sensors, the use of smart nanodevices is an active field of research and several interesting examples have been published in the last years applied to the detection of certain types of cells.¹⁸⁸ These nanodevices are mainly constituted by inorganic or organic nanoparticles carrying a certain cargo and sometimes functionalized with (bio)molecules acting as targeting ligands.¹⁸⁹ These complex nanoarchitectures are finding promising biomedical applications. Taking this into account, it is not surprising that several functional nanoparticles targeting senescent cells have been described recently.¹⁹⁰ These nanodevices are based on MSNs, carbon quantum dots (CQDs), porous CaCO₃ nanoparticles and molecularly imprinted polymer nanoparticles (nanoMIPs).

Martínez-Máñez et al. developed a nanodevice able to selectively release its cargo in senescent cells. The nanodevice consisted of MSNs, loaded with rhodamine B (Rh B), functionalised with (3-aminopropyl)triethoxysilane (APTES) and capped with a galacto-oligosaccharide.¹⁶⁴ A similar system capped with lactose was previously reported by the same authors in 2009.¹⁹¹ The release profile of the gated nanoparticles revealed a poor cargo delivery, whereas a remarkable amount of Rh B was released after 24 h in presence of β -Gal enzyme (Figure 13a). Cargo release in the presence of β -Gal was ascribed to the enzymatic hydrolysis of the capping galacto-oligosaccharide. Besides, the nanoparticles were

188 E. Aznar, M. Oroval, L. Pascual, J. R. Murguía, R. Martínez-Máñez and F. Sancenón. "Gated materials for on-command release of guest molecules". *Chem Rev.* **2016**, 116, 561-518.

189 B. Lozano-Torres, L. Pascual, A. Bernardos, M. D. Marcos, J. O. Jeppesen, Y. Salinas et al. "Pseudorotaxane capped mesoporous silica nanoparticles for 3,4-methylenedioxyamphetamine (MDMA) detection in water". *Chem Commun.* **2017**, 53, 3559-3562.

190 D. Muñoz-Espín. "Nanocarriers targeting senescent cells". *Trans Med Aging.* **2019**, 3, 1-5.

191 A. Bernardos, E. Aznar, M. D. Marcos, R. Martínez-Máñez, F. Sancenón, J. Soto et al. "Enzyme-responsive controlled release using mesoporous silica supports capped with lactose". *Angew Chem Int Ed.* **2009**, 48, 5884-5887.

tested in the cells lines DC1787, X-DC 1774 and X-DC4646 from patients suffering congenital dyskeratosis, in which lysosomal β -Gal is overexpressed. High emission signals were found in DC1787, X-DC 1774 and X-DC4646 cells lines, whereas poor cargo delivery was found in H460 control cells where endogenous β -Gal is not overexpressed. As stated above, Martínez-Mañez and Serrano developed mesoporous silica nanoparticles loaded with Rh B or Indocyanine Green (ICG) and capped with a β -1,4-galactose hexamer (**GalNP**).¹²⁰ In the presence of the β -Gal enzyme, the capping oligosaccharide was hydrolysed and cargo was released. These nanoparticles were tested in a mouse model of pulmonary fibrosis and in a cancer mouse model of senescence induced by chemotherapy. The authors observed that the combination of palbociclib treatment with **GalNP** loaded with Rh B or ICG presented a more efficiently release of the fluorophore in senescent tumours, observing an enhancement of fluorescence. Moreover, the induction of pulmonary fibrosis by treating mice with bleomycin followed by intravenous injection with the fluorophore-loaded **GalNP** led to an increased fluorescent signal with respect to mice not treated with bleomycin, which did not present cellular senescence in lungs. Finally, drug-loaded nanoparticles with doxorubicin (**GalNP(Dox)**) or navitoclax (**GalNP(Nav)**) facilitated tumour regression in xenografted mice concomitantly treated with palbociclib and also the recovery in the pulmonary capacity in mice subjected to bleomycin-induced lung fibrosis. Besides, the authors found that the encapsulation of doxorubicin and navitoclax reduced their toxicity.

A sensing method for cellular senescence using nanoparticles was developed by Feng and co-workers, who employed β -cyclodextrin-functionalized carbon quantum dots (β -CD-CQDs) for β -Gal activity evaluation *in vitro* (Figure 13b). PBS solutions of β -CD-CQDs showed a marked emission band at 445 nm upon excitation at 365 nm. The authors observed that this emission was quenched

upon addition of gradual amounts of *p*-nitrophenol due to the formation of an inclusion complex with the β -CDs grafted onto the external surface of the CQDs.¹⁹²

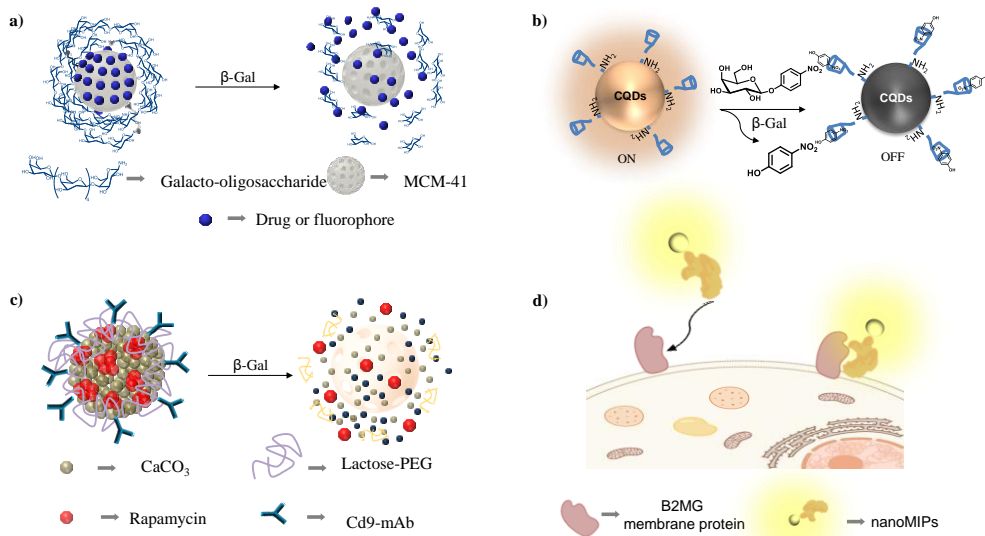


Figure 13. (a) MSNs capped with a galacto-oligosaccharide. In the presence of lysosomal β -Gal the galacto-oligosaccharide cap is hydrolysed and cargo is released. (b) Mechanism of detection of β -Gal using probe **4-nitrophenyl- β -D-galactopyranoside** and β -CD-CQDs. (c) CaCO_3 nanocarriers that selectively deliver the cargo in senescent cells. (d) Molecularly imprinted nanoparticles (nanoMIPs) targeting B2MG membrane protein associated to senescence.

Taking this into account, the authors monitored β -Gal activity using a mixture of β -CD-CQDs and **4-nitrophenyl- β -D-galactopyranoside**. β -Gal is able to hydrolyse the glycosidic bond in **4-nitrophenyl- β -D-galactopyranoside** releasing *p*-nitrophenol which formed supramolecular inclusion complexes with the grafted β -CD. As a consequence, the emission of β -CD-CQDs was quenched (Figure 12b). β -Gal enzyme was detected in a 1.9 to 70 U L⁻¹ range of concentrations and with a limit of detection as low as 0.6 U L⁻¹. MTT viability assays showed that β -CD-CQDs

192 C. Tang, J. Zhou, Z. Qian, Y. Ma, Y. Huang and H. A. Feng. "Universal fluorometric assay strategy for glycosidases based on functional carbon quantum dots: β -Galactosidase activity detection *in vitro* and in living cells". *J Mater Chem B*. **2017**, 5, 1971-1979.

were non-toxic for OVCAR-3, a cell line presenting high lysosomal β -Gal activity *per se* and that is typically used to validate β -Gal probes. OVCAR-3 cells incubated with β -CD-CQDs showed a marked fluorescence but when exposed to both β -CD-CQDs and the galactose derivative **4-nitrophenyl- β -D-galactopyranoside** a marked emission quenching was observed.

Detection and elimination of senescent cells has also been achieved with porous calcium carbonate nanoparticles loaded with a fluorophore (coumarin-6) or a drug (rapamycin).¹⁹³ The authors reacted lactose with a poly(ethylene glycol) derivative containing amine and carboxylate moieties in opposite sides and the poly(ethylene glycol) derivative was adsorbed onto the external surface of the loaded nanoparticles. Finally, an anti-CD-9 antibody (CD-9 receptor is overexpressed in senescent cells) was grafted onto the external surface of the nanoparticles using an EDC/NHS mediated esterification reaction (Figure 13c). Aqueous suspensions of the coumarin-6-loaded nanoparticles at pH 7.4 showed a poor cargo release after 48 h. However, in the presence of β -Gal, a marked cargo release was observed due to lactose hydrolysis and subsequent detachment of the PEG chain from the surface of the nanoparticles. Confocal microscopy studies carried out with the coumarin-loaded-material showed that nanoparticles were preferentially internalized by old/senescent human dermal fibroblasts (HDF) when compared to the same young cells due to the overexpression of CD-9 membrane receptors, resulting in the subsequent release of coumarin-6 by β -Gal activity. The same nanoparticles loaded with rapamycin, an mTOR inhibitor that prevents senescence by affecting the p53/p21 pathway, displayed a senomorphic effect due to the rapamycin release, inducing marked reductions in β -Gal levels, p53/p21, CD-9 expression and also decreased senescence-associated secretory

193 R. K. Thapa, H. T. Nguyen, J. H. Jeong, J. R. Kim, H. G. Choi, C. S. Yong et al. "Progressive slowdown/prevention of cellular senescence by CD9-targeted delivery of rapamycin using lactose-wrapped calcium carbonate nanoparticles". *Sci Rep.* **2017**, 7, 43299.

phenotypes (IL-6, IL-1 β) together with reduced senescent cells population numbers and prevention of cell cycle arrest.

More recently, another method for the detection of senescent cells based on molecularly imprinted nanoparticles (nanoMIPs) capable of recognizing a membrane protein associated with senescence was proposed.¹⁹⁴ It has been reported that senescent EJ bladder cancer cells (EJ), fibrosarcoma cells (HT1080) and human diploid fibroblasts (HDF) overexpressed the B2MG membrane protein.¹⁹⁵ Bearing this idea in mind, the authors developed nanoMIPs recognising an extracellular epitope of B2MG. For nanoMIPs synthesis, in a first step, the epitope (amino acids 101-115) of β 2 microglobulin (used as template) was covalently grafted onto the external surface of thiol-functionalised glass beads as a solid support by using succinimidyl-iodo acetate as linker. Then, in a second step, this hybrid material was suspended in a mixture of fluorescein-based acrylic monomers solution in order to obtain a polymer around the template (Figure 13d). Finally, nanoMIPs were separated from the solid support washing with water at 65°C. The affinity of nanoMIPs for B2MG protein was tested in EJ bladder cancer cells after genetically-induced senescence by overexpressing p16 with a tetracycline(tet)-regulatable system. Flow cytometry assays and fluorescence microscopy images revealed the preferential accumulation of nanoMIPs in the external membrane of senescent cells. Moreover, the senolytic activity of dasatinib-loaded nanoMIPs was demonstrated in EJp16 cells. Finally, *in vivo* studies revealed that nanoMIPs tagged with the dye DyLight 800 NHS Ester were

194 A. E. Ekpenyong-Akiba, F. Canfarotta, H. B. Abd, M. Poblocka, M. Casulleras, L. Castilla-Vallmanya et al. "Detecting and targeting senescent cells using molecularly imprinted nanoparticles". *Nanoscale Horiz.* **2019**, 4, 757-768.

195 M. Althubiti, L. Lezina, S. Carrera, R. Jukes-Jones, S. M. Giblett, A. Antonov et al. "Characterization of novel markers of senescence and their prognostic potential in cancer". *Cell Death Dis.* **2014**, 5, e1528.

able to distinguish between young (2 months) and old (11 months) C57/BL6J mice observing a preferential signal in the intestine, specifically in the jejunum.

Chapter 2 | Objectives

Given the relevance of senescence in ageing related diseases and the role of senescent cells in cancer, the present PhD thesis aims to contribute to the field of cellular senescence by the design, synthesis, characterization and *in vitro* and *in vivo* evaluation of different molecular probes, nanodevices and prodrugs whose response is related with the overexpression of β -Gal in senescent cells.

The specific objectives referred to each chapter are:

- To develop an OFF-ON probe to target senescent cells using a new two-photon naphthalimide-based fluorophore and its validation *in vivo* in mice bearing tumor xenografts treated with senescence-inducing chemotherapy.
- To develop a new naphthalimide-styrene based two photon fluorescence probe to target senescent cells and its validation *in vivo* in an orthotopic breast cancer mouse model treated with senescence-inducing chemotherapy, and in a renal fibrosis mouse model.
- To develop a renally clearable non-invasive Cy7-based NIR-fluorescent molecular probe to detect cellular senescence *in vivo* through a simple readable signal in urine.
- To design and validate MSNs loaded with Nile Blue (NIR-FDA-approved fluorophore) and capped with an galactooligosaccharide as a new nanodevice to detect cellular senescence *in vitro* and *in vivo*.
- To develop and validate *in vitro* and *in vivo* a new prodrug reducing side effects of the most potent and widely used commercially available senolytic: Navitoclax.

**Chapter 3 | An OFF-ON two-photon
fluorescent probe for tracking
cell senescence *in vivo*.**

An OFF-ON two-photon fluorescent probe for tracking cell senescence *in vivo*

Beatriz Lozano-Torres,^{a,b,c,d} Irene Galiana,^{a,b,c,d} Miguel Rovira,^e Eva Garrido,^{a,b,c,d} Selim Chaib,^e Andrea Bernardos,^{a,b,c,d} Daniel Muñoz-Espín,^{e,f} Manuel Serrano,^{e,*} Ramón Martínez-Mañez^{a, b, c, d,*} and Félix Sancenón^{a, b, c, d}

^a Instituto Interuniversitario de Investigación de Reconocimiento Molecular y Desarrollo Tecnológico (IDM), Universitat Politècnica de València, Universitat de València. Spain.

^b Unidad Mixta UPV-CIPF de Investigación en Mecanismos de Enfermedades y Nanomedicina, Universitat Politècnica de València, Centro de Investigación Príncipe Felipe, Valencia, Spain.

^c CIBER de Bioingeniería, Biomateriales y Nanomedicina (CIBER-BBN).

^d Unidad Mixta de Investigación en Nanomedicina y Sensores. Universitat Politècnica de València, IIS La Fe, Valencia, Spain

^e Tumor Suppression Group. Spanish National Cancer Research Centre (CNIO). Madrid, Spain

^f CRUK Cancer Centre Early Detection Programme, Department of Oncology. University of Cambridge. Hutchison/MRC Research Centre. Cambridge, UK

Published online: January 18, 2017

(Reprinted with permission from *J. Am. Chem. Soc.*, **2017**, *139*, 8808-8811.

Copyright © 2017, American Chemical Society. All rights reserved.)

3.1 Abstract

A naphthalimide-based two-photon probe (**AHGa**) for the detection of cell senescence has been designed. The probe contains a naphthalimide core, an L-histidine methyl ester linker and an acetylated galactose bonded to one of the aromatic nitrogen atoms of the L-histidine through a hydrolysable *N*-glycosidic bond. Probe **AHGa** is transformed into **AH** in senescent cells resulting in an enhanced fluorescent emission intensity. Importantly, *in vivo* detection of senescence was validated in mice bearing tumor xenografts treated with senescence-inducing chemotherapy. Our work provides a potential technology for diagnostic applications in a wide variety of clinical disorders.

3.2 Introduction

Senescent cells show a flat and enlarged morphology with increased cytoplasmic and nuclear volume, and an altered phenotype. The main purpose of cellular senescence is to prevent the proliferation of damaged or stressed cells and, at the same time, to trigger tissue repair.¹ However, upon persistent damage or during aging, the dynamic process of tissue repair becomes inefficient and senescent cells tend to accumulate. This accumulation in tissues is believed to impair tissue functions and accelerate aging.¹ Several markers and phenotypic characteristics have been described to define senescence: (i) a complex paracrine response termed as senescence-associated secretory phenotype (SASP),² (ii) the expression of cell cycle inhibitors and/or tumor suppressors (p16, p21 or p53)³ and (iii) high levels of lysosomal β -galactosidase (β -Gal) activity (known as senescence-associated β -galactosidase, SA- β -Gal)⁴ and several other hydrolases.⁵

It has been demonstrated that genetic ablation of senescent cells ameliorates a variety of ageing-associated diseases, reverts long-term degenerative processes

and extends longevity.⁶ Inspired by these findings, strategies to prevent, replace or remove senescent cells have become of interest both from basic research and application viewpoints. In fact, there is an increasing interest in the development of senolytics, molecules that are able to induce apoptosis preferentially in senescent cells.⁷ Such senolytics would contribute to the therapeutic treatment of senescence-associated diseases and may boost the long-term concept that rejuvenation might be possible.⁸ A related key issue in this field, is the design of tools able to accurately detect *in vivo* the presence of senescence. These probes are expected to be a fundamental instrument for the detection of senescent cells in aged or damaged tissues and to be a suitable tool to monitor the action of senolytics in multiple age-related disorders.¹ However, one of the major obstacles limiting progress in this research area, is the nearly lack of real-time methods to selectively track senescence in *in vivo* systems.

Detection of senescent cells usually relies on the detection of the senescence-associated β -Gal (SA- β -Gal) activity, and several fluorescent or chromogenic molecular probes have been reported for the visualization of this enzymatic activity.⁹ However, these first-generation probes are usually unsuitable for *in vivo* imaging as they rely on chromogenic changes or on the use of classical one-photon fluorescence excitation. As an alternative, the synthesis of probes using two-photon fluorescence has recently attracted attention.¹⁰

Two-photon probes provide prolonged observation time, increased imaging depth, minimized fluorescence background, ameliorated light scattering and rather minimize tissue injury.

In this context, recent stimulating studies developing fluorescent probes for the visualization of β -Gal activity have been described (Table S1). However, most of the reported probes are synthesized by using tedious multistep protocols. Another common drawback of these molecular sensors is the fact that are tested

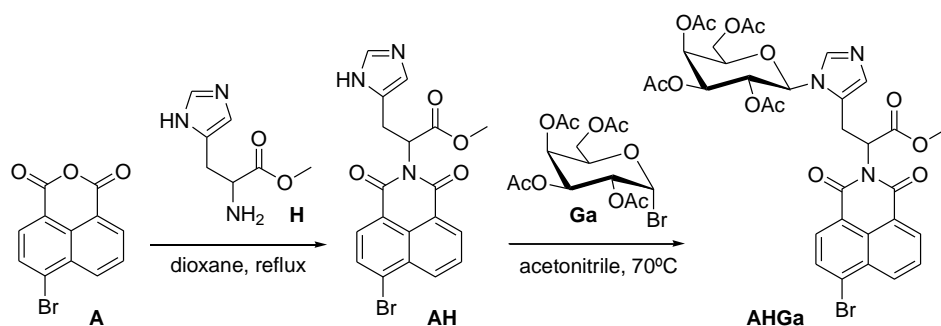
in cultured cells or in animal models that were not directly related to senescence. The methodology used in these studies, is based on a *lacZ* gene transfection, which results in high levels of bacterial β -Gal expression in the cell cytoplasm (unlike the lysosomal β -Gal activity associated with senescent cells).¹¹ A limited number of works describe the use of human cell lines overexpressing endogenous β -Gal per se, as it is the case of ovarian cancer cell lines.¹² However, these cancer cell lines are obviously not senescent because senescent cells do not proliferate. As regards *in vivo* studies with mice, probes are tested in models that (i) labeled tumors with avidin- β -Gal¹³ or (ii) transfected tumor cells with pCMV-*lacZ* plasmid.¹⁴ In both cases a bacterial β -Gal overexpression is achieved.

In this scenario, the development of more specific and reliable two-photon fluorescence-based probes for *in vivo* detection of senescence is still a challenge. In view of the aspects mentioned above, we report herein a novel molecular probe for the two-photon fluorogenic *in vivo* detection of senescence. The probe (**AHGa**) is based on a naphthalimide fluorophore as signaling unit containing an L-histidine methyl ester linker and an acetylated galactose attached to one of the aromatic nitrogen atoms of the L-histidine through a hydrolysable *N*-glycosidic bond. Probe **AHGa** is transformed into **AH** in senescent cells (Figure 1a) resulting in an enhanced fluorescent emission intensity. *In vivo* detection of senescence was additionally demonstrated in mice bearing tumor xenografts treated with senescence-inducing chemotherapy.

3.3 Results and discussion

The synthesis of **AHGa** is shown in Scheme 1. The probe was easily prepared using a two-step protocol. In the first step, 4-bromo-1,8-naphthalic anhydride (A) and L-histidine methyl ester (H) were reacted in refluxing dioxane yielding fluorophore **AH**. Then, a nucleophilic substitution reaction between **AH** and 2,3,4,6-tetra-O-

acetyl- α -D-galactopyranosyl bromide (**Ga**) yielded the final **AHGa** probe. Both, **AH** and **AHGa**, were characterized by using ^1H and ^{13}C NMR and HRMS (Figures S1-S6). Figure 1b summarizes the fluorogenic behavior of **AHGa** and **AH**. Excitation at 405 nm of **AHGa** in PBS (pH 4.5)-DMSO (0.01%) did not show any emission band ($\phi_{\text{AHGa}} = 0.002$), whereas under the same experimental conditions **AH** displayed an intense fluorescence ($\phi_{\text{AH}} = 0.458$, 286-fold enhancement) at 540 nm (Figure 1b and S7). Moreover, the emission intensity of **AH** remained unchanged in the 4-8 pH range (Figure S8).



Scheme 1. Synthetic route used for the preparation of **AHGa** probe.

Targeting of senescent cells *in vivo* with **AHGa** was validated with the SK-Mel-103 (human melanoma) cell line treated with palbociclib (Figure 2). Palbociclib is a specific CDK4/6 inhibitor, which has been displayed to induce cell cycle arrest in melanoma cells.¹⁵ In a common experiment, SK-Mel-103 cells were treated with 5 μM palbociclib during two weeks in order to induce senescence. After this treatment, SK-Mel-103 cells presented a typical larger and flatten phenotype associated with senescence (Figure 2b and 2f). Cellular senescence was also assessed by SA- β -Gal activity assay¹⁶ (Figure 2a and 2e). Then, the cytotoxicity of **AH** and **AHGa** was evaluated by a luminescence-based cell viability assay. **AH** and **AHGa** proved to be not toxic for both control and palbociclib-treated SK-Mel-103 cells after 48 h at concentrations of up to 20 μM (Figure S9).

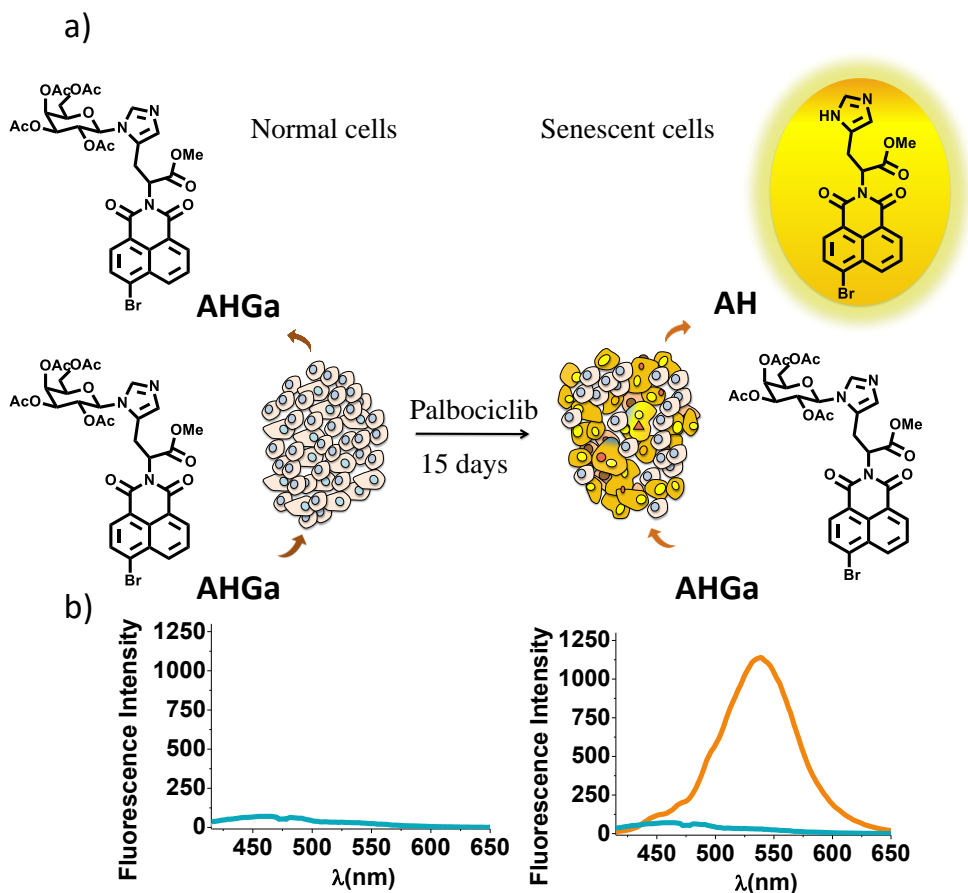


Figure 1. a) Schematic representation of **AHGa** activation in senescent cells. b) Emission spectra of PBS (pH 4.5)-DMSO (0.01%) solutions of 10^{-5} M **AHGa** (blue) and **AH** (orange) when excited at 405 nm.

Both, control and palbociclib-treated SK-Mel-103 cells were seeded in flat-bottom-clear 96 well plates and incubated with a solution containing **AHGa** (10 μ M in DMEM, 0.1% DMSO) for 2 h. Cells were then analyzed by two-photon confocal microscopy using 750 nm as excitation wavelength. Control SK-Mel-103 cells in the absence (Figure 2c) or presence (Figure 2d) of **AHGa** did not exhibit any noticeable fluorescence signal. Similarly, in the absence of the probe, senescent SK-Mel-103 cells did not show significant auto-fluorescence (Figure 2g).

In contrast, senescent cells treated with **AHGa** showed a clear bright emission (Figure 2h). Fluorescence is related to the presence of an emission band centered at ca. 540 nm, and attributed to the hydrolysis of **AHGa** into **AH** that selectively occurred in senescent cells. The quantification of the fluorescence associated to **AH** was also determined for each treatment from confocal images (Figure 2i). A remarkable fluorescence emission enhancement (ca. 10-fold) for palbociclib-treated SK-Mel-103 cells in the presence of **AHGa** when compared with control SK-Mel-103 cells was observed. The above results indicate that **AHGa** was cell membrane-permeable and that can be specifically activated in palbociclib-treated SK-Mel-103 cells, thereby providing an OFF-ON two-photon readout for the *in situ* quantitative tracking of senescent cells.

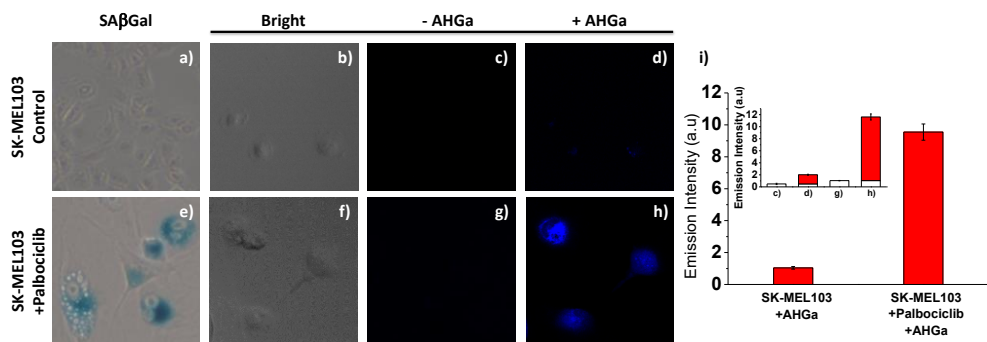


Figure 2. (a,e) Conventional X-Gal chemical assay for SA- β -Gal expression of control (a) and palbociclib-treated (senescent) (e) SK-Mel-103 cells. (b,f) Bright channel for control SK-Mel-103 (b) and senescent SK-Mel-103 (f) cells. (c,d,g,h) Two-photon images of (c,d) control SK-Mel-103 and (g, h) senescent SK-Mel-103 cells in the absence (c,g) and in the presence (d,h) of **AHGa** probe. Cells were incubated with **AHGa** (10 μ M) with DMEM (10% FBS, 0.1% DMSO) in 20% O₂ and 5% CO₂ at 37°C for 2 h, and then images were acquired by using a femtosecond pulse laser (excitation at 750 nm) with a Leica TCS SP5 laser scanning confocal. Representative images from repeated experiments (n = 3) are shown. (i) Quantification of the fluorescence emission intensity of control and palbociclib-treated SK-Mel-103 cells incubated with **AHGa**. Inset: Basal fluorescence is represented in white bars and **AHGa** ascribed fluorescence is represented in red. Error bars represent s.d.

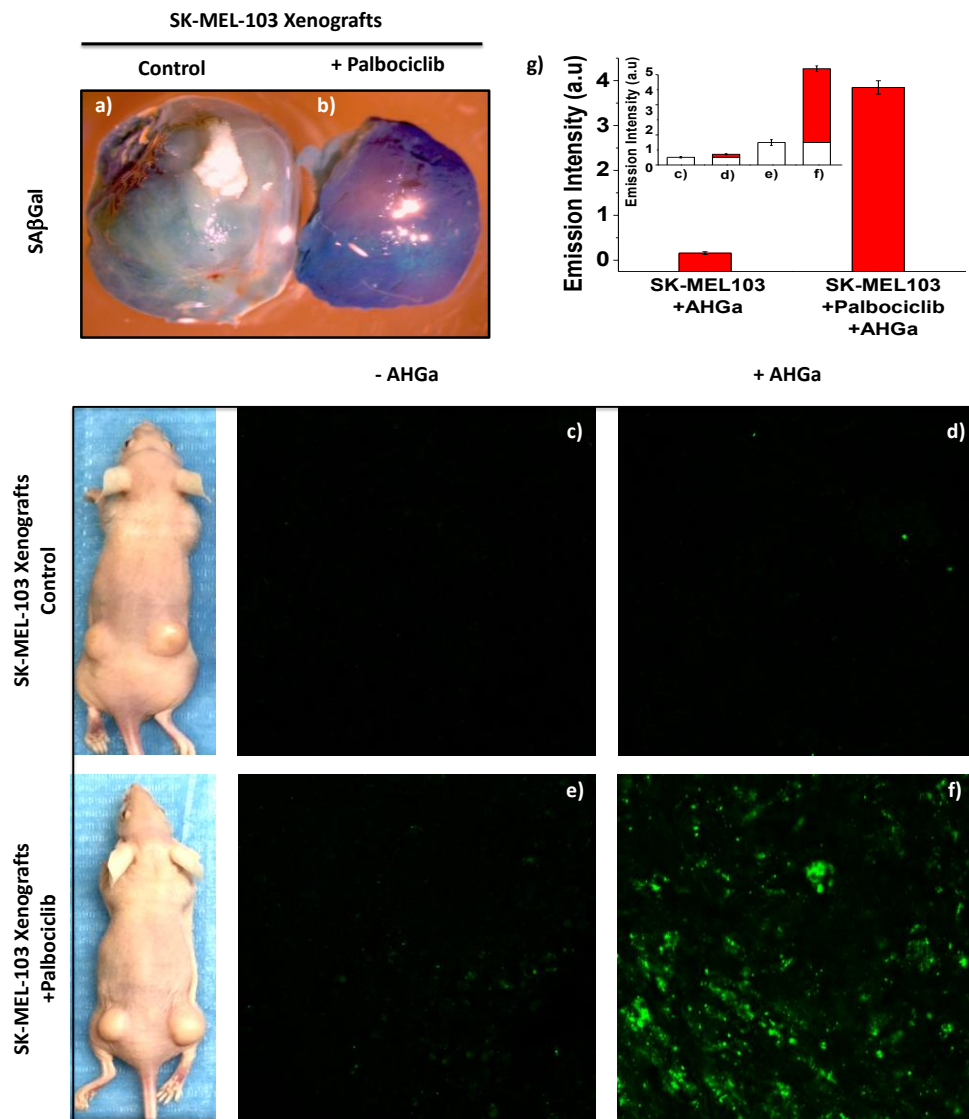


Figure 3. (a,b) Tissue portions of SK-Mel-103 control tumors (a) or SK-Mel-103 senescent tumors after whole-mount SA- β -Gal staining. (c-f) Confocal images of representative portions of SK-Mel-103 control tumors (c,d) and SK-Mel-103 senescent tumors (e,f) vehicle (c,e) and after intravenous tail injection (d,f) of **AHGa** probe (10 mg/ml, 200 μ l). Mice were sacrificed at 3 h post-treatment. Quantification of the fluorescence emission intensity of SK-Mel-103 (control) and SK-Mel-103 treated with palbociclib (senescent) in the absence or in the presence of the **AHGa** probe. Inset: Basal fluorescence is represented in white bars and **AH** ascribed fluorescence is represented in red. Error bars represent s.d. (n = 6 tumors for each condition).

Once assessed the activation of **AHGa** in senescent cultured cells, the probe was validated by the use of mice bearing tumor xenografts treated with senescence-inducing chemotherapy. In a typical experiment, tumor xenografts were generated by injecting subcutaneously SK-Mel-103 melanoma cells. Upon tumor formation (~200 mm³ average volume), mice were treated daily with palbociclib for 10 days in order to induce senescence and arrest tumor growth. Finally, **AHGa** probe was injected intravenously in the tail vein and mice were subsequently sacrificed at 3 h after the treatment. Next, tumors were extracted and cellular senescence was assessed by a SA- β -Gal staining. Tumors from palbociclib-treated mice showed the characteristic blue SA- β -Gal staining indicative of high levels of accumulated senescent cells (Figure 3b). The absence of the proliferative marker Ki67, and the reduction in phosphorylated Rb in tumors were also indicative of senescence.¹⁷ Then, fresh tumor sections were analyzed using confocal microscopy. The obtained results are shown in Figures 3c-3f. As observed, control tumors showed negligible fluorescence either in the absence or in the presence of **AHGa** (Figures 3c and 3d). Tumors from mice treated with palbociclib in the absence of the probe were used as a control for tissue auto-fluorescence, and showed a weak emission (Figure 3e). In sharp contrast, isolated tumors from mice treated with palbociclib and intravenously injected with **AHGa** showed a strong fluorescent signal (Figure 3f). Quantification of the associated **AH** fluorescence was determined for each condition (Figure 3g). A marked emission enhancement (ca. 15-fold) in tumors treated with palbociclib compared to control tumors was observed.

In addition, *ex vivo* imaging of fresh sections from different organs showed that emission from **AH** was only observed in senescent tumors, yet no significant emission enhancement was observed in other organs (i.e. liver, spleen, kidney, lung and heart) at 3 h post-injection (Figure S10). Although the probe was

administered by intravenous tail injection, **AHGa** was able to reach the senescent tumor, whereas no signal emission was observed in the rest of organs. These results pointed out the ability of **AHGa** probe to detect senescence *in vivo*.

3.4 Conclusions

Altogether, we describe a two-photon fluorescent probe (**AHGa**) for the *in vivo* detection of cell senescence. **AHGa** is based on a naphthalimide core with an L-histidine methyl ester linked to an acetylated galactose through a hydrolysable *N*-glycosidic bond. **AHGa** was not emissive upon excitation at 405 nm whereas its **AH** derivative showed a clear and intense fluorescence at 540 nm. Targeting of senescent cells *in vivo* with **AHGa** was validated with the SK-Mel-103 cancer cell line treated with palbociclib. A remarkable fluorescence emission enhancement (ca. 10-fold) in the presence of **AHGa** for palbociclib-treated SK-Mel-103 (senescent) cells was observed when compared with control SK-Mel-103 cells, due to the formation of **AH** that selectively occurs in senescent cells. The ability of tracking senescence of probe **AHGa** was also studied *in vivo* by employing mice bearing subcutaneous tumor xenografts generated with SK-Mel-103 melanoma cells and treated with palbociclib. Tumors in palbociclib-untreated mice showed negligible fluorescence emission both in the absence or in the presence of **AHGa**, whereas tumors in mice treated with palbociclib and intravenously injected with **AHGa** showed a clear fluorescent signal. A marked emission enhancement (ca. 15-fold) in tumors treated with palbociclib compared to non-treated tumors was observed. **AH** fluorescence was only found in senescent tumors and no significant emission enhancement was detected in other organs including liver, spleen, kidney, lung and heart. The combination of selectivity, sensitivity and straightforward synthesis make **AHGa** and efficient OFF-ON two-photon probe for the *in vivo* signaling of senescence. We believe that our study may provide an

efficient tool for detection of senescence in realistic *in vivo* models and inspire the design of probes with potential clinical applications.

3.5 Acknowledgments

The authors thank the financial support from the Spanish Government (projects MAT2015-64139-C4-1-R and AGL2015-70235-C2-2-R) and the Generalitat Valenciana (project PROMETEOII/2014/047). B.L.T. is grateful to the Spanish Ministry of Economy for her PhD grant. I.G. thanks the Generalitat Valenciana for her PhD grant. A.B. thanks the Spanish Government for the financial support “Juan de la Cierva-Incorporación”. M.R. is grateful to “La Caixa” foundation for his PhD scholar-ship. Work in M.S.’s group was funded by the CNIO and by grants from Spanish Ministry of Economy, the European Regional Development Fund (SAF project) the European Research Council (ERC Advanced Grant), and the Botin Foundation and Banco Santander (Santander Universities Global Division). D.M.-E. was funded by a “Ramón y Cajal” Programme Senior Grant and the “RETOS” National Programme for Research (MINECO), Cancer Research UK, and the CRUK Cambridge Centre Early Detection Programme.

3.6 References

1. Muñoz-Espin, D.; Serrano, M. *Nat. Rev. Mol. Cell Biol.* **2014**, *15*, 482-496.
2. (a) Yun, M. H.; Davaapil, H.; Brookes J. P. *eLife* **2015**, *4*, e05505. (b) Chiche, A.; Le Roux, I.; von Joest, M.; Sakai, H.; Aguin, S. B.; Czin, C.; Salam, R.; Fiette, L.; Alegria, O.; Flamant, P.; Tajbakhsh, S.; Li, H. *Cell Stem Cell* **2017**, *20*, 407-414. (c) Demaria, M.; Ohtani, N.; Youssef, S. A.; Rodier, F.; Touissant, W.; Mitchell, J. R.; Laberge, R. M.; Vijg, J.; Van Steeg, H.; Dollé, M. E. T.; Hoeijmakers, J. H. J.; de Bruin, A.; Hara, E.; Campisi, J. *Dev. Cell* **2014**, *31*, 722-733. (d) Krizhanovsky, V.; Yon, M.; Dickins, R. A.; Hearn, S.; Simon, J.; Miething, C.; Yee, H.; Zender, L.; Lowe, S. W. *Cell* **2008**, *134*, 657-667.
3. (a) Haber, D. A. *Cell* **1997**, *91*, 555-558. (b) Jung, Y. -S.; Qian, Y.; Chen, X. *Cell. Signal.* **2010**, *22*, 1003-1012.

4. Dimri, G. P.; Lee, X.; Basile, G.; Acosta, M.; Scott, G.; Roskelley, C.; Medrano, E. E.; Linskens, M.; Rubel, J.; Pereira-Smith, O.; Peacocke, M.; Campisi, J. *Proc. Natl. Acad. Sci. USA* **1995**, 92, 9363-9367.
5. Knás, M.; Zalewska, A.; Kretowski, R.; Niczyporuk, M.; Waszkiewicz, N.; Cechowska-Pasko, M.; Waszkiel, D.; Zwierz, K. *Folia Histochem. Cytobiol.* **2012**, 50, 220-227.
6. (a) Baker, D. J.; Childs, B. J.; Durik, M.; Wijers, M. E.; Sieben, C. J.; Zhong, J.; Saltness, R. A.; Jeganathan, K. B.; Verzosa, G. C.; Pezeshki, A.; Khazaie, K.; Miller, J. D.; van Deursen, J. M. *Nature* **2016**, 530, 184-189. (b) Childs, B. G.; Baker, D. J.; Wijshake, T.; Conover, C. A.; Campisi, J.; van Deursen, J. M. *Science* **2016**, 354, 472-477.
7. Zhu, Y.; Tchkonina, T.; Pirstkhalava, T.; Gower, A. C.; Ding, H.; Giorgadze, N.; Palmer, A. K.; Ikeno, Y.; Hubbard, G. B.; Lengurg, M.; O'Hara, S. P.; LaRusso, N. F.; Miller, J. D.; Roos, C. M.; Verzosa, G. C.; LeBrasseur, N. K.; Wren, J. D.; Farr, J. N.; Khosla, S.; Stout, M. B.; McGowan, S. J.; Fuhrmann-Stroissnigg, H.; Gurkar, A. U.; Zhao, J.; Colangelo, D.; Dorronsoro, A.; Ling, Y. Y.; Barghouthy, A. S.; Navarro, D. C.; Sano, T.; Robbins, P. D.; Niedernhofer, L. J.; Kirkland, J. L. *Aging Cell* **2015**, 14, 644-658.
8. (a) Zhu, Y.; Tchkonina, T.; Fuhrmann-Stroissnigg, H.; Dai, H. M.; Ling, Y. Y.; Stout, M. B.; Pirstkhalava, T.; Giorgadze, N.; Johnson, K. O.; Giles, C. B.; Wren, J. D.; Niedernhofer, L. J.; Robbins, P. D.; Kirkland, J. L. *Aging Cell* **2016**, 14, 428-435. (b) Chang, J.; Wang, Y.; Shao, L.; Laberge, R. M.; Demaria, M.; Campisi, J.; Janakiraman, K.; Sharpless, N. E.; Ding, S.; Feng, W.; Luo, Y.; Wang, X.; Aykin-Burns, N.; Krager, K.; Ponnappan, U.; Hauer-Jensen, M.; Meng, A.; Zhou, D. *Nat. Med.* **2016**, 22, 78-83. (c) Yosef, R.; Pilpel, N.; Tokarsky-Amiel, R.; Biran, A.; Ovayda, Y.; Cohen, S.; Vadai, E.; Dassa, L.; Shahar, E.; Condiotti, R.; Ben-Porath, I.; Krizhanovsky, V. *Nat. Commun.* **2016**, 7, 11190. (d) Baar, M. P.; Brandt, R. M.; Putavet, D. A.; Klein, J. D.; Derks, K. W.; Bourgeois, B. R.; Stryeck, S.; Rijksen, Y.; van Willigenburg, H.; Feijtel, D. A.; van der Pluijm, I.; Essers, J.; van Cappellen, W. A.; van IJcken, W. F.; Houtsmuller, A. B.; Pothof, J.; de Bruin, R. W.; Madl, T.; Hoeijmakers, J. H.; Campisi, J.; de Keizer, P. L. *Cell* **2017**, 169, 132-147.
9. (a) Gee, K. R.; Sun, W. C.; Bhalgat, M. K.; Upson, R. H.; Klaubert, D. H.; Latham, K. A.; Haugland, R. P. *Anal. Biochem.* **1999**, 273, 41-48. (b) Wang, P.; Du, J.; Liu, H.; Bi, G.; Zhang, G. *Analyst* **2016**, 141, 1483-1487. (c) Otsubo, T.; Minami, A.; Fujii, H.; Taguchi, R.; Takahashi, T.; Suzuki, T.; Teraoka, F.; Ikeda, K. *Bioorg. Med. Chem. Lett.* **2013**, 23, 2245-2249. (d) Mandal, P. K.; Cattiaux, L.; Bensimon, D.; Mallet, J. M. *Carbohydr. Res.* **2012**, 358, 40-46. (e) Ho, N. H.; Weissleder, R.; Tung, C. H. *ChemBioChem* **2007**, 8, 560-566. (f) Na, S. Y.; Kim, H. J. *Dyes Pigm.* **2016**, 134, 526-530. (g) Miranda, O. R.; Cehn, H. T.; You, C. C.; Mortenson, D. E.; Yang, X. C.; Bunz, U. H. F.; Rotello, V. M. *J. Am. Chem. Soc.* **2010**, 132, 5285-5289. (h) Chilvers, K. F.; Perry, J. D.; James, A. L.; Reed, R. H. *J. Appl. Microbiol.* **2001**, 91, 1118-1130. (i) Zhang, C.; Wang, D.; Zhang, L.; Guo, J. F.; Rem, A. M. *RSC Adv.* **2016**, 6, 70960-70961.
10. Kim, H. M.; Cho, B. R. *Chem. Rev.* **2015**, 115, 5014-5055.
11. (a) Tung, C. H.; Zeug, Q.; Shah, K.; Kim, D. E.; Schel-ingerhout, D.; Weissleder, R. *Cancer Res.* **2004**, 64, 1579-1583. (b) Urano, Y.; Kamiya, M.; Kanda, K.; Ueno, T.; Hirose, K.; Nagano, T. *J. Am. Chem. Soc.* **2005**, 127, 4888-4894. (c) Lee, H. W.; Heo, C. H.; Sen, D.; Byun, H. O.; Kwak, I. H.; Yoon, G.; Kim, H. M. *Anal. Chem.* **2014**, 86, 10001-10005. (d) Egawa, T.; Koide, Y.; Hanaoka, K.; Komatsu, T.; Terai, T.; Nagano, T. *Chem. Commun.* **2011**, 47, 4162-4164. (e) Kamiya, M.; Asanuma, D.; Kuranaga, E.; Takeishi, A.; Sakabe, M.; Miura, M.; Nagano, T.; Urano, Y. *J. Am. Chem. Soc.* **2011**, 133, 12960-12963. (f) Sakabe, M.; Asanuma, D.; Kamiya, M.; Iwatate, R. J.; Hanaoka, K.; Terai, T.;

- Nagano, T.; Urano, Y. *J. Am. Chem. Soc.* **2013**, 135, 409-414. (g) Peng, L.; Gao, M.; Cai, X.; Zhang, R.; Li, K.; Feng, G.; Tong, A.; Liu, B. *J. Mater. Chem. B* **2015**, 3, 9168-9172. (h) Han, J.; Han, M. S.; Tung, C. H. *Mol. BioSyst.* **2013**, 9, 3001-3008. (i) Zhang, X. X.; Wu, H.; Li, P.; Qu, Z. J.; Tan, M. Q.; Han K. L. *Chem. Commun.* **2016**, 52, 8283-8286.
12. (a) Asanuma, D.; Sakabe, M.; Kamiya, M.; Yamamoto, K.; Hiratake, J.; Ogawa, M.; Kosaka, N.; Choyke, P. L.; Nagano, T.; Kobayashi, H.; Urano, Y. *Nat. Commun.* **2015**, 6, 6463-6470. (b) Gu, K.; Xu, Y.; Li, H.; Guo, Z.; Zhu, S.; Shi, P.; James, T. D.; Tian, H.; Zhu, W. H. *J. Am. Chem. Soc.* **2016**, 138, 5334-5340.
13. (a) Kamiya, M.; Kobayashi, H.; Hama, Y.; Koyama, Y.; Bernardo, M.; Nagano, T.; Choyke, P. L. Urano, Y. *J. Am. Chem. Soc.* **2007**, 129, 3918-3929. (b) Gu, K.; Xu, Y.; Li, H.; Guo, Z.; Zhu, S.; Zhu, S.; Shi, P.; James T. D.; Tian, H.; Zhu, W. H. *J. Am. Chem. Soc.* **2016**, 138, 5334-5340.
14. Oushiki, D.; Kojima, H.; Takahashi, Y.; Komatsu, T.; Te-rai, T.; Hanaoka, K.; Nishikawa, M.; Takakura, Y.; Nagano, T. *Anal. Chem.* **2012**, 84, 4404-4410.
15. Whittaker, S. R.; Mallinger, A.; Workman, P.; Clarke, P. A. *Pharmacol. Ther.* **2017**, 173, 83-105.
16. Horwitz, J. P., Chua, J., Curby, R. J., Thomsom, A. J., Da Rooge, M. A., Fisher, B. E., Mauricio, J., Klundt, I. *J. Med. Chem.* **1964**, 7, 574-575.
17. Takahashi, A., Ohtani, N., Hara, E. *Cell Div.* **2007**, 2, 10-15.

3.7 Supporting Information

3.7.1 Materials and methods

All solvents: dioxane, methanol (MeOH), acetonitrile (ACN), diethylether (Et₂O), ethyl acetate (AcOEt), dimethylsulphoxide (DMSO) and phosphate-buffered saline (PBS) were purchased from Scharlab S.L. in anhydrous or analytical grade and used without further purification. The chemical reagents: 4-bromo-1,8-naphthalic anhydride (**A**), L-histidine methyl ester (**H**), triethylamine (TEA), acetobromo- β -D-galactose (**Ga**) and potassium carbonate (K₂CO₃) were purchased from Sigma-Aldrich. Palbociclib was purchased from Selleckchem. Dulbecco's Modified Eagle Medium (DMEM) and fetal bovine serum (FBS) were purchased from Gibco. Flat-bottom-clear 96 well plates were purchased from Greiner Bio-One. CellTiter-GLO Luminescent Cell Viability Assay was purchased from Promega. ¹H and ¹³C NMR spectra were recorded on a Bruker FT-NMR Avance 400 (Ettlingen, Germany) spectrometer at 300K, using TMS as an internal standard. High resolution mass spectrometry (HRMS) data were obtained with a TRIPLETOF T5600 (ABSciex, USA) spectrometer. Absorption spectra were collected in a JASCO V-650 spectrophotometer, and fluorescence spectra measurements were performed by a JASCO FP-8500 fluorescence spectrophotometer. Luminescence was measured in a VICTOR Multilabel Plate Reader (Pelkin Elmer). Confocal fluorescence images were taken on a Leica TCS SP5 laser scanning confocal microscope and analysed by using the LAS AF software and the HCS-A. SK-Mel-103 (human melanoma) cancer cell line was acquired from the American Type Culture Collection (ATCC). Athymic nude mice (Hsd:Athymic Nude-Foxn1nu) were purchased from Envigo.

3.7.2 Synthesis of AH

A mixture of 4-bromo-1,8-naphthalic anhydride (1.5 g, 5.41 mmol) and L-histidine methyl ester (3.5 g, 16.24 mmol) was dissolved in anhydrous dioxane (150 ml) in a two-neck round bottom flask provided of condenser. Then, the system was purged with argon and triethylamine (8 ml) was added. The mixture was refluxed under argon for 10 h and stirred at room temperature for 15 h. Dioxane was removed under vacuum. The product was precipitated with cool water and filtered in vacuum. Since L-histidine was insoluble, the desired solid was dissolved in cool methanol, then filtered off to eliminate the unreacted L-histidine, then the solvent was eliminated in vacuum. **AH** was obtained as a yellow solid in 85% yield (1.98 g, 4.6 mmol). $^1\text{H-NMR}$ (400 MHz, CDCl_3): δ (ppm) = 8.59 – 8.47 (m, 2H), 8.27 (d, $J = 7.9$ Hz, 1H), 7.95 (d, $J = 7.9$ Hz, 1H), 7.76 (dd, $J = 8.5, 7.3$ Hz, 1H), 7.55 (s, 1H), 6.73 (s, 1H), 5.88 (dd, $J = 8.1, 6.1$ Hz, 1H), 3.67 (s, 3H), 3.64 – 3.56 (m, 1H), 3.39 – 3.30 (m, 1H). $^{13}\text{C-NMR}$ (400 MHz, CDCl_3) δ (ppm) = 170.43, 163.24, 163.21, 134.98, 133.82, 132.62, 131.78, 131.28, 130.91, 130.81, 129.23, 128.25, 122.66, 121.77, 53.31, 52.68, 26.39. HRMS-EI m/z : calcd for $\text{C}_{19}\text{H}_{14}\text{BrN}_3\text{O}_4 + \text{H}^+$: 428.0168; measured: 428.0239. See Figures S1, S2 and S3.

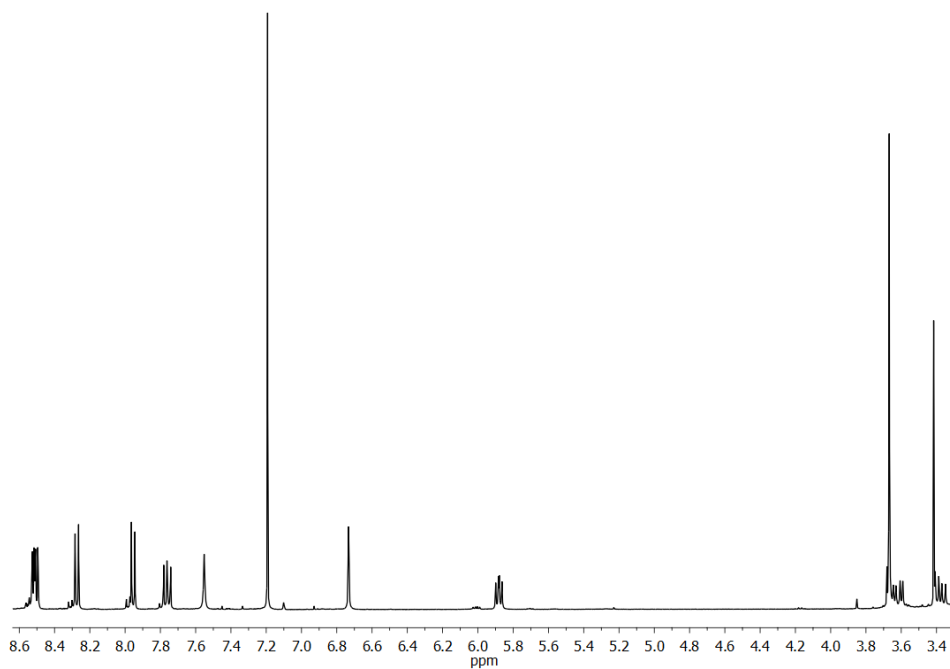


Figure S1. ¹H-NMR of AH.

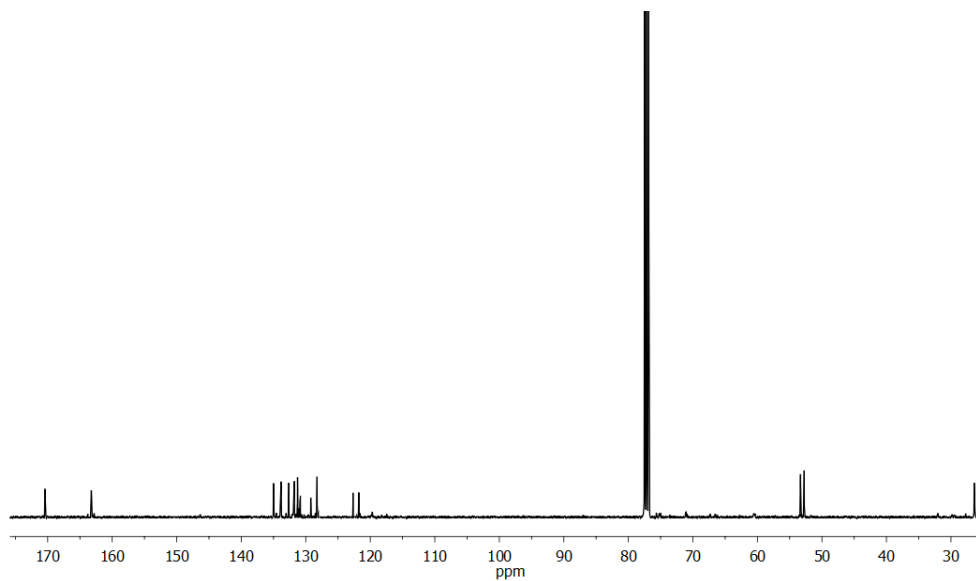


Figure S2. ¹³C-NMR of AH.

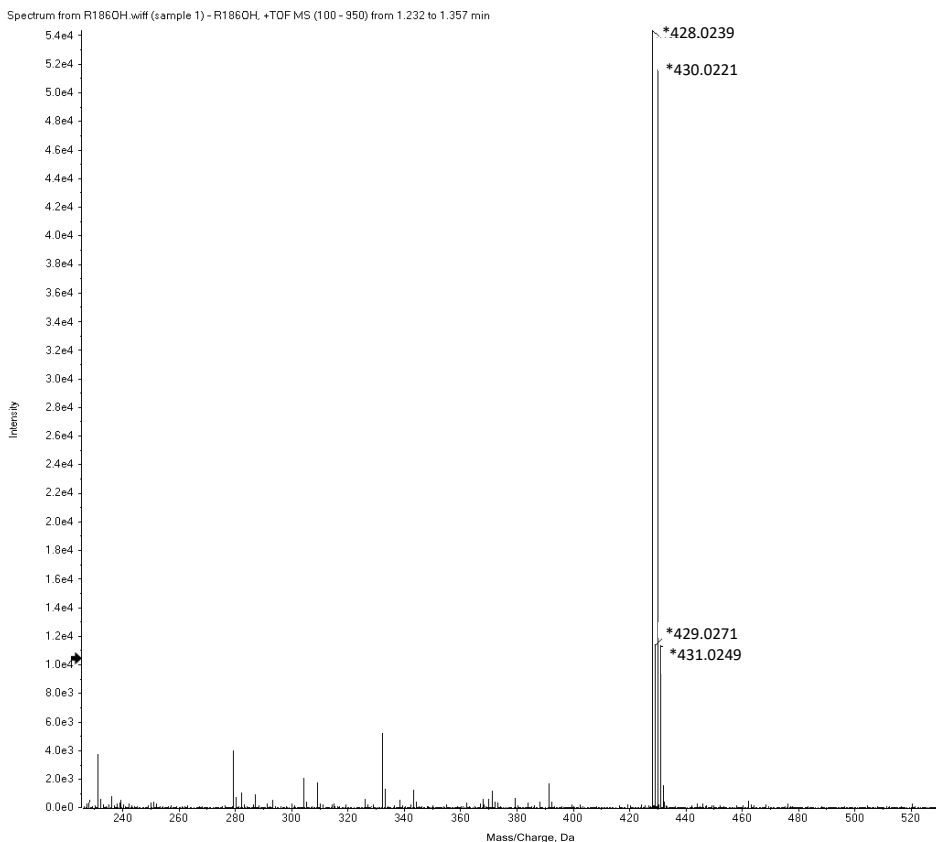


Figure S3. HRMS of AH.

3.7.3 Synthesis of AHGa

AH (200 mg, 0.46mmol), acetobromo- α -D-galactose (287 mg, 0.70 mmol) and K_2CO_3 (86.15 mg, 0.88 mmol) were mixed in a two-necked round-bottomed flask and purged with argon. Then 15 ml of anhydrous acetonitrile were added and purged again with argon. The mixture was stirred at 70°C for 4 h under argon atmosphere. Then the solvent was eliminated under vacuum and the reaction crude was precipitated with water and filtered off. The residue was purified by silica gel column chromatography using diethylether-ethyl acetate as eluent (100:5 v/v) to obtain the final product **AHGa** as a light yellow solid (234.2 mg, 0.31 mmol). Yield 67%. 1H -NMR (400 MHz, $CDCl_3$) δ (ppm) = 8.53 (dd, $J = 7.2, 0.95, 1H$), 8.50 (dd, $J = 8.5, 1 Hz, 1H$), 8.30 (d, $J = 7.0$

Hz, 1H), 7.98 (d, $J = 9.3$ Hz, 1H), 7.77 (dd, $J = 7.35, 8.39$, 1H), 7.53 (s, 1H), 6.90 (s, 1H), 6.01 (dd, $J = 9.5, 5.1$ Hz, 1H), 5.38 (d, $J = 3.21$ Hz, 1H), 5.25 (t, $J = 9.85$ Hz, 1H), 5.05 – 4.95 (m, 2H), 4.09 – 3.95 (m, 3H), 3.67 (s, 3H), 3.61 (dd, $J = 15.5, 5.0$ Hz, 1H), 3.42 (dd, $J = 15.2, 9.49$ Hz, 1H), 2.21 – 1.80 (m, 12H). ^{13}C -NMR (400 MHz, CDCl_3) δ (ppm) = 171.29, 170.55, 170.12, 170.07, 169.85, 163.21, 163.18, 139.22, 133.67, 132.47, 131.64, 131.29, 130.72, 128.26, 122.87, 121.99, 113.50, 110.05, 98.13, 72.87, 71.25, 69.58, 65.98, 65.50, 61.55, 60.53, 53.69, 52.67, 27.81, 21.18, 20.85, 20.82, 20.67. HRMS m/z : calcd for $\text{C}_{33}\text{H}_{32}\text{BrN}_3\text{O}_{13}+\text{H}^+$: 758.1119; measured: 758.1191. See Figures S4, S5 and S6.

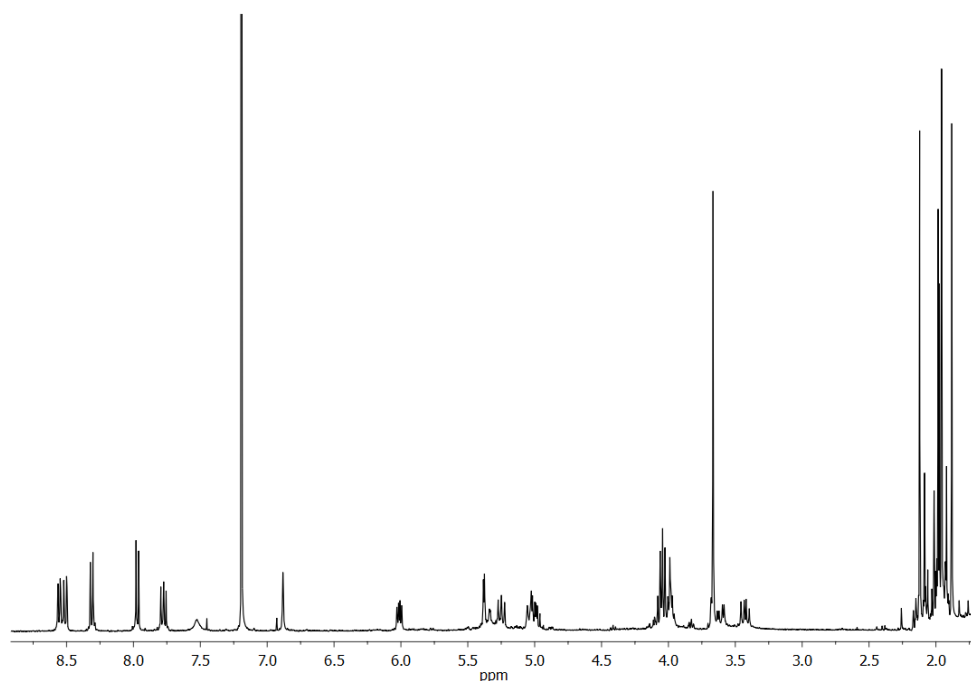


Figure S4. ^1H -NMR of AHGa.

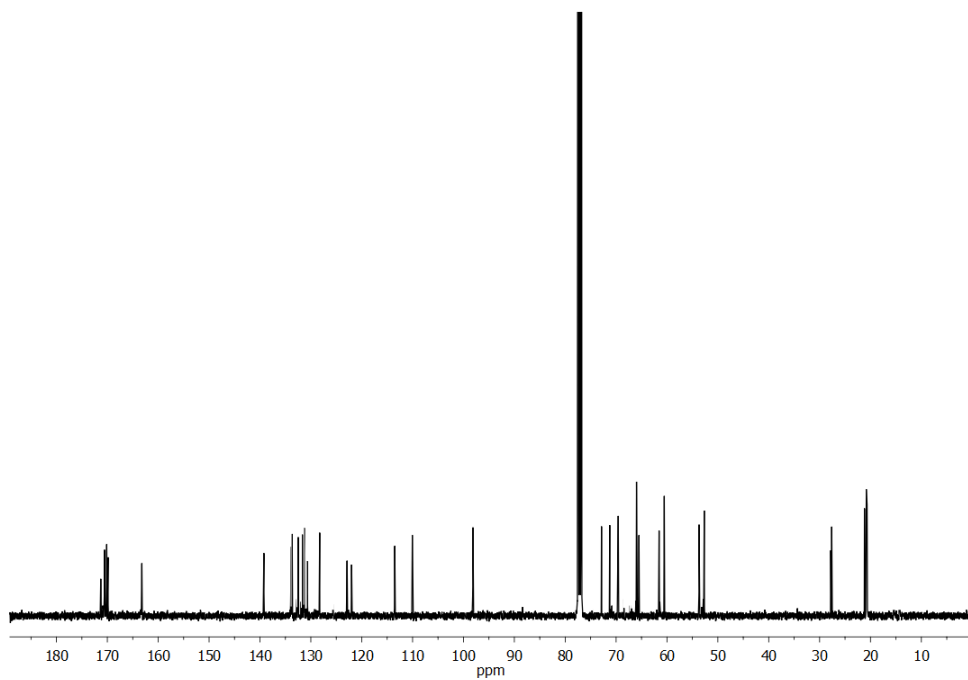
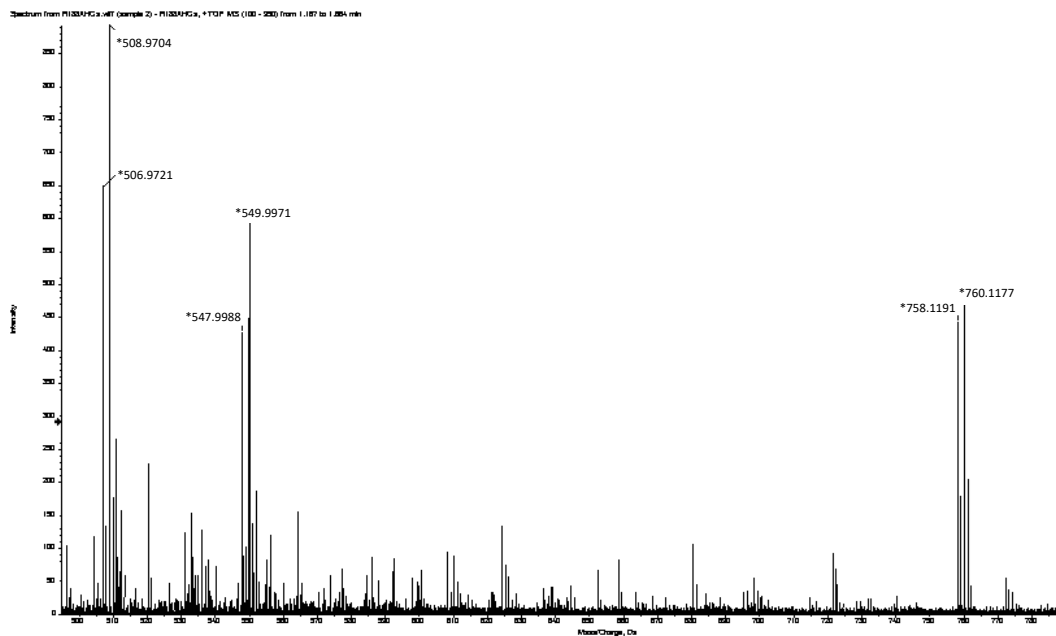
Figure S5. ^{13}C -NMR of AHGa.

Figure S6. HRMS of AHGa.

Table S1. Fluorogenic molecular probes for *in vivo* and *in vivo* β gal detection.

Reference	<i>In vivo</i>		<i>In vivo</i>	
	Cell line	β gal expression	<i>In vivo</i> model	β gal expression
1. Tung et al., <i>Cancer Res.</i> , 2004 , 64, 1579–1583	9L	<i>LacZ</i> gene transfection	9L xenografts	<i>LacZ</i> gene transfection
2. Urano et al., <i>J. Am. Chem. Soc.</i> , 2005 , 127, 4888-4894	GP293	<i>LacZ</i> gene transfection	-	-
3. Ho et al., <i>ChemBioChem.</i> , 2007 , 8, 560 – 566	-	-	-	-
4. Kamiya et al., <i>J. Am. Chem. Soc.</i> 2007 , 129, 3918-3929	HEK293	<i>LacZ</i> gene transfection	SHIN3 xenografts	Avidin- β -galactosidase
5. Egawa et al., <i>Chem. Commun.</i> , 2011 , 47, 4162–4164	HEK293	<i>LacZ</i> gene transfection	-	-
6. Kamiya et al., <i>J. Am. Chem. Soc.</i> , 2011 , 133, 12960–12963	HEK	<i>LacZ</i> gene transfection	-	-
7. Oushiki et al., <i>Anal. Chem.</i> , 2012 , 84, 4404–4410	HEK293	<i>LacZ</i> gene transfection	liver	pCMV- β -gal
8. Sakabe et al., <i>J. Am. Chem. Soc.</i> , 2013 , 135, 409–414	HEK293	<i>LacZ</i> gene transfection	-	-
9. Han et al., <i>Mol. BioSyst.</i> , 2013 , 9, 3001-3008	C6	<i>LacZ</i> gene transfection	-	-
10. Lee et al., <i>Anal. Chem.</i> 2014 , 86, 10001–10005	HDFs	splitting or H ₂ O ₂	-	-
11. Peng et al., <i>J. Mater. Chem. B</i> , 2015 , 3, 9168-9172	C6	<i>LacZ</i> gene transfection	-	-
12. Asanuma et al., <i>Nat. Commun.</i> , 2015 , 6, 6463-6470	SHIN3, SKOV3, OVK18, OVCAR3, OVCAR4, OVCAR5, OVCAR8	<i>per se</i>	Peritoneal metastases	<i>per se</i>
13. Gu et al., <i>J. Am. Chem. Soc.</i> , 2016 , 138, 5334-5340	293T	<i>LacZ</i> gene transfection	LoVo xenografts	Avidin- β -galactosidase
	OVCAR3	<i>per se</i>		
14. Zhang et al., <i>Chem. Commun.</i> , 2016 , 52, 8283-8286	C6	<i>LacZ</i> gene transfection	U-87 MG xenografts	pCMV- β -gal
15. Wang et al., <i>Chem. Commun.</i> , 2017 , 53, 4505-4508	OVCAR3	<i>per se</i>	-	-
16. Hong et al., <i>Biomaterials</i> , 2017 , 122, 83-90	HepG2	<i>LacZ</i> gene transfection	HepG2 xenografts	pCMV- β -gal
This work	SK-MEL103	Chemotherapy induced senescence	SK-MEL103 xenografts	Chemotherapy induced senescence

3.7.4 Optical studies of AH and AHGa

3.7.4.1 UV, excitation and fluorescence spectra of AH and AHGa

PBS-DMSO (99:1 v/v) solutions of **AH** (pH=7.5) were prepared at 10^{-5} M and UV, excitation and fluorescence spectra were measured. PBS (pH 7.5)-DMSO (0.01%) solutions of **AH** and **AHGa** showed the typical absorption of the naphthalimide chromophore centred, for both compounds, at ca. 350 nm. Fluorescence spectra of solutions of **AH** and **AHGa** at 350 nm showed, for both compounds, the typical broad unstructured naphthalimide emission centred at ca. 430 nm. However, excitation spectra of **AH** and **AHGa** are different. At this respect, excitation spectra of **AH** showed the presence of a remarkable band centred at 405 nm which was absent in **AHGa**. Using 405 nm as excitation wavelength, solutions of **AHGa** are non-fluorescent whereas **AH** presented an intense fluorescence at 540 nm (Figure S7).

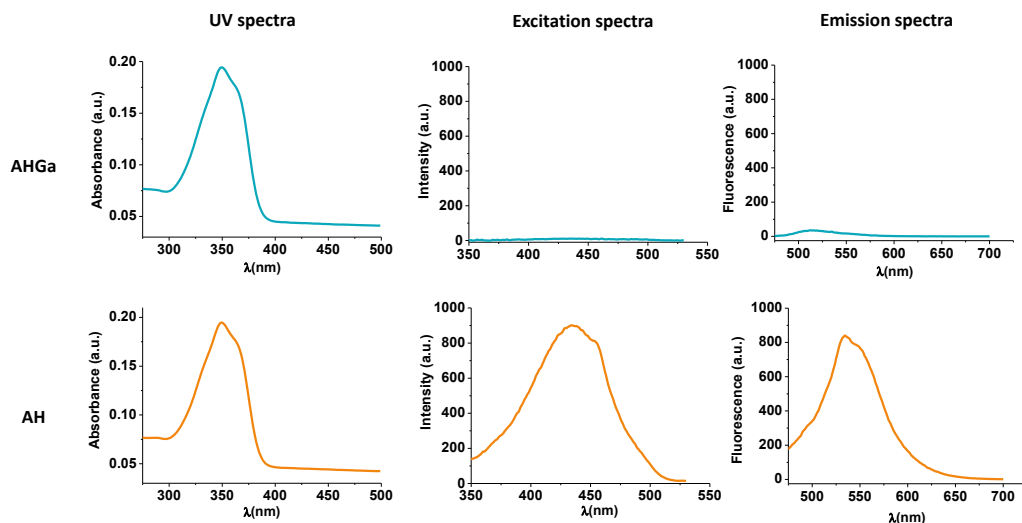


Figure S7. UV, excitation and emission spectra of **AH** and probe **AHGa** (10^{-5} M) in PBS-DMSO (99:1 v/v) solutions at pH 7.5.

This could be explained by the assumption of the formation of an excimer. When the NH group of the indole heterocycle in the amino acid linker is free can establish a strong hydrogen bond with one of the oxygen atoms of the naphthalimide fluorophore. This hydrogen bond confers rigidity and planarity to **AH** and, as a consequence, this compound is highly emissive.¹⁷ The presence of an acetylated galactose fragment in the final probe disables the formation of the hydrogen bond and, as a consequence, **AHGa** is nearly non-emissive (upon excitation at 405 nm).

3.7.4.2 AH fluorescence changes with pH

PBS-DMSO (99:1 v/v) solutions of **AH** at different pH were prepared at 10^{-5} M and fluorescence spectra from each solution were measured ($\lambda_{\text{ex}} = 405$ nm). Note that the emission intensity of **AH** did not change in the 4-8 pH range (Figure S8).

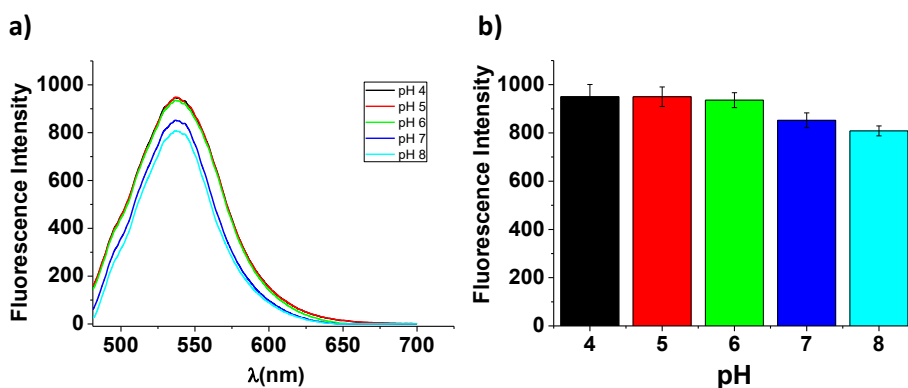


Figure S8. a) Fluorescence spectra ($\lambda_{\text{ex}} = 405$ nm) of **AH** (10^{-5} M) in PBS-DMSO (99:1 v/v) at pH 4, 5, 6, 7 and 8. b) Emission intensity at 540 nm ($\lambda_{\text{ex}} = 405$ nm) of **AH** (10^{-5} M) PBS-DMSO (99:1 v/v) solutions at pH 4, 5, 6, 7 and 8.

3.8.7.3 AH and AHGa quantum yield measurements

Quantum yield values were measured respect to fluorescein as standard ($\Phi = 0.95$) using the equation:

$$\frac{\Phi_x}{\Phi_s} = \frac{S_x}{S_s} \times \frac{1 - 10^{-A_s}}{1 - 10^{-A_x}} \times \frac{n_x^2}{n_s^2}$$

where x and s indicate the unknown and standard solution, respectively, Φ is the quantum yield, S is the area under the emission curve, A is the absorbance at the excitation wavelength and n is the index of refraction.

3.7.5 *In vitro* experiments

3.7.5.1 Cell lines

SK-Mel-103 (human melanoma) cancer cells were obtained from ATCC. Cells were maintained in DMEM, supplemented with 10% FBS, and incubated in 20% O₂ and 5% CO₂ at 37°C. Cells were routinely tested for *mycoplasma* contamination using the *mycoplasma* tissue culture NI (MTC-NI) Rapid Detection System (Gen-Probe). For senescence induction, cells were supplemented for 2 weeks with media containing 5 μ M palbociclib.

3.7.5.2 Cell viability assays

SK-Mel-103 (human melanoma) cancer cells were used for cell viability assays. Cells were maintained in DMEM supplemented with 10% FBS, and incubated in 20% O₂ and 5% CO₂ at 37°C. For senescence induction, cells were supplemented with DMEM media containing 5 μ M palbociclib for 2 weeks. Control and senescent cells were plated in flat-bottom-clear 96 well plates at a density of 6,000 and 4,000 cells per well, respectively. The following day, media was changed to DMEM supplemented with 0.1% FBS, and cells were treated with serial dilutions of **AHGa** or **AH**. Viability was assessed 24 h or 48 h later with CellTiter-GLO Luminescent Cell Viability Assay. Raw data were

obtained by measuring luminescence in a VICTOR Multilabel Plate Reader (Pelkin Elmer) (Figure S9).

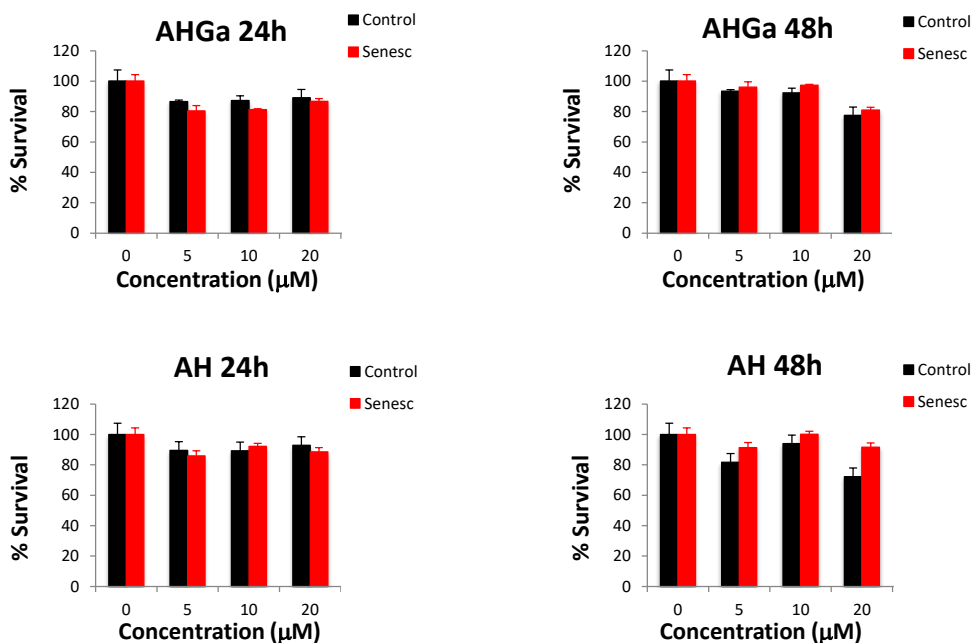


Figure S9. Relative *in vivo* viability of control and senescent SK-MEL-103 cells after incubation with AHGa or AH for 24 h or 48 h at different concentrations. Note: both AHGa and AH have minimal toxicity and superior biocompatibility toward cultured cells.

3.7.6 *In vivo* experiments

3.7.6.1 Mice

Mice were maintained at the Spanish National Cancer Research Centre (CNIO) under specific pathogen-free conditions in accordance with the recommendations of the Federation of European Laboratory Animal Science Associations (FELASA). All animal procedures were approved by the CNIO-ISCIII Ethics Committee for Research and Animal Welfare (CElyBA) and conducted in accordance with the recommendations of the Federation of European Laboratory Animal Science Associations (FELASA).

3.7.6.2 Xenograft assays

Tumor xenografts were established by using SK-MEL-103 cells. Cells were routinely cultured in DMEM supplemented with 10% FBS and penicillin-streptomycin. For tumor xenografts, cells were trypsinised, counted with a haemocytometer and injected subcutaneously in both dorsolateral flanks of 8- to 10-week-old athymic nude female mice at a concentration of 10^6 cells in a volume of 100 μ l per flank. Tumor volume was measured every two days with a calliper and calculated as $V = (a \times b^2) / 2$ where a is the longer and b is the shorter of two perpendicular diameters. For the induction of senescence, palbociclib was administered by daily oral gavage for 10 to 14 days at 100 mg/kg dissolved in 50 mM sodium lactate. **AHGa** was then administered by tail intravenous injection at a concentration of 10 mg/ml in a volume of 200 μ l. Mice were sacrificed 3 h later by CO₂ exposure in an Euthanasia Chamber, and tumor xenografts were immediately removed. Tumor xenografts were analyzed immediately after harvesting. **AH** was detected using an excitation wavelength of 405 nm and an emission wavelength of 540 nm. Confocal fluorescence images were taken on a Leica TCS SP5 laser scanning confocal microscope and analyzed by using the LAS AF software and the HCS-A. Experiments were repeated 3-times and the obtained results were nearly coincident.

3.7.6.3 *Ex vivo* imaging of different sections of fresh organs after AHGa treatment

For *ex vivo* imaging, mice were sacrificed by CO₂ exposure in an Euthanasia Chamber, and organs were analyzed immediately after harvesting. Confocal fluorescence images were taken on a Leica TCS SP5 laser scanning confocal

microscope by using an excitation wavelength of 405 nm and an emission wavelength of 540 nm and analyzed by using the LAS AF software and the HCS-A (Figure S10).

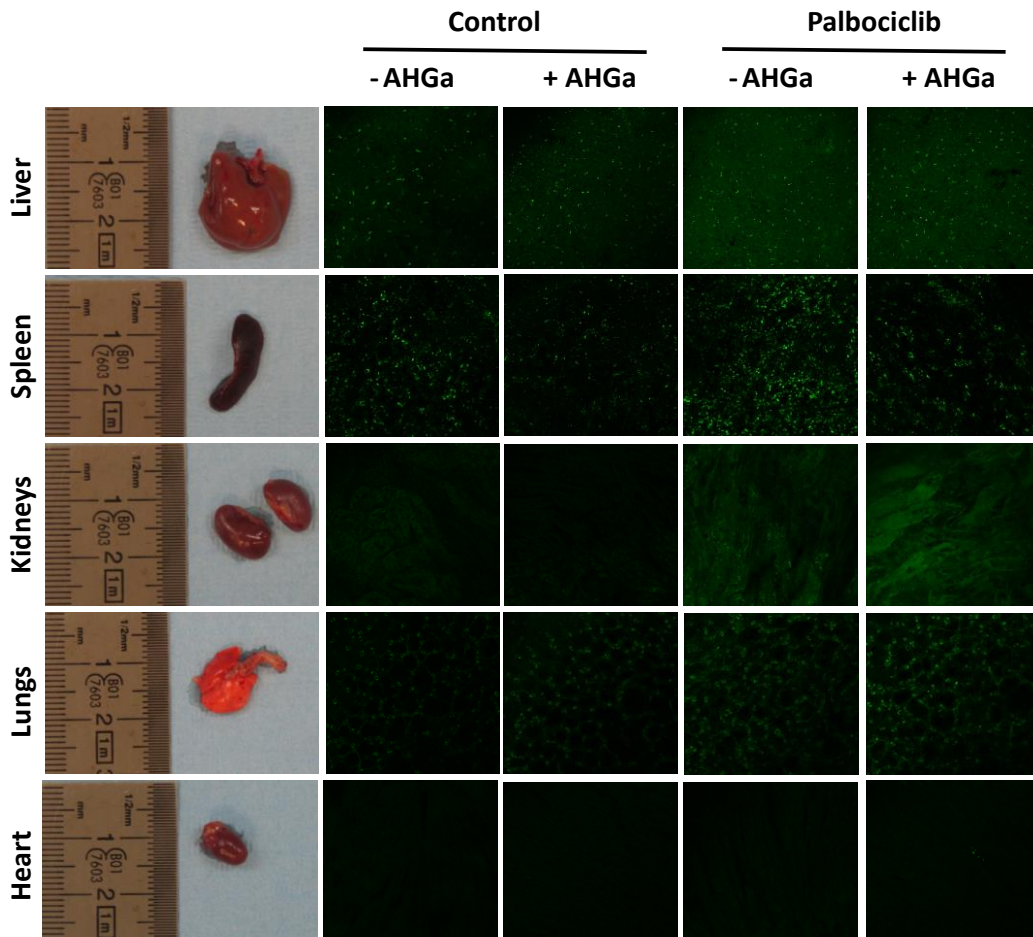


Figure S10. *Ex vivo* imaging of sections of fresh organs of athymic nude mice at 3 h post tail intravenous injection of **AHGa** (10 mg/ml). Organs were analyzed by confocal microscopy immediately after removal (**AH** λ_{ex} = 405 nm and **AH** λ_{em} = 540 nm).

3.7.7 References

1. Tung, C. H.; Zeug, Q.; Shah, K.; Kim, D. E.; Schellingerhout, D.; Weissleder, R. *Cancer Res.* **2004**, 64, 1579-1583.
2. Urano, Y.; Kamiya, M.; Kanda, K.; Ueno, T.; Hirose, K.; Nagano, T. *J. Am. Chem. Soc.* **2005**, 127, 4888-4894.
3. Ho, N. H.; Weissleder, R.; Tung, C. H. *ChemBioChem* **2007**, 8, 560-566.

4. Kamiya, M.; Kobayashi, H.; Hama, Y.; Koyama, Y.; Bernardo, M.; Nagano, T.; Choyke, P. L. Urano, Y. *J. Am. Chem. Soc.* **2007**, *129*, 3918-3929.
5. Egawa, T.; Koide, Y.; Hanaoka, K.; Komatsu, T.; Terai, T.; Nagano, T. *Chem. Commun.* **2011**, *47*, 4162-4164.
6. Kamiya, M.; Asanuma, D.; Kuranaga, E.; Takeishi, A.; Sakabe, M.; Miura, M.; Nagano, T.; Urano, Y. *J. Am. Chem. Soc.* **2011**, *133*, 12960-12963.
7. Oshiki, D.; Kojima, H.; Takahashi, Y.; Komatsu, T.; Terai, T.; Hanaoka, K.; Nishikawa, M.; Takakura, Y.; Nagano, T. *Anal. Chem.* **2012**, *84*, 4404-4410.
8. Sakabe, M.; Asanuma, D.; Kamiya, M.; Iwatate, R. J.; Hanaoka, K.; Terai, T.; Nagano, T.; Urano, Y. *J. Am. Chem. Soc.* **2013**, *135*, 409-414.
9. Han, J.; Han, M. S.; Tung, C. H. *Mol. BioSyst.* **2013**, *9*, 3001-3008.
10. Lee, H. W.; Heo, C. H.; Sen, D.; Byun, H. O.; Kwak, I. H.; Yoon, G.; Kim, H. M. *Anal. Chem.* **2014**, *86*, 10001-10005.
11. Peng, L.; Gao, M.; Cai, X.; Zhang, R.; Li, K.; Feng, G.; Tong, A.; Liu, B. *J. Mater. Chem. B* **2015**, *3*, 9168-9172.
12. Asanuma, D.; Sakabe, M.; Kamiya, M.; Yamamoto, K.; Hiratake, J.; Ogawa, M.; Kosaka, N.; Choyke, P. L.; Nagano, T.; Kobayashi, H.; Urano, Y. *Nat. Commun.* **2015**, *6*, 6463-6470.
13. Gu, K.; Xu, Y.; Li, H.; Guo, Z.; Zhu, S.; Shi, P.; James, T. D.; Tian, H.; Zhu, W. H. *J. Am. Chem. Soc.* **2016**, *138*, 5334-5340.
14. Zhang, X. X.; Wu, H.; Li, P.; Qu, Z. J.; Tan, M. Q.; Han K. L. *Chem. Commun.* **2016**, *52*, 8283-8286.
15. Jiang, G.; Zeng, G.; Zhu, W.; Li, Y.; Dong, X.; Zhang, G.; Fan, X.; Wang, J.; Wu Y.; Tang, B. Z. *Chem. Commun.* **2017**, *53*, 4505-4508.
16. Kim, E. J.; Kumar, R.; Sharma, A.; Yoon, B.; Kim, H. M.; Lee, H.; Hong, K. S.; Kim, J. S. *Biomaterials* **2017**, *122*, 83-90.
17. Pardo, A.; Poyato, J. M. L.; Martin, E. J. *Photochem.* **1987**, *36*, 323-329.

**Chapter 4 | A two-photon probe based
on naphthalimide-styrene
fluorophore for the *in vivo* tracking
of cellular senescence**

A two-photon probe based on naphthalimide-styrene fluorophore for the *in vivo* tracking of cellular senescence

Beatriz Lozano-Torres,^{a,b,c,d} Juan F Blandez,^{a,b} Irene Galiana,^{a,b,c,d} José A Lopez-Dominguez,^e Miguel Rovira,^e Marta Paez-Ribes,^f Estela González-Gualda,^f Daniel Muñoz-Espín,^f Manuel Serrano,^{e,g} Félix Sancenón^{a,b,c,d,*} and Ramón Martínez-Máñez^{a,b,c,d,*}

^a Instituto Interuniversitario de Investigación de Reconocimiento Molecular y Desarrollo Tecnológico (IDM), Universitat Politècnica de València, Universitat de València, Valencia, 46022, Spain.

^b Unidad Mixta UPV-CIPF de Investigación en Mecanismos de Enfermedades y Nanomedicina, Universitat Politècnica de València, Centro de Investigación Príncipe Felipe, Valencia, 46012, Spain.

^c CIBER de Bioingeniería, Biomateriales y Nanomedicina (CIBER-BBN), Madrid, 28019, Spain

^d Unidad Mixta de Investigación en Nanomedicina y Sensores. Universitat Politècnica de València, IIS La Fe, Valencia, 46026, Spain.

^e Institute for Research in Biomedicine (IRB Barcelona). Barcelona Institute of Science and Technology (BIST), 08028, Barcelona, Spain.

^f CRUK Cancer Centre Early Detection Programme, Department of Oncology, University of Cambridge, Hutchison/MRC Research Centre, Cambridge, CB2 0XZ, UK

^g Catalan Institution for Research and Advanced Studies (ICREA), Barcelona, Spain

*Correspondence: rmaez@qim.upv.es

Published online: January 27, 2021

(Reprinted with permission from *Anal. Chem.*, **2021**, *93*, *5*, 3052.
Copyright © 2021, American Chemical Society. All rights reserved.)

4.1 Abstract

Cellular senescence is a state of stable cell cycle arrest that can negatively affect the regenerative capacities of tissues, and can contribute to inflammation and to the progression of various ageing-related diseases. Advances in the *in vivo* detection of cellular senescence are still crucial to monitor the action of senolytic drugs and also to assess the early onset or accumulation of senescent cells. Here, we describe a naphthalimide-styrene-based probe (**HeckGal**) for the detection of cellular senescence both *in vivo* and *in vivo*. **HeckGal** is hydrolyzed by the increased lysosomal β -galactosidase activity of senescent cells, resulting in fluorescence emission. The probe was validated *in vivo* using normal human fibroblasts and various cancer cell lines undergoing senescence induced by different stress stimuli. Remarkably, **HeckGal** was also validated *in vivo* in an orthotopic breast cancer mouse model treated with senescence-inducing chemotherapy, and in a renal fibrosis mouse model. In all cases, **HeckGal** allowed the unambiguous detection of senescence *in vivo* as well as in tissues and tumors *in vivo*. This work is expected to provide a potential technology for senescence detection in aged or damaged tissues.

4.2 Introduction

Cellular senescence is a biological process occurring in response to stress or damage and whose main role is to trigger tissue repair and to prevent the proliferation of stressed or damaged cells.¹ Senescence triggered by excessive proliferation is known as “replicative senescence”,² but senescence can also be triggered through diverse procedures such as activation of oncogenes, inhibition of tumor suppressor genes, accumulation of DNA damage, presence of reactive

oxygen species (ROS), or nucleolar stresses among others. This type of senescence is known as stress-induced premature senescence (SIPS).³ Senescence has a relevant physiological role during development and promotes tissue regeneration in response to circumstantial damage, but the inefficient elimination of senescent cells during aging or upon persistent damage can produce inflammation, fibrosis, tissue aging, tumorigenesis, and metastasis.^{1,4-6}

Evidence is accumulating that the selective elimination of senescent cells ameliorates a wide variety of aging-associated diseases, reverts long-term degenerative processes, and extends both lifespan and healthspan in mice.^{7,8} Inspired by these findings, there is a growing interest in developing drugs capable to induce apoptosis preferentially in senescent cells. In fact, senotherapies (treatments with senolytic or senomorphic drugs) are a new strategy to prevent cell-autonomous and non-cell-autonomous effects of senescent cells.⁹⁻¹¹ Senolytic drugs kill senescent cells preferentially over non-senescent cells; whereas senomorphic drugs reduce the secretion of pro-inflammatory and pro-fibrotic factors by senescent cells but without killing them.^{12,13} Such drugs would contribute to the therapeutic treatment of senescence-associated diseases and may stimulate the long-term idea that rejuvenation might be possible.⁶ A related important issue in the field of senotherapy is the development of new highly selective and sensitive tools to detect cellular senescence.¹⁴ These probes are expected to play an essential role in the detection of senescent cells in aged or damaged tissues, help in the discrimination between senolytic (selectively killing senescent cells) and senomorphic (selectively suppressing SASP) drugs or monitor the action of senotherapeutics in multiple age-related disorders.^{12,13}

Some of the most important markers of senescent cells are senescence-associated heterochromatic foci (SAHF),^{15,16} activation of tumor suppressors and cell cycle inhibitors (e.g. p53, p16INK4a and p21),¹⁷⁻²⁰ the overexpression of anti-apoptotic proteins (e.g. BCLs),²¹ the absence of proliferative markers (Ki67),²² the

loss of important chromatin structural proteins (Lamin B1, HMGB1, and HGMGB2),²³ a senescence-associated secretory phenotype (SASP)²⁴ and the presence of high levels of lysosomal β -galactosidase (β -Gal) activity, known as senescence-associated β -galactosidase, (SA- β Gal).²⁵ Monitoring β -Gal activity using chromo-fluorogenic molecular-based probes represents a simple and accurate manner to track senescence in most of the cases and several β -Gal probes are commercially available. However, most of these probes cannot be applied to *in vivo* models.^{12,13} For example, fluorescein-di-(β -D-galactopyranoside) (FDG) requires the use of chloroquine in order to increase lysosomal pH,^{26,27} 4-methylumbelliferyl β -D-galactopyranoside (MUG) is not permeable to cells,²⁸ and 5-bromo-4-chloro-3-indolyl- β -D-galactopyranoside (X-Gal)²⁹ is toxic and therefore cells need to be previously fixed. These drawbacks have boosted the interest in developing molecular sensors for the monitoring of β -Gal activity that could work on live cells and tissues. More recently, ((E)-2-(2-(6-hydroxy-2,3-dihydro-1H-xanthen-4-yl)vinyl)-3,3-dimethyl-1-propyl-3H-indol-1-ium), known as Spider-Gal, has gained importance as SA- β Gal kit detection, especially for flow cytometry since the fluorophore is covalently anchored to the cell after hydrolysis. But this could be a problem when applying *in vivo* and cause long-term toxicity.³⁰ Most of the described probes are based on classical one-photon fluorophores linked to the anomeric carbon of β -galactose. In one-photon probes, the biological target is only detected by an intensity-responsive fluorescent signal, which can be interfered with the excitation and emission efficiency, probe concentration, and surrounding conditions.^{31,32} As an alternative, the design of molecular probes using two-photon fluorophores has attracted great attention in the last years due to their improved three-dimensional spatial localization, prolonged observation time, increased imaging depth, minimized fluorescence background and light scattering, and lower tissue injury.³³ Besides, one typical inaccuracy when developing SA- β -Gal probes is their validation in biological models not directly

related to senescence. In most cases, the method used in previous *in vitro* studies are based on *lacZ* gene transfection and *in vivo* using mouse models in which tumors are labelled with avidin- β -Gal^{34,35} or transfected with the pCMV-*lacZ* plasmid,³⁶ that results in high levels of cytosolic β -Gal expression,³⁷⁻⁴⁴ which is unrelated to the lysosomal human β -Gal, encoded by GLB1 gene, naturally overexpressed in senescent cells. As a consequence, there are still a very limited number of selective two-photon fluorescent probes for the detection of bona-fide cellular senescence *in vivo* models. Specifically, SG1 was the first two-photon ratiometric probe to detect senescent cells *in vitro*,⁴⁵ and AHGa was the first two-photon probe to detect cellular senescence *in vivo*.⁴⁶

Taking into account our interest in the development of fluorogenic sensors,⁴⁷⁻⁵¹ we report herein the synthesis and characterization of a new two-photon naphthalimide-styrene probe (**HeckGal** in Figure 1A) for *in vivo* detection of senescence. The **HeckGal** probe consists of a naphthalimide-styrene fluorophore (**Heck** in Figure 1A) covalently linked to an acetylated β -galactose through the anomeric carbon. **HeckGal** is poorly emissive, whereas a sudden revival of the emission is observed in the presence of lysosomal β -Gal activity. The probe is tested *in vitro* in human cancer cell lines, including SK-Mel-103 and A549 cells, a breast murine cancer line (4T1), and in a human BJ fibroblast cell line, undergoing senescence by different triggers. The probe is also tested *in vivo* in BALB/cByJ female mice bearing 4T1 breast cancer tumors treated with senescence-inducing chemotherapy, and in a model of renal fibrosis induced by treatment with folic acid in C57BL/6J male mice.

4.3 Experimental section

4.3.1 Materials.

All chemical reagents were purchased from Sigma-Aldrich while anhydrous solvents and phosphate-buffered saline (PBS, 0.01M) were purchased from Sharlab S.L., and used without further purification. Palbociclib was purchased from Selleckchem and Dulbecco's Modified Eagle Medium (DMEM) and fetal bovine serum (FBS) were purchased from Gibco. Flat-bottom-clear 96 well plates were purchased from Promega. High-resolution mass spectrometry (HRMS) and the data was recorded with a TRIPLETOF T5600 (ABSciex, USA) spectrometer. ^1H and ^{13}C NMR spectra were collected on a Bruker FT-NMR Avance 400 (Ettlingen, Germany) spectrometer at 300K, using TMS as an internal standard. HPLC measures were obtained by a Walters 1525 binary HPLC pump and spectra were recorded by a Walters 2998 photodiode array at 260 nm. Fluorescence spectra were recorded by a JASCO FP-8500 fluorescence spectrophotometer, Luminescence was collected in a VICTOR Multilabel Plate Reader (Perkin Elmer). Confocal fluorescence images were taken on a Leica TCS SP8 AOBS and two-photon images were acquired by using a multiphoton Olympus FV1000MPE confocal microscope. Images were analyzed using the Image J software. SK-Mel-103 (human melanoma) cancer cell line and 4T1 (breast cancer cells) were acquired from the American Type Culture Collection (ATCC). BALB/CBY female mice were purchased from Charles River laboratories, France.

4.3.2 Hydrolysis reaction.

The hydrolysis reaction of the **HeckGal** probe by β -Gal enzyme was analyzed by fluorescence spectroscopy and by HPLC-UV techniques. For this purpose, 2 μl of human β -Gal enzyme was added to PBS (pH 7)-DMSO (0.01%) solutions of **HeckGal** (10^{-5} M), and the emission spectrum at 552 nm was recorded with time (Figure S7a). After 15 min, **HeckGal** was completely hydrolyzed and the emission

band of the product closely correlated with the emission intensity of pure Heck fluorophore solution. Furthermore, in the same reaction condition HPLC-UV studies (Figure S7b) corroborated these results. Time-conversion plots of **HeckGal** and its reaction intermediated (**Heck** and β -Gal) were determined by analyzing reaction aliquots by reversed-phase liquid chromatography using a KromasilC18 column as the stationary phase, eluting under isocratic conditions 0.8 mL/min (87.4:12.5:0.1 vol% H₂O/CH₃CN/CH₃COOH) and using photodiode array detector. Retention time (Rt) for Heck was 18.17 min, while Rt for **HeckGal** was 8.55 min and 4.60 min for human β -Gal enzyme.

4.3.3 Cell lines.

SK-Mel-103 (human melanoma) cancer cells and 4T1 (mouse breast cancer cells) were obtained from ATCC. Cells were maintained in DMEM, supplemented with 10% FBS, and incubated in 20% O₂ and 5% CO₂ at 37°C. Cells were routinely tested for mycoplasma contamination using the mycoplasma tissue culture NI (MTC-NI) Rapid Detection System (Gen-Probe). For senescence induction, cells were supplemented for 2 weeks with media containing 5 μ M palbociclib.

4.3.4 In vitro viability assays.

SK-Mel-103 (human melanoma) cancer and 4T1 (mouse breast cancer) cells were used for cell viability assays. Cells were maintained in DMEM supplemented with 10% FBS and incubated in 20% O₂ and 5% CO₂ at 37°C. For senescence induction, cells were supplemented with DMEM media containing 5 μ M palbociclib for 2 weeks. Control and senescent cells were placed in flat-bottom-clear 96 well plates at a density of 6,000 and 4,000 cells per well, respectively. The following day cells were treated with serial dilutions of **HeckGal** or **Heck**. Viability was assessed 48 h later with CellTiter-GLO Luminescent Cell Viability Assay. Raw data were obtained by measuring luminescence in a VICTOR Multilabel Plate Reader (Pelkin Elmer).

4.3.5 Mouse models.

Balb/cByJ mice were maintained at the Spanish Research Centre Principe Felipe (CIPF) in accordance with the recommendations of the Federation of European Laboratory Animal Science Associations (FELASA). Breast 4T1 tumors were established by using 4T1 cells. Cells were routinely cultured in DMEM supplemented with 10% FBS and penicillin-streptomycin. In order to generate breast tumors, cells were trypsinised, counted with a LUNA™ Automated Cell Counter, and injected subcutaneously in the left breast of 28- to 34-week-old BALB/cByJ female mice at a concentration of 0.5×10^6 cells in a volume of 100 μ l. Tumor volume was measured every two days with a caliper and calculated as $V = (a \times b^2)/2$ where a is the longer and b is the shorter of two perpendicular diameters. Palbociclib or vehicle was administered by daily oral gavage for 7 days at 100 mg/kg dissolved in 50 mM sodium lactate, pH 5 in order to induce senescence. Then, **Heck-Gal** was intraperitoneally (i.p.) administered at a concentration of 6 mg/ml in DMEM (5% DMSO) in a volume of 200 μ l. Mice were sacrificed 2 hours later by CO₂ exposure in a Euthanasia Chamber, and tumors and organs (lung, liver, kidney, or spleen) were immediately removed. Tumors and organs were analyzed immediately after harvesting. **Heck** was detected using an excitation wavelength of 500 nm and an emission wavelength of 540 nm. Fluorescence images were taken on an IVIS spectrum imaging system and analyzed by using the Living Imaging software from Caliper Life Sciences. On the other hand, two months-old C57BL/6J male mice were maintained at the Institut de Recerca Biomèdica (IRB). All animal procedures were carried out in compliance with the regulations of the Animal Care and Use Ethical Committee of the Barcelona Science Park (CEEA-PCB) and the Catalan Government under the recommendations of the FELASA. In order to generate renal fibrosis, mice were i.p injected with a single dose of either 250 mg/kg of folic acid or vehicle. 34 days

after treatment, the animals were administered either with a single i.p dose of **Heck-Gal** (13.33 mg/ml 200 μ l) in DMSO 1%-Corn oil or with vehicle. Animals were euthanized 5 hours later by CO₂ exposure in a Euthanasia Chamber and the kidneys were excised for observation with an IVIS imager (Perkin Elmer).

4.3.6 Preparation of mouse tumour slices for imaging experiments.

Tumours from Balb/cByJ mice orthotopically injected with 4T1 cells treated or not treated with palbociclib were excised and cut in half. They were pasted onto a petri dish exposing a tumor surface as smooth as possible. The slices were incubated with a 10 mM solution of **HeckGal** for 2 h at 37 °C in a dry incubator, and then washed three times with PBS, and observed under two-photon confocal microscope (OLYMPUS FV1000MPE). The images were acquired at different penetration depths ($\lambda_{\text{ex}} = 820$ nm).

4.4 Results and discussion

4.4.1 Synthesis, Characterization, Spectroscopic Features, and Mechanism.

HeckGal probe was synthesized following the synthetic procedure shown in Figure 1A. Naphthalimide **1** was obtained by the reaction between 4-bromo-1,8-naphthalic anhydride and methoxyamine in refluxing dioxane. In parallel, the hydroxyl group of 4-hydroxybenzaldehyde was protected with *t*-butylchlorodiphenylsilane (TBDPSCI) yielding compound **2**, in which the aldehyde was converted into a double bond using a Wittig reaction resulting in compound **3**. A Heck cross-coupling reaction between **1** and **3** yielded **Heck** fluorophore. Finally, **Heck** was consecutively reacted with NaOH, in order to remove the phenolic proton, and with 2,3,4,6-tetra-O-acetyl- α -D-galactopyranosyl bromide (Gal) yielding the **HeckGal** probe. The final probe and intermediate compounds were fully characterized by ¹H-NMR, ¹³C-NMR, and HRMS (Figure S1-S5). PBS (pH

7)-DMSO (0.01%) solutions of **Heck** fluorophore (10^{-5} M) presented an intense emission band centered at 550 nm ($\Phi_{\text{Heck}} = 0.875$) when excited at 488 nm (Figure 1B, iii)). In contrast, excitation at 488 nm of PBS (pH 7)-DMSO (0.01%) solutions of **HeckGal** resulted in a weak broad emission ($\Phi_{\text{HeckGal}} = 0.074$) (Figure 1B, iii). The low emission intensity of **HeckGal**, when compared to that of **Heck**, is ascribed to a photoinduced electron transfer process from the galactose unit to the excited fluorophore. It was also assessed that the emission intensity of **Heck** remained unchanged in the 4-9 pH range (Figure S6). After assessing the photophysical properties, time-dependent fluorescent measurements in PBS (pH 7)-DMSO (0.01%) solutions of **HeckGal** in the presence of β -Gal were carried out (Figure S7, A). Progressive enhancement of the emission at 550 nm was observed due to the generation of free **Heck** produced by the enzyme-induced hydrolysis of the O-glycosidic bond in **HeckGal**. The reaction was also analyzed by HPLC (Figure S7, B) which showed the progressive vanishing of the **HeckGal** peak (at ca. 8.5 min) with the subsequent appearance of **Heck** signal at ca. 8.2 min.

HeckGal displays several advantages when compared with the recently reported AHGa probe. **HeckGal** presents a more extended conjugated framework which is reflected in a marked increase, of almost 100 nm, in the two-photon excitation wavelength. This increase in excitation wavelength might allow greater tissue penetrability, less photo-toxicity, and reduced light scattering. Moreover, the molecule generated after **HeckGal** hydrolysis with β -Gal enzyme (i.e. the **Heck** fluorophore) shows a remarkable higher quantum yield of 0.875, making the **HeckGal** probe more suitable for the differentiation between senescent from non-senescent cells with high basal levels of the β -Gal enzyme. Besides, a comparative table of **HeckGal** and other cell senescence probes published in the last three years is shown in the Supporting Information (Table S1).

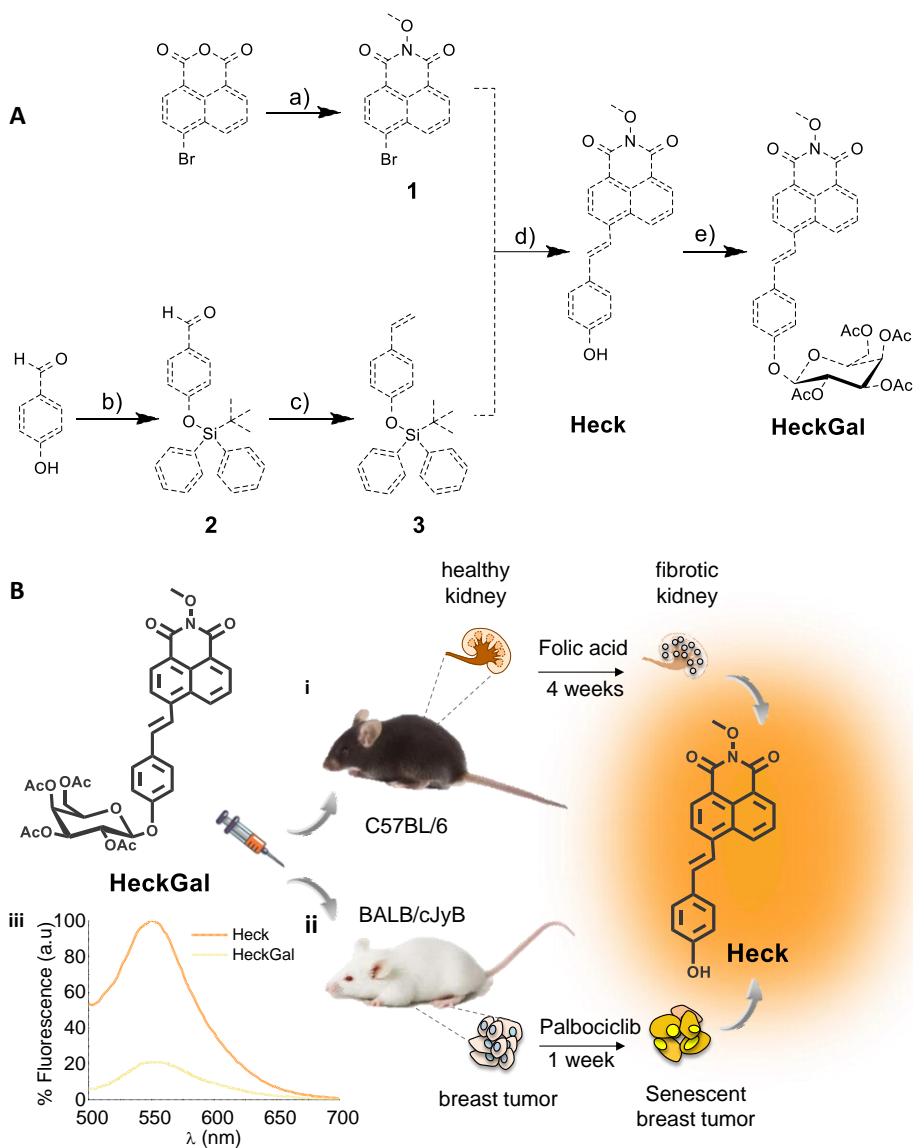


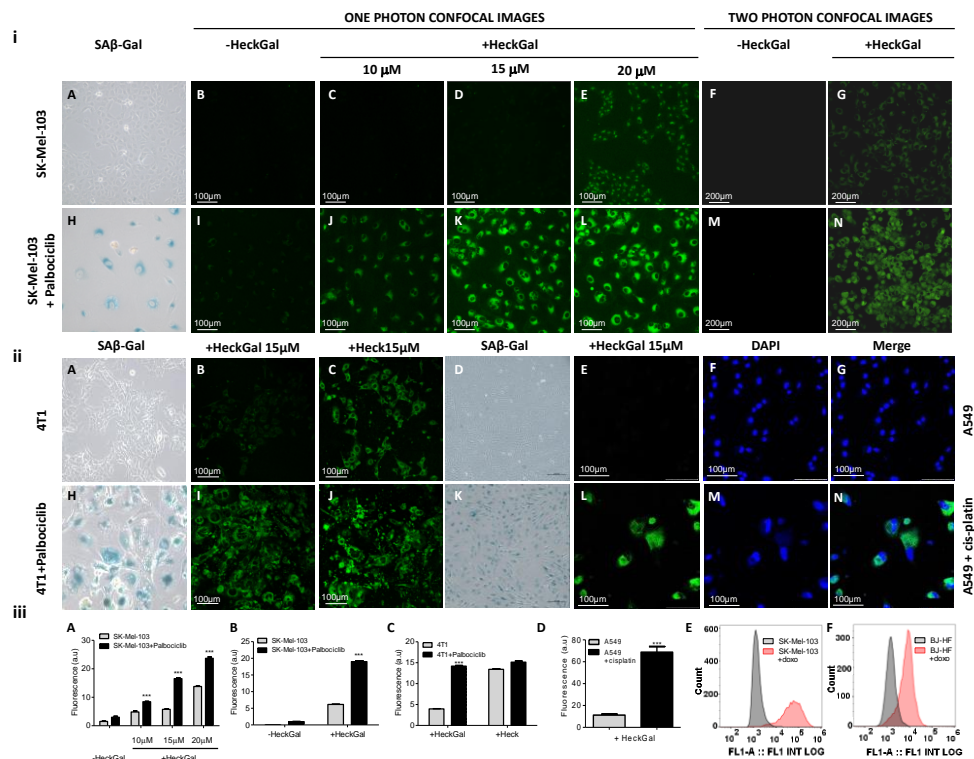
Figure 1. Synthesis of probe and mechanism of action in mice. (A) Synthetic route used for the preparation of the probe: a) $\text{CH}_3\text{ONH}_2 \cdot 3\text{HCl}$, Et_3N , dioxane; b) TBDPSCI , imidazole, DMF; c) $n\text{-BuLi}$, Ph_3PCH_3 , THF; d) $\text{Pd}(\text{OAc})_2$, $(\text{O-tolyl})_3\text{P}$, Et_3N , DMF; e) NaOH/MeOH , acetobromo- $\alpha\text{-D-galactose}$. (B) Schematic representation of the application of the probe in two in vivo models of senescence: i) kidney fibrotic C57BL/6J male mice induced by treatment with folic acid and ii) BALB/cJyB female mice bearing 4T1 breast cancer tumours treated with senescence-inducing chemotherapy. iii) Fluorescence emission spectra ($\lambda_{\text{ex}} = 488 \text{ nm}$) of **HeckGal** (yellow) and **Heck** fluorophore (orange) in aqueous solutions (pH 7)-DMSO (0.01%).

4.4.2 *In Vitro* Validation of HeckGal probe.

To study the cellular toxicity after prolonged exposure to the **HeckGal** probe, human melanoma SK-Mel-103 and murine breast cancer 4T1 cells were used in cell viability assays and the results showed that after 48 h neither **Heck** nor **HeckGal** were toxic for SK-Mel-103 or 4T1 cells, in both senescence and non-senescence states, at concentrations of up to 100 μM (Figure S8). Once proven the probe's biocompatibility, the preferential activation of **HeckGal** in senescent cells *in vitro* was assessed in senescent SK-Mel-103, 4T1, A549 (human lung carcinoma), and BJ (human fibroblast) cell lines. Senescence was induced in SK-Mel-103 and 4T1 cells by treatment with 5 μM palbociclib, a well-known specific CDK4/6 inhibitor,⁵² for two weeks. After palbociclib treatment, the cell morphology changed, presenting an enlarged and flattened appearance typical of cellular senescence. Cellular senescence was assessed by SA- β -Gal activity assay (Figure 2i (A and H) and 2ii (A and H)). Next, control and senescent SK-Mel-103 cells were seeded in flat-bottom-clear 96 wells plates and incubated with 10, 15, and 20 μM solutions of **HeckGal** in DMEM (0.1% DMSO) for 2 h in the case of one-photon studies. In the case of two-photon studies, cells were seeded in p6 wells plates and incubated with a 10 μM solution of the probe. Cells were imaged by confocal microscopy using an excitation wavelength of 488 nm, and by two-photon confocal microscopy using a 950 nm excitation wavelength. Control (Figure 2i (B and F)) and senescent (Figure 2i (I and M)) SK-Mel-103 cells did not show significant background signal before incubation with **HeckGal**, especially in two-photon studies (Compare I and M in Figure 2i). Non-senescent SK-Mel-103 cells showed weak emission in the presence of increasing concentrations (10, 15, and 20 μM) of the **HeckGal** probe (Figure 2i (C, D, E, and G)), while palbociclib-treated SK-Mel-103 displayed an intense fluorescent signal, increased for higher **HeckGal** concentrations (Figure 2i (J, K, L, and N)). The fluorescent signal in the cells is attributed to the hydrolysis of **HeckGal** into **Heck** fluorophore that

occurred preferably in senescent cells, which present an increased β -galactosidase activity. Moreover, the emission spectrum of **Heck**, obtained after two-photon excitation (Figure S9), corresponds to that obtained in a fluorimeter when using one-photon 488 nm excitation wavelength (Figure 1B iii). Fluorescence quantification from the confocal images associated with each treatment showed a fluorescence enhancement (ca. 2.9 fold) in palbociclib-treated SK-Mel-103 incubated with 15 μ M of the probe in one-photon confocal images (Figure 2iii A) and ca. 3.1 fold for cells incubated with 10 μ M of the probe in two-photon images (Figure 2iii B). Moreover, the ability of **HeckGal** to detect senescent 4T1 cells was also confirmed. Non-treated and palbociclib-treated (senescent) 4T1 cells were incubated with 15 μ M solutions of **HeckGal** or **Heck** in DMEM (0.1% DMSO) for 2 h. Figure 2ii shows that control 4T1 cells treated with **HeckGal** (Figure 2ii B) showed a minimal fluorescence when compared to senescent 4T1 cells (Figure 2ii I) in the same conditions (3.6-fold enhancement, Figure 2iii C). This marked difference was not observed when control and senescent 4T1 cells were treated with **Heck** (Figure 2ii C and J), demonstrating the selectivity of **HeckGal** to detect cellular senescence. The versatility of the **HeckGal** probe was also validated in other cell lines where senescence was induced with different chemotherapy. Thus, human lung adenocarcinoma (A549) cells were treated with cisplatin 15 μ M for 3 weeks. Further incubation with **HeckGal** resulted in an enhanced fluorescence (ca. 6.1 fold, see Figure 2iii D for quantification of images) in cisplatin-treated A549 cells when compared with non-treated A549 cells (Figure 2ii, E and L). Finally, co-staining with typical staining kits did not affect the **Heck** fluorescence signal or hydrolysis of **HeckGal** (Figure S10). The use of the **HeckGal** probe was also assessed by Fluorescence-Activated Cell Sorting (FACS) (Figure 2iii E and F) For these studies, control SK-Mel-103 cells and BJ human fibroblasts were exposed to 250 nM doxorubicin for 24 h to induce cellular senescence (red). On day 14, control and senescent cells from both cell lines were treated with 7 μ M

solutions of **HeckGal** for 2 h, detached from the plates, and fluorescence was subsequently evaluated through FACS. The studies demonstrated that **HeckGal** can distinguish between control and senescent cell populations in doxorubicin-induced SK-Mel-103 and BJ human fibroblasts.



probe (A) or 15 μM of **Heck** (B) and 4T1 treated with palbociclib (I, J) in presence of 15 μM of **HeckGal** probe (l) or 15 μM of **Heck** (J). SA β -Gal staining of non-treated (D) and cisplatin-treated A549 cells(K). Note that senescent A549 cells present the typical blue staining. Confocal microscopy images of non-treated (E-F) and cisplatin-treated A549 cells (L-N), exposed to the **HeckGal** probe. Cells were incubated with **HeckGal** (15 μM) in DMEM + 10% FBS in 20% O₂ and 5% CO₂ at 37°C for 2 h, and images were acquired by using a confocal microscope (excitation at 488 nm). (iii) Quantification of the fluorescence emission intensity relative to the cell surface of control and palbociclib-treated SK-Mel-103 cells incubated with **HeckGal** visualized with one photon confocal imaging (A) and two-photon confocal imaging (B). Quantification of the fluorescence emission intensity relative to the cell surface of control and palbociclib-treated 4T1 cells incubated with **HeckGal** or **Heck** visualized with one photon confocal imaging (C). Quantification of the fluorescence emission intensity relative to the cell surface of control and cisplatin-treated A549 cells incubated with **HeckGal** visualized with one photon confocal imaging (D). Error bars represent SEM (n=3) (E) Fluorescence-Activated Cell Sorting (FACS) analysis for control Sk-Mel-103 (grey) human melanoma cells and doxorubicin-treated SK-Mel-103 (red) cells after treatment with **HeckGal**. (F) FACS analysis for control BJ (grey) human fibroblast cells and doxorubicin-treated BJ (red) cells after treatment with **HeckGal**. Both cell lines were treated with 250 nM doxorubicin for 24 hours in order to induce cellular senescence, or with DMSO as vehicle. 14 days later, upon complete development of the senescent phenotype, cells were incubated with 7 μM **HeckGal** for 2 hours, detached from the plates, and washed twice with PBS. **HeckGal** fluorescence was subsequently evaluated by a Sony SA3800 Spectral Analyzer.

4.4.3 *In Vivo* Validation of HeckGal probe

Encouraged by the ability of **HeckGal** to detect cellular senescence *in vitro*, we took a step forward and studied the potential of the **HeckGal** probe to detect cellular senescence *in vivo* in two different disease models of senescence: (i) BALB/cByJ female mice bearing 4T1 breast cancer tumors treated with palbociclib and (ii) C57BL/6J male mice with renal fibrosis induced by treatment with folic acid (FA). BALB/cByJ female mice were orthotopically injected in the mammary fat pad with 4T1 cells (0.5×10^6 cell/mouse) in order to generate breast tumors. Seven days later, palbociclib was administered daily by oral gavage to arrest tumor growth and induce cellular senescence. One week after, palbociclib treatment was started, 100 μl of **HeckGal** was injected intraperitoneally (i.p.) at a concentration of 13.3 mg/ml, and mice were sacrificed 3 h after treatment. Different organs (i.e. lungs, liver, kidney, and spleen) and tumors were harvested. Cellular senescence in palbociclib-treated tumors was assessed by SA- β Gal

staining (Figure 3A). The reduction of Ki67, a proliferative marker, observed by immunohistochemistry (IHC) was also indicative of cellular senescence in palbociclib-treated tumors (Figure 3B). Figure 3G shows the quantification of the Ki67 signal. *Ex vivo* IVIS images demonstrated that no fluorescent signal was observed in control animals, neither in tumors nor in lungs, liver, kidney, or spleen (Figure 3C, 3D, 3E and 3F), either in the presence or absence of **HeckGal**. Tumors of mice treated with palbociclib in the absence of **HeckGal** were used to monitor tissue auto-fluorescence and displayed a weak emission. In contrast tumors from mice previously treated with palbociclib and i.p. injected with **HeckGal** showed a strong emission signal in IVIS images (Figure 3F). Quantification of the average radiance intensity from organs and tumors was determined for each condition (Figure 3H). An emission enhancement of ca. 4.6 fold was observed in tumors treated with palbociclib when compared to control tumors. These results demonstrate that **HeckGal** is a potent tool to visualize senescence in a breast cancer tumor model treated with senescence-inducing therapy. Moreover, to evaluate **Heck-Gal** penetrability and their ability for two-photon imaging of senescent cells in the depth of tissues, fluorescence intensities of tumour slices from vehicle, and palbociclib-treated mice at different depths were measured by a Z-scan model (Fig. 3I and 3J). As could be seen in Figure 3I and 3J, a marked emission intensity was observed for the palbociclib-treated tumours treated with **HeckGal** probe, and senescent cells could be visualized up to a depth of 150 μm . These results clearly indicated the ability of **HeckGal** probe for tracking β -Gal activity at different depths using two-photon microscopy.

To assess the versatility of the probe, **HeckGal** was also tested to detect cellular senescence in a renal fibrosis model. For this purpose, C57BL/6J male mice were i.p. injected with a single dose of 250 mg/kg of FA in order to generate renal fibrosis. 34 days post-FA injection, the presence of cellular senescence in the kidneys was evaluated with p21 IHC immunostaining. An increase in p21 signal

was observed in the kidneys of FA treated-mice, confirming cellular senescence (Figure 4A). Figure 4C shows the quantification of positive p21 nuclei. Once cellular senescence was assessed in this model, 200 μ l of **HeckGal** were i.p. injected at a concentration of 6.6 mg/ml (DMSO 1%- Corn oil).

Mice were euthanized 5 hours post-**HeckGal** treatment, kidneys were excised and analyzed by IVIS imaging. Kidneys from control mice treated with **HeckGal** presented a very weak fluorescent signal (Figure 4B left), whereas kidneys from FA-treated mice and injected with **HeckGal** (Figure 4B middle) exhibited an intense emission (5.8-fold higher). FA-treated mice did not present any significant auto-fluorescence in the absence of the **HeckGal** probe (Figure 4B, right). Figure 4D showed the quantification of average radiance intensity from kidneys showed in 4B images.

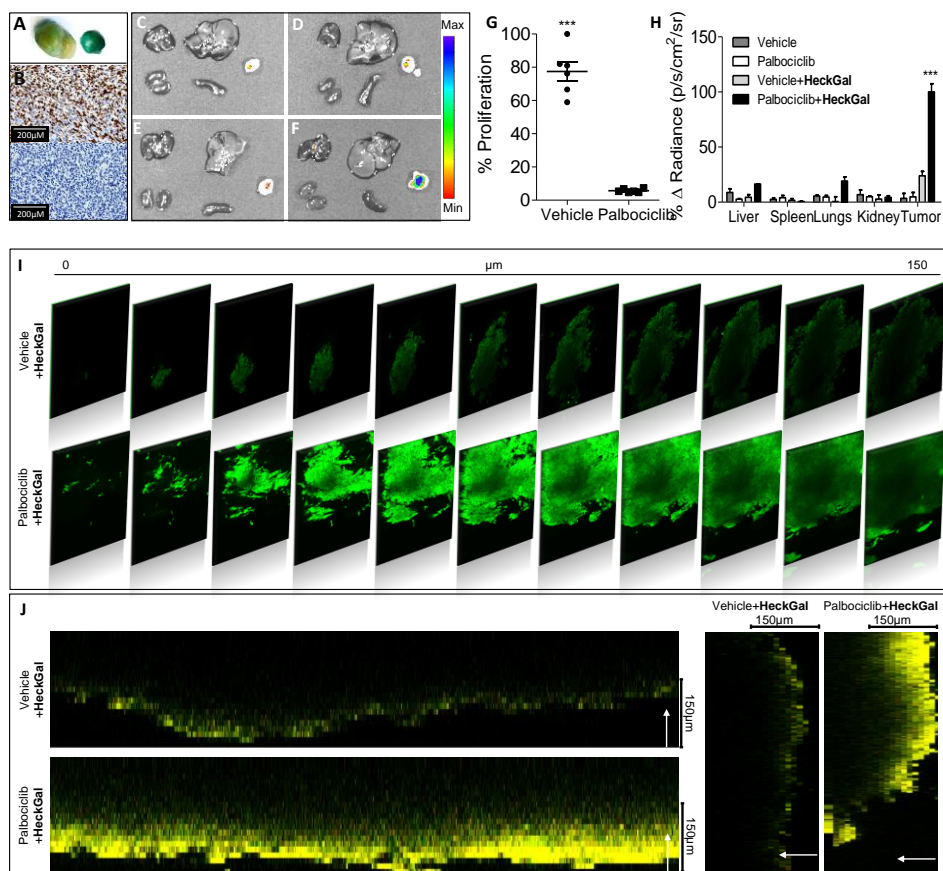


Figure 3. HeckGal probe enables the detection of senescence in different disease models of senescence.

(A) Representative images of tumours stained for the SA-β-Gal assay. Tumours from vehicle (left) and palbociclib-treated mice (right). (B) Immunohistochemical detection of the proliferation marker Ki67 in paraffin sections of tumours from vehicle (top) and palbociclib-treated mice (bottom). (C-F) IVIS images of organs and tumours from BALB/cByJ female mice bearing 4T1 breast cancer cells. From left to right and from top to bottom: lungs, liver, tumour, kidney, and spleen. (C) Vehicle mice. (D) Vehicle mice treated with (13.33 mg/ml 100μl). (E) Mice treated with palbociclib for 1 week. (F) Palbociclib-treated mice injected with HeckGal (13.33 mg/ml 100μl). Mice were sacrificed two hours post-HeckGal treatment. (G) Quantification of Ki67 signal in paraffin sections of tumours from vehicle (top) and palbociclib-treated mice (bottom). Error bars represent s.d. (H) Quantification of average radiance intensity from organs and tumours showed in images C,D,E, and F. Error bars represent SEM (n=3 for each condition). (I) Two-photon fluorescence depth images of HeckGal in tumour tissue slices from vehicle (up) and palbociclib-treated mice (down). The slices were incubated with HeckGal (10 mM) for 2 h at 37°C in a dry incubator. The images were acquired at different penetration depths ($\lambda_{ex} = 820$ nm). (J) 3D representation of images shown in Figure 3I demonstrating the greater penetrability of HeckGal in tumour tissue slices from palbociclib-treated mice (down) compared to tumour tissue slices from vehicle (up).

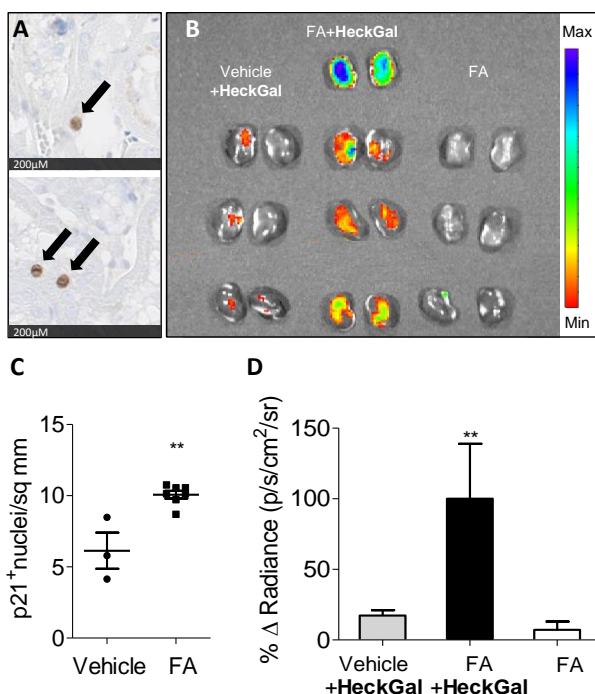


Figure 4. (A) Immunostaining for p21 in kidney slides. (B) IVIS images of kidneys from mice with renal fibrosis induced by FA treatment. From left to right: Vehicle mice + **HeckGal** (6 mg/ml 200 μl); FA-treated mice (with renal fibrosis) + **HeckGal** (6.6 mg/ml 200 μl); and FA-treated mice (with renal fibrosis). Mice were sacrificed five hours post-**HeckGal** injection. (C) Quantification of p21 signal in paraffin sections of kidney from vehicle and FA-treated mice. Error bars represent SEM. (D) Quantification of average radiance intensity from kidneys showed in 3B image. Error bars represent SEM (n=3 for control mice treated with probe and FA-treated mice and n=4 for FA-treated mice+**HeckGal**).

4.5 Conclusions

In summary, we report herein the synthesis of a new two-photon fluorescent probe for the detection of cellular senescence *in vivo*. **HeckGal** is based on a naphthalimide core linked to an acetylated galactose which quenches the emission of **Heck** fluorophore. **HeckGal** is hydrolysed into the highly fluorescent **Heck** fluorophore in presence of the β-Gal enzyme. *In vitro* detection of cellular senescence using **HeckGal** was assessed in senescent SK-Mel-103, A549, 4T1, and

BJ cell lines, in which senescence was induced by treatment with different therapies. The probe was validated to detect cellular senescence by one-photon and by two-photon confocal images and by FACS. The use of **HeckGal** to detect cellular senescence was also validated *in vivo* in BALB/C mice bearing 4T1 breast tumours, where senescence was induced with palbociclib. *Ex vivo* IVIS images showed that fluorescence ascribed to the hydrolyzed **HeckGal** probe (**Heck** fluorophore) was only observed in senescent tumours, whereas a negligible emission was found in other organs. Besides, **HeckGal** probe was also tested in a renal fibrosis model induced with FA. In this model, emission was only observed in fibrotic senescent kidneys from FA-treated mice. We hope that the studies presented here will help in the field of cellular senescence diagnosis in more translatable *in vivo* models. We also envisage that **HeckGal** or similar probes can be essential tools in the detection of senescent cells in aged or damaged tissues, and to assess treatment response of senolytics in aging-related diseases.

4.6 Associated content

Supplemental Information includes chemical characterization of the probe and reaction intermediates, experimental procedures, studies of the mechanism of hydrolysis, studies of fluorescence emission vs. pH, and calculations of quantum yields. Toxicity of **HeckGal** and **Heck** in SK-Mel-103 and 4T1 cells is also shown in the supplementary information, as well as some confocal images of SK-Mel-103 with different confocal objectives. The immunohistochemical detection of Ki67 is provided in the supplemental material.

4.7 Acknowledgments

R.M laboratory members thank the financial support from the Spanish Government (project RTI2018-100910-B-C41) and the Generalitat Valenciana (project PROMETEO 2018/024). B.L-T. is grateful to the Spanish Ministry of Economy for their PhD grants (FPU15/02707). I.G. thanks her contract from IDM. J. F.-B thanks to his postdoctoral fellowship (CD19/00038). J.A.L-D. thanks the financial support from the Ministry of Science/MICINN (IJCI-2017-33047). Work in the laboratory of MS was funded by the IRB and by grants from the Spanish Ministry of Economy co-funded by the European Regional Development Fund (ERDF) (SAF2013-48256-R), the European Research Council (ERC-2014-AdG/669622), and the “laCaixa” Foundation. D.M.-E. laboratory is supported by the Cancer Research UK (CRUK) Cambridge Centre Early Detection Programme, by a CRUK Early Detection OHSU Project Award (C62187/A26989), by a Medical Research Council (MRC) New Investigators Research Grant (NIRG, MR/R000530/1).

4.8 Author contribution

B. L.-T., J. F. B., and R. M.-M. conceived and designed the research, performed experiments, contributed to the experimental designs, data analysis, discussion and writing. J. F. B. synthesized and characterized all organic molecules with the help of B. L.-T. J. F. B. performed HPLC and UV studies. B. L.-T., carried out *in vitro* studies with SK-Mel-103 and 4T1 cell lines. J.A. L.-D. performed flow cytometry experiments. M. P.-R., E. G.-G. and D.M-E. performed the experiments with human lung carcinoma and contributed to the discussion of the manuscript. B. L.-T. and I. G. carried out *in vivo* experiments with 4T1 breast cancer model. M.S. provided expertise on cellular senescence, contributed to the discussion and

designed the *in vivo* experiment with renal fibrosis model, which was accomplished by J.A. L.-D., M. R and B.L.-T. B. L.-T., J. F. B., F.S.-G. and R. M.-M. analyzed the data. B. L.-T., J. F. B., F. S and R. M.-M. wrote the manuscript with feedback from all the authors.

4.9 References

1. Munoz-Espin, D., and Serrano, M. (2014). Cellular senescence: from physiology to pathology. *Nat. Rev. Mol. Cell. Biol.* **15**, 482–496.
2. Hayflick, L., and Moorhead, P. S. (1961). The serial cultivation of human diploid cell strains. *Exp. Cell Res.* **25**, 585-621.
3. Bielak-Zmijewska, A., Mosieniak, G., and Sikora, E. (2018). Is DNA damage indispensable for stress-induced senescence?. *Mech. Ageing Dev.* **170**, 13-21.
4. Mosteiro, L., Pantoja, C., de Martino, A., and Serrano, M. (2018). Senescence promoted *in vivo* reprogramming through p16INK4a and IL-6. *Aging Cell* **17**, e12711.
5. Ritschka, B., Storer, M.; Mas, A., Heinzmann, F., Ortells, M. C., Morton, J. P., Sansom, O. J., Zender, L., and Keyes, W. M. (2017). The senescence-associated secretory phenotype induces cellular plasticity and tissue regeneration. *Genes Dev.* **31**, 172-183.
6. McHugh, D., and Gil, J. (2018). Senescence and aging: Causes, consequences, and therapeutic avenues. *J. Cell Biol.* **217**, 65–77.
7. Baker, D. J., Childs, B. G., Durik, M., Wijers, M. E., Sieben, C., J., Zhong, J., Saltness, R. A., Jeganathan, K. B., Verzoza, G. C., Pezeshki, A., Khazaie, K., Miller, J. D., and van Deursen, J. M. (2016). Naturally occurring p16INK4a-positive cells shorten healthy lifespan. *Nature* **530**, 184–189.
8. Baker, D. J., Wijshake, T., Tchkonja, T., LeBrasseur, N. K., Childs, B. G., van de Sluis, B., Kirkland, J. L., and van Deursen, J. M. (2011). Clearance of p16INK4a-positive senescent cells delays ageing-associated disorders. *Nature* **479**, 232–236.
9. Soto-Gamez, A., and Demaria, M. (2017). Therapeutic interventions for aging: The case of cellular senescence. *Drug Discov. Today* **22**, 786–795.
10. González-Gualda, E., Pàez-Ribes, M., Lozano-Torres, B., Macias, D., Wilson III, J. R., González-López, C., Ou, H.-L., Mirón-Barroso, S., Zhang, Z., Lérida-Viso, A. Blandez, J. F., Bernardos, A., Sancenón, F., Rovira, M., Fruk, L., Martins, C. P., Serrano, M., Doherty, G. J., Martínez-Máñez, R., Muñoz-Espín, D. Galacto-conjugation of Navitoclax as an efficient strategy to increase senolytic specificity and reduce platelet toxicity. *Aging Cell.* **2020**, 19(4), e13142.
11. Galiana, I., Lozano-Torres, B., Sancho, M., Alfonso, M., Bernardos, A., Bisbal, V., Serrano, M., Martínez-Máñez, R., Orzáez, M. Preclinical antitumor efficacy of senescence-inducing chemotherapy combined with a nanoSenolytic. **2020**, 323, 624-634.
12. Lozano-Torres, B., Estepa-Fernández, A., Rovira, M., Orzáez, M., Serrano, M., Martínez-Máñez, R., and Sancenón, F. (2109). The Chemistry of Senescence. *Nat. Rev. Chem.* **3**, 426-441.
13. Lozano-Torres, B., Blandez, J. F., Galiana, I., García-Fernández, A., Alfonso, M. Marcos, M. D., Orzáez, M. Sancenón, F., Martínez-Máñez, R. Real-Time In Vivo Detection of Cellular Senescence through the Controlled Release of the NIR Fluorescent Dye Nile Blue. *Angew. Chem. Int. Ed.* **2020**, 59(35), 15152-15156.

14. Paez-Ribes, M., González-Gualda, E., Doherty, G. J., and Muñoz-Espín, D. (2019). Targeting senescent cells in translational medicine. *EMBO Mol. Med.* **11**, e10234
15. Funayama, R., and Ishikawa, F. (2007). Cellular senescence and chromatin structure. *Chromosoma* **116**, 431-440.
16. Zhang, R., and Adams, P. D. (2007). Heterochromatin and its relationship to cell senescence and cancer therapy. *Cell Cycle* **6**, 784–789.
17. Serrano, M., Hannon, G. J., and Beach, D. A. (1993). New regulatory motif in cell-cycle control causing specific inhibition of cyclin D/CDK4. *Nature* **366**, 704–707.
18. Serrano, M., Lin, A. W., McCurrach, M. E., Beach, D., and Lowe, S. W. (1997). Oncogenic Ras provokes premature cell senescence associated with accumulation of p53 and p16INK4a. *Cell* **88**, 593–602.
19. Sharpless, N. E., and Sherr, C. J. (2015). Forging a signature of *in vivo* senescence. *Nat. Rev. Cancer* **15**, 397–408.
20. Hernandez-Segura, A., Nehme, J., and Demaria, M. (2018). Hallmarks of cellular senescence. *Trends Cell Biol.* **28**, 436–453.
21. Childs, B. G., Baker, D. J., Kirkland, J. L., Campisi, J., and van Deursen, J. M. (2014). Senescence and apoptosis: dueling or complementary cell fates?. *EMBO Rep.* **15**, 1139–1153.
22. Takahashi, A., Ohtani, N., and Hara, E. (2007). Irreversibility of cellular senescence: dual roles of p16INK4a/Rb-pathway in cell cycle control. *Cell Div.* **2**, 10-15.
23. Guerrero, A., and Gil, J. (2016). HMGB2 holds the key to the senescence-associated secretory phenotype. *J. Cell Biol.* **215**, 297-299.
24. Krtolica, A., Parrinello, S., Lockett, S., Desprez, P. Y., and Campisi, J. (2001). Senescent fibroblasts promote epithelial cell growth and tumorigenesis: A link between cancer and aging. *Proc. Natl. Acad. Sci. U.S.A.* **98**, 12072-12077.
25. Dimri, G. P., Lee, X., Basile, G., Acosta, M., Scott, G., Roskelley, C., Medrano, E. E., Linskens, M., Rubelj, I., and Pereira-Smith, O. (1995). A biomarker that identifies senescent human cells in culture and in aging skin *in vivo*. *Proc. Natl. Acad. Sci. U.S.A.* **92**, 9363-9367.
26. Rotman, B. (1961). Measurement of activity of single molecules of beta-D-galactosidase. *Proc. Natl. Acad. Sci. U.S.A.* **47**, 1981–1991.
27. Rotman, B., Zderic, J. A., and Edelstein, M. (1963). Fluorogenic substrates for beta-D-galactosidases and phosphatases derived from fluorescein (3,6-dihydroxyfluoran) and its monomethylether. *Proc. Natl. Acad. Sci. U.S.A.* **50**, 1–6.
28. Strachan, R., Wood, J., and Hirschmann, R. (1962). Synthesis and properties of 4-methyl-2-oxo-1,2-benzopyran-7-yl β -D-galactoside (galactoside of 4-methylumbelliferone). *J. Org. Chem.* **27**, 1074–1075.
29. Horwitz, J. P., Chua, J., Curby, R. J., Tomson, A. J., Da Rooze, M. A., Fisher, B. E., Mauricio, J., and Klundt, I. (1964). Substrates for cytochemical demonstration of enzyme activity. I. Some substituted 3-indolyl- β -D-glycopyranosides. *J. Med. Chem.* **7**, 574–575.
30. Zhang, J., Li, C., Dutta, C., Fang, M., Zhang, S., Tiwari, A., Werner, T., Luo, F. T., and Liu, H. (2017). A novel near-infrared fluorescent probe for sensitive detection of β -galactosidase in living cells. *Anal. Chim. Acta* **968**, 97–104.
31. Dai, Z. R., Ge, G. B., Feng, L., Ning, J., Hu, L. H., Jin, Q., Wang, D. D., Lv, X., Dou, T. Y., Cui, J. N., and Yang, L. (2015). A highly selective ratiometric two-photon fluorescent probe for human cytochrome P450 1A. *J. Am. Chem. Soc.* **137**, 14488-14495.
32. Zhou, L., Zhang, X., Wang, Q., Lv, Y., Mao, G., Luo, A., Wu, Y., Wu, Y., Zhang, J., and Tan, W. (2014). Molecular engineering of a TBET-based two-photon fluorescent probe for ratiometric imaging of living cells and tissues. *J. Am. Chem. Soc.* **136**, 9838-9841.
33. Cefruga, C., Gallavardin, T., Marotte, S., Lanoë, P. H., Mulatier, J. C., Lerouge, F., Parola, S., Lindgren, M., Baldeck, P. L., Marvel, J., Maury, O., Monnereau, C., Favier, A., Andraud, C., Leverrier, Y., and Charreyre, M. T. (2013). Biocompatible well-defined chromophore-polymer conjugates for photodynamic therapy and two-photon imaging. *Polym. Chem.* **4**, 61-67.

34. Kamiya, M., Kobayashi, H., Hama, Y., Koyama, Y., Bernardo, M., Nagano, T., Choyke, P. L., and Urano, Y. (2007). An enzymatically activated fluorescence probe for targeted tumor imaging. *J. Am. Chem. Soc.* **129**, 3918-3929.
35. Gu, K., Xu, Y., Li, H., Guo, Z., Zhu, S., Shi, P., James T. D., Tian, H., and Zhu, W. H. (2016). Real-time tracking and *in vivo* visualization of β -galactosidase activity in colorectal tumor with a ratiometric near-infrared fluorescent probe. *J. Am. Chem. Soc.* **138**, 5334-5340.
36. Oshiki, D., Kojima, H., Takahashi, Y., Komatsu, T., Terai, T., Hanaoka, K., Nishikawa, M., Takakura, Y., and Nagano, T. (2012). Near-infrared fluorescence probes for enzymes based on binding affinity modulation of squarylium dye scaffold. *Anal. Chem.* **84**, 4404-4410.
37. Tung, C. H., Zeug, Q., Shah, K., Kim, D. E., Schellingerhout, D., and Weissleder, R. (2004). *In vivo* imaging of β -galactosidase activity using far red fluorescent switch. *Cancer Res.* **64**, 1579-1583.
38. Urano, Y., Kamiya, M., Kanda, K., Ueno, T., Hirose, K., and Nagano, T. (2005). Evolution of fluorescein as a platform for finely tunable fluorescent probes. *J. Am. Chem. Soc.* **127**, 4888-4894.
39. Egawa, T., Koide, Y., Hanaoka, K., Komatsu, T., Terai, T., and Nagano, T. (2011). Development of a fluorescein analogue, TokyoMagenta, as a novel scaffold for fluorescence probes in red region. *Chem. Commun.* **47**, 4162-4164. (b) Kamiya, M., Asanuma, D., Kuranaga, E., Takeishi, A., Sakabe, M., Miura, M., Nagano, T., and Urano, Y. (2011). β -Galactosidase fluorescence probe with improved cellular accumulation based on a spirocyclized rhodol scaffold. *J. Am. Chem. Soc.* **133**, 12960-12963.
40. Kamiya, M., Asanuma, D., Kuranaga, E., Takeishi, A., Sakabe, M., Miura, M., Nagano, T., and Urano, Y. β -Galactosidase fluorescence probe with improved cellular accumulation based on a spirocyclized rhodol scaffold. *J. Am. Chem. Soc.* **2011**, *133*, 12960-12963.
41. Sakabe, M., Asanuma, D., Kamiya, M., Iwatate, R. J., Hanaoka, K., Terai, T., Nagano, T., and Urano, Y. Rational design of highly sensitive fluorescence probes for protease and glycosidase based on precisely controlled spirocyclization. *J. Am. Chem. Soc.* **2013**, *135*, 409-414.
42. Peng, L., Gao, M., Cai, X., Zhang, R., Li, K., Feng, G., Tong, A., and Liu, B. A fluorescent light-up probe based on AIE and ESPIT processes for β -galactosidase activity detection and visualization in living cells. *J. Mater. Chem. B* **2015**, *3*, 9168-9172.
43. Han, J., Han, M. S., and Tung, C. H. A fluorogenic probe for β -galactosidase activity imaging in living cells. *Mol. Biosyst.* **2013**, *9*, 3001-3008.
44. Zhang, X. X., Wu, H., Li, P., Qu, Z. J., Tan, M. Q., and Han K. L. A versatile two-photon fluorescent probe for ratiometric imaging *E. coli* β -galactosidase in live cells and *in vivo*. *Chem. Commun.* **2016**, *52*, 8283-8286.
45. Lee, H. W., Heo, C. H., Sen, D., Byun, H. O., Kwak, I. H., Yoon, G., and Kim, H. M. Ratiometric two-photon fluorescent probe for quantitative detection of β -Galactosidase activity in senescent cells. *Anal. Chem.* **2014**, *86*, 10001-10005.

4.10 Supporting information

4.10.1 Table S1. Recently published fluorogenic molecular probes for cellular senescence detection.

Probe	λ_{exc}	λ_{em}	Cell line	Cellular senescence induction	In vivo model	Senescence induction in vivo	Multi photon	IVIS	Reference
AHGa	750 nm	540 nm	SK-Mel-103	Palbociclib	SK-Mel-103 xenograft	Palbociclib	YES	NO	Lozano-Torres, B. et al. <i>J. Am. Chem. Soc.</i> 2017, 139 , 8808
NIR-BG	680 nm	708 nm	MCF7	Camptothecin or Radiation	CT26 xenograft	Camptothecin	NO	YES	Wang, Y. et al. <i>Sci. Rep.</i> 2019, 9 , 2102
			HeLa		HeLa xenograft				
NIR-BG2	650 nm	709 nm	HeLa	Camptothecin	HeLa xenograft	Camptothecin	NO	YES	Liu, J. et al. <i>bioRxiv.</i> 2020, https://doi.org/10.1101/2020.03.27.010827
SRP	495 nm	545 nm	HUVEC	H ₂ O ₂	-	-	-	-	Kim, E. J. et al. <i>Sens Actuators B Chem.</i> 2018, 274 , 194
CBT- β -Gal	365 nm	510 nm	HeLa	H ₂ O ₂	-	-	-	-	Makau J. N. et al. <i>ACS Omega</i> , 2020, 5 , 11299
β Gal-1-4	361 - 370 nm	426 - 480 nm	A375	Hydroxyurea	-	-	-	-	Filho, M. S, et al. <i>Analyst</i> , 2018, 143 , 2680
			HT-29						
Heck Gal	950 nm	550 nm	SK-Mel-103	Palbociclib	4T1 orthotopic breast tumour	Palbociclib	YES	YES	This work
			4T1						
			A549	Cisplatin	Renal fibrosis	Folic acid			
			SK-Mel-103	Doxorubicin					
			BJ fibroblast						

4.10.2 Synthesis of Heck and HeckGal.

6-Bromo-2-methoxy-1H-benzo[de]isoquinoléine-1,3(2H)-dione (**1**): A mixture of 4-bromo-1,8-naphthalic anhydride (2.7 g, 10 mmol) and methoxylamine hydrochloride (1.25 g, 15 mmol) were dissolved in anhydrous dioxane (150 mL). Then the system was purged with argon and trimethylamine was added (15 mL), maintaining the mixture overnight. The product was precipitated with cool water, filtered in vacuum and washed with cold water. The product was obtained as a yellow-brown solid 2.97 g. Yield 98%. ¹H NMR (400 MHz, CDCl₃) δ 8.71 (dd, J = 7.3, 1.1 Hz, 1H), 8.62 (dd, J = 8.5, 1.1 Hz, 1H), 8.46 (d, J = 7.9 Hz, 1H), 8.07 (d, J = 7.9 Hz, 1H), 7.88 (dd, J = 8.5, 7.3 Hz, 1H), 4.12 (d, J = 4.8 Hz, 3H). ¹³C NMR (101 MHz, CDCl₃) δ 160.39 (2C), 134.18 (1C), 132.71 (1C), 131.80 (1C), 131.47 (1C), 131.31 (2C), 131.03 (1C), 128.41 (1C), 123.40 (1C), 122.51 (1C), 64.51 (1C).

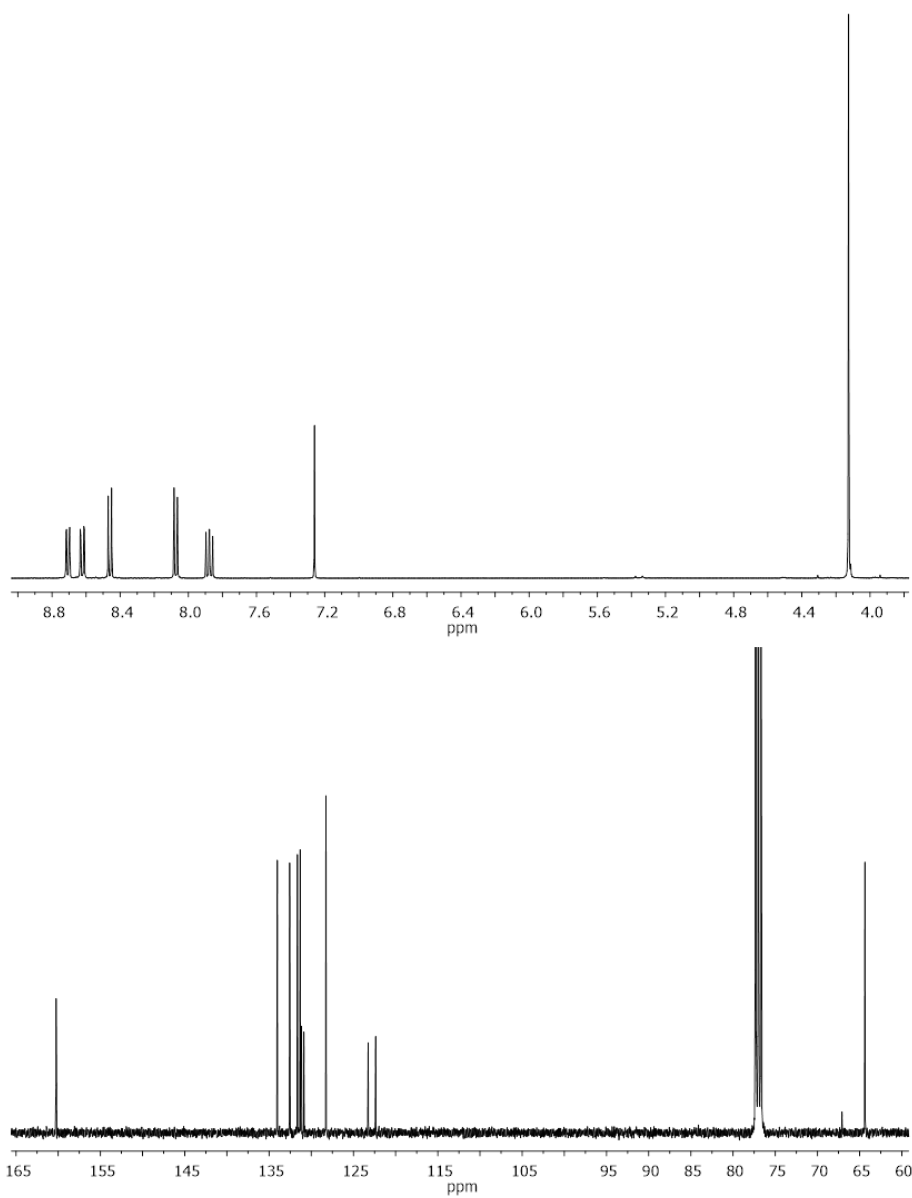


Figure S1. $^1\text{H-NMR}$ and $^{13}\text{C-NMR}$ of compound **1**.

4-[[[(2-Methyl-2-propanyl)(diphenyl)silyl]oxy]benzaldehyde (**2**): A mixture of 4-hydroxybenzaldehyde (3 g, 24.6 mmol) and imidazole (1.68 g, 28.56 mmol) was added in a round bottom flask and purged with argon. The mixture was dissolved in anhydrous DMF (40 mL) and stirred at room temperature until the complete dissolution of the reagents. Then, tert-butylchlorodiphenylsilane was added dropwise (5.12 mL, 19.64 mmol) and the reaction was stirred for 4 h at room temperature. After complete reaction, the DMF was partially removed under vacuum. The reaction mixture was poured into water (50 mL) and the product was extracted with petroleum ether (2 x 50 mL). The organic layer was washed with brine (3 x 20 mL) and dried over MgSO₄. The petroleum ether was removed under vacuum and the product was obtained as a white solid, 6.75 g. Yield 76%. ¹H NMR (400 MHz, CDCl₃) δ 9.81 (s, 1H), 7.73 – 7.68 (m, 4H), 7.65 (d, J = 8.7 Hz, 2H), 7.48 – 7.43 (m, 2H), 7.42 – 7.35 (m, 4H), 6.86 (d, J = 8.6 Hz, 2H), 1.12 (s, 9H). ¹³C NMR (101 MHz, CDCl₃) δ 191.00 (1C), 161.35 (1C), 135.53 (6C), 132.09 (1C), 131.84 (4C), 130.40 (2C), 128.12 (2C), 120.43 (2C), 26.52 (3C), 19.61 (1C).

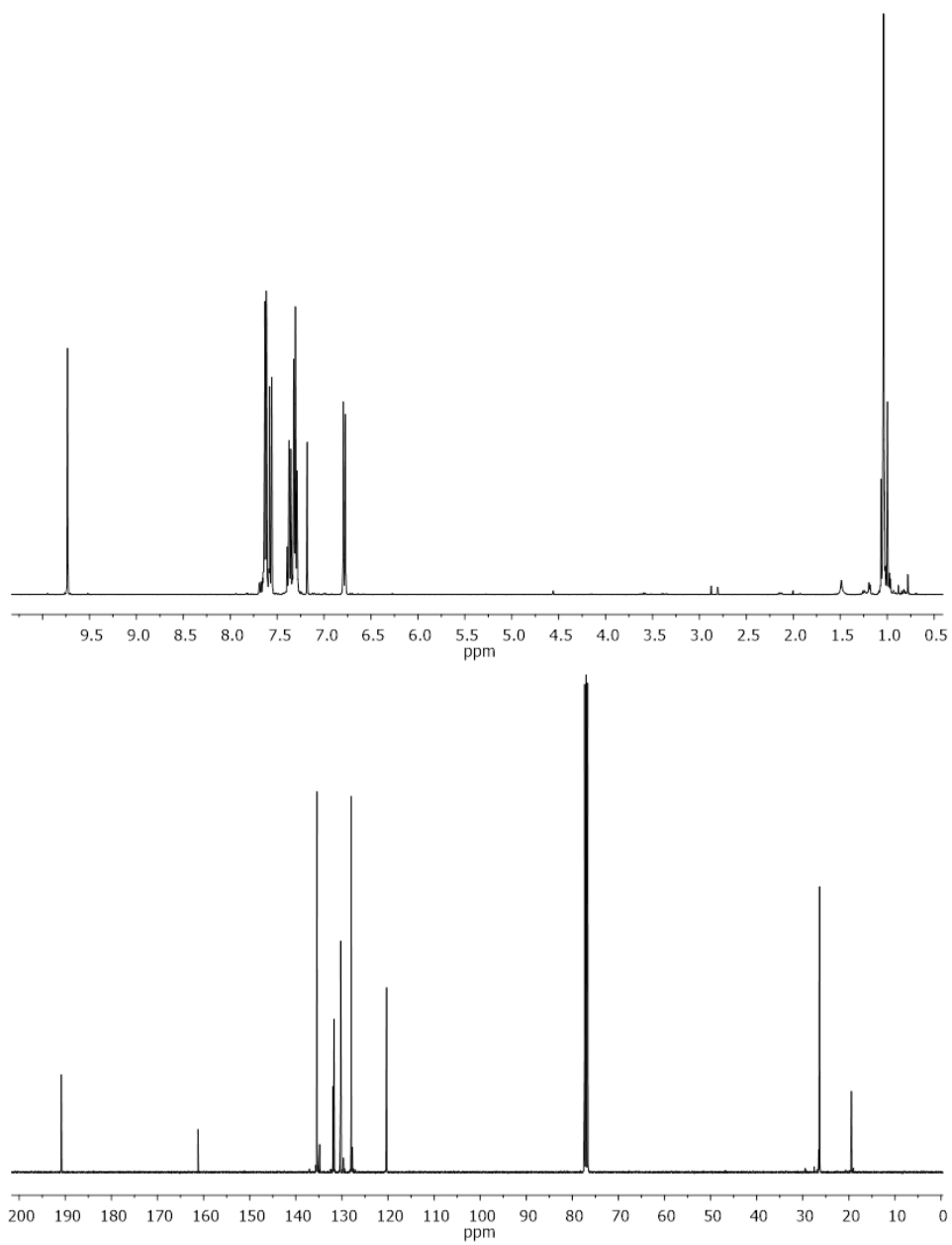
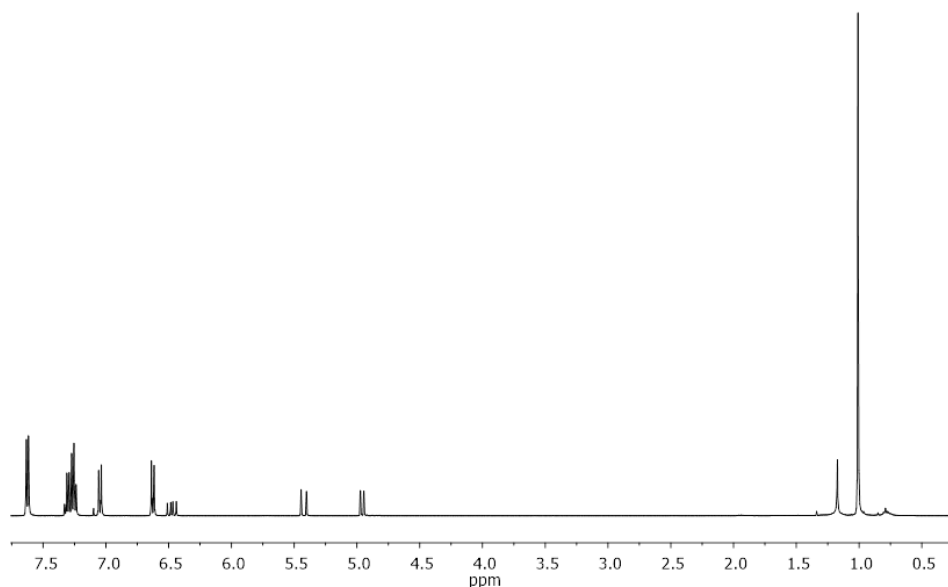


Figure S2. $^1\text{H-NMR}$ and $^{13}\text{C-NMR}$ of compound **2**.

4-[[[(2-Methyl-2-propanyl)(diphenyl)silyl]oxy]styrene (**3**): $\text{Ph}_3\text{PCH}_3\text{I}$ (6.4 g, 15.8 mmol) was added in a two-neck round bottom flash and then was purged with argon. Afterward, the solid was dissolved in anhydrous THF (40 mL) and a solution of n-BuLi was added dropwise (6.0 mL, 2.5 M in hexane, 15.8 mmol) at 0°C. After stirring 15 min, a solution of compound **2** (3.67 g, 10.2 mmol) in anhydrous THF (20 mL) purged with argon was added dropwise. The mixture was stirred for 5 h and quenched with cold brine (50 mL). The product was extracted in diethyl ether (3 x 25 mL). The combined organic layers were dried over MgSO_4 , filtered off and concentrated in vacuum. The crude product was purified in a silica flash column using diethyl ether as eluent. The product was obtained as a white solid, 3.06 g. Yield: 84 %. ^1H NMR (400 MHz, CDCl_3) δ 7.70 – 7.56 (m, 4H), 7.37 – 7.21 (m, 6H), 7.08 – 7.01 (m, 2H), 6.67 – 6.59 (m, 1H), 6.48 (dd, $J = 17.6, 10.9$ Hz, 1H), 5.43 (dd, $J = 17.6, 1.0$ Hz, 1H), 4.96 (dd, $J = 10.9, 0.9$ Hz, 1H), 1.01 (s, 3H). ^{13}C NMR (101 MHz, CDCl_3) δ 155.58 (1C), 136.44 (1C), 135.64 (2C), 133.01 (4C), 130.83 (1C), 130.06 (4C), 127.93 (2C), 127.30 (2C), 119.86 (2C), 111.71 (1C), 26.66 (3C), 19.61 (1C).



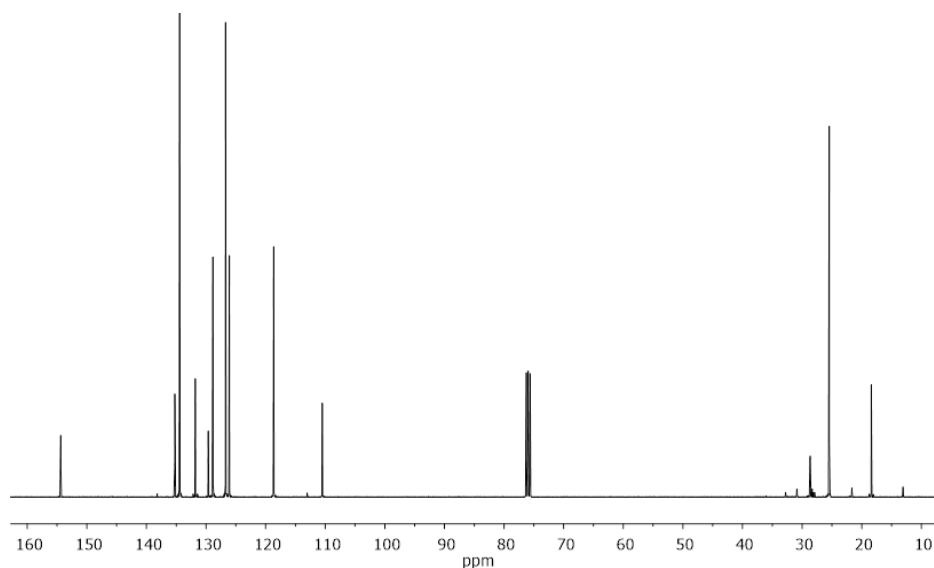
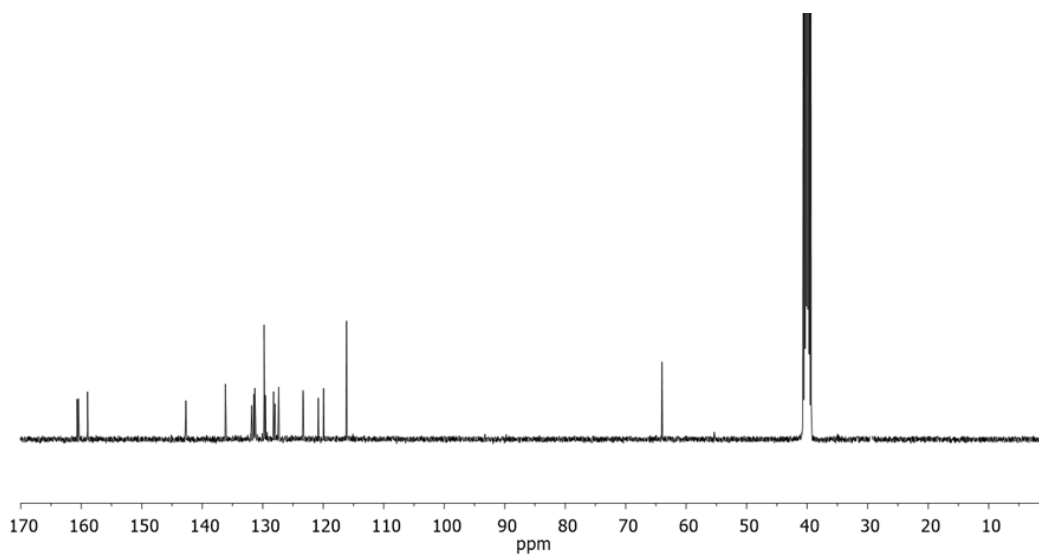
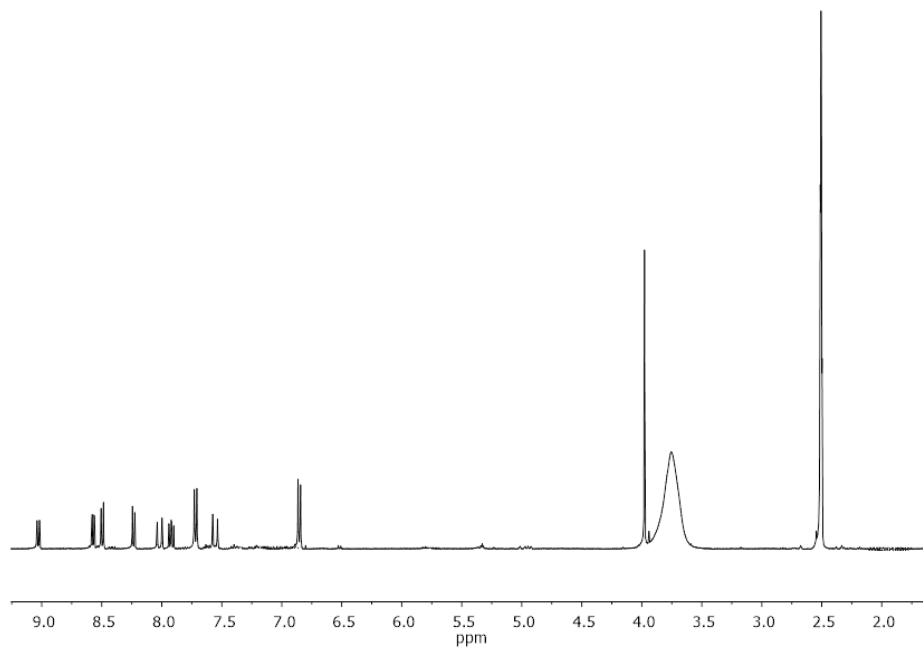


Figure S3. ^1H -NMR and ^{13}C -NMR of compound **3**.

E-2-(methoxyamine)-6-(4-hydroxystyryl)-1H-benzo[d]isoquinoline-1,3(2H)-dione (**Heck**): A mixture of compound **2** (1.1 g, 3.1 mmol), **3** (1.1 g, 3.6 mmol), Pd(AcO)₂ (0.035 g, 0.15 mmol) and P(o-tolyl)₃ (0.095 g, 0.312 mmol) were added into a two-neck round bottom flask. The system was purged with argon and the solids were dissolved in DMF (10 mL). After complete dissolution of the mixture, trimethylamine was added (2.17 g, 21.5 mmol). The mixture was heated at 90°C for 24 h. After this time, the reaction was poured into cold water (20 mL) and the solid was washed with water and dried under vacuum. The solid was dissolved in THF and tetra-n-butylammonium fluoride was added (1.30 g, 5 mmol) to the solution. The mixture was stirred overnight at room temperature. The solvent was removed under vacuum and a brown solid was obtained. The crude product was purified by column chromatography using silica gel (eluent: dichloromethane/methanol 50:1) to obtain a red solid, 0.63 g. Yield 62 %. ^1H NMR (400 MHz, DMSO) δ 9.02 (dd, J = 8.6, 0.8 Hz, 1H), 8.56 (dd, J = 7.3, 0.8 Hz, 1H), 8.49 (d, J = 7.9 Hz, 1H), 8.23 (d, J = 7.9 Hz, 1H), 8.01 (d, J = 16.1 Hz, 1H), 7.91 (dd, J = 8.6, 7.3 Hz, 1H), 7.71 (d, J = 8.6 Hz, 2H), 7.55 (d, J = 16.0 Hz, 1H), 6.85 (d, J = 8.6 Hz, 2H), 3.97 (s, 3H). ^{13}C NMR (101 MHz, DMSO) δ 160.23 (1C), 159.99 (1C), 158.49 (1C), 142.24 (1C), 135.69 (1C), 131.35 (1C), 131.01 (1C), 130.82 (1C), 129.29 (2C), 129.08 (1C), 127.73 (1C), 127.48 (1C), 126.88 (1C), 122.87 (1C), 122.82 (1C), 120.34(1C), 119.46 (1C), 115.67 (1C), 63.53 (1C). HRMS: Calculated for C₂₁H₁₅NO₄ (M⁺H⁺) 346.1079 m/z; measured 346.1063 m/z (M⁺H⁺).



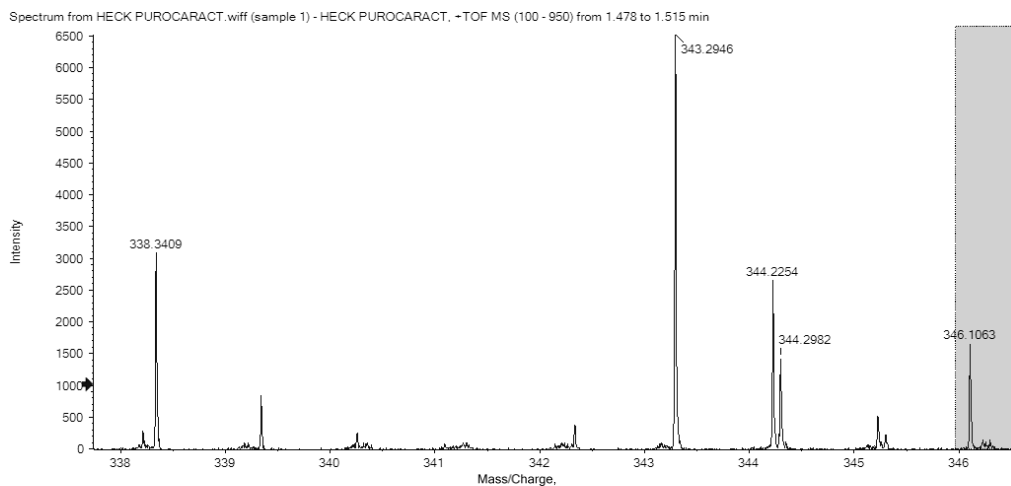
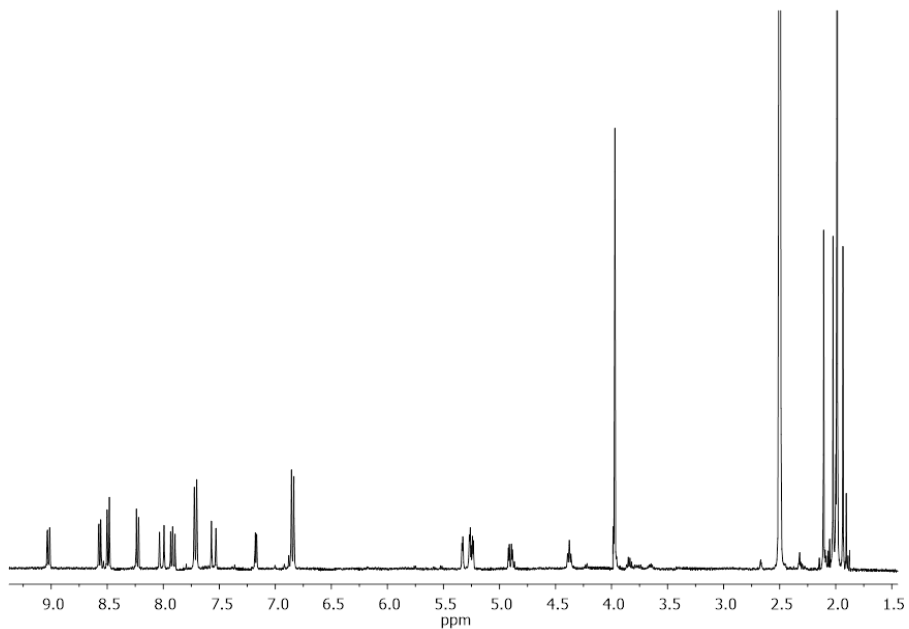
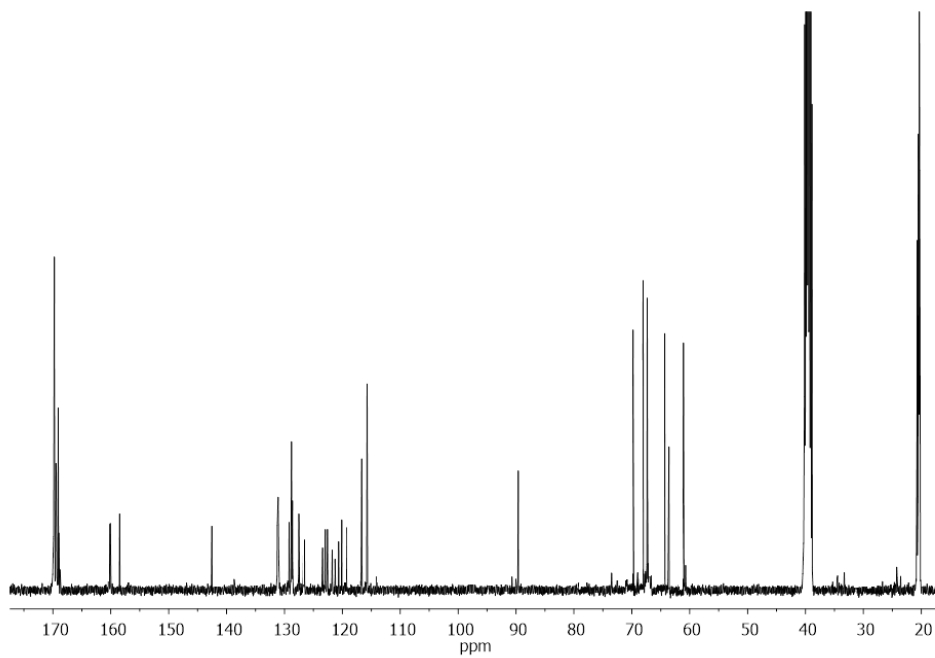


Figure S4. ^1H -NMR, ^{13}C -NMR and HRMS of Heck fluorophore.

E-2-(methoxyamine)-6-[4-(acetogalactoxy)styryl]-1H-benzo[de]isoquinoline-1,3(2H)-dione (**HeckGal**): A round bottom flask was charged with compound **Heck** (0.345 g, 1 mmol) and dissolved in methanol (10 mL). Then, NaOH (120 mg, 3 mmol) was added. The red color of the mixture changed to dark-red. The mixture was stirred for 1 h at room temperature. After complete reaction, the solvent was removed under vacuum pressure. Then, in a round bottom flask, acetobromo- α -D-galactose (822 mg, 2 mmol) and the solid obtained were mixed and the crude was purged with argon atmosphere. The mixture was dissolved in anhydrous acetonitrile. The reaction was stirred for 4 h at 70°C and then the solvent was removed under vacuum pressure. The crude product was purified by column chromatography using silica gel (eluent: hexane/ethyl acetate 2:1) to obtain a red-orange solid 0.405 g. Yield 60 %. ^1H NMR (400 MHz, DMSO) δ 9.02 (dd, J = 8.6, 0.8 Hz, 1H), 8.57 (dd, J = 7.3, 0.8 Hz, 1H), 8.49 (d, J = 8.0 Hz, 1H), 8.23 (d, J = 8.0 Hz, 1H), 8.01 (d, J = 16.1 Hz, 1H), 7.91 (dd, J = 8.6, 7.3 Hz, 1H), 7.71 (d, J = 8.6 Hz, 2H), 7.55 (d, J = 16.1 Hz, 1H), 7.17 (d, J = 3.5 Hz, 1H), 6.85 (d, J = 8.6 Hz, 2H), 5.33 (dd, J = 1.1, 3.4 Hz, 1H), 5.28 – 5.19 (m, 2H), 4.90 (dd, J = 10.7, 3.5 Hz, 1H), 4.38 (t, J = 5.9 Hz, 2H), 3.97 (s, 3H), 2.14 – 1.90 (m, 12H). ^{13}C NMR (101 MHz, DMSO) δ 169.86 (1C), 169.80 (1C), 169.75 (1C), 169.09 (1C), 160.31 (1C), 160.09 (1C), 158.47 (1C), 142.55 (1C), 131.09 (1C), 129.20 (1C), 128.79 (1C), 128.62 (1C), 127.51 (1C), 126.54 (1C), 123.42 (1C), 122.95 (1C), 122.57 (1C), 121.76 (1C), 121.26 (1C), 120.64 (1C), 120.10 (1C), 119.33 (1C), 116.66 (1C), 115.73 (1C), 91.67 (1C), 69.79

(1C), 68.06(1C), 67.35 (1C), 64.32 (1C), 63.61 (1C), 61.08 (1C), 20.51 (1C), 20.42 (1C), 20.35 (1C), 20.29 (1C). HRMS: Calculated for $C_{35}H_{34}NO_{13}$ (M^+H^+) 676.2030 m/z; measured 676.2013 m/z (M^+H^+). Calculated for (M^+K^+) 714.1589; measured 714.1573 m/z (M^+K^+).





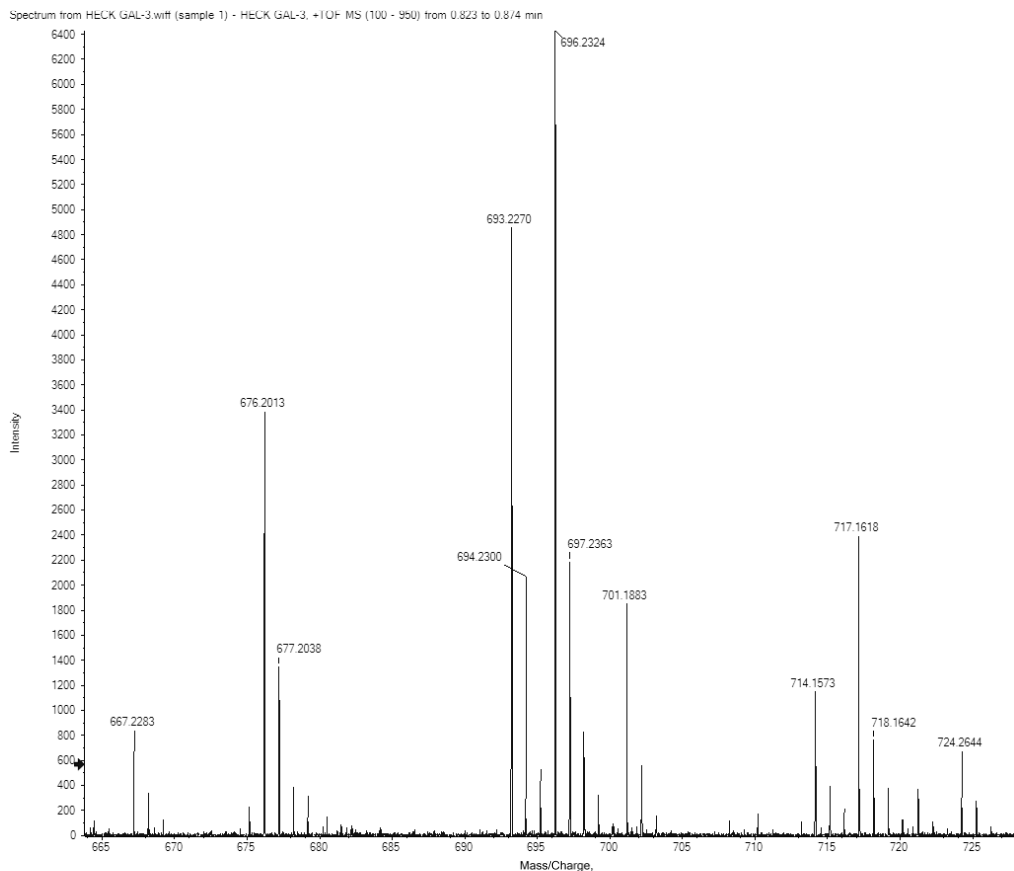


Figure S5. $^1\text{H-NMR}$, $^{13}\text{C-NMR}$ and HRMS of HeckGal fluorophore.

4.10.3 Heck fluorescence emission not depends on pH

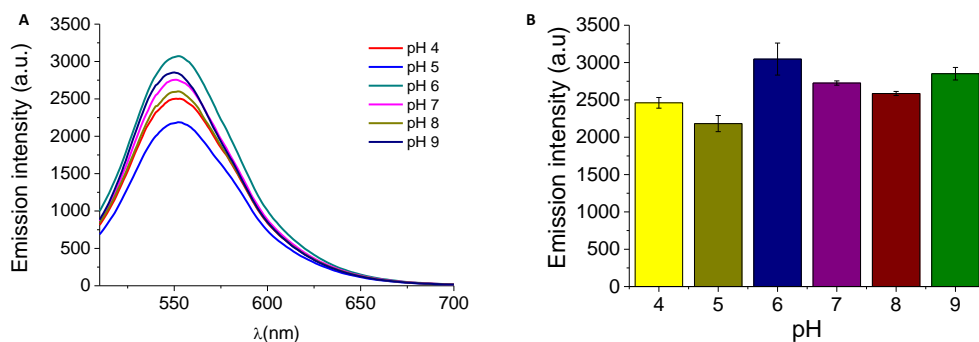


Figure S6. (A) Fluorescence spectra ($\lambda_{\text{ex}} = 488 \text{ nm}$) of Heck (10^{-5} M) $\text{H}_2\text{O-DMSO}$ (0.01%) at pH 4, 5, 6, 7, 8 and 9. (B) Emission intensity at 552 nm ($\lambda_{\text{ex}} = 488 \text{ nm}$) of Heck (10^{-5} M) $\text{H}_2\text{O-DMSO}$ (0.01%) solutions at pH 4, 5, 6, 7, 8 and 9. Error bars represent SD ($n=3$)

4.10.4 Hydrolysis reaction of Heck-Gal into Heck fluorophore

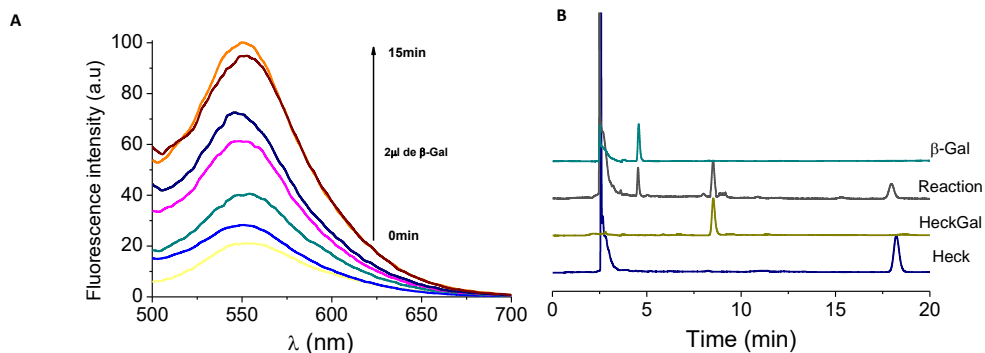


Figure S7. (A) Time dependence of fluorescence emission of **HeckGal** (yellow) aqueous solutions (pH 7)-DMSO (0.01%) in the presence of human β -Gal ($\lambda_{\text{ex}} = 488 \text{ nm}$). The enhancement of emission band is ascribed to the conversion of **HeckGal** into **Heck** fluorophore (orange). (B) HPLC-UV studies of **HeckGal** aqueous solutions (pH 7)-DMSO (0.01%) hydrolysis in presence of human β -Gal.

4.10.5 Heck and HeckGal quantum yield measurements

Quantum yield values were measured with respect to rhodamine 6G as standard ($\Phi = 0.95$) using the equation:

$$\frac{\Phi_x}{\Phi_s} = \frac{S_x}{S_s} \times \frac{1 - 10^{-A_s}}{1 - 10^{-A_x}} \times \frac{n_x^2}{n_s^2}$$

where x and s indicate the unknown and standard solution, respectively, Φ is the quantum yield, S is the area under the emission curve, A is the absorbance at the excitation wavelength and n is the index of refraction.

4.10.6 *In vitro* viability assays

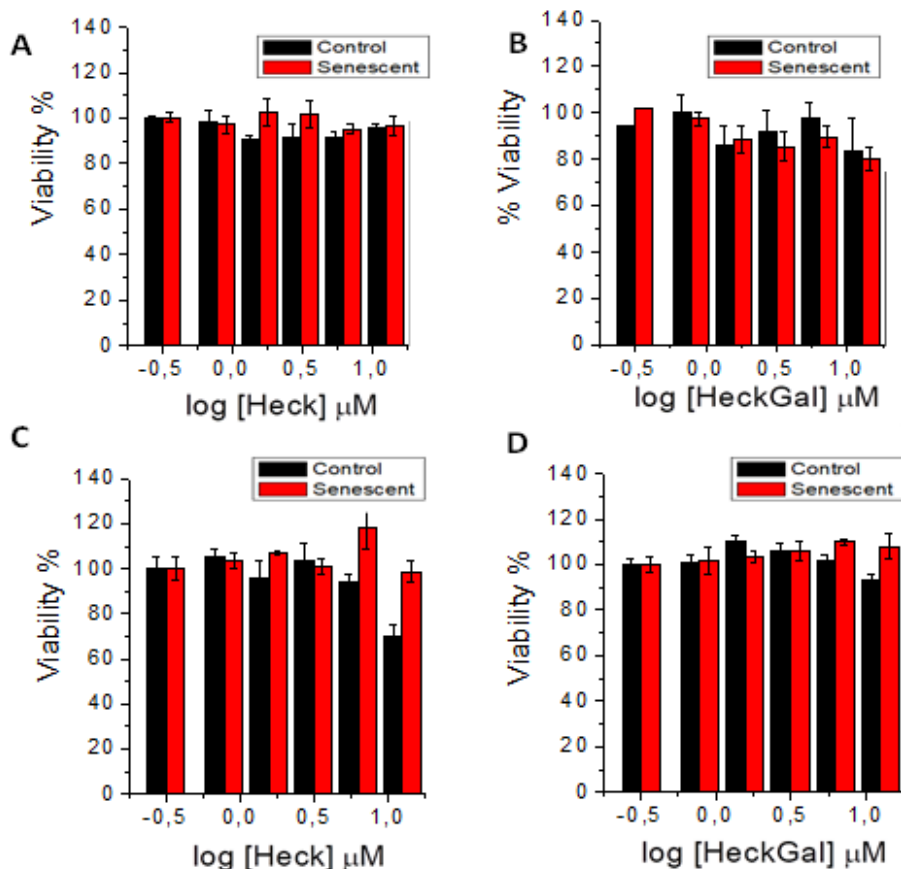


Figure S8. Relative *in vitro* viability in cultured cells. (A) Control (black) and senescent (red) SK-Mel-103 cells after incubation with **Heck** for 48 h at different concentrations. (B) Control (black) and senescent (red) SK-Mel-103 cells after incubation with **HeckGal** for 48 h at different concentrations. (C) Control (black) and senescent (red) 4T1 cells after incubation with **Heck** for 48 h at different concentrations. (D) Control (black) and senescent (red) 4T1 cells after incubation with **HeckGal** for 48 h at different concentrations. Note: both **HeckGal** and **Heck** have minimal toxicity and superior biocompatibility toward cultured cell line until 25 μM .

4.10.7 Emission spectrum of Heck after two-photon excitation

Fluorescence spectrum obtained from bright images of SK-Mel-103 cells treated with Palbociclib incubated with 10 μ M of **HeckGal** was measured with confocal microscope (OLYMPUS FV1000MPE) after two-photon confocal excitation. The obtained fluorescence spectrum corresponds to fluorescence spectrum of **Heck** fluorophore obtained in a two-photon fluorescence spectrophotometer.

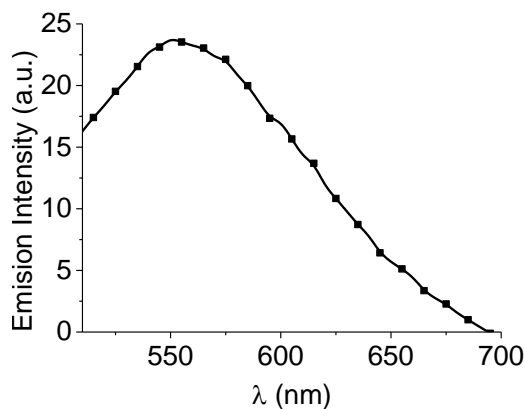


Figure S9. Fluorescence spectrum of **Heck** after confocal two-photon excitation.

4.10.8 Co-staining does not affect to Heck signal

In order to demonstrate that other typical staining kits do not affect to Heck fluorescence signal and the hydrolysis of **HeckGal**, confocal images from co-stained SK-Mel-103 with **HeckGal** (10 μ M) and Wheat Germ Agglutinin (WGA) stain (1 μ g/ml).

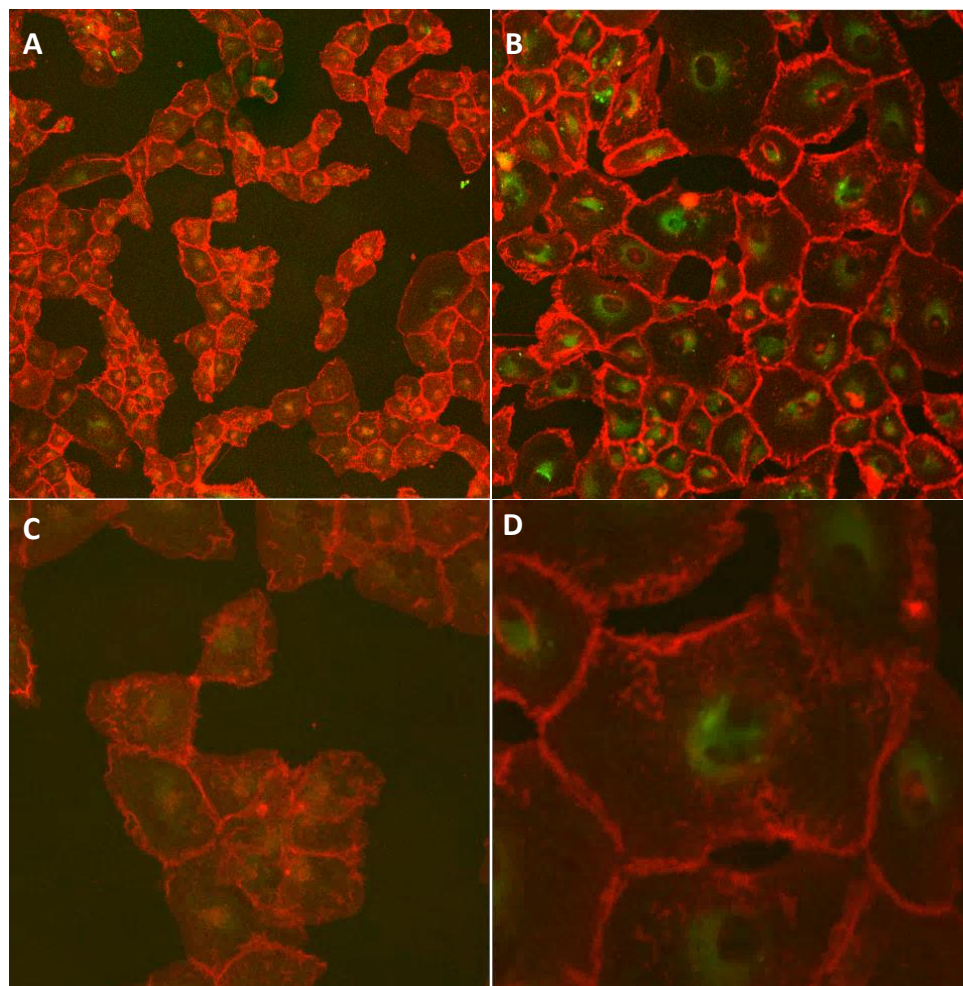


Figure S10. One photon confocal images of control SK-Mel-103 (A,C) in presence of 10 μ M of **HeckGal** probe and Wheat Germ Agglutinin (WGA) stain (1 μ g/ml) (Objectives: 20x a, 63x c) and SK-Mel-103 treated with palbociclib (B,D) in presence of 10 μ M of **HeckGal** probe (Objectives: 20x b, 63x d).

**Chapter 5 | A renal clearable
fluorogenic probe for in vivo
detection of cellular senescence**

A renal clearable fluorogenic probe for in vivo detection of cellular senescence

B. Lozano-Torres,^{a,b,c,d} A. García-Fernández,^{a,b,c,d} I. Galiana,^{a,b,d} S. Rojas-Vázquez,^{a,e} I. Fariñas,^{e,f,g} M. Orzáez,^{b,h} F. Sancenón,^{a,b,c,d} J. F. Blandez,^{a,b,d} and R. Martínez-Máñez,^{a,b,c,d*}

^a Instituto Interuniversitario de Investigación de Reconocimiento Molecular y Desarrollo Tecnológico (IDM), Universitat Politècnica de València, Universitat de València. Camino de Vera s/n, 46022-Valencia, Spain. E-mail: rmaez@qim.upv.es

^b Unidad Mixta UPV-CIPF de Investigación en Mecanismos de Enfermedades y Nanomedicina, Universitat Politècnica de València, Centro de Investigación Príncipe Felipe, Valencia, Spain.

^c CIBER de Bioingeniería, Biomateriales y Nanomedicina (CIBER-BBN).

^d Unidad Mixta de Investigación en Nanomedicina y Sensores. Universitat Politècnica de València, IIS La Fe, Valencia, Spain.

^e Departamento de Biología Celular, Biología Funcional y Antropología Física, Universitat de València, Spain

^f Estructura de Recerca Interdisciplinar en Biotecnologia i Biomedicina (ERI BIOTECMED), Universidad de Valencia, Spain

^g Centro de Investigación Biomédica en Red de Enfermedades Neurodegenerativas (CIBERNED)

^h Centro de Investigación Príncipe Felipe, Valencia, Spain

*Correspondence: rmaez@qim.upv.es

Submitted

5.1 Abstract

There is a growing need for non-invasive, cheap, and versatile diagnostic methods and the development of low-cost point-of-care assays constitutes a potential solution. Here, we describe the design of a renal clearable fluorogenic probe (**Cy7Gal**) which produces a fluorogenic signal readable in the urine. The **Cy7Gal** probe is applied to the detection of the burden of senescence in several *in vivo* models. The probe is composed of a dye (**Cy7**) conjugated with a galactose derivative. Upon administration of the probe *in vivo*, the up-regulated β -galactosidase enzyme in senescent cells cleaves the O-glycosidic bond in **Cy7Gal**, releasing the highly emissive **Cy7** dye that is renally cleared and measured in unmodified urine by an IVIS imaging system or by a fluorimeter. A good correlation between the burden of senescence and emission in urine is observed. **Cy7Gal** probe is the first example for the fluorogenic *in vivo* detection of senescence in urine and may serve as a basis for the development of generalized fluorogenic diagnostic platforms for the easy diagnosis in the urine of different diseases as well as for monitoring therapeutic treatments without the use of expensive equipment or trained personnel.

5.2 Introduction

The design and development of new cost-effective and of easy implementation diagnostic tools is an important goal in health.¹⁻⁴ However, diagnosis of many diseases in remote or less developed countries or resource-limited settings is difficult as in many cases it is necessary the use of costly imaging techniques, well-equipped laboratories, and trained personnel.⁵⁻⁷ The design of low-cost easy-to-use diagnostic systems, able to detect target biomarkers from readily accessible bio-fluids, constitutes a potential solution.⁸ An approach that fulfils these

characteristics is the design of probes able to be transformed by the action of certain biomarkers in cells and tissues and have a rapid renal clearance thus allowing detection in the urine. Based on this concept of renal clearable probes, some very few reports describe the use of multiplexed protease-responsive nanoparticles that release small reporter probes into the urine in response to proteolytic cleavage in disease environments.^{5,9,10} In such systems, the reporters are finally detected in urine by mass spectrometry or immunoassays. This approach has also recently been elegantly exploited to detect acute kidney injury (AKI) with fluorescent and chemiluminescent derivatives equipped with the (2-hydroxypropyl)- β -cyclodextrin (HP β CD) moiety that allowed a renal clearance of the probes.^{11,12} A more recent example describes a nanosensor based on ultra-small renally removable nanoparticles able to recognize deregulated protease in cells. In this case, a colorimetric signal is indirectly detected by measuring the ability of excreted nanoparticles in urine to oxidize a chromogenic peroxidase substrate in the presence of hydrogen peroxide.¹³ However, some of these systems still rely on the use of complex techniques, expensive analytical assays, or use nanoparticles which could result in undesired accumulation or side effects.¹⁴ In this scenario, the design of probes able to be transformed by the action of certain biomarkers in tissues and have a rapid renal clearance allowing its detection is appealing. In this approach, the dye or fluorophore, in an OFF state, is for instance hydrolysed in the presence of a certain deregulated enzyme at the site of the disease, turning ON the fluorescence of the dye that is renally cleared allowing its detection in the urine. The rapid optical readout of diseases through a simple urine measurement after injection of the probe in the patient can revolutionize the field of biosensors and it represents an attractive new diagnostic alternative to other procedures. However, such a simple idea has not been widely developed. Exploring this paradigm, and as a proof of concept, we report herein the preparation of a cyanine-7-based dye (**Cy7Gal**) for the in vivo detection of

cellular senescence in the urine. Cellular senescence is a stress response mechanism characterized by cell cycle/proliferation arrest and complex changes in morphology, chromatin organization, secretome, and overexpression of lysosomal β -galactosidase, also referred to as senescence-associated β -galactosidase (SA- β -Gal).¹⁵⁻¹⁷ Cellular senescence is one hallmark of aging and it has been reported that quantification of the global burden of senescence across tissues can be informative toward assessing biological aging.¹⁸ Moreover, there is clear evidence that the accumulation of senescent cells is involved in the pathophysiology of many aging related diseases.¹⁹⁻²² However, although the quantification of senescence in biopsies from different human tissues is an active area of research, there are not simple non-invasive procedures to monitor cellular senescence *in vivo*.^{15,23} The probe we develop here (**Cy7Gal**) is used to detect SA- β -Gal activity in senescent cells. SA- β -Gal hydrolyses in cells the poorly-emissive **Cy7Gal** into the highly fluorescent dye **Cy7**.²⁴ Moreover, **Cy7** is quickly renally cleared allowing its detection and measurement in urine (Figure 1b). We validate the procedure *in vivo* by monitoring chemotherapy-induced cellular senescence in breast tumour syngeneic model in BALB/cByJ mice and physiological senescence in aged mice.

5.3 Results and discussion

5.3.1 Synthesis, spectroscopic characterization, and mechanism studies.

The **Cy7Gal** probe was prepared following a two-step synthetic procedure shown in Figure 1a. First, 2,3,4,6-tetra-O-acetyl- α -D-galactopyranosyl bromide was reacted with 4-hydroxyisophthalaldehyde in anhydrous acetonitrile yielding compound **1**. Then, a Knoevenagel condensation between **1** and 2,3,3-trimethyl-1-(4-sulfobutyl)indolium (**2**) yielded the **Cy7Gal** probe. Besides, the **Cy7** fluorophore was synthesized by protecting the hydroxyl group of 4-hydroxyisophthalaldehyde

with *t*-butyldimethylsilyl chloride followed by a Knoevenagel condensation with **2** and the subsequent deprotection of the hydroxyl group (Supplementary Information, Scheme S1). **Cy7Gal** and **Cy7** were fully characterized by ¹H-NMR, ¹³C-NMR, and HRMS (see Supplementary Information). PBS (pH 7) solutions of **Cy7** (1.0×10^{-5} M) show an intense broad emission band centered at ca. 660 nm ($\Phi_{\text{Cy7}} = 0.43$) when excited at 580 nm (Figure 1c), whereas as a clear contrast, PBS (pH 7) solutions of **Cy7Gal** are poorly fluorescent at the same excitation wavelength ($\Phi_{\text{Cy7Gal}} = 0.0062$) (Figure 1c). Besides, the emission intensity of **Cy7** fluorophore and **Cy7Gal** remains unchanged in the 5-10 pH range (Supplementary Information, Figure S1). The hydrolysis of **Cy7Gal** in PBS (pH 7) solutions in the presence of the β -galactosidase enzyme was studied by HPLC (Supplementary Information, Figure S2a). The obtained chromatograms show the progressive disappearance of the **Cy7Gal** peak with the subsequent appearance of **Cy7** signal in the presence of the enzyme, whereas **Cy7Gal** remains stable in PBS in the absence of β -galactosidase. Moreover, specificity and selectivity of the probe to β -galactosidase was demonstrated after incubation of **Cy7Gal** with different interfering species such as cations, anions, small peptides and enzymes (Supplementary Information, Figure S2b) for 0.5 h. Of all the species tested, only β -galactosidase induced a marked emission enhancement at ca. 660 nm due to the hydrolysis of **Cy7Gal** which generates the **Cy7** fluorophore. Besides, a more marked emission enhancement was observed when **Cy7Gal** was incubated in the presence of both esterase and β -galactosidase enzymes. This greater enhancement, when compared to that observed when only β -galactosidase was present, is ascribed to the hydrolysis of the acetate moieties in **Cy7Gal** by esterase and then to the rupture of the O-glycosidic bond by β -galactosidase yielding free **Cy7**.

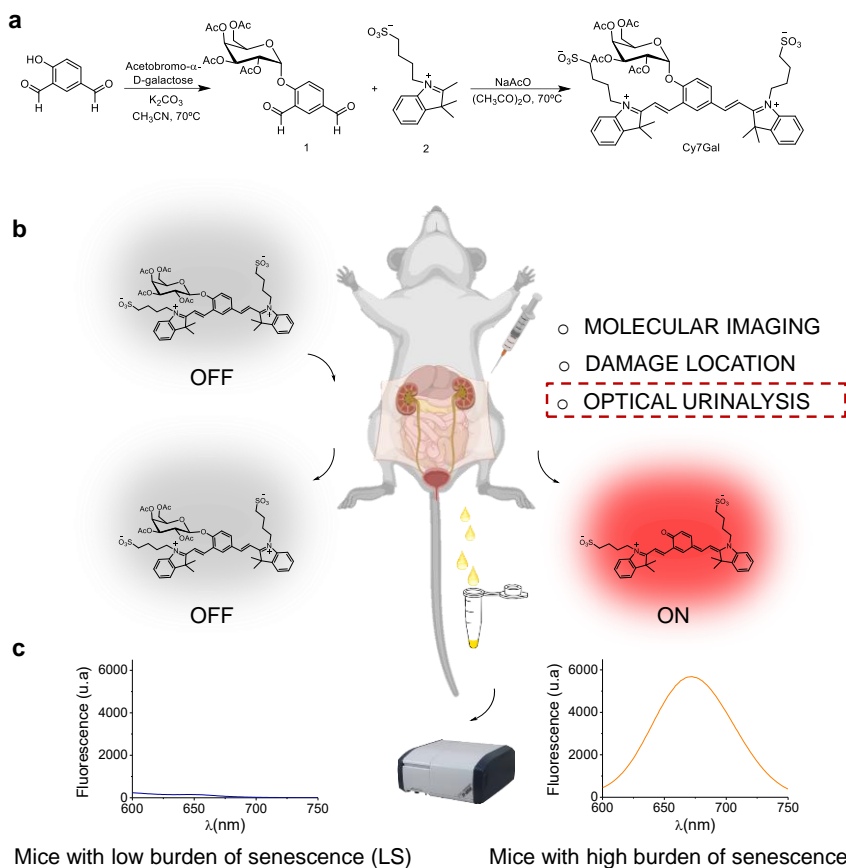


Figure 1. Design and synthesis of the diuretic probe, mechanism of action in mice, and optical features. (a) Synthetic route used for the preparation of **Cy7Gal** probe. (b) Schematic representation of the application of **Cy7Gal** in an *in vivo* model of senescence. **Cy7Gal** probe is administered to mice, hydrolysed into **Cy7** fluorophore by SA-β-Gal, and excreted through urine. Fluorescence of urine is directly measured in a fluorimeter. (c) Fluorescence emission spectra ($\lambda_{exc} = 580$ nm) of **Cy7Gal** (left) and **Cy7** fluorophore (right) in aqueous solutions at pH 7.

5.3.2 Cy7Gal monitors senescence induction in mouse mammary tumour cells *in vitro*.

In order to validate the ability of **Cy7Gal** to monitor senescence induction in cells, we used the 4T1 mouse mammary tumour cell line, which is considered a murine model of triple negative-breast cancer cells.^{25,26} Cells were treated with palbociclib (5 μ M) for two weeks. Palbociclib is a CDK4/6 inhibitor which has been reported to induce cell cycle arrest and senescence in 4T1 cells.²⁷ Cellular senescence

induction was corroborated by the increase in SA- β -Gal activity assay using the X-Gal test (Figure 2a and 2d). Besides, western blot experiments demonstrated the overexpression of β -galactosidase in 4T1 senescent cells (Supplementary Information, Figure S3a). Treatment with palbociclib was also accompanied by an increase in cell size and in the number of intracellular vesicles, in agreement to morphological features described for senescent phenotypes.²⁸ Subsequently, 4T1 control and senescent cells were treated with **Cy7Gal** (20 μ M) and analyzed by confocal microscopy 2 h post-treatment. Both control (Figure 2b) and palbociclib treated 4T1 cells (Figure 2e) did not exhibit any noticeable fluorescence signal in the absence of the probe when excited at 580 nm. Similarly, control non-senescent 4T1 cells displayed poor fluorescence emission after exposure to 20 μ M of **Cy7Gal** (Figure 2c). In contrast, senescent 4T1 cells treated with **Cy7Gal** showed intense red emission (Figure 2f) which is attributed to the hydrolysis of **Cy7Gal** into **Cy7** by increased SA- β -Gal activity in senescent cells. Quantification of the fluorescence signal associated with **Cy7** from confocal images was determined for all treatments. A significant increase in the fluorescence signal (ca. 3.2 fold) was observed in palbociclib-treated 4T1 cells treated with **Cy7Gal** when compared with control 4T1 cells (Figure 2m).

To further confirm the β -galactosidase-catalysed cleavage of **Cy7Gal**, we found (Figure 2g-2l) that a marked reduction in the emission intensity (ca. 60%) was obtained after pre-incubation of senescent 4T1 cells with D-galactose (a specific inhibitor of β -galactosidase, 5 mM) for 0.5 h and then treated with **Cy7Gal**, when compared to senescent cells administered only with the probe. Besides, the response of **Cy7Gal** probe was demonstrated to be dependent on the increased lysosomal β -galactosidase activity in senescent cells. For this purpose, two siRNAs were used to knock-down the expression of GLB1,¹⁹ the gene that encodes lysosomal β -galactosidase in 4T1 cells. As shown in the Supplementary Information (Figure S3b), hs.Ri.GLB1.13.3 siRNA efficiently downregulated the

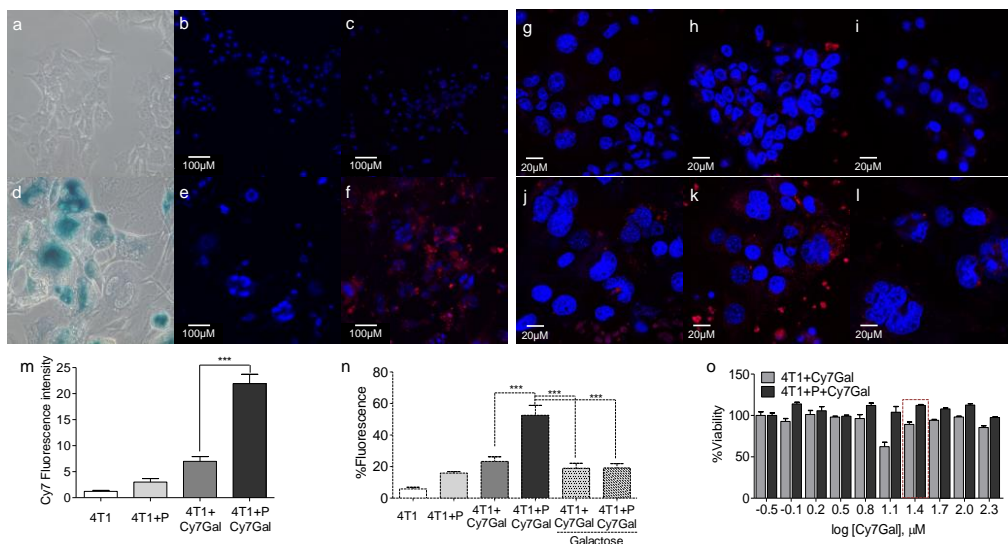


Figure 2. Cy7Gal monitors senescence induction in breast cancer cells. (a,d) Typical X-Gal assay for SA- β -Gal activity in control 4T1 (a) and 4T1 cells treated with palbociclib (d). Senescent 4T1 cells present the typical blue staining. (b-f) Confocal images of control 4T1 (b,c) and 4T1 treated with palbociclib (e,f) in the absence (b,e) or in presence of 20 μ M of **Cy7Gal** probe (c,f). Cells were seeded in a clear flat bottom 96-well plate and after 24 h incubated with **Cy7Gal** in DMEM (10% FBS, 0.1% DMSO) in 20% O₂ and 5% CO₂ at 37 °C for 2 h; next, cellular nuclei were stained with Hoechst 33342 and then fluorescence images were acquired by using a confocal microscope (Leica TCS SP8 AOBS). Representative images from repeated experiments (n = 3) are shown. (g-l) Confocal images of control 4T1 (g-i) and 4T1 cells treated with palbociclib (j-l) in the absence (g,j), in the presence of 20 μ M of **Cy7Gal** probe (h,k), and pre-treated with D-galactose (a specific inhibitor of β -galactosidase) and then with 20 μ M of **Cy7Gal** probe (i,l). Cells were seeded in a clear glass 6-well plate and, after 24 h, cells were pre-incubated or not with D-galactose for 30 min and treated with **Cy7Gal** in DMEM (10% FBS, 0.1% DMSO) in 20% O₂ and 5% CO₂ at 37 °C for 2 h, next, cellular nucleus were stained with Hoechst 33342, finally confocal images were acquired by using a confocal microscope (Leica TCS SP8 AOBS). Representative images from repeated experiments (n = 3) are shown. (m) Quantification of the fluorescence emission intensity from (b-f) confocal images. Error bars represent SEM. (n) Quantification of the fluorescence emission intensity from (g-l) confocal images. Error bars represent SEM. (o) Relative *in vitro* viability in cultured cells treated with serial concentrations of **Cy7Gal** probe after 48 h. Note that the red dotted box corresponds to 25 μ M.

transcription of GLB1 at 48 h post-transfection and resulted in a significantly decreased number of SA- β -Gal-positive cells, when compared to a scrambled siRNA. Confocal microscopy images of control and senescent 4T1 treated with **Cy7Gal** showed a marked decrease in the emission in the red channel (ca. 54 %, Supplementary Information, Figure S3d) for cells transfected with hs.Ri.GLB1.13.3

siRNA, when compared to non-transfected cells or cells transfected with scrambled siRNA (Supplementary Information, Figure S3c). Finally, viability assays indicated that the probe was innocuous for both normal and senescent cells (Figure 2o). Thus, **Cy7Gal** is an appropriate probe to monitor senescence induction in cell cultures.

5.3.3 Renal clearance of Cy7 fluorophore allows cell senescence burden evaluation *in vivo* in a 4T1 breast cancer model treated with senescence-inducing chemotherapy

Once assessed the activation of **Cy7Gal** in 4T1 senescent cells, the probe was validated in a chemotherapy-induced senescence triple-negative breast cancer mouse model. For tumour generation, 4T1 cells were injected subcutaneously into the left mammary fat pad of young female BALB/cByJ mice. Mice were subsequently treated for 7 days with palbociclib at concentrations of 10 mg/Kg, 50 mg/Kg or 100 mg/Kg by daily oral gavage in order to induce different degrees of senescence burden in the tumours. Tumour volume was measured every two days with a calliper. Figure 3a shows that tumours from mice treated with 10 mg/Kg of palbociclib grew similarly to the untreated ones, while tumours from mice treated with 50 and 100 mg/Kg of palbociclib displayed a reduction in their size. Immunohistochemical staining of the proliferation biomarker Ki67 in autopsy samples revealed that samples from mice treated with 50 or 100 mg/Kg of palbociclib exhibited a significantly lower proportion of Ki67 positive nuclei than those from untreated mice or mice treated with the lowest palbociclib dose (Figures 3b and 3c). Moreover, X-Gal staining in cryosections of mice treated or not with palbociclib revealed the specific induction of senescence (SA- β -Gal activity) in the tumours but not in organs, such as liver or kidney (Supplementary Information, Figure S4). This is indicative of an enhancement in cellular senescence in tumours when palbociclib treatment increases.²⁹

In order to test the ability of probe **Cy7Gal** for cellular senescence detection *in vivo*, BALB/cByJ mice bearing 4T1 tumours and treated with palbociclib at different concentrations (i.e. 10 to 50 and 100 mg/Kg) were anesthetized and the **Cy7Gal** probe was intraperitoneally (i.p.) administered (2.5 μ mol). *Ex vivo* studies demonstrated that the **Cy7Gal** probe allows to detect cellular senescence in palbociclib treated tumours. In fact, *ex vivo* IVIS images from mice treated with **Cy7Gal** revealed a strong fluorescence signal in tumours from mice administered with 100 mg/Kg of palbociclib, while the fluorescent signal decreases as a function of the reduction in palbociclib dose (Figure 3f). In addition, no significant fluorescent signal in the liver, lungs, heart, spleen, or kidney from mice injected with **Cy7Gal** was found and no auto-fluorescence was observed for palbociclib treated mice at 100 mg/Kg dose in any organ (Figure 3g).

Interestingly, fluorescence analysis *in vivo* using an IVIS[®] spectrum 15 min after **Cy7Gal** administration, clearly showed fluorescence accumulation in the bladder suggesting a rapid renal clearance of the **Cy7** fluorophore (Supplementary Information, Figure S5). Urine was, therefore, collected after mice recovered from anesthesia and analyzed by IVIS. The emission in urine was higher in mice treated with increasing amounts of palbociclib (Figure 3d). The emission of **Cy7** in the urine was also measured in a fluorimeter and the amount of the fluorophore determined from a calibration curve indicating a correlation between palbociclib doses and μ moles of **Cy7** in urine (Figure 3e).

To further study the renal clearance of the **Cy7Gal** probe, we synthesized and characterize (Supplementary Information, Scheme 2) an analogous molecule lacking the sulfonic groups (**WOS-Cy7Gal**) that make the **Cy7Gal** a more hydrophobic dye disfavoring its accumulation in bladder.³⁰

In a comparative experiment **Cy7Gal** or **WOS-Cy7Gal** were i.p. administered (2.5 μ mol) to BALB/cByJ mice bearing 4T1 tumours induced by palbociclib (100 mg/Kg). Both probes gave a strong positive signal in the tumours and,

interestingly, we detected signal accumulated in the bladder, but not the kidney of animals injected with the **Cy7Gal**, but not the **WOS-Cy7Gal** probe (Supplementary Information, Figures S6a and S6b). The concentrations of **Cy7** and **WOS-Cy7** fluorophores were measured in plasma and in the excreted urine. In agreement with a renal clearance of the **Cy7** fluorophore, we found a detectable concentration in the urine (2.34 μmol) while the plasma concentration was significantly lower (0.33 μmol) (Supplementary Information, Figure S6c). In contrast, concentrations of **WOS-Cy7** fluorophore were basically undetectable in plasma (0.02 μmol) and urine (0.01 μmol). These results were also corroborated by measuring the average radiance intensity of **Cy7** and **WOS-Cy7** in urine (Supplementary Information, Figure S6d) and indicate the crucial role of the sulfonic acid moieties in the renal clearance of the **Cy7** fluorophore.

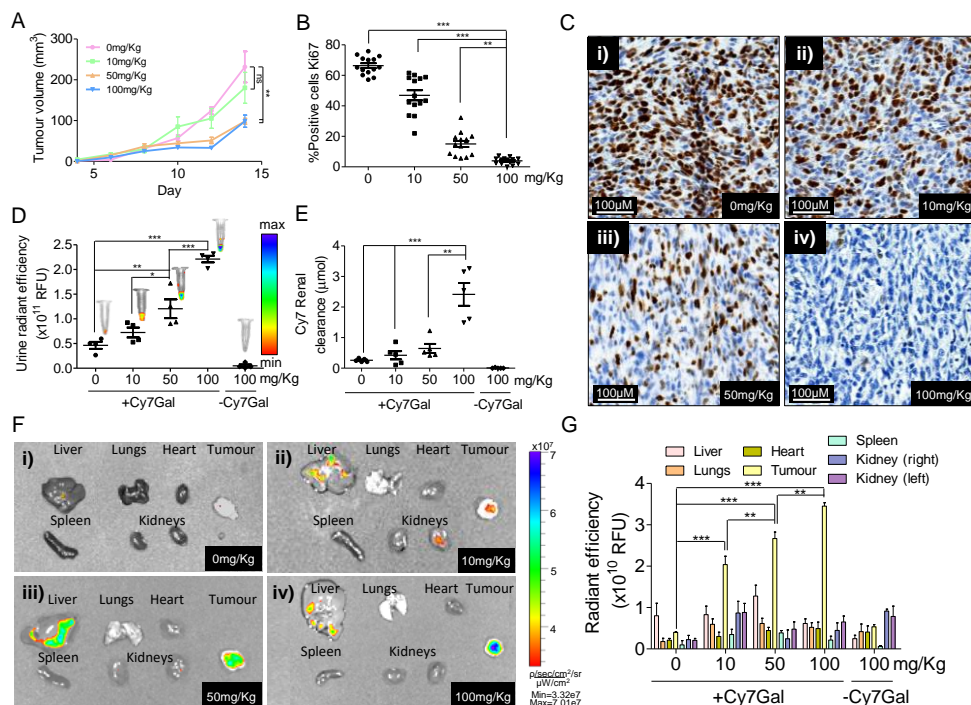


Figure 3. Renal clearance of **Cy7** fluorophore correlates with chemotherapy-induced senescence *in vivo* in a 4T1 breast cancer model. (A) BALB/cByJ female mice carrying orthotopic 4T1 mammary tumours were treated daily with different doses of palbociclib (oral gavage, 10, 50 or 100 mg/Kg). For each tumour, the relative volume change was calculated as $V = (a \times b^2)/2$ where *a* is the longest and *b* is the shortest of two perpendicular diameters. Values are expressed as mean \pm SEM. (B) Quantification of immunohistochemical detection of Ki67 in paraffin sections of tumours as a measurement of the burden of cellular senescence. The number of Ki67 positive cells decreases as the dose of palbociclib increases. (C) Images of immunohistochemical detection of Ki67 in paraffin sections of tumours. From left to right and from top to bottom: (i) Control, (ii) palbociclib 10 mg/Kg, (iii) palbociclib 50 mg/Kg, (iv) palbociclib 100 mg/Kg. Ki67, which is indicative of proliferation of the cells, decreases as a function of the appearance of senescent cells in tumours. (D) Average radiance intensity from urine ascribed to the renal clearance of **Cy7** fluorophore in mice treated with different doses of palbociclib (oral gavage, 10, 50 or 100 mg/Kg) and intraperitoneally administered with **Cy7Gal** (23.3 mg/ml, 100 μ l). Values are expressed as mean \pm SEM. (E) Amount (μ moles) of **Cy7** excreted through urine in mice treated with different doses of palbociclib (oral gavage, 10, 50 or 100 mg/Kg). Values are expressed as mean \pm SEM. (F) IVIS images of organs (From left to right and from up to bottom: liver, lungs, heart, spleen, left kidney right kidney) and tumours from BALB/cByJ female mice bearing 4T1 breast cancer cells (i) control, (ii) palbociclib 10 mg/Kg, (iii) palbociclib 50 mg/Kg, (iv) palbociclib 100 mg/Kg injected with **Cy7Gal** probe (23.3 mg/ml, 100 μ l (2.5 μ mol) per mouse). Mice were sacrificed 20 min post-treatment. (G) Quantification of average radiance intensity from organs and tumours showed in f images. Values are expressed as mean \pm SEM.

5.3.4 *In vivo* cell senescence burden evaluation in naturally aged BALB/cByJ mice

Aging is a universal physiological state with a progressive functional decline, which is accompanied by the development of age-related diseases.³¹ Senescence has been associated with age-dependent organismal changes, and the progressive increase of senescent cells with time is known to contribute to the functional impairment of different organs.³² In fact, strong correlations have been reported between aging and certain phenotypes such as mitochondria dysfunction,³³ epigenetic changes,³⁴ and an increase in cellular senescence.³⁵ In this scenario, tools to measuring easily the pace of aging are of interest.³⁶ Regarding this matter, we tested the ability of probe **Cy7Gal** to evaluate the burden of senescence in healthy old and young individuals. For this purpose, 2 and 14 months old BALB/cJyB mice were i.p. injected with the **Cy7Gal** probe. IVIS images of the anesthetized mice 15 min post **Cy7Gal** injection revealed fluorescence accumulation in the bladder of 14 months old mice (Supplementary Information, Figure S7). Urine collected in an Eppendorf tube after recovery from anesthesia was analyzed by IVIS (Figure 4a). A stronger fluorescent signal (ca. 5.4 fold) in urine from old mice treated with **Cy7Gal** was observed when compared with the fluorescence in the urine of young mice also administered with the probe. The amount in μmol of **Cy7** in the urine was also calculated and a significantly large amount of **Cy7** in urine (8.1 fold) from old animals was found compared with young individuals (Figure 4b). Moreover, 2 and 14 months old control mice not treated with **Cy7Gal** showed negligible fluorescence in urine (Figure 4a and 4b). A simple mass balance of the amount of **Cy7Gal** injected and that of **Cy7** in urine allows calculating that, on average, 49% of injected **Cy7Gal** was excreted in urine as **Cy7** in old mice whereas for young mice this was only 6.1% (Figure 4b). These differences are in agreement with a larger burden of cellular senescence in old animals.³⁷ Then, mice were sacrificed and the bladder, brain and lungs were

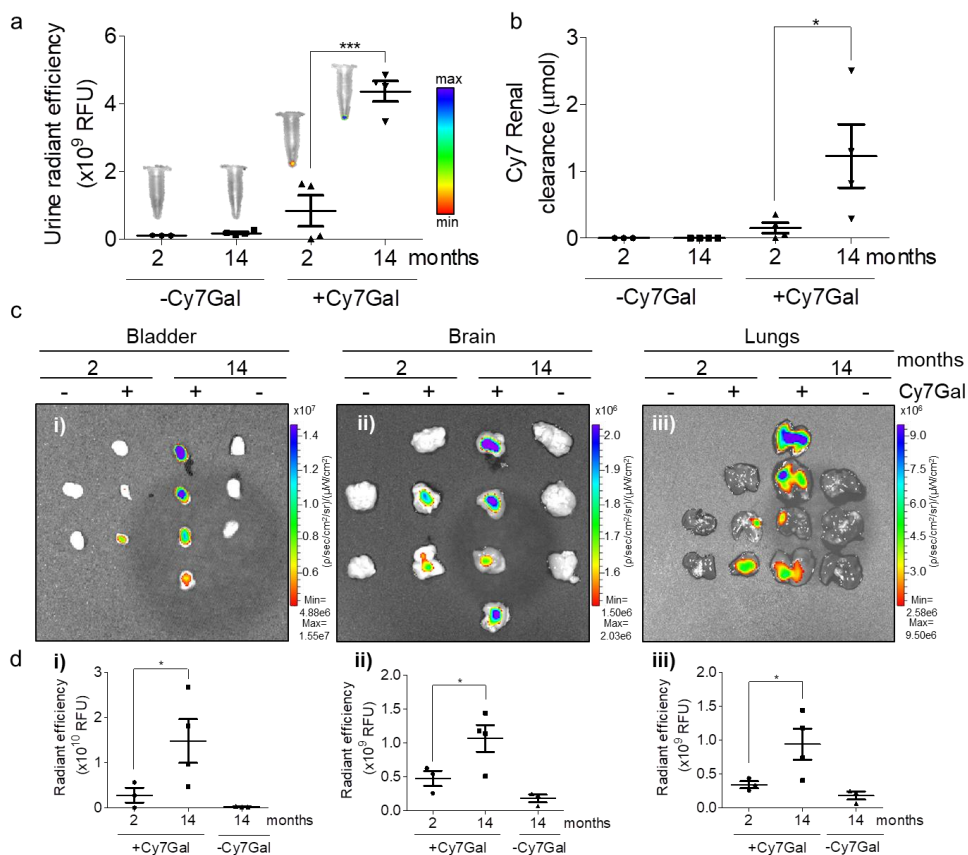


Figure 4. *In vivo* cell senescence burden evaluation by **Cy7Gal** in naturally aged BALB/cByJ mice. (a) Average radiance intensity from urine ascribed to the renal clearance of **Cy7** fluorophore in young (2 months) and aged (14 months) BALB/cByJ mice. Values are expressed as mean \pm SEM. (b) Amount (μmol) of **Cy7** excreted through urine from young (2 months) and aged (14 months) BALB/cByJ mice. Values are expressed as mean \pm SEM. (c) IVIS images of (i) bladders, (ii) brains and (iii) lungs; from left to right in each image 2 months old mice (1st column), 2 months old mice intraperitoneally injected with **Cy7Gal** (23.3 mg/ml, 100 μl) (2nd column), 14 months old mice intraperitoneally injected with **Cy7Gal** (23.3 mg/ml, 100 μl) (3rd column) and 14 months old mice (from left to right) (4th column). (d) Average radiance intensity from organs showed in c images. Values are expressed as mean \pm SEM.

studied by IVIS imaging (Figure 4c (i), (ii) and (iii) respectively). Control mice not treated with **Cy7Gal** showed negligible fluorescence in these organs at any age. In contrast, quantification of the emission intensity in IVIS images revealed an increase of 5.2 in the bladder of aged mice. We also observed increases of 2.3 and

3-fold for brain and lungs respectively in aged mice when compared to young animals (Figure 4d (i), (ii) and (iii) respectively). This observation is in agreement with increases in cell senescence incidence in lungs reported with aging.^{38,39} In the brain, SA- β -gal activity is not a specific marker of neuronal senescence, as many healthy neurons have large lysosomal compartments with increased levels of β -galactosidase.⁴⁰ Interestingly, however, the results suggest the capacity of the probe to permeate the blood-brain barrier.

5.3.5 *In vivo* senescence burden evaluation in a senescence-accelerated mouse model

In addition to natural aging, we next decided to test the probe in a strain of accelerated senescence mice (SAM). Inbreeding of AKR/J mice and selection for the early appearance of features such as hair loss, skin coarseness, and short life span, led to the isolation of senescence-prone (P) and senescence-resistant (R) series of mice which were crossed separately to establish the inbred SAMP and SAMR strains. Relative to their genetic background-controls (SAMR1 mice), SAMP8 mice exhibit several traits that are known to occur during aging at earlier physiological ages and, therefore, constitute a suitable model to test aging phenotypes.⁴¹

The SAMP8 model has been widely used in aging research to study immune dysfunction,⁴² osteoporosis⁴³ or brain atrophy.⁴⁴ Because the phenotypic age-related differences between SAMP8 and SAMR1 mice begin to be evident after approximately 6 months of age,⁴⁵⁻⁴⁷ 2 and 14 months old SAMR1 and SAMP8 mice were i.p. injected with the **Cy7Gal** probe. As in the models above, urine was collected after mouse recovery from anesthesia and analyzed by IVIS (Figure 5a).

The amount of **Cy7** in the urine was also determined from a calibration curve (Figure 5b). Even though urine collection from SAMP8 and SAMR1 was more challenging than in the BALB/cByJ mice models describe above due to the general

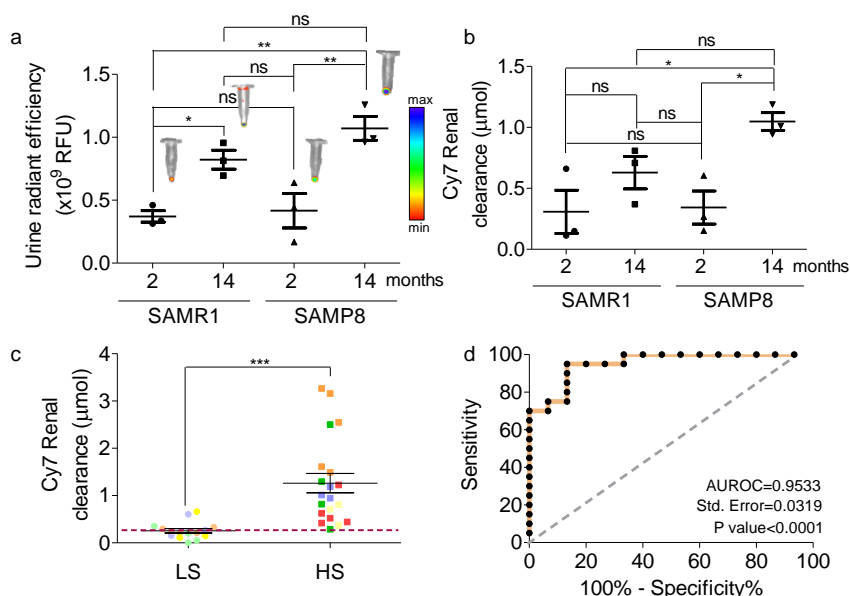


Figure 5. *In vivo* senescence burden evaluation by **Cy7Gal** in a senescence-accelerated mice model. (a) Average radiance intensity in urine in young (2 months) and aged (14 months) SAMP8 and SAMR1 mice treated or not with **Cy7Gal**. Values are expressed as mean \pm SEM. (b) Amount of **Cy7** excreted (expressed in μmol) through urine from young (2 months) and aged (14 months) SAMP8 and SAMR1 mice treated or not with **Cy7Gal**. Values are expressed as mean \pm SEM. (c) Representation of the amount of urine-excreted **Cy7** fluorophore in mice with low senescence (LS) burden treated with **Cy7Gal** (● BALB/cJyB female mice carrying orthotopic 4T1 breast tumours, ● 2 months old BALB/cJyB mice, ● 2 months old SAMR1 mice and ● 2 months old SAMP8 mice) and in mice with high senescence (HS) burden treated with **Cy7Gal** (■ BALB/cJyB female mice carrying orthotopic 4T1 breast tumours treated with 50 mg/Kg of Palbociclib, ■ BALB/cJyB female mice carrying orthotopic 4T1 breast tumours treated with 100 mg/Kg of Palbociclib, ■ 14 months old BALB/cJyB mice, ■ 14 months old SAMR1 mice and ■ 14 months old SAMP8 mice). Values are expressed as mean \pm SEM. (d) Receiver operating characteristic curve by moles of excreted fluorophore discriminated healthy from diseased mice with an area under the curve of 0.95 ($N = 3$ independent experiments, $n = 3$ or 5 mice per group as in Fig. 3, 4 and 5, $P < 0.0001$ from a random classifier shown by the dashed line).

lower amount of urine collected, the results still clearly show a stronger fluorescent signal in the urine (due to a larger amount of **Cy7**) in old mice treated with the probe when compared with the emission in urine from young mice. Thus, 14-month-old SAMR1 mice excreted approximately 2.0-fold μmol s of **Cy7** fluorophore (after **Cy7Gal** hydrolysis) compared to young SAMR1 mice, while a

3.1-fold **Cy7** amount increase in urine is observed for SAMP8 mice aged 14 months with respect to young animals. Moreover, a larger **Cy7** quantity (1.7 fold) in urine is found for 14 months old SAMP8 when compared with 14 months old SAMR1 mice in agreement with the reported large burden of cell senescence in SAMP8 animals.

5.3.6 Cy7Gal is a sensitive and specific probe for senescence burden evaluation regardless of the murine model

Finally, to determine the accuracy of the **Cy7Gal** probe as a tool for evaluation of senescence we divided mice in those with a low (LS) and high (HS) burden of senescence regardless of the murine models used. Mice in the first group include 2 months old BALB/cJyB, SAMR1 and SAMP8 mice, and BALB/cByJ mice bearing 4T1 tumours (not treated with palbociclib), whereas the second group includes 14 months old BALB/cJyB, SAMR1 and SAMP8 mice, and BALB/cByJ mice bearing 4T1 tumours treated with 50 and 100 mg/kg of palbociclib (Figure 5c). The plot revealed a mean urinary signal increase of ca. 4.8 fold in the HS group relative to LS mice. Besides the rate of true positives and false positives (one-specificity) by receiver operating characteristic (ROC) curve shows that the probe discriminated well HS and LS groups with an area under the curve of 0.95 (Figure 5d, $P < 0.0001$).

5.4 Conclusions

Precision medicine aims to guide health care decisions toward the most effective treatment for a certain patient to improve care quality.⁴⁸ Regarding this, the development of new cost-effective and easy implementation diagnostic tools is an important goal.⁴⁹ One attractive approach in this area is to detect biomarkers from readily accessible biofluids using detection systems as simple as possible that are inexpensive and do not require trained personnel.⁵⁰⁻⁵² For instance, tools that

can detect the activity of a certain enzyme *in vivo* with a simple readout can be of importance for the diagnosis of certain diseases.⁵³ An approach that fulfills these characteristics is the design of fluorogenic probes (in an OFF state) able to be transformed by the action of certain biomarkers (i.e an overexpressed enzyme) in cells and tissues to give a final product (in an ON highly emissive state) that has a rapid renal clearance thus allowing its ready detection in the urine using a simple fluorimeter. As an example towards the development of renal clearable fluorogenic probes we report herein the case of detection of cellular senescence, based on the detection of overexpression of lysosomal β -galactosidase, using the fluorogenic probe **Cy7Gal**. This enzyme hydrolyses *in vivo* the poorly-emissive **Cy7Gal** into the highly fluorescent dye **Cy7**, which is renally cleared and detected in urine. We provide evidence of the ability of the probe to monitor the burden of cellular senescence *in vivo* BALB/cByJ mice bearing breast cancer tumour treated with senescence-inducing chemotherapy and in aged mice models. **Cy7Gal** probe is the first diagnostic tool for the *in vivo* detection of senescence in the urine. Our findings demonstrate that renal clearable fluorogenic probes are a versatile modular tool that opens new opportunities to develop simple diagnoses in urine for a variety of diseases where the abnormal enzymatic activity is a biomarker. We anticipate that this technology can also be applied in the monitoring of therapeutic treatments. Such adaptive detection platform could be applicable in low-resource environments and might democratize access to advanced and sensitive diagnoses.

5.5 Acknowledgments

R.M.-M. laboratory members thank the financial support from the Spanish Government (project RTI2018-100910-B-C41) and the Generalitat Valenciana (project PROMETEO 2018/024). B.L.-T. is grateful to the Spanish Ministry of

Economy for their PhD grants (FPU15/02707). A.G.-F. thanks her contract from CIBER-BBN. I.G. thanks her contract from IDM. M.O. thanks the financial support from the Spanish Government (SAF2017-84689-R project MINECO/AEI/FEDER, UE) and the Generalitat Valenciana (project PROMETEO/2019/065). Work in the laboratory of I.F. is supported by grants from the Spanish Government (SAF2017-86690-R), Instituto de Salud Carlos III (CIBERNED and RETIC Terce), and Generalitat Valenciana (Prometeo 2017/030). S. R.-V. is the recipient of an FPU predoctoral fellowship from the Spanish Ministerio de Educación. J.F.B. thanks to his postdoctoral fellowship (PAID-10-17).

5.6 Author Contributions

B. L.-T., J. F. B., F. S. G. and R. M.-M. conceived and designed the research. B. L.-T. and J. F. B. synthesized and characterized all organic molecules. J. F. B. performed HPLC studies. B. L.-T., carried out all *in vitro* and *in vivo* studies and analyzed the data. A. G.-F, I. G. and S. R.-V. assisted with the *in vivo* experiments. M. O. helped in designing the *in vivo* experiment in the chemotherapy-induced 4T1 breast cancer model. S. R.-V. and I. F. maintained SAMR1 and SAMP8 strains mice. B. L.-T., J. F. B., F. S and R. M.-M. wrote the manuscript with feedback from all the authors.

5.7 Competing Interest Statement

B. L.-T., A. G.-F., I. G., M. O., R. M.-M., F. S, and J. F. B. have filed a patent application related to this research with the “Oficina Española de Patentes y Marcas”. R.M.-M. is co-founder of Senolytic Therapeutics, Inc. (USA) and Senolytic Therapeutics, S.L. (Spain)

5.8 Data availability statement

The authors declare that the data supporting the findings of this study are available within the paper and its supplementary information files.

5.9 References

1. Jute, A. Sociology of diagnosis: A preliminary review. *Sociol. Health Illn.* **31**, 278-299 (2009).
2. Schito, M. Peter, T. F. Cavanaugh, S. Piatek, A. S. Young, G. J. Alexander, H. Coggin, W. Domingo, G. J. Ellenberger, D. Ermantraut, E. Jani, I. V. Katamba, A. Palamountain, K. M. Essajee, S. & Dowdy, D. W. Opportunities and Challenges for Cost-Efficient Implementation of New Point-of-Care Diagnostics for HIV and Tuberculosis. *J. Infect. Dis.* **205**, S169-S180 (2012).
3. Palamountain, K. M. Baker, J. Cowan, E. P. Essajee, S. Mazzola, L. T. Metzler, M. Schito, M. Stevens, W. S. Young, G. J. & Domingo, G. J. Perspectives on Introduction and Implementation of New Point-of-Care Diagnostic Tests. *J. Infect. Dis.* **205**, S181-S190 (2012).
4. Shikha, S. Zapatero-Rodríguez, J. Estrela, P. & O'Kennedy, R. Point-of-Care Diagnostics in Low Resource Settings: Present Status and Future Role of Microfluidics. *Biosensors* **5**, 577-601 (2015).
5. Hay Burgess, D. C. Wasserman, J. & Dahl, C. A. Global health diagnostics. *Nature* **444**, 1-2 (2006).
6. Urdea, M. Penny, L. A. Olmsted, S. S. Giovanni, M. Y. Kaspar, P. Shepherd, A. Wilson, P. Dahl, C. A. Buchsbaum, S. Moeller, G. & Hay Burgess, D. C. Requirements for high impact diagnostics in the developing world. *Nature* **444**, 73-79 (2006).
7. Yager, P. Domingo, G. J. & Gerdes, J. Point-of-care diagnostics for global health. *Annu. Rev. Biomed. Eng.* **10**, 107-144 (2008).
8. Warrena, A. D. Kwonga, G. A. Wood, D. K. Lin, & K. Y. Bhatia, S. N. Point-of-care diagnostics for non-communicable diseases using synthetic urinary biomarkers and paper microfluidics. *Proc. Natl. Acad. Sci. USA* **111**, 3671-3676 (2014).
9. Kwong, G. A. von Maltzahn, G. Murugappan, G. Abudayyeh, O. Mo, S. Papayannopoulos, I. A. Sverdlov, D. Y. Liu, S. B. Warren, A. D. Popov, Y. Schuppan, D. & Bhatia, S. N. Mass-encoded synthetic biomarkers for multiplexed urinary monitoring of disease. *Nat. Biotech.* **31**, 63-71 (2013).
10. Lin, K. Y. Kwong, G. A. Warren, A. D. Wood, D. K. & Bhatia, S. N. Nanoparticles that sense thrombin activity as synthetic urinary biomarkers of thrombosis. *ACS Nano* **7**, 9001-9009 (2013).
11. Huang, J. Li, J. Lyu, Y. Miao, Q. & Pu, K. Molecular optical imaging probes for early diagnosis of drug-induced acute kidney injury. *Nat. Mater.* **18**, 1133-1143 (2019).
12. Choi, H. S. Liu, W. Misra, P. Tanaka, E. Zimmer, J. P. Ipe, B. I. Bawendi, M. G. & Frangioni, J. V. Renal clearance of quantum dots. *Nat. Biotechnol.* **25**, 1165-1170 (2007).

13. Loynachan, C. N. Soleimany, A. P. Dudani, J. S. Lin, Y. Najer, A. Bekdemir, A. Q. Bhatia, S. N. & Stevens, M. M. Renal clearable catalytic gold nanoclusters for *in vivo* disease monitoring. *Nat. Nanotech.* **14**, 883-890 (2019).
14. Wolfram, J. Zhu, M. Yang, Y. Shen, J. Gentile, E. Paolino, D. Fresta, M. Nie, G. Chen, C. Shen, H. Ferrari, M. & Zhao, Y. Safety of nanoparticles in medicine. *Curr. Drug. Targets.* **16**, 1671-1681 (2015).
15. Munoz-Espin, D. & Serrano, M. Cellular senescence: from physiology to pathology. *Nat. Rev. Mol. Cell Biol.* **15**, 482-496 (2014).
16. Ritschka, B. Storer, M. Mas, A. Heinzmann, F. Ortells, M. C. Morton, J. P. Sansom, O. J. Zender, L. & Keyes, W. M. The Senescence-Associated Secretory Phenotype induces cellular plasticity and tissue regeneration. *Genes Dev.* **31**, 172-183 (2017).
17. Lozano-Torres, B. Estepa-Fernández, A. Rovira, M. Orzáez, M. Serrano, M. Martínez-Máñez, R. & Sancenón, F. The Chemistry of Senescence. *Nat. Rev. Chem.* **3**, 426-441 (2019).
18. Ferrucci, L. Gonzalez-Freire, M. Fabbri, E. Simonsick, E. Tanaka, T. Moore, Z. Salimi, S. Sierra, F. & de Cabo, R. Measuring biological aging in humans: A quest. *Aging Cell* **19**, e13080 (2020).
19. González-Gualda, E. Páez-Ribes, M. Lozano-Torres, B. Macias, B. D. Wilson, J. R. González-López, C. Ou, H. -L. Mirón-Barroso, S. Zhang, Z. Lérida-Viso, A. Blandez, J. F. Bernardos, A. Sancenón, F. Rovira, M. Fruk, L. Martins, C. P. Serrano, M. Doherty, G. J. Martínez-Máñez, R. & Muñoz-Espín, D. Galacto-conjugation of navitoclax as an efficient strategy to increase senolytic specificity and reduce platelet toxicity. *Aging Cell* **19**, e13142 (2020).
20. Xu, M. Pirtskhalava, T. Farr, J. N. Weigand, B. M. Palmer, A. K. Weivoda, M. M. Inman, C. L. Ogrodnik, M. B. Hachfeld, C. M. Fraser, D. G. Onken, J. L. Johnson, K. O. Verzosa, G. C. Langhi, L. G. P. Weigl, M. Giorgadze, N. LeBrasseur, N. K. Miller, J. D. Jurk, D. Singh, R. J. Allison, D. B. Ejima, K. Hubbard, G. B. Ikeno, Y. Cubro, H. Garovic, V. D. Hou, X. Weroha, S. J. Robbins, P. D. Niedernhofer, L. J. Khosla, S. Tchkonja, T. & Kirkland, J. L. Senolytics improve physical function and increase lifespan in old age. *Nat. Med.* **24**, 1246-1256 (2018).
21. Páez-Ribes, M. González-Gualda, E. Doherty, G. J. & Muñoz-Espín, D. Targeting senescent cells in translational medicine. *EMBO Mol. Med.* **11**, e10234 (2019).
22. Soto-Gamez, A. & Demaria, M. Therapeutic interventions for aging: The case of cellular senescence. *Drug Discov. Today* **22**, 786-795 (2017).
23. Lozano-Torres, B. Galiana, I. Rovira, M. Garrido, E. Chaib, S. Bernardos, A. Muñoz-Espín, D. Serrano, M. Martínez-Máñez, R. & Sancenón, F. An OFF–ON two-photon fluorescent probe for tracking cell senescence *in vivo*. *J. Am. Chem. Soc.* **139**, 8808-8811 (2017).
24. Karton-Lifshin, N. Segal, E. Omer, L. Portnoy, M. Satchi-Fainaro, R. & Shabat, D. A unique paradigm for a turn-on near-infrared cyanine-based probe: Non-invasive intravital optical imaging of hydrogen peroxide. *J. Am. Chem. Soc.* **133**, 10960-10965 (2011).
25. Kaur, P. Nagaraja, G. M. Zheng, H. Gizachew, D. Galukande, M. Krishnan, S. & Asea, A. A mouse model for triple-negative breast cancer tumor-initiating cells (TNBC-TICs) exhibits similar aggressive phenotype to the human disease. *BMC Cancer* **12**, 1-12 (2012).
26. Galiana, I. Lozano-Torres, B. Sancho, M. Alfonso, M. Bernardos, A. Bisbal, V. Serrano, M. Martínez-Máñez, R. & Orzáez, M. Preclinical antitumor efficacy of senescence-inducing chemotherapy combined with a nanoSenolytic. *J. Control. Release* **323**, 624-634 (2020).
27. Whittaker, S. R. Mallinger, A. Workman, P. & Clarke, P. A. Inhibitors of cyclin-dependent kinases as cancer therapeutics. *Pharmacol. Ther.* **173**, 83-105 (2017).
28. He, S. & Sharpless, N. E. Senescence in health and disease. *Cell* **169**, 1000-1011 (2017).
29. Bollard, J. Miguela, V. Ruiz de Galarreta, M. Venkatesh, A. Bian, C. B. Roberto, M. P. Tovar, V. Sia, D. Molina-Sánchez, P. Nguyen, C. B. Nakagawa, S. Llovet, J. M. Hoshida, Y. &

- Lujambio, A. Palbociclib (PD-0332991), a selective CDK4/6 inhibitor, restricts tumour growth in preclinical models of hepatocellular carcinoma. *Gut* **66**, 1286-1296 (2017).
30. Hamann, F. M. Brehm, R. Pauli, J. Grabolle, M. Frank, W. Kaiser, W. A. Fischer, D. Resch-Genger, U. & Hilger, I. Controlled modulation of serum protein binding and biodistribution of asymmetric cyanine dyes by variation of the number of sulfonate groups. *Mol. Imaging* **10**, 258-269 (2011).
 31. Amarya, S. Singh, K. & Sabharwal, M. Ageing process and physiological changes. *Gerontol.* Book chapter. DOI: 10.5772/intechopen.76249 (2018).
 32. Khan, S. S. Singer, B. D. & Vaughan, D. E. Molecular and physiological manifestations and measurement of aging in humans. *Aging Cell* **16**, 624-633 (2017).
 33. Sun, N. Youle, R. J. & Finkel, T. The mitochondrial basis of aging. *Mol. Cell* **61**, 654-666 (2016).
 34. Franceschi, C. Garagnani, P. Morsiani, C. Conte, M. Santoro, A. Grignolio, A. Monti, D. Capri, M. & Salvioli, S. The continuum of aging and age-related diseases: common mechanisms but different rates. *Front. Med.* **5**, 1-23 (2018).
 35. van Deursen, J. M. The role of senescent cells in ageing. *Nature* **509**, 439-446 (2014).
 36. Belsky, D. W. Caspi, A. Houts, R. Cohen, H. J. Corcoran, D. Danese, L. A. Harrington, H. Israel, S.. Levine, M. E Schaefer, J. D. Sugden, K. Williams, B. Yashin, A. I. Poulton, R. & Moffitt, T. E. Quantification of biological aging in young adults. *Proc. Natl. Acad. Sci. USA* **112**, 4104-4110 (2015).
 37. Pignolo, R. J. Passos, J. F. Khosla, S. Tchkonina, T. & Kirkland, J. L. Reducing senescent cell burden in aging and disease. *Trends Mol. Med.* **26**, 630-638 (2020).
 38. Rashid, K. Sundar, I. K. Gerloff, J. Li, D. & Rahman, I. Lung cellular senescence is independent of aging in a mouse model of COPD/emphysema. *Sci. Rep.* **13**, 9023 (2018).
 39. Chen, L. He, P. -L. Yang, J. Yang, Y. -F. Wang, K. Amend, B. Stenzl, A. Zhang, Y. -M.. Wang, Z. -L. Xing, S. -S. & Luo, X. NLRP3/IL1 β inflammasome associated with the aging bladder triggers bladder dysfunction in female rats. *Mol. Med. Rep.* **19**, 2960-2968 (2019).
 40. Piechota, M. Sunderland, P. Wysocka, A. Nalberczak, M. Sliwinska, M. A. Radwanska, K. & Sikora, E. Is senescence-associated β -galactosidase a marker of neuronal senescence? *Oncotarget* **7**, 81099-81109 (2016).
 41. Yanai, S. & Endo, S. Early onset of behavioral alterations in senescence-accelerated mouse prone 8 (SAMP8). *Behav. Brain Res.* **15**, 187-195 (2016).
 42. Abe, Y. Yuasa, M. Kajiwara, Y. & Hosono, M. Defects of immune cells in the senescence-accelerated mouse: a model for learning and memory deficits in the aged. *Cell. Immunol.* **157**, 59-69 (1994).
 43. Zhang, N. Chow, S. K. H. Leung, K. S. Lee, H. H. & Cheung, W. H. An animal model of co-existing sarcopenia and osteoporotic fracture in senescence accelerated mouse prone 8 (SAMP8). *Exp. Gerontol.* **15**, 1-8 (2017).
 44. Akiguchi, I. Pallàs, M. Budka, H. Akiyama, H. Ueno, M. Han, J. Yagi, H. Nishikawa, T. Chiba, Y. Sugiyama, H. Takahashi, R. Unno, K. Higuchi, K. & Hosokawa, M. SAMP8 mice as a neuropathological model of accelerated brain aging and dementia: Toshio Takeda's legacy and future directions. *Neuropathology* **37**, 293-305 (2017).
 45. Higuchi, K. Hosokawa, M. & Takeda, T. Senescence-accelerated mouse. *Meth. Enzymol.* **309**, 674-686 (1999).
 46. Carter, T. A. Greenhall, J. A. Yoshida, S. Fuchs, S. Helton, R. Swaroop, A. Lockhart, D. J. & Barlow, C. Mechanisms of aging in senescence-accelerated mice. *Genome Biol.* **6**, R48 (2005).
 47. Pallàs, M. Senescence-Accelerated Mice P8: A tool to study brain aging and alzheimer's disease in a mouse model. *ISRN Cell Biol.* **917167**, 1-12, (2012).
 48. Ginsburg, G. S. & Phillips, K. A. Precision medicine: From science to value. *Health Aff.* **37**, 694-701 (2018).

49. Vashist, S. K. Point-of-Care Diagnostics: Recent advances and trends. *Biosensors* **7**, 62-66 (2017).
50. Singh, A. T. Lantigua, D. Meka, A. Taing, S. Pandher, M. & Camci-Unal, G. Paper-Based Sensors: Emerging themes and applications. *Sensors* **18**, 1-22 (2018).
51. Khanna, P. & Walt, D. R. Salivary diagnostics using a portable point-of-service platform: A Review. *Clin. Ther.* **37**, 498-504 (2015).
52. Sanjay, S. T. Fu, G. Dou, M. Xu, F. Liu, R. Qie, H. & Li, X. Biomarker detection for disease diagnosis using cost-effective microfluidic platforms. *Analyst* **140**, 7062-7081 (2015).
53. Zhang, J. Chai, X. He, X. -P. Kim, H. -J. Yoon, J. & Tiana, H. Fluorogenic probes for disease-relevant enzymes. *Chem. Soc. Rev.* **48**, 683-722 (2019).

5.10 Supporting information

5.10.1 Materials. 5-Formylsalicylaldehyde was purchased from Tokyo Chemical Industry Co., Ltd. (TCI) while α -acetobromogalactose, potassium carbonate and 1-(4-sulfobutyl)-2,3,3-trimethylindolium) inert salt, sodium acetate and acetic anhydride were obtained from Sigma-Aldrich and used without further purification. Anhydrous acetonitrile was purchased from Acros Organics.

5.10.2 Synthesis and characterization of Cy7Gal. 5-formylsalicylaldehyde (75 mg, 0.5 mmol), α -acetobromogalactose (607 mg, 1.5 mmol) and potassium carbonate (400 mg, 4 mmol) were mixed in a round bottom flask under argon atmosphere and dissolved in 30 mL of anhydrous acetonitrile. The reaction mixture was heated to 70°C, and stirred for 4 hours under argon atmosphere and the solvent was removed under vacuum. The residue was purified by column chromatography on silica gel (hexane-ethyl acetate 2:1 v/v as eluent) to obtain product 1 as pale green oil (230 mg, 0.46 mmol, 92.6% yield). Then, compound 1 (90 mg, 0.17 mmol), 1-(4-sulfobutyl)-2,3,3-trimethylindolium inner salt (2) (100 mg, 0.35 mmol) and sodium acetate (47.80 mg, 0.35 mmol) were dissolved in 2 mL of acetic anhydride in a Schlenk flask under an argon atmosphere. The reaction mixture was heated to 70 °C and stirred for 4 hours under argon atmosphere and solvent was eliminated under vacuum. The crude was purified by reverse phase column chromatography (dicholoromethane-methanol 10:1 v/v as eluent) to obtain **Cy7Gal** as a red-brown solid. (120 mg, 0.116 mmol, 68.1% yield).

^1H NMR (400 MHz, CDCl_3) δ = 7,72 – 7,62 (m, 1H), 7,53 (dd, J = 7,5; 1,6 Hz, 1H), 7,49 – 7,43 (m, 2H), 7,42 – 7,32 (m, 2H), 7,00 (d, J = 7,3 Hz, 2H), 6,79 (t, J = 7,2 Hz,

¹H), 6,69 (t, J = 7,3 Hz, 1H), 6,37 (d, J = 1,7 Hz, 1H), 5,69 (d, J = 8,3 Hz, 1H), 5,49 (d, J = 1,3 Hz, 1H), 5,42 (dd, J = 3,4; 0,9 Hz, 1H), 5,34 – 5,32 (m, 2H), 5,24 (s, 1H), 5,07 (dd, J = 10,4; 3,4 Hz, 1H), 4,17 – 4,04 (m, 4H), 3,48 (s, 4H), 2,91 (s, 4H), 2,03 (s, 12H), 1,93 (s, 4H), 1,82 (s, 4H), 1,58 (s, 12H) ppm.

¹³C NMR (400 MHz, CDCl₃) δ = 193.63 (2C), 170.52 (1C), 170.28 (1C), 170.15 (1C), 169.80 (1C), 169.07 (1C), 144.10 (1C), 143.12 (1C), 140.70 (2C), 140.11 (2C), 139.11 (1C), 130.30 (1C), 130.21 (1C), 129.96 (1C), 129.88 (1C), 127.64 (1C), 124.61 (1C), 124.50 (1C), 121.86 (1C), 121.61 (1C), 115.77 (1C), 114.70 (1C), 114.19 (1C), 112.51 (1C), 108.17 (1C), 92.29 (1C), 70.97 (1C), 68.89 (1C), 67.55 (1C), 66.57 (1C), 61.15 (1C), 53.56 (2C), 52.87 (2C), 48.15 (2C), 32.27 (1C), 31.56 (1C), 29.82 (4C), 23.34 (2C), 21.02 (1C), 20.94 (1C), 20.78 (1C), 20.67 (1C) ppm.

HRMS: Calculated for C₅₂H₆₃N₂O₁₆S₂ (M+H⁺) 1035.3619 m/z; measured 1035.3606 m/z (M+H⁺), 1051.3546 (M+H₂O-2H⁺).

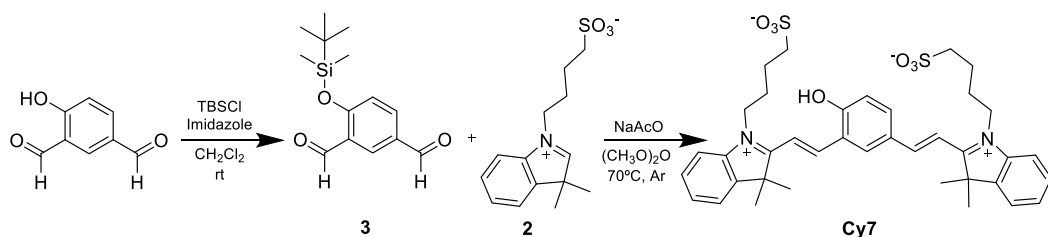
5.10.3 Synthesis and characterization of Cy7. 4-hydroxyisophthalaldehyde (1.5 g, 9.9 mmol) and imidazole (1.7 g, 25 mmol) were dissolved in 100 mL of anhydrous dichloromethane. Tert-butyldimethylsilyl chloride (1.8 g, 12 mmol) was then added dropwise to the solution. The reaction was stirred at room temperature overnight. Afterwards, the mixture was washed with brine (2x100 mL) and the organic phase was dried with MgSO₄. The solvent was removed under vacuum and the crude was purified by silica column using a mixture hexane:ethyl acetate (10:1) as eluent. Product 3 (2.48 g, 9.39 mmol, 94.8% yield) was obtained as colorless oil. Subsequently, 3 (79.24 mg, 0.3 mmol) was added in a Schlenk tube with sodium acetate (83.9 mg, 1.02 mmol) and 2,3,3-trimethyl-1-(4-sulfobutyl)-indolium. The mixture was dissolved in acetic anhydride under argon atmosphere. The reaction was stirred at 80 °C for 4 hours. Acetic anhydride was removed

under vacuum and treated with dichloromethane and the solvent was eliminated again under vacuum. Finally, deprotection of hydroxyl group was assessed by stirring the obtained product in a solution of $\text{KF}\cdot 2\text{H}_2\text{O}$ (47 mg, 0.5 mmol) in acetonitrile (2 mL) for 2 h at room temperature. Then, the mixture was treated with saturated NaHCO_3 water solution (1 mL) and extracted with CH_2Cl_2 (3x20 mL). The organic layer was washed with brine and dried with MgSO_4 . The crude was purified by reverse phase column chromatography (dichloromethane-methanol 8:1 v/v as eluent). **Cy7** was obtained as brown-green solid (85 mg, 0.120 mmol, 40 % yield).

^1H NMR (400 MHz, CDCl_3) δ = 7.60 – 7.45 (m, 4H), 7.35 (d, J = 2.5 Hz, 2H), 7.28 (d, J = 2.0 Hz, 1H), 7.15 – 6.96 (m, 3H), 6.84 – 6.69 (m, 1H), 5.81 (ddt, J = 16.9, 10.2, 6.7 Hz, 1H), 5.37 (dt, J = 9.1, 4.1 Hz, 1H), 5.02 – 4.90 (m, 2H), 2.04 (dd, J = 14.9, 7.3 Hz, 4H), 1.77 (d, J = 4.7 Hz, 4H), 1.67 (dt, J = 15.4, 7.6 Hz, 4H), 1.45 (dd, J = 14.8, 7.5 Hz, 4H), 1.37 (s, 12H) ppm.

^{13}C NMR (101 MHz, CDCl_3) δ = 174.97 (2C), 160.73 (1C), 154.00 (1C), 149.87 (1C), 140.72 (2C), 140.08 (2C), 130.71(1C), 130.12 (1C), 128.89 (1C), 128.44 (2C), 125.20 (2C), 124.39 (1C), 123.17 (2C), 117.05 (1C), 114.61 (2C), 109.08 (1C), 107.48 (1C), 53.97 (2C), 48.90 (2C), 42.15 (2C), 28.67 (2C), 26.23 (2C), 19.29 (2C) ppm.

HRMS Calculated for $\text{C}_{38}\text{H}_{44}\text{N}_2\text{O}_7\text{S}_2$ ($\text{M}+\text{H}^+$) 705,269 m/z; measured 705,2673 m/z ($\text{M}+\text{H}^+$).



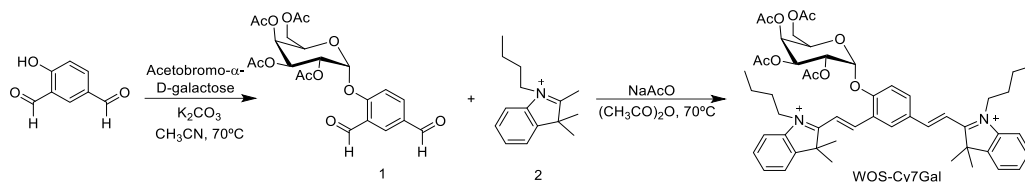
Scheme S1. Synthetic route of fluorophore **Cy7**.

5.10.4 Synthesis and characterization of WOS-Cy7Gal. Product 1 (90 mg, 0.17 mmol) 1-butyl-2,3,3-trimethyl-3H-indol-1-ium iodide (120 mg, 0.35 mmol) and sodium acetate (47.80 mg, 0.35 mmol) were mixed in a Schlenk flask under argon atmosphere and dissolved in 2 mL of acetic anhydride. The reaction mixture was heated to 70 °C and stirred under argon atmosphere. After 4 hours, the solvent was removed under vacuum and the crude product was purified in a silica flash column using diethyl ether as eluent. **WOS-Cy7Gal** was obtained as red-brown oil (50 mg, 0.05 mmol, 33% yield).

^1H NMR (400 MHz, CDCl_3) δ = 7.60 – 7.51 (m, 2H), 7.20 – 7.14 (m, 4H), 7.08 (dd, J = 21.5, 6.2 Hz, 2H), 6.97 (t, J = 7.4 Hz, 2H), 6.71 (d, J = 7.7 Hz, 2H), 6.38 (bs, 1H), 5.70 (d, J = 8.3 Hz, 1H), 5.50 (d, J = 1.3 Hz, 1H), 5.43 (d, J = 2.5 Hz, 1H), 5.08 (dd, J = 10.4, 3.4 Hz, 1H), 4.34 (t, J = 6.4 Hz, 1H), 4.14 (t, J = 6.6 Hz, 2H), 4.10 (dd, J = 6.7, 4.0 Hz, 1H), 4.08 – 4.03 (m, 1H), 3.61 (t, J = 7.6 Hz, 4H), 2.04 (s, 3H), 2.02 (s, 3H), 2.01 (s, 3H), 2.00 (s, 3H), 1.72 (s, 12H), 1.66 (dd, J = 13.9, 6.1 Hz, 4H), 1.62 – 1.55 (m, 4H), 0.99 (t, J = 7.3 Hz, 6H).

^{13}C NMR (101 MHz, CDCl_3) δ = 193.44 (2C), 170.49 (1C), 170.26 (1C), 170.00 (1C), 169.50 (1C), 169.05 (1C), 147.19 (1C), 143.36 (1C), 142.18 (1C), 140.38 (1C), 139.41 (1C), 136.17 (1C), 135.60 (1C), 127.66 (1C), 127.46 (1C), 124.58 (1C), 124.10 (1C), 122.50 (1C), 122.29 (1C), 122.01 (1C), 121.95 (1C), 119.23 (1C), 119.21 (1C), 114.19 (1C), 108.44 (1C), 107.75 (2C), 93.69 (1C), 71.83 (1C), 68.89 (1C), 67.94 (1C), 67.54 (1C), 61.37 (1C), 48.31 (2C), 42.61 (2C), 31.56 (1C), 30.31 (1C), 29.82 (4C), 24.58 (1C), 22.81 (1C), 21.01 (1C), 20.93 (1C), 20.77 (1C), 20.73 (1C), 20.67 (1C), 20.47 (1C).

HRMS Calculated for C₅₂H₆₄N₂O₁₀ (M +H⁺) 876.459 m/z; measured 876.7992 m/z (M +H⁺).



Scheme S2. Synthetic route of probe **WOS-Cy7Gal**.

5.10.5 Characterization. All obtained products were characterized by 1H and ^{13}C NMR spectra on a Bruker FT-NMR Avance 400 (Ettlingen, Germany) spectrometer at 300 K, using TMS as internal standard and by high resolution mass spectrometry (HRMS) with a TRIPLETOF T5600 (ABSciex, USA) spectrometer. Fluorescence was characterized in a JASCO FP-8500 fluorescence spectrophotometer.

5.10.6 Hydrolysis of Cy7Gal by human- β Gal. 2 μ l of human β -Gal enzyme (Biotechne) were added to PBS (pH 7) solutions of **Cy7Gal** (10^{-5} M). Chromatograms of **Cy7Gal**, **Cy7** and **Cy7Gal**+ β -Gal after 30 min were obtained by reversed-phase liquid chromatography using a KromasilC18 column as the stationary phase, a mixture water-acetonitrile under gradient conditions (flow: 0.8 mL/min, initial condition 90:10 vol. %, final condition 10:90 vol. %) as mobile phase and a photodiode array detector.

5.10.7 Interferents. To study the specificity and selectivity of the probe to β -galactosidase, fluorescence intensity of solutions of **Cy7Gal** (20 μ M, PBS, pH 7.4) was measured in the presence of cations (150 μ M), anions (150 μ M), small peptides (150 μ M), proteins (150 μ g/mL) and enzymes (150 μ g/mL) (Figure S2b) at

37 °C after 30 min in a JASCO FP-8500 fluorescence spectrophotometer ($\lambda_{\text{ex}} = 580$ nm; $\lambda_{\text{em}} = 665$ nm).

5.10.8 Cell culture. The 4T1 mouse mammary tumour cell line was obtained from the American Type Culture Collection (ATCC), cultured in DMEM supplemented with 10% FBS (Sigma) and maintained in 20% O₂ and 5% CO₂ at 37 °C. Cells were routinely tested for *Mycoplasma* using the universal mycoplasma detection kit (ATCC). For senescence induction, 4T1 cells were treated with 5 μ M palbociclib (Eurodiagnostico) for 14 days. Cellular senescence was assessed by senescence β -galactosidase KIT acquired from Cell Signaling.

5.10.9 Confocal *in vitro* experiments. 4T1 control and senescent cells were seeded in a clear flat bottom 96-well plate at a density of 3,000 and 4,000 cells per well respectively. After 24 h cells were treated with **Cy7Gal** (20 μ M) and confocal images were acquired 2 h post-treatment in a Leica TCS SP8 AOBS confocal microscope ($\lambda_{\text{exc}} = 552$ nm; $\lambda_{\text{em}} = 574$ -765 nm). Images were analyzed by using the Image J software.

5.10.10 Competition experiments with D-Galactose. A total of 200,000 control or 500,000 senescent 4T1 cells were seeded per well in a clear glass 6-well plate. The following day, cells were pre-incubated or not with D-galactose (5 mM) for 30 min and then treated with **Cy7Gal** (20 μ M) in DMEM (10% FBS, 0.1% DMSO) in 20% O₂ and 5% CO₂ at 37 °C for 2 h. Finally, confocal images were acquired by using a confocal microscope (Leica TCS SP8 AOBS) ($\lambda_{\text{exc}} = 552$ nm; $\lambda_{\text{em}} = 574$ -765 nm). Images were analyzed by using the Image J software.

5.10.11 Downregulation experiments. . For transient downregulation of GLB1, a total of 20,000 control or 50,000 senescent 4T1 cells were seeded per well in a 24-well plate. After 24 h, cells were transfected with TriFECTa® Kit DsiRNA Duplex siRNAs (Integrated DNA Technologies) hs.Ri.GLB1.13.3 or scrambled siRNA, using lipofectamine RNAiMAX reagent (Thermo Fisher Scientific) as per manufacturer's instructions. 48 h after transfection, cells were washed once with PBS and fixed for 10 min with SA- β -Gal staining kit fixative. Then, cells were stained overnight using the SA- β -Gal staining kit (Cell Signaling) following manufacturer's instructions. The following day, cells were thoroughly washed with PBS and imaged using a colored bright field microscope. On the other hand, 48 h after transfection, cells were treated with **Cy7Gal** solutions (20 μ M) and imaged in a Leica TCS SP8 AOBS confocal microscope (λ_{exc} = 552 nm; λ_{em} = 574-765 nm). Images were analyzed by using the Image J software.

5.10.12 Western blot analysis of β -galactosidase expression. To determine the levels of β -galactosidase protein in 4T1 cells (control and senescent), whole-cell extracts were obtained by using lysis buffer (25 mM Tris-HCl pH 7.4, 1 mM EDTA, 1% SDS, plus protease and phosphatase inhibitors). Cell lysates were resolved by SDS-PAGE, transferred to nitrocellulose membranes, blocked with 5% nonfat milk and incubated overnight with the primary antibody for β -galactosidase detection (β -galactosidase (E2U2I) rabbit mAb #27198 from Cell Signaling). Besides, GAPDH (#14C10 from Cell Signaling) was used as reference. Then, membranes were washed and probed with the secondary antibody conjugated to horseradish peroxidase, anti-rabbit IgG peroxidase antibody (#A6154, Sigma) for enhanced chemiluminescence detection (Amersham Pharmacia Biotech).

5.10.13 *In vitro* cytotoxicity studies. For the *in vitro* cytotoxicity studies, 4T1 cells were plated in a 96-well plate (6,000 control and 4,000 senescent cells per well) and allowed to adhere to the wells. At 24 h post-seeding, the cells were incubated with varying concentrations of the **Cy7Gal** probe (diluted in DMEM) for 24 h. The cell viability was evaluated using the cellTiter-Glo® Luminescent Cells assay (Promega). Luminescence was collected in a VICTOR Multilabel Plate Reader (Pelkin Elmer).

5.10.14 Animals. BALB/cByJ mice were acquired from Charles River laboratories, France, and maintained at the Spanish Centro de Investigación Príncipe Felipe (CIPF). SAMR1 and SAMP8 mice were housed and bred at the Universitat de València (UV). All animal procedures were approved by the CIPF and UV Ethics Committees for Research and Animal Welfare (CEBA) and conducted in accordance with the recommendations of the Federation of European Laboratory Animal Science Associations (FELASA).

5.10.15 *In vivo* 4T1 breast cancer model treated with senescence-inducing chemotherapy. Breast 4T1 tumours were established by using 4T1 cells in Balb/cByJ mice. Cells were routinely cultured in DMEM supplemented with 10% FBS and penicillin-streptomycin. In order to generate mammary tumours, cells were trypsinised, counted with a LUNA™ Automated Cell Counter and 0.5×10^6 cells in a volume of 100 μ l were injected subcutaneously in the left mammary fat pad of 28- to 34-week-old Balb/cByJ female mice. Palbociclib dissolved in 50 mM sodium lactate, pH 4, at different doses was administered by daily oral gavage for 7 days. Tumour volume was measured every two days with a caliper and was calculated as $V = (a \times b^2)/2$ where a is the longest and b is the shortest of two perpendicular diameters.

5.10.16 Renal clearance of Cy7Gal. Mice were anesthetized intraperitoneally (i.p.) injected with **Cy7Gal** at a concentration of 23.3 mg/ml (100 μ l, 2.5 μ mol per mice) and maintained in an IVIS spectrum (Perkin Elmer) for 15 min taking photographs every 2 minutes (λ_{exc} = 535 nm; λ_{em} = 640 nm; Time exposure: 10 s). Urine was collected after mice recovered from anesthesia in an Eppendorf tube and analyzed directly by IVIS (λ_{exc} = 535 nm; λ_{em} = 640 nm; Time exposure: 1s). Radiance quantification of images was performed using the software of live image from Caliper Life Sciences. Besides, fluorescence of urine from all mice was analyzed with a fluorescence spectrophotometer (JASCO FP-8500). For this purpose, 5 μ l of urine was diluted in 95 μ l of distilled water and fluorescence spectra was recorded at λ_{em} = 560 nm (λ_{exc} = 535 nm). The amount of **Cy7** fluorophore excreted in urine was calculated through a calibration curve. For the calibration curve, a stock solution of **Cy7** in blank urine from mouse was prepared. Serial dilutions were prepared in the same urine and 5 μ l of each **Cy7** urine solution was added to 95 μ l of distilled water and measured in the fluorimeter under the same condition.

5.10.17 Experiments with WOS-Cy7Gal. To demonstrate that sulfonic groups are responsible of the renal clearance of **Cy7**, a similar molecule to **Cy7Gal** without sulfonic acid moieties (**WOS-Cy7Gal**) was i.p. injected in chemotherapy-induced 4T1 breast cancer BALB/cByJ mice at the same dose expressed in moles (2.5 μ mol per mice, 19.7 mg/ml, 100 μ l). Urine was collected following the same protocol as above and compared with urine from mice injected with **Cy7Gal** probe (λ_{exc} = 535 nm; λ_{em} = 640 nm; Time exposure: 1 s). Furthermore, in order to assess the biodistribution of the fluorophores from the **Cy7Gal** and **WOS-Cy7Gal** probes, fluorescence was measured in both urine and plasma. Plasma samples were obtained 10 minutes after the probe or vehicle injection by submandibular puncture of mice with a 25G needle. Blood was collected in heparinised tubes

and, subsequently, these samples were centrifuged at 350 g for 4 minutes and the supernatant (plasma) was collected. 10 μ l of each plasma sample was diluted in 90 μ l of distilled water and fluorescence reading was performed in a fluorimeter (λ_{exc} = 535 nm; λ_{em} = 566 nm). For the calibration curve, a stock solution of **Cy7** in blank plasma from mouse was prepared. Serial dilutions were prepared in the same plasma and 10 μ l of each **Cy7** urine solution was added to 90 μ l of distilled water and measured in the fluorimeter under the same condition.

5.10.18 Ex vivo IVIS studies. Mice were immediately sacrificed after collecting the urine by CO₂ exposure in a euthanasia chamber, and tumours and organs (lungs, liver, kidney, spleen, brain or bladder) were immediately harvested and freshly analyzed by IVIS. **Cy7** fluorophore was detected using an excitation wavelength of 535 nm and an emission wavelength of 640 nm, time exposure 1 s. Fluorescence Images were taken on an IVIS spectrum imaging system and analyzed and quantified by using the Living Imaging software from Caliper Life Sciences.

5.10.19 Ki67 immunohistochemistry. Tumours were fixed with 4% paraformaldehyde (PFA) in PBS for 4 h, embedded in paraffin, sectioned at 5 μ m and mounted onto pre-coated slides. Sections were dewaxed, incubated with the primary antibody Ki67 (Cell Signaling, at 1:800) and then with the corresponding peroxidase-conjugated secondary antibody in an automated immunostaining platform (Leica Microsystems Bond RXm). After the peroxidase detection, the sections were counterstained with hematoxylin, dehydrated, and coverslipped.

5.10.20 Statistical analyses. All the statistical analyses were conducted in GraphPad 5.0 (Prism). All the sample sizes and statistical tests are specified in the figure legends. Comparisons of results between groups were made by One-way

ANOVA at 95% confidence. For each animal experiment, groups were established before tumourigenesis or treatment with **Cy7Gal** or **WOS-Cy7Gal**, and therefore no randomization was used in the allocation of groups. Investigators were not blinded to the groups and treatments during the experiments.

5.10.21 Cy7 and Cy7Gal quantum yield measurements

Quantum yields values were measured employed rhodamine 6G as standard ($\Phi = 0.95$) using the equation:

$$\frac{\Phi_x}{\Phi_s} = \frac{S_x}{S_s} \times \frac{1 - 10^{-A_s}}{1 - 10^{-A_x}} \times \frac{n_x^2}{n_s^2}$$

where x and s indicate the unknown and standard solution, respectively, Φ is the quantum yield, S is the area under the emission curve, A is the absorbance at the excitation wavelength and n is the refraction index.

5.10.22 Cy7 fluorescence emission at different pH.

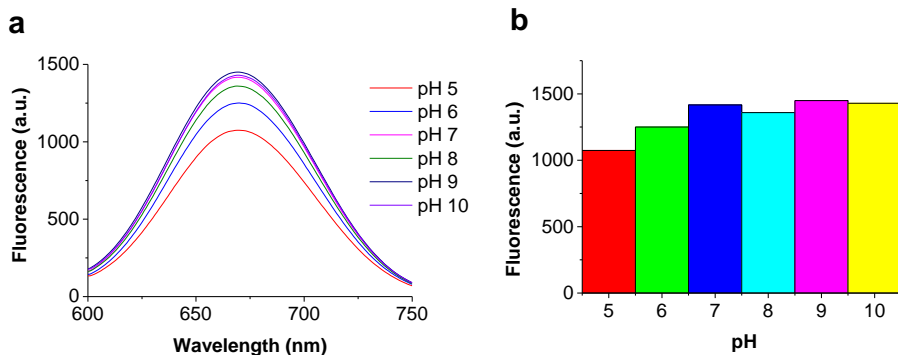


Figure S1. . (a) Fluorescence spectra ($\lambda_{\text{ex}} = 580$ nm) of **Cy7** (10^{-5} M) H_2O at pH 5, 6, 7, 8, 9 and 10. (b) Emission intensity at 665 nm ($\lambda_{\text{ex}} = 580$ nm) of **Cy7** (10^{-5} M) H_2O solutions at pH 5, 6, 7 8, 9 and 10.

5.10.23 Hydrolysis of Cy7Gal by human β -Galactosidase and interferents.

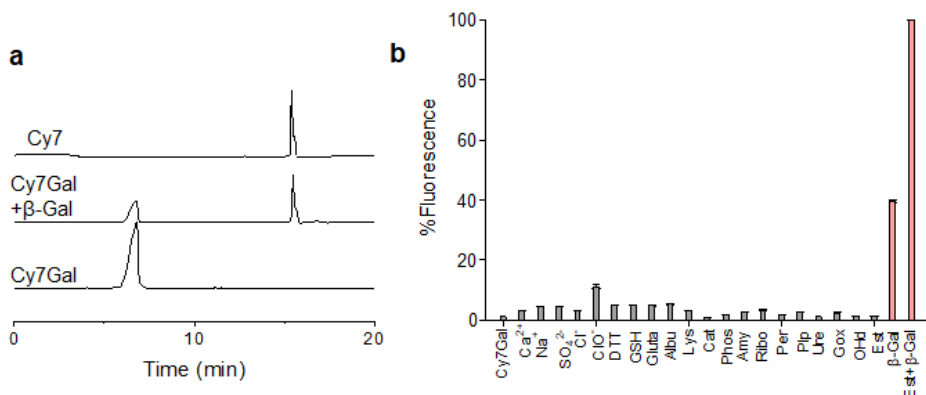


Figure S2. (a) Chromatograms of **Cy7**, **Cy7** + β -Gal and **Cy7Gal**. For hydrolysis studies, aqueous solutions of **Cy7** and **Cy7Gal** at a concentration of 10^{-5} M (pH 7) were prepared. Human β -galactosidase was then added (5 μ l) to **Cy7Gal** solutions and chromatograms were acquired after 30 min ($\lambda_{\text{abs}} = 358$ nm for **Cy7Gal** and $\lambda_{\text{abs}} = 254$ nm for **Cy7**) with a Waters 1525 binary HPLC pump equipped with a Waters 2990 diode array detector. Chromatograms were obtained using Empower 3 software. Conditions: Kromasil-C18 column, 0.8 mL/min, H₂O:MeOH gradient elution: 90:10 to 10:90. Data analysis was performed using OriginPro8 software. (b) Fluorescence intensity changes of **Cy7Gal** solutions (20 μ M) treated with β -galactosidase and with interfering species. From left to right: Blank (only **Cy7Gal**, 20 μ M), Ca²⁺, Na⁺, SO₄⁻, Cl⁻, ClO⁻, DTT (DL-dithiothreitol), GSH (γ -L-glutamyl-L-cysteinyl-glycine), Glu (glutamate), Albu (albumin from human serum), Lys (lysozyme from chicken egg white), Cat (catalase from bovine liver), Phos (phosphatase Alkaline from porcine kidney), Amy (alfa-amylase from porcine pancreas), Ribo (ribonuclease A from bovine pancreas), Per (peroxidase from horseradish), Plp (Pphosphorylase a from rabbit muscle), Ure (urease from *Canavalia ensiformis* (Jack bean) Type III), Gox (glucose oxidase from *Aspergillus niger*), OHd (alcohol dehydrogenase from *Saccharomyces cerevisiae*), Est (esterase from porcine liver), β -Gal (human β -galactosidase). Cations (150 μ M), anions (150 μ M), amino acids (150 μ M), proteins (150 μ g/mL) and enzymes (150 μ g/mL). All measurements were acquired at 37 $^{\circ}$ C for 0.5 h. The data are the mean \pm s.d. n = 3 independent experiments. $\lambda_{\text{ex}} = 580$ nm, $\lambda_{\text{em}} = 665$ nm.

5.10.24 Silencing and western blotting experiments of β -galactosidase

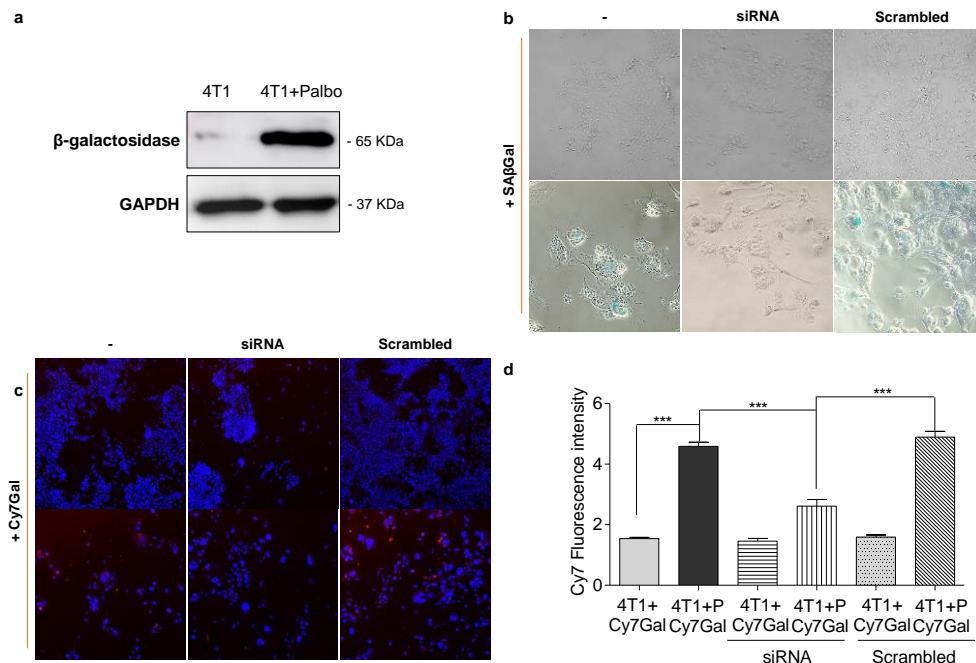


Figure S3. GLB1 transient downregulation inhibits **Cy7Gal** fluorescence in senescent cells and western blotting support the overexpression of β -Galactosidase in senescent 4T1 cells. (a) Western blot analysis of β -galactosidase expression in the control or senescent 4T1 cells. (b) Representative images of SA- β -Gal staining of control and palbociclib-treated 4T1 cells 48 h after transfection with hs.Ri.GLB1.13.3 siRNA and scrambled siRNA. (c) Confocal images of control 4T1 and 4T1 treated with palbociclib before and after transfection with hs.Ri.GLB1.13.3 siRNA and scrambled siRNA in presence of 20 μ M of **Cy7Gal** probe. Cellular nucleus was stained with Hoechst 33342. (d) Quantification of the fluorescence emission intensity from obtained confocal images of control 4T1 and 4T1 cells treated with palbociclib before and after transfection with hs.Ri.GLB1.13.3 siRNA and scrambled siRNA in presence of 20 μ M of **Cy7Gal** probe.

5.10.25 X-Gal staining of kidney, liver and tumors from BALB/cByJ female mice carrying orthotopic 4T1 mammary tumors with or without palbociclib treatment

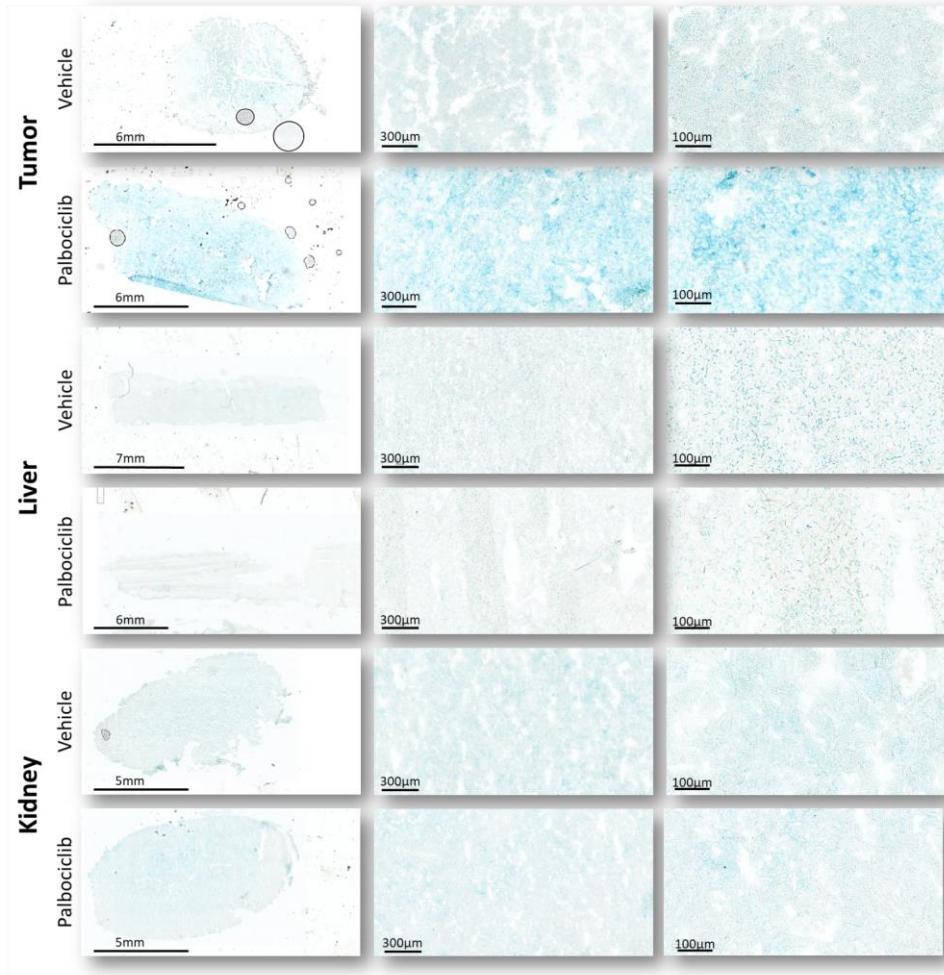


Figure S4. Representative images of kidney, liver and tumors from BALB/cByJ mice treated with vehicle or with palbociclib after X-Gal assay for SA-β-Gal activity. Note that tumours from palbociclib-treated mice show a prominent blue staining after X-Gal assay, indicating a higher SA-β-Gal activity in comparison to the rest of organs.

5.10.26 Images of BALB/cByJ female mice bearing 4T1 mammary tumors treated with palbociclib and i.p. injected with Cy7Gal

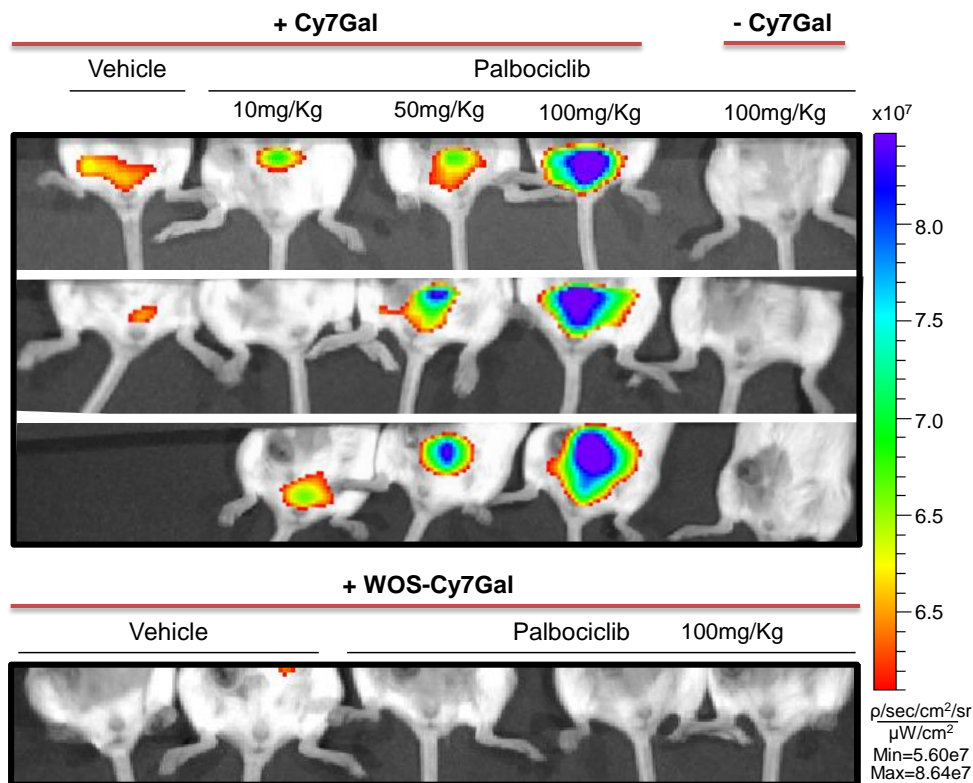


Figure S5. Top: IVIS images of BALB/cByJ female mice bearing 4T1 breast tumor treated by oral gavage with palbociclib (10, 50 and 100 mg/Kg) i.p. injected with **Cy7Gal** (left) and BALB/cByJ female mice bearing 4T1 orthotopic tumors treated by oral gavage with 100 mg/Kg palbociclib (right). Bottom: IVIS images of BALB/cByJ female mice bearing 4T1 breast tumor i.p. injected with **WOS-Cy7Gal** (left) and BALB/cByJ female mice bearing 4T1 orthotopic tumors treated by oral gavage with 100 mg/Kg palbociclib and i.p. injected with **WOS-Cy7Gal** (right).

5.10.27 Fluorophore biodistribution in BALB/cByJ mice bearing 4T1 mammary tumours treated with palbociclib and in the animal model of accelerated aging SAMP8 and its control SAMR1, after i.p. injection with Cy7Gal or WOS-Cy7Gal.

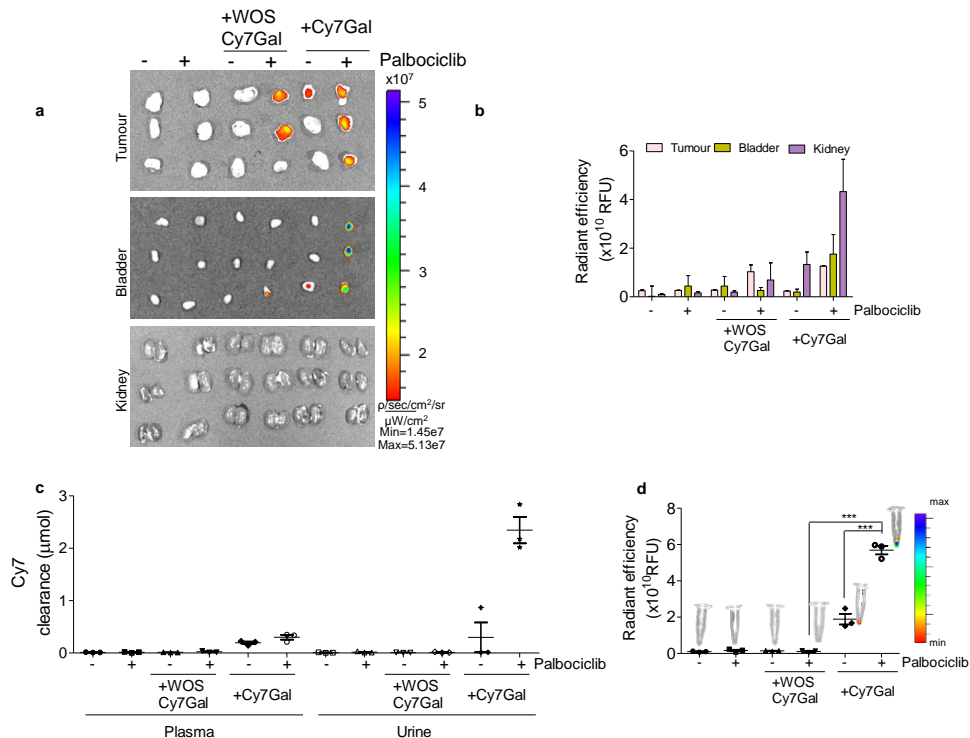


Figure S6. *In vivo* biodistribution study of **Cy7Gal** and **WOS-Cy7Gal** using two different animal models. (a) IVIS images of tumours, bladder and kidney. From left to right: vehicle mice, mice treated with 100 mg/Kg of palbociclib, vehicle mice i.p. injected with **WOS-Cy7Gal** probe, mice treated with 100 mg/Kg of palbociclib and i.p. injected with **WOS-Cy7Gal** probe, vehicle mice i.p. injected with **Cy7Gal** probe, mice treated with 100 mg/Kg of palbociclib and i.p. injected with **Cy7Gal** probe. (b) Quantification of average radiance intensity from organs and tumors showed in (a) images. (c) μ moles of **Cy7** excreted through urine or present in plasma of vehicle mice or mice treated with 100 mg/Kg of palbociclib. Values are expressed as mean \pm SEM. (d) Average radiance intensity from urine ascribed to the renal clearance of **Cy7** or **WOS-Cy7** fluorophores in vehicle mice or mice treated with 100 mg/Kg of palbociclib.

5.10.28 Images of 2 and 14 months old BALB/cByJ female mice i.p. injected with Cy7Gal

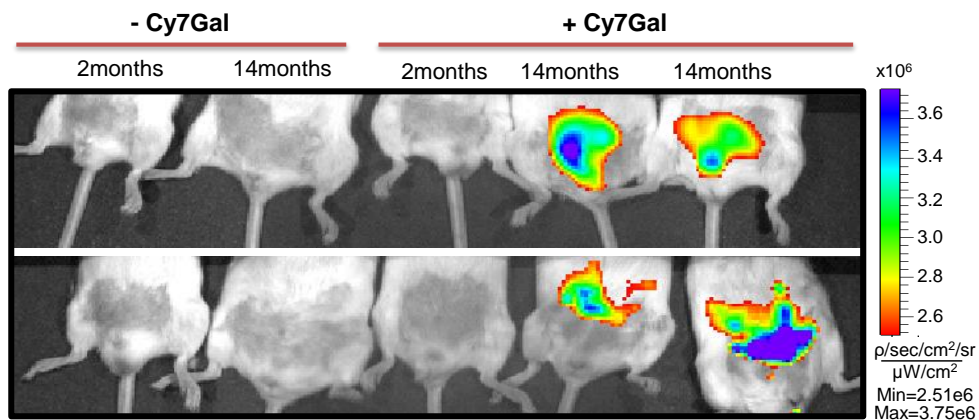


Figure S7. IVIS images of 2 and 14 months old BALB/cByJ female mice (left) and images of 2 and 14 months old BALB/cByJ female mice i.p. injected with **Cy7Gal** (right).

**Chapter 6 | Real time *in vivo* detection
of cellular senescence through the
controlled release of the NIR
fluorescent dye Nile Blue**

Real time *in vivo* detection of cellular senescence through the controlled release of the NIR fluorescent dye Nile Blue

Beatriz Lozano-Torres,^{a,b,c,d,†} Juan F. Blandez,^{a,b,d,†} Irene Galiana,^{a,b} Alba García-Fernández,^{a,b,c} María Alfonso,^a María D. Marcos,^{a,b,c,d} Mar Orzáez,^{b,e} Félix Sancenón,^{a,b,c,d*} and Ramón Martínez-Mañez^{a,b,c,d*}

^a Instituto Interuniversitario de Investigación de Reconocimiento Molecular y Desarrollo Tecnológico (IDM), Universitat Politècnica de València, Universitat de València. Camino de Vera s/n, 46022-Valencia, Spain. E-mail: rmaez@qim.upv.es

^b Unidad Mixta UPV-CIPF de Investigación en Mecanismos de Enfermedades y Nanomedicina, Universitat Politècnica de València, Centro de Investigación Príncipe Felipe, Valencia, Spain.

^c CIBER de Bioingeniería, Biomateriales y Nanomedicina (CIBER-BBN).

^d Unidad Mixta de Investigación en Nanomedicina y Sensores. Universitat Politècnica de València, IIS La Fe, Valencia, Spain.

^e Centro de Investigación Príncipe Felipe. Eduardo Primo Yúfera, 3. Valencia 46012, Spain.

[†]Both authors contributed equally to this work

Published online: May 16, 2020

(Reprinted with permission from *Angew. Chem. Int. Ed.*, **2020**, *59*, 15152

Copyright © 2020 Wiley-VCH Verlag GmbH & Co. KGaA, Weinheim

6.1 Abstract

In vivo optical detection of cellular senescence is accomplished by using mesoporous silica nanoparticles loaded with the NIR-FDA approved Nile Blue (**NB**) dye and capped with a galactohexasaccharide (**S3**). Emission at 672 nm of **NB** is highly quenched inside **S3**, yet a remarkable emission enhancement is observed upon cap hydrolysis in the presence of β -galactosidase and dye release. The efficacy of the probe to optically detect cellular senescence is tested *in vitro* in melanoma SK-Mel-103 and breast cancer 4T1 cells and *in vivo* in palbociclib-treated BALB/cByJ mice bearing breast cancer tumor.

6.2 Introduction

Cellular senescence is a stable state of cell cycle arrest necessary for maintaining the organism homeostasis.^[1] However, the improper elimination of senescent cells, provokes local inflammation, tissue degeneration and contributes to aging.^[2] Today scientific evidence supports that accumulation of senescent cells is involved in the pathophysiology of many age-related diseases^[3] and has boosted the concept that senescent cells is an attractive therapeutic target.^[4,5] Recent reports, using *in vivo* models, evidence that a wide variety of diseases can be ameliorated by the elimination of senescent cells.^[6,7] Characteristic signs of cellular senescence include changes in cell morphology,^[8] the appearance of condensed nuclear chromatin foci, known as senescence-associated heterochromatic foci (SAHF),^[9] and the overexpression or activation of tumor suppressor proteins such as p53, p16^{INK4a} and p21 that contribute to cell cycle arrest.^[10] Moreover, one of the most widely used markers to detect cellular

senescence is the overexpression of lysosomal β -galactosidase, also referred to as senescence-associated β -galactosidase (SA- β -Gal).^[11]

Measurement of SA- β -Gal activity using chromo-fluorogenic probes has become popular as an easy and simple procedure to detect senescence.^[12,13] The use of molecularly imprinted nanopartilces has also been described recently for senescence detection.^[14,15] However, most of the actual probes are suitable for *in vitro* studies, whereas probes to detect cellular senescence *in vivo* in realistic senescence models are scarce. One general drawback of most of these probes is that, even in realistic senescence models, detection is only possible after the animal sacrifice. Consequently, the development of suitable methods for *in vivo* senescence detection remains an unresolved problem.^[2]

Based on the above, we report herein the use of nanoparticles^[16] for *in vivo* detection of cellular senescence using a NIR fluorophore. The probe consists of galactohexasaccharide-capped mesoporous silica nanoparticles (MSNs) which are able to release their cargo in senescent cells due to the hydrolysis of the capping oligosaccharide by SA- β -Gal.^[17] We tested a number of fluorophores as cargo and finally selected Nile Blue (**NB**) due to its remarkable features as *in vivo* imaging agent. **NB** is an organic dye approved by the Food and Drug Administration (FDA) for human use^[18] and it exhibits near infrared (NIR) emission at 672 nm.^[19,20] Most importantly, **NB** is an aromatic planar fluorophore, which is highly quenched at high concentrations or in confined spaces as it forms non-emissive π -stacked aggregates.^[21]

MSNs have been widely used as drug delivery systems due to their properties, such as biocompatibility and easy functionalization.^[22] In addition to MSNs, other carriers for cargo delivery such as liposomes, micelles, polymers, etc have also been used in recent years.^[23] In our case, MSNs were chosen as nanocarriers, due

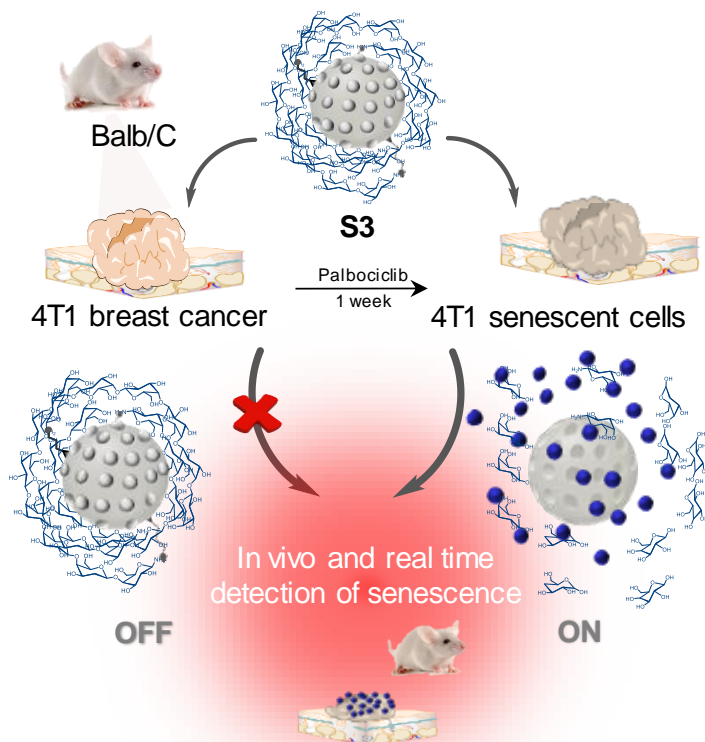


Figure 1. Representation of **S3** activation in BALB/cByJ female mice orthotopically injected with 4T1 cells to generate breast tumors. After tumor formation, mice were administered with palbociclib to generate senescence and treated with **S3** achieving *in vivo* detection of cellular senescence.

to their high loading capacity, allowing the **NB** dye to be entrapped at high concentration resulting in effective dye-dye π -stacking interactions and quenching. This compact packaging together with the gating capability exerted by the capping galactohexasaccharide (*vide infra*) would hardly be obtained using other nanocarriers. In fact, MSNs are well suited for the preparation of on-command delivery carriers by the functionalization of the outer surface with (bio)molecules that prevent payload release unless exposed to specific stimuli.^[23] Besides, in MSN the cargo is simply encapsulated, while in some other nanoparticles cargo molecules need to be covalently linked.

The prepared nanoparticles (i.e. **S3** in Figure 1) are therefore poorly emissive, yet SA- β -Gal-induced hydrolysis of the capping hexagalacto-saccharide to give galactose residues, is expected to result in **NB** release, selectively inducing a marked NIR emission enhancement in senescent cells. Targeting of senescent cells *in vitro* with **S3** is validated in SK-Mel-103 (human melanoma) and 4T1 (murine breast cancer) cell lines treated with palbociclib. Moreover, *in vivo* detection of cellular senescence is demonstrated in BALB/cByJ mice bearing breast cancer tumor treated with senescence-inducing chemotherapy.

6.3 Results and discussion

6.3.1 Synthesis, Characterization, Spectroscopic Features and Mechanism

S3 is easily prepared from mesoporous silica nanoparticles,^[24] which are loaded with **NB**, externally functionalized with APTES and finally capped with $\beta(1,4)$ -hexagalacto-saccharide (Scheme S1). The mesoporous structure in **S3** and the starting mesoporous silica material (**S0**) was clearly observed by HR-TEM (Figure 2a, b and S1a) and by powder X-ray diffraction (Figure S1b). **S3** was also characterized by porosimetry (Figure S2a, b and Table S1), ATR (Figure S3) and DLS (Figure S4). Moreover, from dye delivery experiments and thermogravimetric studies, the content of **NB** in **S3** was determined to be 0.45 mmol g⁻¹ of solid (Figure S5).

Quenching of **NB** inside the pores of **S3**, was assessed. Free **NB** solutions presented much higher fluorescence than suspensions of **S3**, which showed negligible emission at equivalent **NB** concentrations (Figure 2c). Moreover, confocal images of **S3** demonstrated that capped nanoparticles were poorly

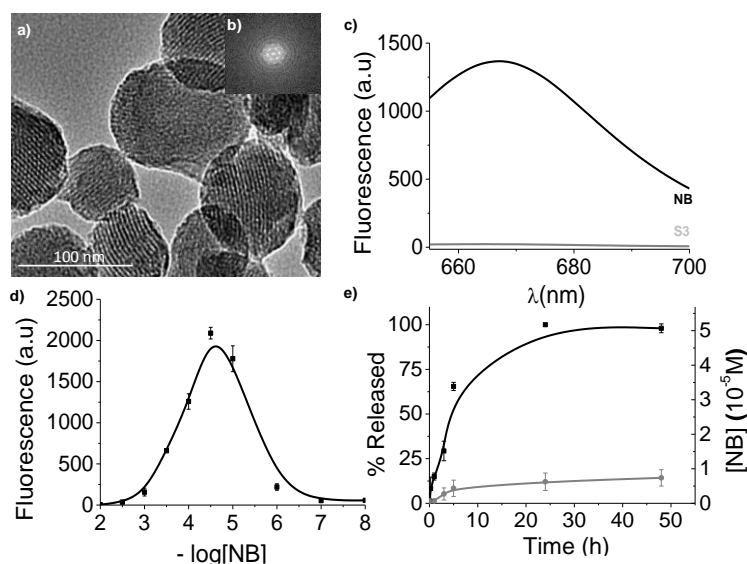


Figure 2. (a) HR-TEM images of **S3**, (b) TEM-EDX of **S3**. (c) Fluorescence of a **NB** solution (1.81×10^{-4} M) and of **S3** suspensions at equivalent concentrations of the dye. (d) Emission intensity of **NB** solutions vs fluorophore concentration. (e) Release profile of **S3** in the absence (grey line) and in the presence of β -Gal (black line). Experiments were carried out in water-DMSO 99:1 v/v mixtures at pH 4.5. Error bars are expressed as 3σ

emissive (Figure S6). Quenching of **NB** at high concentrations was also studied in solution by monitoring the emission of the fluorophore at 666 nm ($\lambda_{\text{exc}} = 635$ nm) at different **NB** concentrations in water (pH = 4.5)-DMSO 99:1 v/v mixtures. Emission of **NB** solutions increased until a concentration of ca. 1.0×10^{-4} M, whereas at higher concentrations the fluorescence decreased. In fact, **NB** concentrations higher than 10^{-3} M are poorly emissive (Figure 2d). From the amount of **NB** loaded and the specific pore volume in **S3** a molar concentration of the dye in the pores of ca. 0.49 M was calculated which is in agreement with the low emission observed for **S3** in Figure 2c.

Delivery of **NB** from **S3** was studied in the presence and in the absence of β -Gal enzyme (Figure 2e). **S3** show a marked **NB** delivery in the presence of β -Gal of ca. 90% of the maximum dye released after 24 h, which corresponded to 31.4 % (5.69×10^{-5} M) of the dye entrapped (Figure S7). In contrast a low **NB** release in the

absence of β -Gal was found. Release in the presence of β -Gal is due to the hydrolysis of glycosidic bonds in the capping galacto-saccharide which reduced steric crowding around the pores allowing **NB** delivery.

6.3.2 *In vitro* validation

Specific targeting of senescent cells *in vitro* with **S3** was demonstrated in SK-Mel-103 (human melanoma) and 4T1 (murine breast cancer) cells treated with 5 μ M palbociclib (a CDK4/6 inhibitor which suppresses DNA replication inducing cell cycle arrest) for two weeks to induce senescence. Senescence was confirmed by X-Gal staining (Figures 3a,3e, 3i and 3m).

Confocal microscopy studies of palbociclib-treated SK-Mel-103 and 4T1 cells, incubated with **S3**, revealed an intense fluorescent signal (Figure 3g and 3o), whereas non-senescent SK-Mel-103 and 4T1 cells treated with **S3** presented weak fluorescence (Figure 3c and 3k). Both control and senescent SK-Mel-103 and 4T1 cells showed also negligible background (Figures 3b, 3f, 3j and 3n respectively). In addition, it was found that control and senescent cells treated with equivalent doses of free **NB** presented nearly the same fluorescence (Figures 3d, 3h, 3l and 3p, see also Figure S8). Quantification of fluorescence showed 7-fold emission enhancement in senescent SK-Mel-103 cells treated with **S3** compared to controls (Figure 3q). For the 4T1 cell line, the emission enhancement of senescent cells treated with **S3** when compared to control 4T1 cells was 10-fold. Results are indicative of **S3** uptake and galacto-oligosaccharide hydrolysis by SA- β -Gal in senescent cells, resulting in **NB** release. Moreover it was found that **S3** nanoparticles were not toxic for both control and senescent cells (Figure S9).

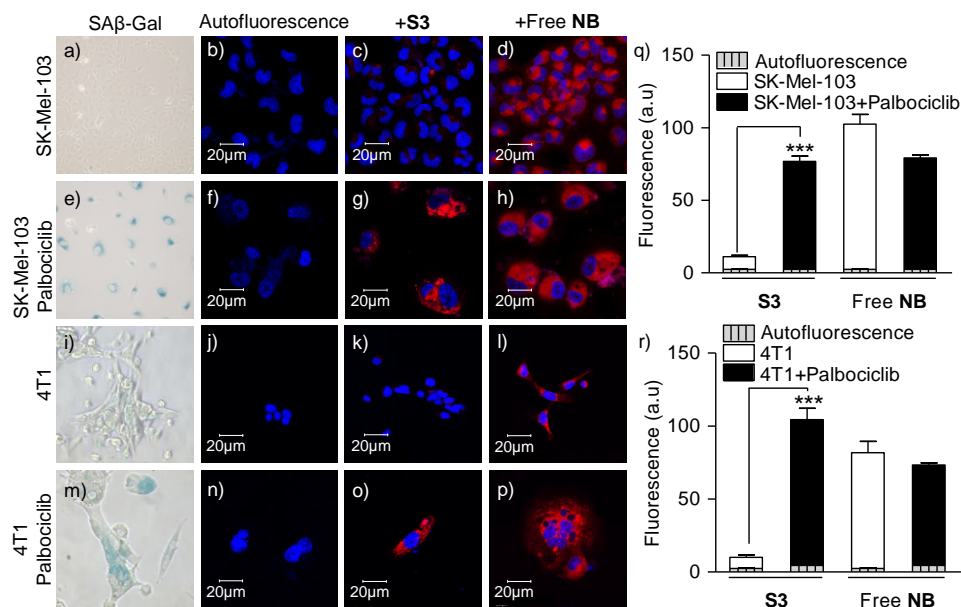


Figure 3. (a,e,i,m) X-Gal assay for detection of SA- β -Gal expression in (a) control and (e) senescent SK-Mel-103 cells and in (i) control 4T1 and (m) senescent 4T1 cells. (b,c) Confocal images of control SK-Mel-103 cells (b) in the absence or (c) in the presence of **S3**. (f,g) SK-Mel-103 cells treated with palbociclib (f) in the absence (g) or in the presence of **S3**. (d,h) Confocal images of (d) control SK-Mel-103 cells or (h) SK-Mel-103 cells treated with palbociclib in the presence of equivalent doses of free **NB**. (j,k) Confocal images of control 4T1 cells (j) in the absence or (k) in the presence of **S3**. (n,o) 4T1 cells treated with palbociclib (n) in the absence (o) or in the presence of **S3**. (l,p) Confocal images of (l) control 4T1 cells or (p) 4T1 treated with palbociclib in the presence of equivalent doses of free **NB**. Cells were incubated with **S3** (7.8 μ g/ml) for 4.5 h in DMEM (10% FBS) in 20% O₂ and 5% CO₂ at 37°C, washed three times and stained with Hoechst (1.5 ng/ml) for 15 min. Confocal images were acquired by using confocal microscope (Leica TCS SP8 AOBS). Representative images from repeated experiments (n=3) are shown. (q) Quantification of fluorescence emission ascribed to released **NB** in control and palbociclib-treated SK-Mel-103 cells incubated with **S3** and quantification of fluorescence emission upon treatment with equivalent doses of free **NB**. Autofluorescence is the emission observed in SK-Mel-103 cells without treatment with **S3** or free **NB**. (r) Quantification of fluorescence emission ascribed to released **NB** in control and palbociclib-treated 4T1 cells incubated with **S3** and quantification of fluorescence emission upon treatment with equivalent doses of free **NB**. Autofluorescence is the emission observed in 4T1 cells without treatment with **S3** or free **NB**. Error bars represent s.d.

6.3.3 *In vivo* validation

In vivo detection of cellular senescence with **S3** was validated in mice bearing breast tumors treated with senescence-inducing chemotherapy. For this purpose,

BALB/cByJ female mice were orthotopically injected with 4T1 (mouse mammary carcinoma) cells (0.5×10^6 cell/mouse) to generate breast tumors.

Mice were divided into four groups: (A) control individuals with 4T1 tumors; (B) control individuals with 4T1 tumors administered with **S3**; (C) mice only administered with palbociclib; and (D) individuals with 4T1 tumors treated with palbociclib and **S3**. Groups C and D were daily treated by oral gavage with palbociclib after tumor development to induce senescence and arrest of tumor growth. Once completed 7 days of palbociclib treatment, **S3** nanoparticles were intravenously administered to groups B and D, and mice were monitored by an *in vivo* imaging system (IVIS) at different time points for 48 h. No autofluorescence was observed from control (A) and palbociclib (C) treated mice (Figure S10). Mice from groups A, B and C showed negligible fluorescence in the tumor area, while a strong fluorescent signal was observed for group D, which was administered both with palbociclib and **S3** (Figure 4a). The peak of maximum fluorescence in mice treated with palbociclib and **S3** (group D) was observed 24-36 h post-injection of the nanoparticles (Figure 4a), whereas a clear decrease in the fluorescence signal was found at 48 h. Quantification of the relative values of radiance ($\text{p/s/cm}^2/\text{sr} \times 10^{10}$) showed an enhancement of 4.3 fold at 24 h and 7.3 fold at 36 h in palbociclib+**S3** treated mice when compared to vehicle ones (Figure 4b).

Mice were euthanized and blood, lungs, liver, kidney, spleen and tumors were *ex vivo* analyzed. Senescence in tumors from mice treated with palbociclib was confirmed by X-Gal staining (Figure 4c) and reduced immunostaining of the Ki67 proliferation marker indicative of cell cycle arrest (Figure S11). IVIS images of excised organs and tumors from vehicle (A) or palbociclib-treated mice (C) did not show any fluorescence (Figures 4c, i) and iii)). Similarly, tumors from vehicle mice injected with **S3** (B) did not show any noticeable fluorescent signal (Figure 4c, ii)). In contrast, strong emission (ca. 17.6 fold) was observed in tumors from mice treated with palbociclib and intravenously injected with **S3** (Figure 4c, iv and

Figure 4d). Biodistribution of nanoparticles was studied by determining silicon levels in various organs by inductively coupled plasma mass spectroscopy (ICP-MS) (Figure S12). Nanoparticles reach both senescent and non-senescent tumors at 24 h whereas levels of Si are significantly reduced 48 h post-injection, which is consistent with the patterns of fluorescence signal (*vide ante*). **S3** also accumulated in spleen, lungs and kidney at 24 h, whereas maximum silicon accumulation was found in spleen at 48 h. Note that even though some mesoporous silica nanoparticles accumulate in liver, spleen or kidney, negligible fluorescence was detected in these organs 24 h post injection. This is due to the very low emission from the capped **S3** (due to π -stacking **NB** interactions in the pores) and also indicates that nanoparticles remain capped in these organs which did not overexpress SA- β -Gal enzyme. Blood biochemistry and hematology analysis of different parameters, such as albumin (ALB), bilirubin (BIL), alkaline phosphatase (AKP), glutamic pyruvic transaminase (GPT) and aspartate transaminase (GOT), showed no noticeable signs of organ damage and systemic inflammatory response after nanoparticles administration (B and D) when compared to **S3** untreated (A and C) groups (Figure S13).

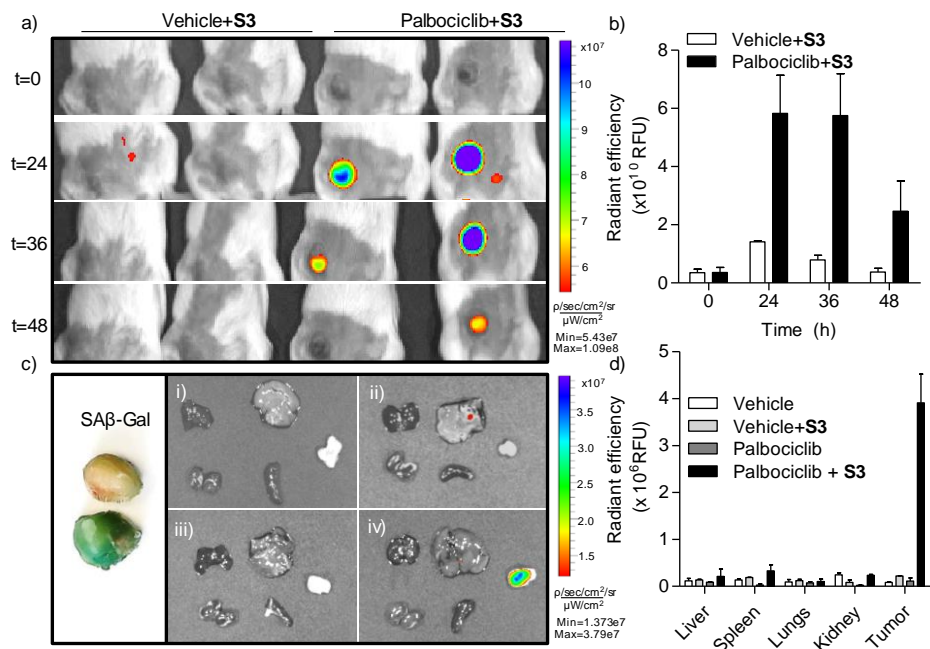


Figure 4. (a) IVIS images at different time points of BALB/cByJ female mice bearing 4T1 breast tumor. From left to right control mice treated with **S3** (two mice from group B) and BALB/cByJ mice treated by oral gavage with palbociclib (senescent tumors) for 1 week and intravenously injected with **S3** (two mice from group D). (b) Quantification of fluorescence emission intensity from tumor signals with time. Error bars represent s.d. (c) X-Gal assay for SA- β -Gal expression in tumors from control group A (up) and palbociclib-treated group C (bottom). (i,ii, iii,iv) IVIS images of organs and tumors from BALB/cByJ female mice bearing 4T1 breast tumor. From left to right and from top to bottom: lungs, liver, tumor, kidney and spleen. (i) Control mice (group A). (ii) Control mice treated with **S3** (group B, 4 mg/ml 200 μ l). (iii) BALB/cByJ female mice bearing 4T1 breast tumor treated oral gavage with palbociclib for 1 week (group C). (iv) Palbociclib-treated mice intravenously injected with **S3** (group D, 4 mg/ml 200 μ l). Mice were sacrificed 24 h post-treatment for these images. (d) Quantification of fluorescence emission from organs and tumors in i,ii,iii and iv images. Error bars represent s.d.

6.4 Conclusions

As summary, we describe here MSN loaded with **NB** dye and capped with a galacto-oligosaccharide for the *in vivo* detection of cellular senescence. **S3** nanoparticles are poorly emissive due to π -stacking interactions of **NB** molecules densely packed onto the mesopores, yet **NB** is selectively released in senescent

cells resulting in a marked emission enhancement. *In vitro* targeting of senescent cells with **S3** was validated in SK-Mel-103 and 4T1 cells treated with palbociclib. A remarkable enhanced emission in palbociclib-treated SK-Mel-103 and 4T1 senescent cells was observed when incubated with **S3** in comparison with control cells. **S3** was validated *in vivo* in BALB/cByJ female mice orthotopically injected with 4T1 cells to generate breast tumors and treated with palbociclib. *In vivo* IVIS images showed a remarkable emission enhancement (4.3 fold at 24 h and 7.3 fold at 36 h) in tumors from mice treated with palbociclib and intravenously injected with **S3**, whereas negligible signal was found in mice only treated with **S3** and in palbociclib-treated mice without **S3** administration. In good accordance, *ex vivo* IVIS images showed that fluorescence ascribed to **NB** was only observed in senescent tumors (17.6-fold enhancement) but not in control tumors or other organs. The performance in terms of selectivity and sensitivity makes **S3** an efficient OFF-ON probe for the *in vivo* detection of senescence. We anticipate that this or similar probes able to detect cellular senescence *in vivo* will become essential tools to follow treatment response and efficacy of senotherapies in a wide range of aged-related diseases.

6.5 Acknowledgements

R.M. thanks financial support from the Spanish Government (RTI2018-100910-B-C41 and RTI2018-101599-B-C22 (MCUI/AEI/FEDER, UE)) and the Generalitat Valenciana (PROMETEO 2018/024). M.O. thanks the financial support from SAF2017-84689-R project and MINECO/AEI/FEDER, UE and the Generalitat Valenciana (PROMETEO/2019/065). B.L.T. is grateful to the Spanish Ministry of Economy for her PhD grant. I.G. thanks her contract from IDM. J. F.-B and M. A. thank the UPV for their postdoctoral fellowship.

6.6 References

1. S. He, N. E. Sharpless, *Cell* **2017**, *169*, 1000–1011.
2. a) B. Lozano-Torres, A. Estepa-Fernández, M. Rovira, M. Orzáez, M. Serrano, R. Martínez-Máñez, F. Sancenón, *Nat. Rev. Chem.* **2019**, *3*, 426-441; b) D. Muñoz-Espín, M. Serrano, *Nat. Rev. Mol. Cell Biol.* **2014**, *15*, 482–496.
3. A. Hernandez-Segura, J. Nehme, M. Demaria, *Trends Cell Biol.* **2018**, *28*, 436–453.
4. D. J. Baker, B. G. Childs, M. Durik, M. E. Wijers, C. J. Sieben, J.A. Zhong, R. Saltness, K. B. Jeganathan, G. C. Verzosa, A. Pezeshki, K. Khazaie, J. D. Miller, J. M. van Deursen, *Nature* **2016**, *530*, 184–189.
5. A. Soto-Gamez, M. Demaria, *M. Drug Discov. Today* **2017**, *22*, 786–795.
6. J. L. Kirkland, T. Tchkonja, Y. Zhu, L. J. Niedernhofer, P. D. Robbins, *J. Am. Geriatr. Soc.* **2017**, *65*, 2297–2301.
7. L. J. Niedernhofer, P. D. Robbins, *Nat. Rev. Drug Discov.* **2018**, *17*, 377–377.
8. L. Hayflick, P. S. Moorhead, *Exp. Cell Res.* **1961**, *25*, 585–621.
9. R. Zhang, P. D. Adams, *Cell Cycle* **2007**, *6*, 784–789.
10. J. Campisi, *Cell* **2005**, *120*, 513–522.
11. G. P. Dimri, X. Lee, G. Basile, M. Acosta, G. Scott, C. Roskelley, E. E. Medrano, M. Linskens, I. Rubelj, O. Pereira-Smith, *Proc. Natl. Acad. Sci. U.S.A.* **1995**, *92*, 9363–9367.
12. B. Lozano-Torres, I. Galiana, M. Rovira, E. Garrido, S. Chaib, A. Bernardos, D. Muñoz-Espín, M. Serrano, R. Martínez-Máñez, F. Sancenón, *J. Am. Chem. Soc.* **2017**, *139*, 8808–8811.
13. D. Asanuma, M. Sakabe, M. Kamiya, K. Yamamoto, J. Hiratake, M. Ogawa, N. Kosaka, P. L. Choyke, T. Nagano, H. Kobayashi, Y. Urano, *Nat. Commun.* **2015**, *6*, 6463.
14. D. Muñoz-Espín, *Transl. Med. Aging* **2019**, *3*, 1–5.
15. A. E. Ekpenyong-Akiba, F. Canfarotta, H. B. Abd, M. Poblocka, M. Casulleras, L. Castilla-Vallmanya, G. Kocsis-Fodor, M. E. Kelly, J. Janus, M. Althubiti, E. Piletska, S. Piletskyc, S. Macip, *Nanoscale Horiz.* **2019**, *4*, 757–768.
16. a) S. Alberti, G. Soler-Illia, O. Azzaroni, *Chem. Commun.* **2015**, *51*, 6050-6075; b) C. de la Torre, I. Casanova, G. Acosta, C. Coll, M.J. Moreno, F. Albericio, E. Aznar, R. Mangués, M. Royo, F. Sancenón, R. Martínez-Máñez, *Adv. Funct. Mater.* **2015**, *25*, 687–695
17. (a) A. Bernardos, E. Aznar, M.D. Marcos, R. Martínez-Máñez, F. Sancenón, J. Soto, J.M. Barat, P. Amorós, *Angew. Chem. Int. Ed.* **2009**, *48*, 5884–5887; (b) A. Agostini, L. Mondragón, A. Bernardos, R. Martínez-Máñez, M.D. Marcos, F. Sancenón, J. Soto, A. Costero, C. Manguan-García, R. Perona, M. Moreno-Torres, R. Aparicio-Sanchís, J.R. Murguía, *Angew. Chem. Int. Ed.* **2012**, *51*, 10556–10560; (c) D. Muñoz-Espín, M. Rovira, I. Galiana, C. Giménez, B. Lozano-Torres, M. Paez-Ribes, S. Llanos, S. Chaib, M. Muñoz-Martín, A. C. Uceró, G. Garaulet, F. Mulero, S. G. Dann, T. Van Arsdale, D. J. Shields, A. Bernardos, J. R. Murguía, R. Martínez-Máñez, M. Serrano, *EMBO Mol. Med.* **2018**, e9355.
18. J. Mérian, J. Gravier, F. Navarro, I. Texier, *Molecules* **2012**, *17*, 5564–5591.
19. X. Zhang, S. Bloch, W. Akers, S. Achilefu, *Curr Prot. Cytom.* **2012**, *60*, 12.27.1–12.27.20.
20. W. Fu, C. Yan, Z. Guo, J. Zhang, H. Zhang, H. Tian, W. –H. Zhu, *J. Am. Chem. Soc.* **2019**, *141*, 3171-3177.
21. O. V. Ovchinnikov, A. V. Evtukhova, T. S. Kondratenko, M. S. Smirnov, V. Y. Khokhlov, O. V. Erina, *Vib. Spectrosc.* **2016**, *86*, 181–189.
22. (a) E. Aznar, M. Oroval, J. R. Murguía, R. Martínez-Máñez, F. Sancenón, *Chem. Rev.* **2016**, *116*, 561–718; (b) A. Llopis-Lorente, B. Lozano-Torres, A. Bernardos, R. Martínez-Máñez, F. Sancenón, *J. Mater. Chem. B* **2017**, *5*, 3069-3083; (c) A. García-Fernández, E. Aznar, R. Martínez-Máñez, F. Sancenón, *Small* **2020**, *16*, 1902242.
23. (a) V. Kozlovskaya, B. Xue, E. Kharlampieva, *Macromolecules* **2016**, *49*, 8373-8386; (b) D. K. Mishra, R. Shandilya, P. K. Mishra, *Nanomedicine* **2018**, *14*, 2023-2050; (c) F. Seidi, R. Jenjof, T. Phakkeeree, D. Crespy, *J. Control. Release* **2018**, *284*, 188-212; (d) W. Chen, S. Zhou, L. Ge, W. Wu, X.

Jiang, *Biomacromolecules* **2018**, *19*, 1732-1745; (e) M. Vazquez-Gonzalez, I. Willner, *Langmuir* **2018**, *34*, 14692-14710; (f) R. M. Farid, N. A. H. A. Youssef, A. A. Kassem, *Curr. Pharm. Des.* **2017**, *23*, 6613-6629; (g) D. Lombardo, P. Calandra, D. Barreca, S. Magazu, M. A. Kiselev, *Nanomaterials* **2016**, *6*, 125/1-125/26; (h) A. Bansal, Y. Zhang, *Acc. Chem. Res.* **2014**, *47*, 3052-3060; (i) N. Kamaly, B. Yameen, J. Wu, O. C. Farokhzad, *Chem. Rev.* **2016**, *116*, 2602-2663.
24. B. G. Trewyn, I. I. Slowing, S. Giri, H. -T. Chen, V. S. -Y. Lin, *Acc. Chem. Res.* **2007**, *40*, 846-853.

6.7 Supporting information

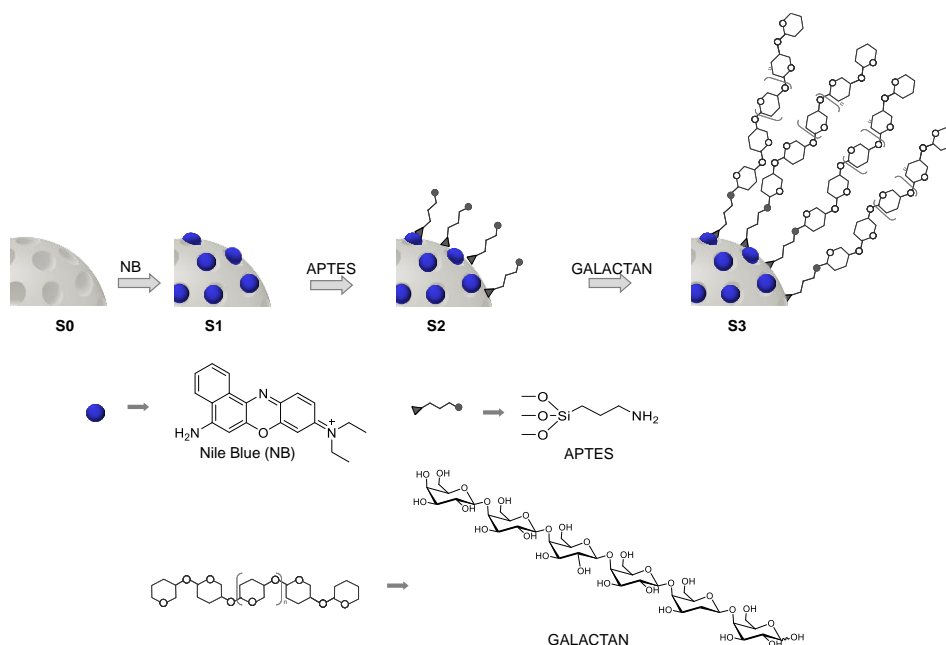
6.7.1 Materials and methods.

Chemical reagents were purchased from Sigma-Aldrich and were used without further purification. Anhydrous solvent and phosphate-buffered saline (PBS) were acquired from Sharlab S.L. Dulbecco's Modified Eagle Medium (DMEM) and fetal bovine serum (FBS) were purchased from Gibco. Palbociclib was acquired from Selleckchem. Flat-bottom-clear 96 well and cellTiter-Glo(R) Luminescent Cell viability were obtained from Promega. Senescence β -Galactosidase Staining KIT was purchased from Werfrem. Anti-Ki67 antibody was acquired from Cell Signaling. Recombinant Human β -Galactosidase-1/GLB1 Protein (Human β -Gal) was purchased from R&D systems a biotechne brand. SK-MEL-103 human melanoma cancer cells and 4T1 breast cancer cells lines were purchased from the American Type Culture Collection (ATCC). BALB/CBY female mice were acquired from Charles River laboratories, France.

High resolution transmission electron microscopy (HR-TEM) images were recorded with a 200 KV in a JEOL JEM 2100F microscope equipped with a X ray detector (XRD) and Powder X-ray diffraction (PXRD) measurements were obtained on a Philips D8 Advance Diffractometer using $\text{CuK}\alpha$ radiation. Thermogravimetric analyses were carried out a TGA/SDTA 851e Mettler Toledo balance, using an oxidant atmosphere (air, 80 mL/min) with a heating program consisting of a heating ramp of 10°C per min from 25°C to 100°C, then temperature was kept at 100°C for 60 min and finally a new heating ramp of 10°C per min from 100°C to 1000°C was applied and an isothermal heating step at the final temperature for 30 min. Porosity of materials was determined by N_2 adsorption-desorption isotherms recorded with a Micromeritics ASAP2010 automated sorption analyzer. Fourier-transform infrared (FTIR) spectra were recorded using a Nicolet 6700 instrument (Thermo scientific, USA) in the 4000–400 cm^{-1} range. Dynamic light scattering

(DLS) measurements were carried out in a Malvern Zetasizer Nano ZS. Absorption spectra were recorded in a JASCO V-650 spectrophotometer and fluorescence spectroscopy was carried out with a JASCO spectrofluorometer FP-8500. Confocal fluorescence images were recorded on a Leica TCS SP8 AOBS. Luminescence was collected in a Wallac VICTOR2™ Multilabel Plate Reader (Pelkin Elmer Sciences) spectrophotometer. Confocal images were analyzed using ImageJ software. IVIS images were analyzed by using the Living Image software. Ki67 immunostainings were performed by an automated immunostaining platform (Leica Microsystems Bond RXm). Silicon determination was performed in an Inductively Coupled Plasma Mass Spectrometer System (ICP-MS) Agilent 7900 in H2 mode, using germanium as internal standard.

6.7.2 Synthesis of materials.



Scheme S1. Synthetic procedure of solid **S3**. NB was loaded into calcined MSNs (**S1**). Then, the external surface of the NB-loaded nanoparticles was functionalized with aminopropyl moieties (**S2**). Finally, $\beta(1,4)$ -hexagalacto-saccharide (GALACTAN) was covalently grafted onto the external surface of **S2** yielding the final solid **S3**.

Synthesis of mesoporous silica nanoparticles (S0). Cetyltrimethyl ammonium bromide (CTAB, 1.00 g, 2.74 mol) was first dissolved in 480 mL of deionized water at 40 °C. Upon total dissolution, aqueous NaOH (2.00 M, 3.5 mL) was added to the CTAB solution, followed by increasing solution temperature to 80 °C. TEOS (5.00 mL, 2.25×10^{-2} mol) was then added dropwise to the surfactant solution. The mixture was allowed to stir for 2 h at 80 °C to obtain a white precipitate. The solid product was obtained by filtration and washed with deionized water until neutral pH and dried at 60 °C for 12 h (mesoporous silica nanoparticles as-made). To prepare the final porous material **S0** the as-synthesized solid was calcined at 550 °C using an oxidant atmosphere for 5 h in order to remove the template phase.

Synthesis of S2. In a typical synthesis, 200 mg of **S0** and Nile Blue (**NB**, 70 mg, 0.16 mmol) were suspended in 5 mL of anhydrous acetonitrile in a round-bottomed flask under inert atmosphere. The mixture was stirred for 24 h at room temperature to obtain **S1**. Then, without the isolation of **S1** nanoparticles, (3-aminopropyl) triethoxysilane, (APTES, 1.4 mg, 6.32 mmol) was added. The final reaction mixture was stirred for 5 h at room temperature. **S2** was recovered by filtration and washed with water (see Scheme S1).

Synthesis of S3. To obtain final **S3**, $\beta(1,4)$ -hexagalacto-saccharide (447 mg) was dissolved in 31 mL of distilled water. After complete dissolution, **S2** (250 mg) and **NB** (7 mg, 0.016 mmol) were added. The suspension was stirred for 20 h at room temperature and the final solid (**S3**) was recovered by centrifugation and washed with distilled water (see Scheme S1).

6.7.3 Materials characterization.

All the prepared solids were characterized using standard techniques. At this respect, Figure S1 shows HR-TEM images of calcined nanoparticles (**S0**) and the PXRD patterns of as made MCM-41 nanoparticles, **S0** and **S3** solids. HR-TEM images show the spherical shape of the nanoparticles (with diameters in the 80-100 nm interval) and the mesoporous structure. Moreover, the PXRD pattern of the as-made mesoporous silica nanoparticles shows the typical low-angle reflections. For the calcined solid (**S0**), a slight displacement of the peaks related to the condensation of silanol groups during the calcination process is found. Besides, the presence of the (100) peak in the PXRD pattern of **S3** indicated that cargo loading and the different surface chemical modifications had not damaged the mesoporous structure.

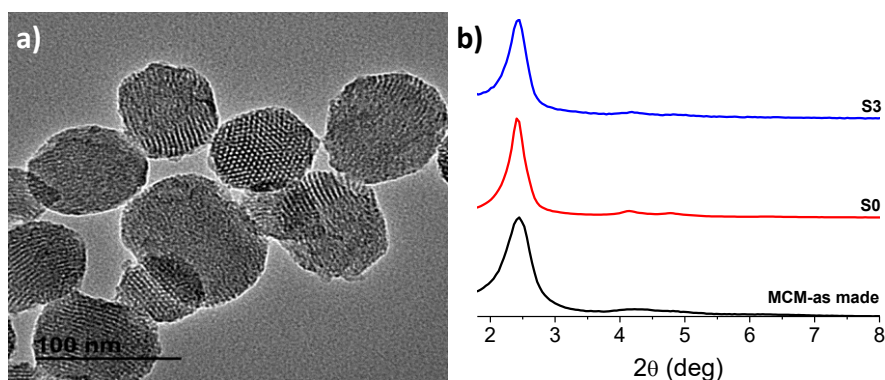


Figure S1. (a) HR-TEM images of **S0**. (b) Powder X-ray diffraction patterns of mesoporous silica nanoparticles as synthesized, calcined (**S0**) and the final material **S3**.

The N_2 adsorption-desorption isotherm of **S0** nanoparticles shows an adsorption step at intermediate P/P_0 value 0.3, which is characteristic for mesoporous solids with empty pores (Figure S2). This step is related to the nitrogen condensation inside the mesopores by capillarity. The absence of a hysteresis loop in this interval and the narrow BJH pore distribution suggest the

existence of uniform cylindrical mesopores. Application of the BET model results in a value for the total specific surface of $1081.2 \text{ m}^2\cdot\text{g}^{-1}$ for **S0** nanoparticles. N_2 adsorption-desorption isotherms for the functionalized and loaded solid **S3** show a significant decrease in N_2 volume adsorbed and are flat when compared (at the same scale) to those of **S0**. Total specific surface area for **S3** significantly decreased to $78.3 \text{ m}^2\cdot\text{g}^{-1}$ due to cargo loading inside the mesopores and external surface functionalization with the oligosaccharide. In order to calculate pore size and total pore volume, the BJH model was applied on the adsorption band of the isotherm for $P/P_0 < 0.6$ (associated to adsorption inside the pores). BET specific values, pore volumes and pore sizes calculated from N_2 adsorption-desorption isotherms for **S0** and **S3** nanoparticles are listed in Table S1.

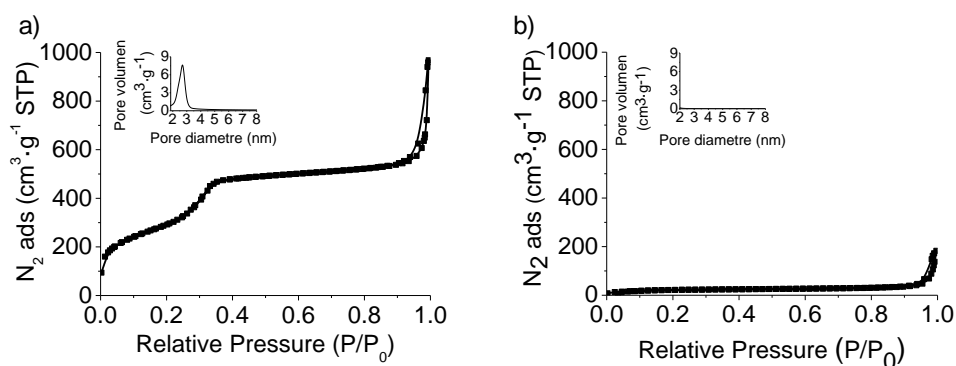


Figure S2. N_2 adsorption-desorption isotherms of (a) **S0** and (b) **S3**. The inset figures show pore sizes.

Loading and functionalization of the calcined **S0** nanoparticles was assessed also by ATR (Figure S3). As could be seen, all the prepared nanoparticles (**S0**, **S1**, **S2** and **S3**) present the typical band of the Si-O-Si vibration at 1095 cm^{-1} . Dealing with **NB**, the most representative bands were located at ca. 2900 and 2500 cm^{-1} (ascribed to the stretching vibrations of C-H bonds) and at ca. 1600 cm^{-1} (due to the N-H bending vibration). These vibrations are also observed, but with lower intensity, in **S1** solid in which **NB** was encapsulated inside the pores of the siliceous support. The most remarkable feature of the final **S3** nanoparticles was

the appearance of a broad band in the 3600-2800 cm^{-1} interval which could be ascribed to the O-H bond stretching vibration of the grafted hexa-galacto oligosaccharide.

Table S1. BET specific surface values, pore volumes and pore sizes calculated from N_2 adsorption-desorption isotherms for selected materials.

Sample	S_{BET} [m^2g^{-1}]	Pore Volume [cm^3g^{-1}]	Pore size [nm]
S0	1081.2	0.92	2.69
S3	78.3	0.04	-- ^a

^a Pore size cannot be observed with N_2 adsorption-desorption isotherms method due to the presence of the galacto-oligosaccharide covering the external surface, however, direct measures obtained by HR-TEM showed similar values in pore size for **S0** and **S3**.

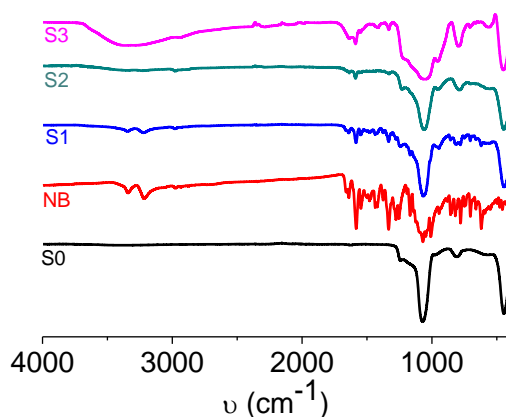


Figure S3. Attenuated total reflectance (ATR) spectra of **S0**, **S1**, **S2** and **S3** nanoparticles and of **NB** dye.

The hydrodynamic size of **S0** and **S3** nanoparticles was measured by dynamic light scattering (DLS) and the obtained results are shown in Figure S4. DLS studies were carried out at 25 °C on previously sonicated suspensions of **S0** and **S3** nanoparticles in water at a concentration of 0.5 mg/mL. DLS measurements showed an increase in the hydrodynamic nanoparticle diameter, from 144 nm for **S0** to 282 nm for **S3** ascribed to the functionalization of the surface with the bulky oligosaccharide.

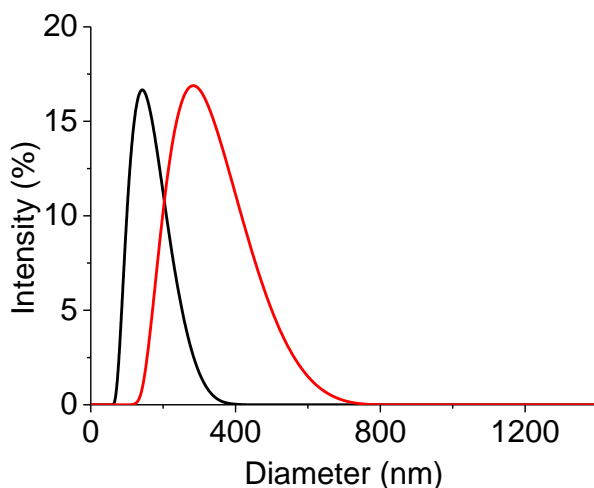


Figure S4. Particle size distribution by intensity obtained by DLS measurements for calcined nanoparticles **S0** (black line) and final solid **S3** (red line).

Thermogravimetric measurements carried out with **S0**, **S1**, **S2** and **S3** (Figure S5) nanoparticles allowed us to calculate the organic matter in the loaded and functionalized solids. At this respect, these curves indicated an organic matter content of 19% for **S1** (loaded with **NB**), 21% for **S2** (loaded with **NB** and functionalized with APTES) and 30% for **S3** (loaded with **NB** and capped with the galacto-oligosaccharide). Besides, from dye delivery experiments and the thermogravimetric studies, the content of **NB** in **S3** was determined to be 0.45 mmol g⁻¹ of solid.

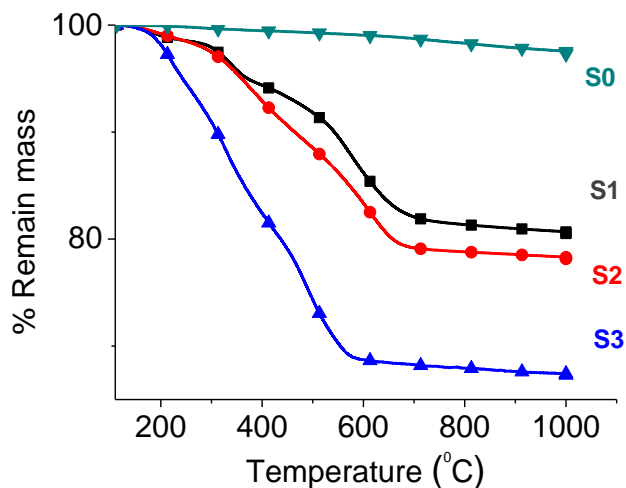


Figure S5. Thermogravimetric curves of **S0**, **S1**, **S2** and **S3** nanoparticles.

Finally, the quenching of **NB**, when inside the pores of **S3**, was assessed. At this respect, Figure S6 shows confocal microscopy images of **S3** nanoparticles in the bright field and in the red channel. As could be seen in the bright field image, **S3** nanoparticles are well dispersed and non-aggregated. On the other hand, in the image of the red channel negligible fluorescence from the nanoparticles was observed. This fact supports that **NB** form non-emissive π -stacking aggregates when confined in the inner of the pores of the mesoporous support.

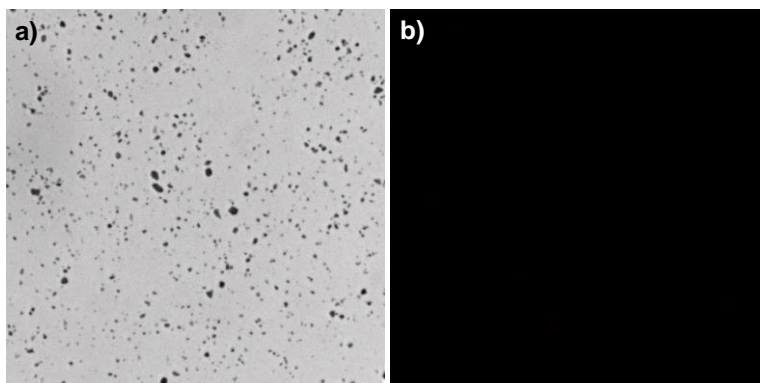


Figure S6. Confocal images of **S3** nanoparticles. (a) Bright field and (b) red channel ($\lambda_{\text{exc}} = 638$ nm and $\lambda_{\text{em}} = 648\text{-}749$ nm).

6.7.4 Calculations of loaded and released NB.

We can calculate the molar concentration of **NB** inside the pores of mesoporous silica nanoparticles from TGA analysis (0.19 g of **NB** per g of solid).

$$\frac{0.19g(NB)}{\frac{417g}{mol}} = 4.55 \cdot 10^{-4} mol\ of\ NB \ \in\ 1g\ of\ S3$$

From the specific pore volume ($0.92\text{ cm}^3\text{g}^{-1}$) of the mesoporous nanoparticles it is possible to calculate the molar concentration of **NB** inside the pores:

$$M = \frac{mol}{V} = \frac{4.55 \cdot 10^{-4} mol_{NB}/g_{S3}}{9.2 \cdot 10^{-4} L/g_{S3}} = 0.49M$$

Moreover, from the release experiments (using 2 mg of **S3**) it was calculated that after 24 h a 31.4 % of the total loaded **NB** (i.e. $2.85 \times 10^{-6} mol_{NB}$) was delivered. The amount of **NB** released was calculated using the calibration curve shown in Figure S7.

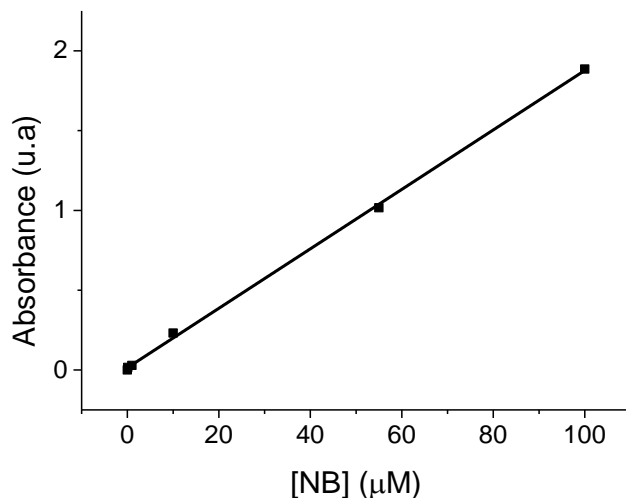


Figure S7. Absorbance of aqueous solutions of **NB** at 608 nm vs dye concentration.

6.7.5 Cargo release experiments.

In a typical experiment, 2 mg of **S3** were suspended in 5 mL of water-DMSO 99:1 v/v mixture at pH 4.5, in the presence or absence of 5 mg of enzyme human β -Gal. The suspension was stirred using a magnetic bar. Sample aliquots of 0.4 mL were taken at scheduled times and were centrifuged to remove **S3**. Free **NB** was monitored via the absorption band of the dye centered at 608 nm.

6.7.6 *In vitro* studies.

SK-MEL-103 (human melanoma) cancer cells were obtained from ATCC. Cells were maintained in DMEM, supplemented with 10% FBS, and incubated in 20% O_2 and 5% CO_2 at 37°C. In a first step, cells were incubated with 5 μM palbociclib in DMEM for one week to induce senescence. Then, cells were seeded in flat-

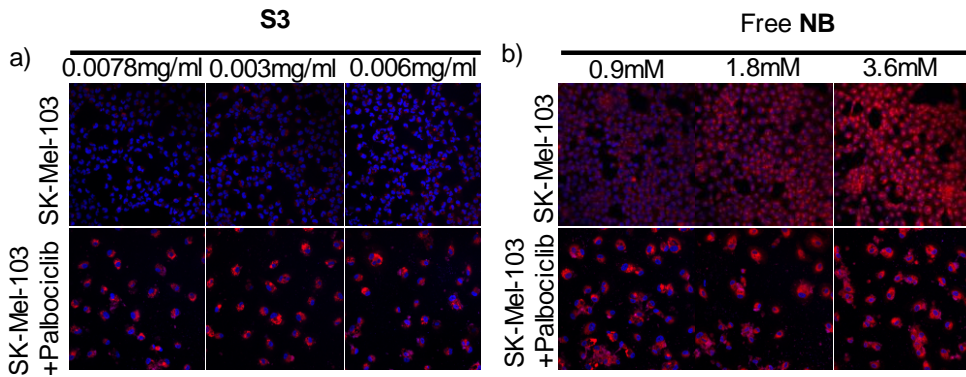


Figure S8. Confocal images of control and palbociclib-treated SK-Mel-103 cells (a) in the presence of different concentrations of **S3** and (b) in the presence of different concentrations of free **NB**. Representative images from repeated experiments (n=3) are shown.

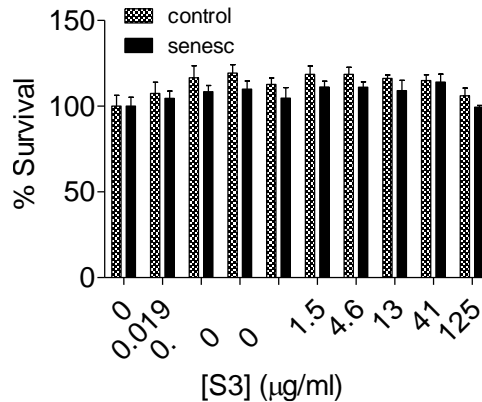


Figure S9. Relative *in vitro* viability of control and senescent SK-Mel-103 cells after incubation with **S3** nanoparticles for 48 h at different concentrations. SK-Mel-103 were maintained in DMEM supplemented with 10% FBS, and incubated in 20% O₂ and 5% CO₂ at 37 °C. For senescence induction, cells were supplemented with DMEM media containing 5 µM palbociclib for 2 weeks. Control and palbociclib-treated cells were plated in flat-bottom-clear 96 well plate at a density of 3,500 and 4,000 cells per well, respectively. The following day, cells were treated with serial suspensions of **S3**. Viability was assessed 48 h later with CellTiter-GLO Luminescent Cell Viability Assay by measuring luminescence in a VICTOR Multilabel Plate Reader.

bottom-clear 96 well plate. After 24 h cells were treated with **S3** (7.8 µg/ml) for 4.5 h in DMEM (10% FBS) in 20% O₂ and 5% CO₂ at 37°C, and washed 3 times with PBS to remove the non-endocytosed nanoparticles. Afterward, cells were treated with Hoechst (1.5 ng/ml) for 15 min (10% FBS) and confocal images were acquired

by using confocal microscope (Leica TCS SP8 AOBS). The obtained results are shown in Figures 3 and S8. Besides, it was found that **S3** nanoparticles were not toxic for both control and senescent SK-Mel-103 cells (Figure S9).

6.7.7 In vivo studies.

Mice were maintained at the Spanish Research Centre Principe Felipe (CIPF) in accordance with the recommendations of the Federation of European Laboratory Animal Science Associations (FELASA). All animal procedures were approved by the CIPF Ethics Committee for Research and Animal Welfare (CElyBA). Breast 4T1 tumors were established by using 4T1 cells. Cells were routinely cultured in DMEM supplemented with 10% FBS and penicillin-streptomycin. In order to generate breast tumor, cells were trypsinised, counted with a LUNA™ Automated Cell Counter and injected subcutaneously in the left breast of 28- to 34-week-old BALB/CBY female mice at a concentration of 0.5×10^6 cells in a volume of 100 μ l. Tumor volume was measured every two days with a calliper and calculated as $V = (a \times b^2) / 2$ where a is the longer and b is the shorter of two perpendicular diameters. Palbociclib was administered by daily oral gavage for 7 days at 100 mg/kg dissolved in 50 mM sodium lactate, pH 5 in order to induce senescence. Then, **S3** was intravenously (i.v.) administered at a concentration of 4 mg/ml in a volume of 200 μ l. 24 h post-injection emission of **NB** was monitored on an IVIS spectrum imaging system and analyzed by using the Living Imaging software from Caliper Life Sciences (Figure S10). Then, mice were sacrificed by CO₂ exposure in a Euthanasia Chamber, and tumors and organs (lung, liver, kidney or spleen) were immediately removed. Tumors and organs were analyzed after harvesting and fluorescence images were taken on an IVIS spectrum imaging system and analyzed by using the Living Imaging software from Caliper Life Sciences.

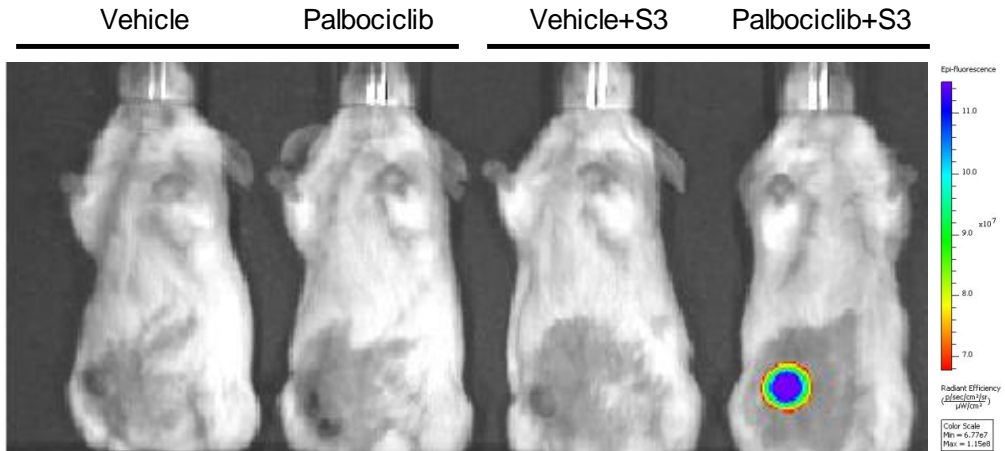


Figure S10. IVIS images 24 h post injection of **S3** of BALB/cByJ female mice bearing 4T1 breast cancer tumors. From left to right vehicle mice (group A), BALB/cByJ mice treated by oral gavage with palbociclib (senescent tumors) for 1 week (group C), vehicle mice intravenously injected with **S3** (group B) and BALB/cByJ mice treated by oral gavage with palbociclib (senescent tumors) for 1 week and i.v. injected with **S3** (group D).

6.7.8 Immunohistochemistry protocol.

Tumors were fixed with 4% PFA for 4h, embedded in paraffin, cut into thin slices and mounted onto slides for analysis. Then, samples were stained by indirect immunoperoxidase immunostaining. For this purpose, slides were incubated with the primary antibody Ki67 and then with the corresponding secondary antibody. Finally, sections were stained with hematoxylin, dehydrated, and coverslipped. The obtained results are shown in Figure S11.

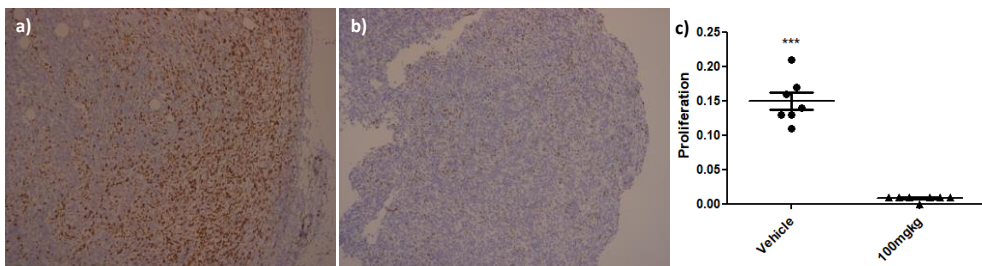


Figure S11. Immunohistochemical detection of Ki67 in paraffin sections of (a) tumors from control and (b) palbociclib-treated mice. The reduction of the proliferative marker Ki67 is indicative of cell cycle arrest which is indicative of intratumoral senescence. (c) Quantification of Ki67 immunohistochemical staining with ImageJ software.

6.7.9 Biodistribution experimental protocol.

For silicon (Si) biodistribution studies, lungs, liver, spleen, kidneys, tail, bladder and tumor were harvested and conserved at -80 °C. Organs were first weighted and then individually introduced in polytetrafluoroethylene (PTFE) bottles. 1mL of tetramethylammonium hydroxide solution (TMAH) was added to each recipient, bottles were firmly closed and digestion was carried out for 2 h at 80 °C using a digestion unit Bloc digest 20. After cooling, digested samples were diluted with milliQ water to 10 mL in polypropylene Erlenmeyer flasks, then filtered with 0.45 µm Nylon filters and kept in polystyrene tubes. Silicon determination was performed in an Inductively Coupled Plasma Mass Spectrometer System (ICP-MS) Agilent 7900 in H2 mode, using germanium as internal standard. Data are expressed as µg Si/g sample. The obtained results are shown in Figure S12. As could be seen Si levels decrease over time in most organs probably due to the degradation and elimination of **S3** through urine and feces.¹

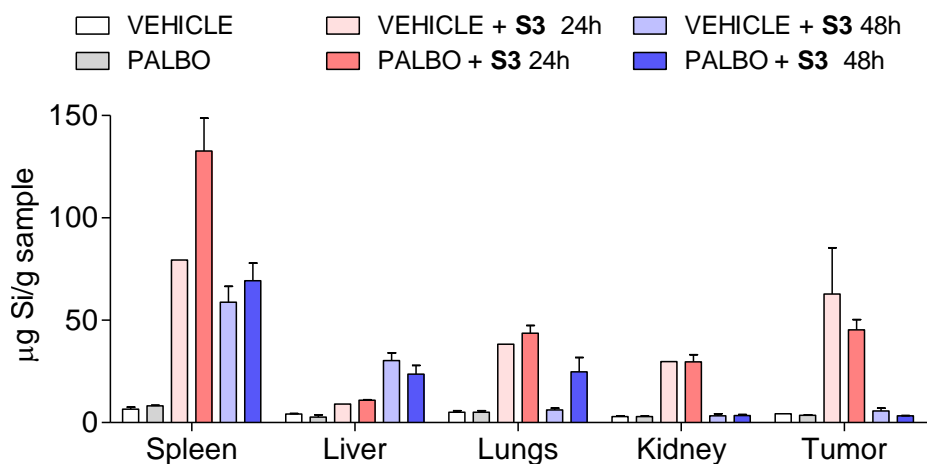


Figure S12. Biodistribution of **S3** nanoparticles. Silicon levels analyzed by Inductively Coupled Plasma Mass Spectroscopy (ICP-MS). Data expressed as mean ± SEM (n=4) and represented as µg Si per g of sample.

1 J. Lu, M. Lion, Z. Li, J. I. Zink and F. Tamanoi, *Small*. **2010**, 16, 6, 1794–1805

6.7.10 Toxicity and pro-inflammatory factors *in vivo* evaluation of S3.

To study the safety of **S3** in *in vivo* applications, blood samples were collected and albumin (ALB), bilirubin (BIL), alkaline phosphatase (AKP), glutamic pyruvic transaminase (GPT) and aspartate transaminase (GOT) were analysed to evaluate the function of liver. Additionally, to discard non-desired pro-inflammatory effect of **S3** nanoparticles, the levels of neutrophils, lymphocytes and monocytes were analysed in blood samples. As shown in Figure S13 no significant differences between animals treated with **S3** nanoparticles or untreated were observed in measured parameters, thus discarding toxicity or side effects derived of nanoparticles administration.

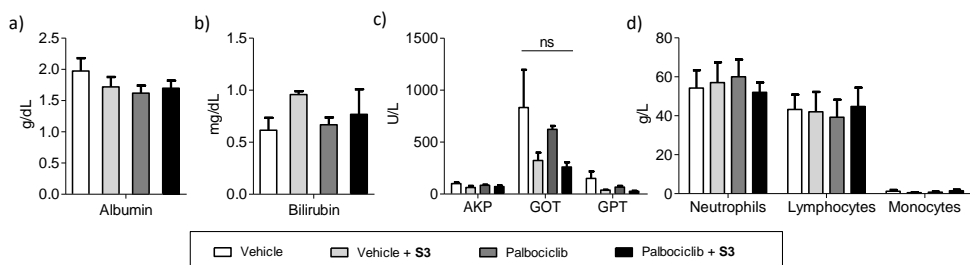


Figure S13. Evaluation of systemic toxicity and pro-inflammatory factors effects derived from **S3** nanoparticles administration. (a) Albumin, (b) Bilirubin, (c) Alkaline phosphatase enzymes (AKP), aspartate transaminase (GOT) and glutamic pyruvic transaminase (GPT). Note that mice groups treated with **S3** present no significant differences in the function of liver compared to non treated ones. (d) Number of neutrophils, lymphocytes and monocytes as systemic inflammation indicators. The data represent the mean \pm SEM (n=4).

**Chapter 7 | Galacto-conjugation of
Navitoclax as an efficient strategy to
increase senolytic specificity and
reduce platelet toxicity**

Galacto-conjugation of Navitoclax as an efficient strategy to increase senolytic specificity and reduce platelet toxicity

Estela González-Gualda,¹ Marta Pàez-Ribes,¹ Beatriz Lozano-Torres,^{2,3,4,5} David Macias,¹ Joseph R. Wilson III,¹ Cristina González-López,¹ Hui-Ling Ou,¹ Sofía Mirón-Barroso,¹ Zhenguang Zhang,¹ Araceli Lérica-Viso,⁵ Juan F. Blandez,² Andrea Bernardos,^{2,3,4,6} Félix Sancenón,^{2,3,4,5} Miguel Rovira,⁷ Ljiljana Fruk,⁸ Carla P. Martins,⁹ Manuel Serrano,⁷ Gary J. Doherty,¹⁰ Ramón Martínez-Máñez,^{2,3,4,5,6} Daniel Muñoz-Espín¹

¹CRUK Cambridge Centre Early Detection Programme, Department of Oncology, Hutchison/MRC Research Centre, University of Cambridge, Cambridge, UK

²Instituto Interuniversitario de Investigación de Reconocimiento Molecular y Desarrollo Tecnológico (IDM), Universitat Politècnica de València, Universitat de València, Valencia, Spain

³Unidad Mixta UPV-CIPF de Investigación en Mecanismos de Enfermedades y Nanomedicina, Centro de Investigación Príncipe Felipe, Universitat Politècnica de València, Valencia, Spain

⁴CIBER de Bioingeniería, Biomateriales y Nanomedicina (CIBER-BBN), Madrid, Spain ⁵Unidad Mixta de Investigación en Nanomedicina y Sensores, IIS La Fe, Universitat Politècnica de València, Valencia, Spain

⁶Senolytic Therapeutics S.L., Parc Científic de Barcelona, Barcelona, Spain

⁷Institute for Research in Biomedicine (IRB Barcelona), The Barcelona Institute of Science and Technology (BIST), Barcelona, Spain

⁸Department of Chemical Engineering and Biotechnology, University of Cambridge, Cambridge, UK

⁹Bioscience, Oncology R&D Unit, AstraZeneca, Cambridge, UK

¹⁰Department of Oncology, Cambridge University Hospitals NHS Foundation Trust, Addenbrooke's Hospital, Cambridge, UK

Estela González-Gualda, Marta Pàez-Ribes, and Beatriz Lozano-Torres contributed equally in this work.

(Reprinted with permission from *Aging Cell*. 2020;00:e13142.

Copyright © 2020, The Authors. *Aging Cell* published by the Anatomical Society and John Wiley & Sons Ltd. All rights reserved.)

7.1 Abstract

Pharmacologically active compounds with preferential cytotoxic activity for senescent cells, known as senolytics, can ameliorate or even revert pathological manifestations of senescence in numerous preclinical mouse disease models, including cancer models. However, translation of senolytic therapies to human disease is hampered by their suboptimal specificity for senescent cells and important toxicities that narrow their therapeutic windows. We have previously shown that the high levels of senescence associated lysosomal β -galactosidase (SA- β -Gal) found within senescent cells can be exploited to specifically release tracers and cytotoxic cargoes from galactose-encapsulated nanoparticles within these cells. Here, we show that galacto-conjugation of the BCL-2 family inhibitor Navitoclax results in a potent senolytic prodrug (**Nav-gal**), that can be preferentially activated by SA- β -Gal activity in a wide range of cell types. **Nav-gal** selectively induces senescent cell apoptosis and has a higher senolytic index than Navitoclax (through reduced activation in nonsenescent cells). **Nav-gal** enhances the cytotoxicity of standard senescence-inducing chemotherapy (cisplatin) in human A549 lung cancer cells. Concomitant treatment with cisplatin (CDDP) and **Nav-gal** *in vivo* results in the eradication of senescent lung cancer cells and significantly reduces tumour growth. Importantly, galacto-conjugation reduces Navitoclax-induced platelet apoptosis in human and murine blood samples treated *ex vivo*, and thrombocytopenia at therapeutically effective concentrations in murine lung cancer models. Taken together, we provide a potentially versatile strategy for generating effective senolytic prodrugs with reduced toxicities.

7.2 Introduction

Senescence is an evolutionarily conserved cellular response to severe stress and damage characterized by stable cell cycle arrest, upregulation of pro-survival signalling pathways and the induction of a complex secretory phenotype, termed the senescence-associated secretory phenotype (SASP).¹ Physiological roles of cellular senescence include prevention of the propagation of damaged or dysfunctional cells and promotion of tissue repair; these processes are facilitated by immune system cells driving the clearance of senescent cells.² Senescence plays an active role in tumour suppression, reprogramming, tissue regeneration, wound healing and embryogenesis. However, the processes of senescence and immune clearance are dysregulated during aging, where senescent cells accumulate in tissues contributing to the onset and progression of multiple age-related disorders through a variety of cell autonomous and paracrine effects that disrupt tissue homeostasis.² Among other pathologies, senescence is associated with fibrotic disorders, cardiovascular diseases, obesity, diabetes, osteoarthritis, neurological disorders, inflammatory diseases and cancer.^{3,4} Conclusive evidence is accumulating that therapy-induced senescent cells (both with a cancerous and stromal origin) can drive tumorigenesis, either by releasing complex pro-inflammatory and tumour-promoting SASP cocktails,^{5,6} or by the reversion of the cell cycle arrest and the acquisition of stemness and aggressive clonogenic growth potentials.⁷ Genotoxic stress, which is induced by many chemotherapies, promotes cellular senescence. Remarkably, it has been shown that chemotherapy-induced senescent breast cancer cells can promote tumour relapse in the lung,⁸ and senescent stromal cells form the niche that promotes metastasis in the bone.⁹ In the case of non-small cell lung cancer (NSCLC), neoadjuvant platinum-based chemotherapy results in the accumulation of senescent cancer cells in patients and evidence has been found of the escape of replicative arrest in

humans (therapy-induced) senescent lung cancer cells.¹⁰ Therefore, treatment modalities that eliminate therapy-induced senescent cells may be critical for tumour eradication. Recent research has identified targetable vulnerabilities of senescent cells that can be exploited by a novel group of drugs called senolytics. These compounds preferentially kill senescent cells by different mechanisms.^{11,12} Senolytics include the BCL-2 family inhibitors Navitoclax (ABT-263)¹³ and ABT-737;¹⁴ the flavonoid fisetin;¹⁵ combinations of tyrosine kinase inhibitors and flavonoids (e.g. dasatinib and quercetin);¹⁶ FOXO4-p53 interfering peptides;¹⁷ HSP90 chaperone inhibitors;¹⁸ and other compounds such as piperlongumine¹⁹ and cardiac glycosides.^{20,21} Senolytics have emerged as promising agents for treatment of pulmonary fibrosis, atherosclerosis, osteoarthritis, type 1 and 2 diabetes mellitus, and neurocognitive decline. They can also rejuvenate aged hematopoietic and muscle stem cells and extend the lifespan of naturally aged mice.¹² Despite successful preclinical proofs-of-concept for senolytics, their potential translatability is hampered by their associated toxicities, necessitating the development of more specific, and less toxic, second-generation senolytics. Navitoclax has been validated in a variety of preclinical models showing high potency in killing senescent cells—however, it also has significant on-target haematological toxicity, including thrombocytopenia.²² This narrows its therapeutic window and can preclude concomitant treatment with other agents with haematological toxicities. While targetable vulnerabilities of senescence have been discovered, these are often also present in nonsenescent tissues leading to problems with specifically targeting senescent cells. One consistent feature of senescent cells is their enrichment in lysosomes and lysosomal proteins, including senescence-associated β -galactosidase (SA- β -Gal) which is widely used as a marker of senescence²³ and can be readily detected.²⁴ We previously showed that the encapsulation of nanoparticles with galacto-oligosaccharides (GalNPs) is an

efficient method to preferentially deliver cytotoxic drugs and tracers to the lysosomes of senescent cells where SA- β -Gal activity hydrolyzed the galacto-oligosaccharides, thereby releasing the cargo.^{25,26} We demonstrated that galacto-encapsulated doxorubicin is preferentially released into fibrotic tissues and tumours accumulating senescent cells, and its concomitant administration with the senescence-inducing anti-cancer treatment palbociclib effectively halts tumour growth in xenograft models of melanoma and NSCLC.²⁶ We have also shown that a fluorescent probe covalently linked to multi-acetylated galactose is preferentially hydrolyzed by senescent cells, releasing the free fluorophore.²⁷ The presence of multiple acetyl moieties in the galactose residue is thought to render it membrane-permeable and therefore accessible to the lysosomal compartment.²⁸

Here, we have modified Navitoclax with an acetylated galactose to exploit the enriched SA- β -Gal activity of senescent cells (Figure 1a). Using a variety of model systems, we show that galacto-conjugation of Navitoclax, which we name **Nav-Gal**, results in a prodrug with selective, pro-apoptotic senolytic activity released in senescent cells that is dependent on GLB1 activity. Concomitant treatment of **Nav-gal** with the senescence-inducing chemotherapy (CDDP) efficiently arrests tumour progression in models of orthotopically transplanted murine lung adenocarcinoma cells, and in a tumour xenograft model of human NSCLC. Importantly, galacto-conjugation of Navitoclax reduces thrombocytopenia in treated mice at therapeutically effective doses, as well as apoptosis of platelets in human blood samples treated *ex vivo*. Overall, we propose galacto-conjugation of cytotoxic drugs as a versatile methodology for developing second-generation prodrugs with high senolytic activity and reduced toxicity. We provide evidence of the efficacy of combining senescence-inducing chemotherapies with senotherapies in cancer, with potential for clinical application.

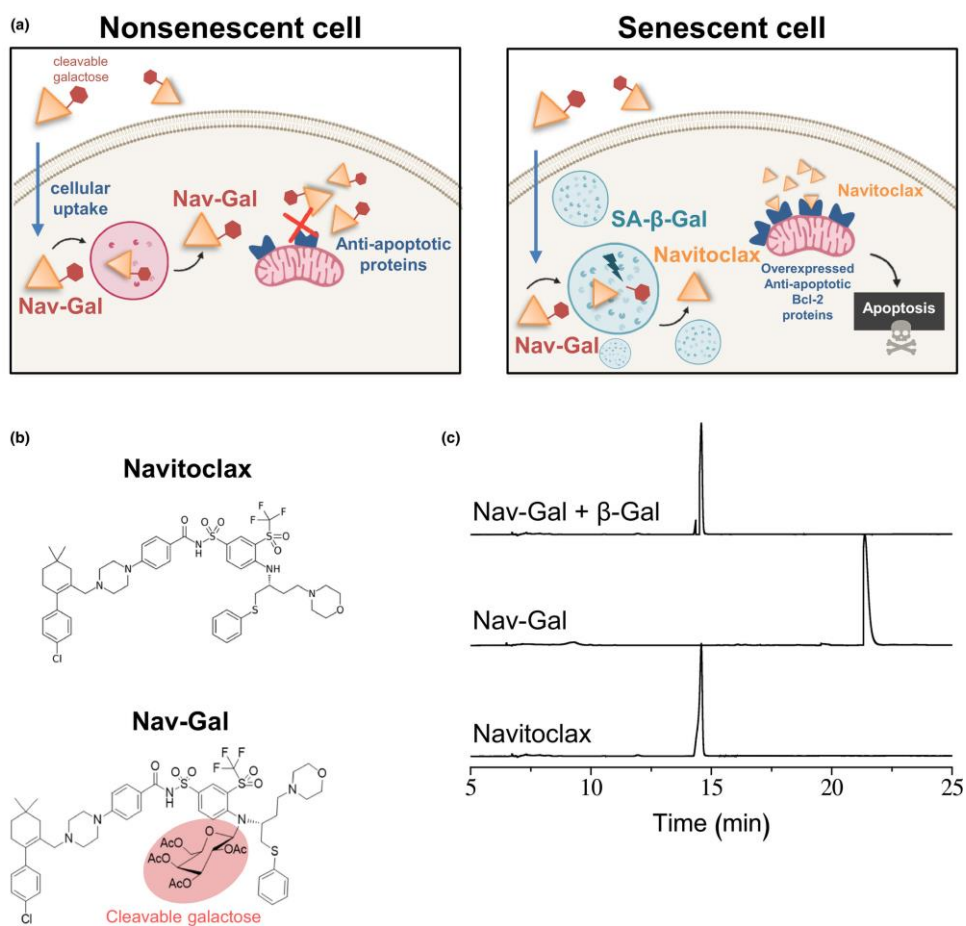


Figure 1. Galacto-conjugation of the senolytic Navitoclax into a new generation senolytic prodrug, namely **Nav-gal**, as an efficient strategy for selective senolysis. (a) Schematic representation of the mechanism of action of **Nav-gal** prodrug. **Nav-gal** is passively taken up by both nonsenescent and senescent cells. In nonsenescent cells, its conjugation with a cleavable galactose renders it inactive and unable to inhibit anti-apoptotic proteins, such as BCL-2, preventing the induction of apoptosis. In senescent cells, the increased lysosomal and galactosidase activity, a hallmark of cellular senescence, allows the hydrolysis of the cleavable galactose, resulting in the release of active Navitoclax into the cytoplasm of senescent cells. Free Navitoclax will inhibit anti-apoptotic BCL-2 proteins, which are overexpressed in senescent cells, driving specific apoptosis of these cells. (b) Chemical structures of **Nav-gal** prodrug and Navitoclax. The presence of galactopyranoside, covalently linked to the N of bis(sulfonyl)aniline as synthesized in this prodrug, hinders two key interactions: (i) π - π interaction between the phenylthioether moiety and the bis(sulfonyl)aniline ring; and (ii) the hydrogen bond between morpholine with Tyr-199,²⁹ thereby preventing the inhibitory effect of the molecule. This moiety, the galactopyranoside, can be hydrolysed in the presence of β -Gal (cleavable galactose). (c) Chromatograms depicting hydrolysis reaction of **Nav-gal** aqueous solutions in the presence of human β -Gal followed by HPLC-UV as described in the text.

7.3 Results

7.3.1 Synthesis, characterisation and hydrolysis reaction studies

RNA interference and drug screening approaches led to the identification of the anti-apoptotic BCL-2 protein family as potential therapeutic targets in senescent cells, and Navitoclax (ABT-263) as a drug with a potent senolytic activity.^{13,30} Here, we have engineered a novel prodrug, namely **Nav-gal**, by modifying the molecular structure of Navitoclax following the synthetic procedure shown in Figure S1A. To do so, Navitoclax was reacted with 2,3,4,6-tetra-O-acetyl- α -D-galactopyranosyl bromide (**Gal**) through bimolecular nucleophilic substitution (S_N2) in the presence of potassium carbonate yielding the **Nav-gal** prodrug (Figure 1b), which was comprehensively characterized by several nuclear magnetic resonance techniques (NMR), including $^1\text{H-NMR}$, $^{13}\text{C-NMR}$ and correlated spectroscopy (COSY) NMR, as well as by attenuated total reflectance (ATR) and high-resolution mass spectrometry (HRMS) (Figures S1B–F). The $^1\text{H-NMR}$ signal centred at 5.6 ppm (Figure S1B) corresponds to the anomeric proton of the attached galactose and indicates the successful covalent linkage of the monosaccharide to Navitoclax. In addition, the appearance of a signal centred at $1,749\text{ cm}^{-1}$ in the ATR spectra (Figure S1E) indicates that galactose remains acetylated after purification. Correct functionalization to the nitrogen atom of bis(sulfonyl)aniline is further corroborated through the fragmentation peaks observed in the mass spectrum (Figure S1F). After extensive structural characterization, we examined the ability of **Nav-gal** to be enzymatically hydrolysed to Navitoclax. GLB1 is the human lysosomal β -Gal responsible for the SA- β -Gal activity.²⁴ We used high performance liquid chromatography (HPLC) to examine the time-dependent hydrolysis reaction of PBS (pH 7)-DMSO (0.01%) solutions containing **Nav-gal** in the presence of recombinant GLB1 and compared the peaks with those of Navitoclax (Figure 1c). The obtained chromatograms showed the **Nav-gal** peak with the subsequent

appearance of free Navitoclax signal in the presence of the β -Gal activity of the lysosomal enzyme and confirmed that **Nav-gal** was completely hydrolysed. No significant spontaneous **Nav-gal** hydrolysis was observed (data not shown).

7.3.2 Nav-gal is a prodrug with effective wide-ranging senolytic activity that depends on GLB1 activity

Since senescent cells are commonly characterized by high lysosomal SA- β -Gal activity, we hypothesized that galacto-conjugated Navitoclax would be preferentially processed and activated in senescent cells and hence could function as a prodrug with more selective senolytic activity. To investigate this, we performed cell viability assays using a model of therapy-induced senescence. The lung carcinoma cell line A549 was treated with cisplatin (CDDP) for 10 days, resulting in elevated SA- β -Gal activity and expression of markers of senescence (Figure S2A–C). Cisplatin-treated A549 cells were then subjected to increasing doses of either Navitoclax or **Nav-gal** for 72 h. As shown in Figure 2a, the concentration of Navitoclax required to induce death in 50% of the cells, termed half maximal inhibitory concentration (IC₅₀), after 72 h of treatment was 1.93 μ M for non-senescent and 0.12 μ M for cisplatin-induced senescent A549 cells, while the IC₅₀ for **Nav-gal** was 9.76 μ M for non-senescent and 0.28 μ M for senescent A549 cells (Figure 2b). A similar approach was performed in a model of palbociclib-induced senescence with a human melanoma cell line (SK-Mel-103) (Figure 2c,d and Figure S2A–C). These results show (in two different models of chemotherapy-induced senescence) that **Nav-gal** has an improved senolytic index over Navitoclax and indicates that this effect is mainly mediated by a higher degree of protection of non-senescent cells from cytotoxic activity. In an attempt to determine whether senolytic activity and non-senescent cell protection by **Nav-gal** were more widely observed, we then performed cell viability assays using a

variety of cell lines and diverse triggers of cellular senescence. Figure 2e-i show the effects on cell viability of both Navitoclax and **Nav-gal** at different concentrations in cisplatin-induced senescent mouse lung adenocarcinoma (KrasG12D/+;p53-/- (KP) L1475(luc) cells),³¹ palbociclib-induced senescent mouse breast cancer 4T1 cells, doxorubicin-induced senescent human colorectal carcinoma HCT116 cells, irradiation-induced senescent mouse lung fibroblasts (MLg) and oncogene-induced senescent human lung fibroblasts (IMR90), versus their nonsenescent counterparts. Efficient implementation of cellular senescence using these triggers was confirmed by SA- β -Gal staining and Western blotting for senescence markers (Figure S2D,E). In all the human/murine cell types tested, and independently of the senescence-inducing trigger used, **Nav-gal** showed effective senolytic activity and a significantly higher degree of protection of nonsenescent cells when compared to Navitoclax. To determine whether the senolytic effect of the prodrug **Nav-gal** depends on the increased lysosomal β -Gal active of senescent cells, siRNAs were used to knock-down the expression of GLB1 in A549 and SK-Mel-103 cells. As shown in Figure 3af, siRNA2 efficiently downregulated the transcription of GLB1 at 48 h post-transfection and resulted in a significantly decreased number of SA- β -Gal-positive cells in both cell lines, when compared to scrambled siRNA and siRNA 1. While the killing efficiency of Navitoclax was maintained in the senescent cells in both cell lines (Figure 3g), transient downregulation of GLB1 significantly prevented the senolytic activity of **Nav-gal** (Figure 3h) in A549 and SK-Mel-103 cells, indicating that the selective senolysis of the prodrug is (at least) partially driven by the increased GLB1 expression of senescent cells.

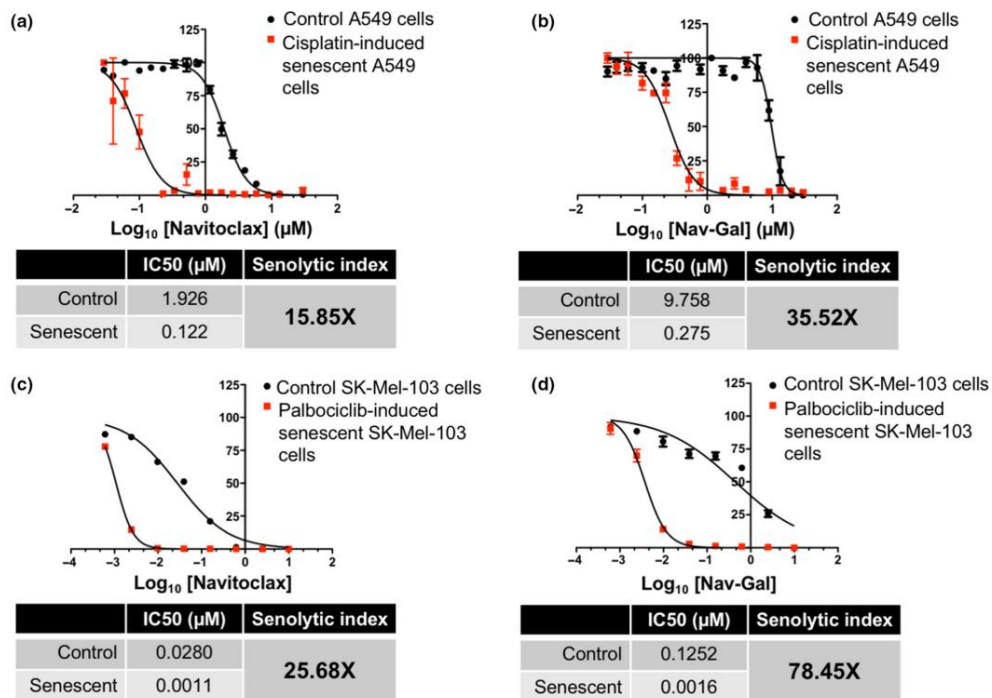


Figure 2. The prodrug **Nav-gal** shows efficient, broad range, senolytic activity and an increased senolytic index, conferring a protective effect on nonsenescent cells. (a, b) Quantification of viability and half maximal inhibitory concentration (IC50) of (a) Navitoclax and (b) **Nav-gal** on control and cisplatin-induced senescent A549 cells. Senolytic indices for each drug are shown in the tables below. Viability assay on A549 cells was performed as n = 5, and graphs depict one representative repeat. (c, d) Quantification of viability and maximal inhibitory concentration (IC50) of (c) Navitoclax and (d) **Nav-gal** on control and palbociclib-induced senescent SK-Mel-103 cells. Senolytic indices of each drug are shown in the tables below. Viability assay on SK-Mel-103 cells was performed as n = 3, and graphs depict one representative repeat. (e–i) Quantification of cell viability upon Navitoclax and **Nav-gal** treatment of control and

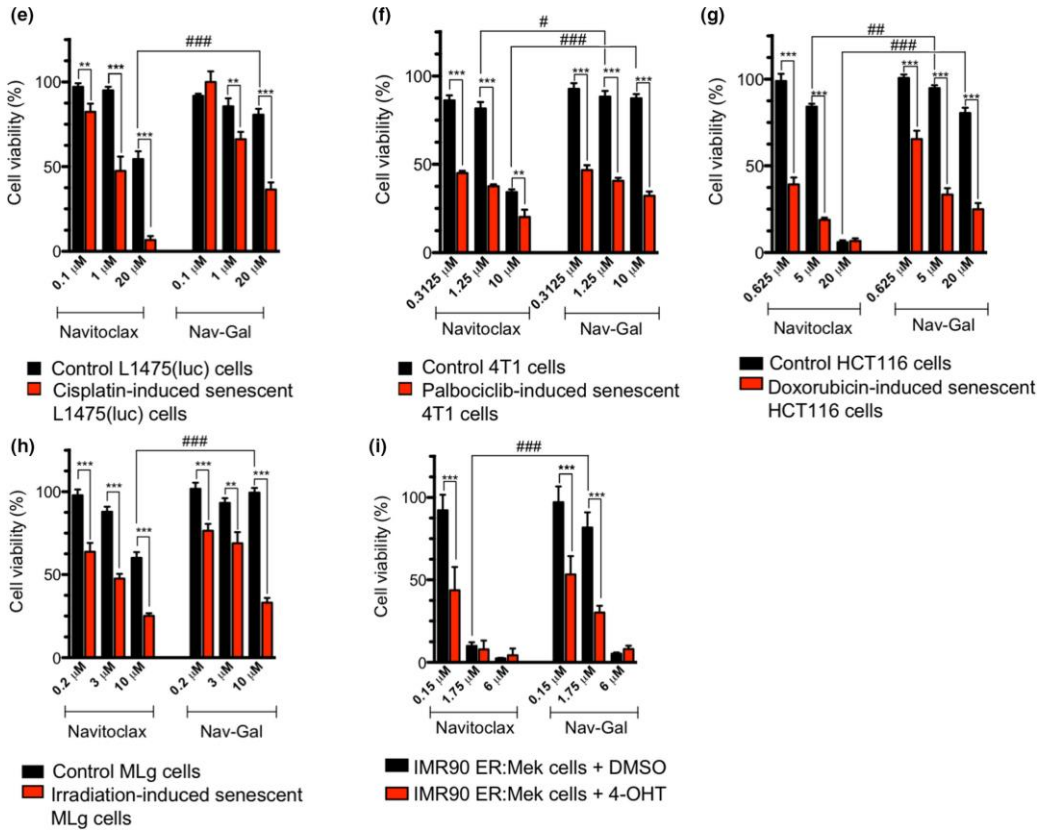


Figure 2. (e) cisplatin-induced senescent KRasG12D/WT;p53^{-/-} lung adenocarcinoma tumour cells L1475(luc) (n = 4), (f) palbociclib-induced senescent 4T1 cells (n = 3), (g) doxorubicin-induced senescent HCT116 cells (n = 2), (h) irradiation-induced senescent MLg cells (n = 3) and (i) oncogene-induced senescent IMR90 cells (previously treated for 72 h with 200 nM 4-hydroxytamoxifen (4-OHT)). Data in (c-g) represent mean \pm SD of replicates, and statistical significance was calculated using a two-tailed Student's t test; *p < .05, **p < .01, ***p < .001

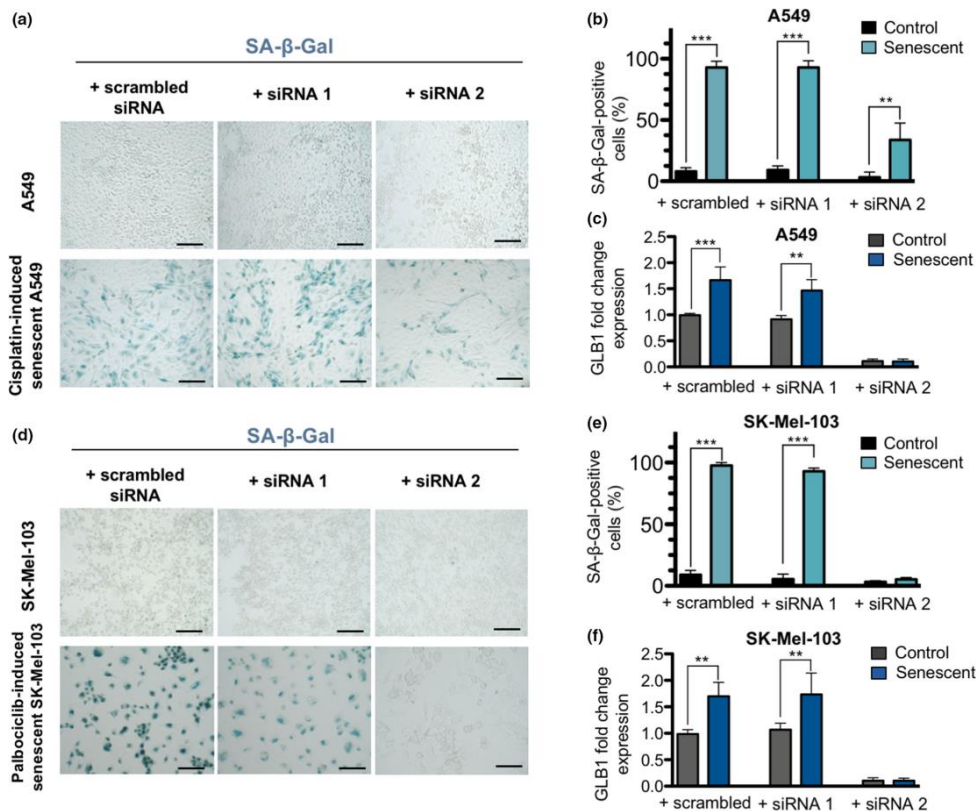


Figure 3. *GLB1* transient downregulation prevents the senolytic activity of *Nav-gal*. (a) representative images of SA-β-Gal staining of control and cisplatin-induced senescent A549 cells 48 h after transfection with scrambled siRNA, siRNA 1 and siRNA 2. Scale bar = 200 μm. (b) Percentage of SA-β-Gal-positive cells in conditions presented in (a). (c) *GLB1* fold change gene expression in control and senescent A549 cells 48 h post-transfection with different siRNAs. (d) Representative images of SA-β-Gal staining of control and palbociclib-induced senescent SK-Mel-103 cells 48 h after transfection with scrambled siRNA, siRNA 1 and siRNA 2. Scale bar = 200 μm. (e) Percentage of SA-β-Gal-positive cells in conditions presented in (d). Bars represent mean ± SD (n = 3). (f) *GLB1* fold change gene expression in control and senescent SK-Mel-103 cells 48 h post-transfection with different siRNAs.

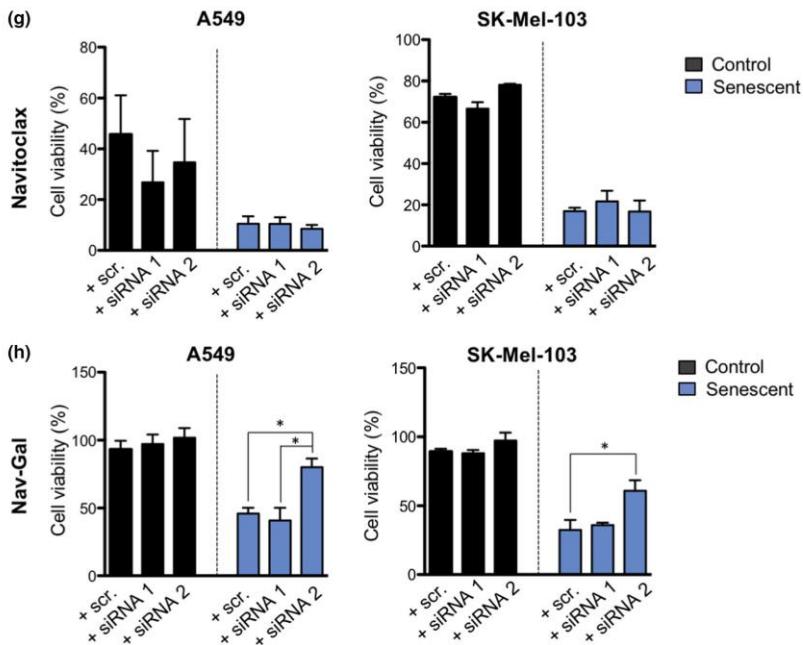


Figure 3. (g) Quantification of cell viability upon 48 h Navitoclax treatment of control and cisplatin-induced senescent A549 cells (10 μ M Navitoclax) (left) and control and palbociclib-induced senescent SK-Mel103 cells (7.5 μ M Navitoclax) (right) previously transfected with different experimental siRNAs against GLB1. (h) Quantification of cell viability upon 48 h Navitoclax treatment of control and cisplatin-induced senescent A549 cells (10 μ M **Nav-gal**) (left) and control and palbociclib-induced senescent SK-Mel103 cells (7.5 μ M **Nav-gal**) (right) previously transfected with different experimental siRNAs against GLB1. All bars represent mean \pm SEM ($n = 3$). One-way ANOVA followed by Tukey's post-tests were performed to calculate the significance of the results; * $p < .05$, ** $p < .01$, *** $p < .001$.

7.3.3 Nav-gal induces apoptosis of senescent cells while preserving viability of non-senescent cells

The use of Navitoclax has been described to induce apoptosis preferentially in senescent cells through inhibition of the BCL-2-regulated pathway.¹³ To assess whether **Nav-gal** and Navitoclax killed senescent cells by the same end mechanism, cisplatin-induced senescent lung cancer A549 cells and palbociclib-

induced senescent melanoma SK-Mel-103 cells were treated with Navitoclax or **Nav-gal** (or vehicle) in parallel, with automated realtime measurement of apoptosis study using a live-cell analysis system. Figure 4a,b and Figure S3A–D show that treatment with either Navitoclax or **Nav-gal** induced apoptosis preferentially in chemotherapy-induced senescent cells (as inferred from an increased annexin V signal). Importantly, and consistent with the results above (Figure 2a,b), the induction of apoptosis was lower in control nonsenescent cells treated with **Nav-gal** compared with Navitoclax (both at a high dose; 10 μ M), particularly at later time points. While over 70% of nonsenescent A549 cells presented a strong signal for annexin V after 36 h of treatment with Navitoclax, this was true for only ~30% of the cells after treatment with the same dose of **Nav-gal** (Figure 4a,b and Figure S3A). Consistent effects were observed with the melanoma cell line SK-Mel-103 (Figure S3B–D). These results indicate that **Nav-gal** kills senescent cells by inducing apoptosis and that it protects against nonsenescent cell death to a higher extent than Navitoclax

7.3.4 Cisplatin and Nav-gal have additive antitumour effects when used concurrently and sequentially

Effective anti-cancer treatments have enhanced clinically beneficial effects when given in combination, including in NSCLC. We therefore next sought to ascertain the efficacy of concurrent cisplatin and **Nav-gal** treatment *in vitro*. We first used clonogenic assays to determine the efficacy of the combination of senescence-inducing cisplatin and Navitoclax, **Nav-gal** or vehicle, administered concomitantly to A549 cells. Compared with monotherapies, the combination of cisplatin and a senolytic drug was substantially more effective at inhibiting cell proliferation (Figure 4c-f). From 0 to 2 μ M cisplatin, as the concentration of both Navitoclax and **Nav-gal** increases, additional impairment of cell growth was observed. There

was also a significant reduction in the concentration of **Nav-gal** required to produce growth inhibition in 1 μM cisplatin versus 0 μM cisplatin (Figure S3G). Similar to the IC₅₀ experiments (Figure 2a,b), a higher dose of **Nav-gal** than Navitoclax was required to achieve the same effect, likely due to the requirement for **Nav-gal** processing and activation by lysosomal $\beta\text{-Gal}$ activity. While both senolytic drugs showed an additive effect in combination with cisplatin, increasing doses of **Nav-gal** exhibited coefficients of drug interactions (CDIs) <1 and closer to 0 in combination with 1 μM cisplatin (Figure 4g), which suggests that the combination of drugs are likely to be synergistic.³²

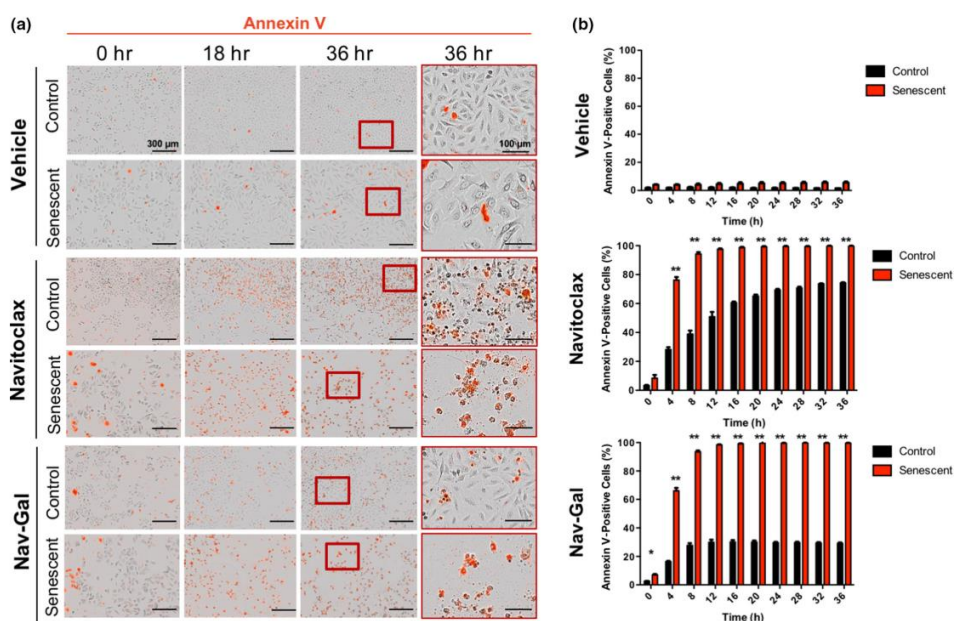


Figure 4. The galacto-conjugated prodrug **Nav-gal** shows an enhanced effect when combined to senescence-inducing cisplatin treatment and a lower induction of apoptosis of nonsenescent cells. (a) Representative images of cell viability showing staining for Annexin V (red) of control or cisplatin-induced senescent A549 cells, exposed to vehicle, Navitoclax (10 μM) or **Nav-gal** (10 μM) treatment over time. Red scale bar = 300 μm ; black scale bar = 100 μm . (b) Average percentage of Annexin V-positive cells in control and cisplatin-induced senescent A549 cells exposed to vehicle (top), Navitoclax (10 μM ; middle) or **Nav-gal** (10 μM ; bottom) treatment over time. Data represent mean \pm SD ($n = 3$), where for each biological repeat the percentage of Annexin V-positive cells was calculated in 3 independent technical repeats per experimental condition. Statistical significance was calculated using two-tailed Student's t tests; * $p < .05$, ** $p < .001$.

Of note, these observations were also validated in the context of a sequential treatment, where colonies were first exposed to increasing concentrations of cisplatin for 7 days, followed by 7 days of senotherapy (Figure S3E,F).

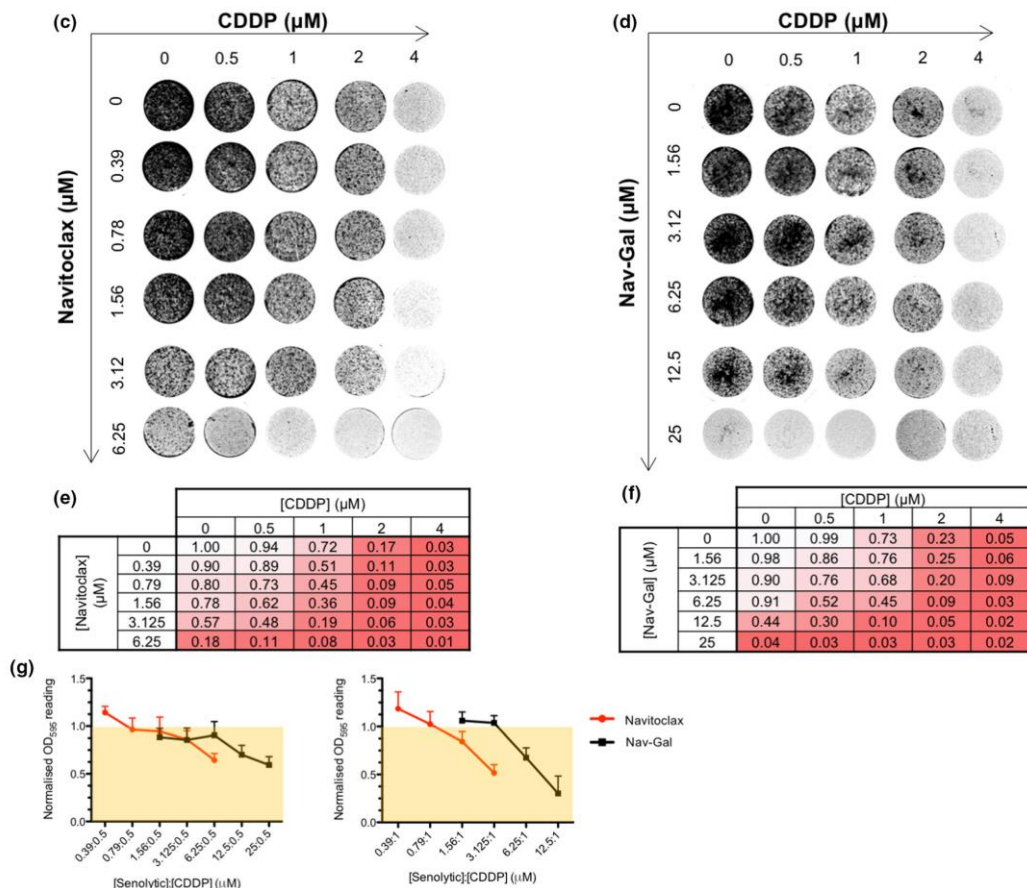


Figure 4. (c, d) Representative images of clonogenic survival of A549 cells exposed to increasing concomitant concentrations of cisplatin (CDDP) and (c) Navitoclax or (d) **Nav-gal** as specified in axis. (e, f) Numerical heat map representation of normalized mean clonogenic potential after 10 days of increasing concomitant treatment with CDDP and (e) Navitoclax or (f) **Nav-gal**, where 1 = maximum clonogenic potential corresponding to untreated condition ($n = 3$). (g) Co-coefficient of drug interaction (CDI) value trend of Navitoclax and **Nav-gal** across 0.5 μM cisplatin treatment (left) and 1 μM cisplatin treatment (right). CDI < 1 (yellow area) indicates a synergistic effect, where CDI values closer to 0 correlate to higher synergy between the drugs concomitantly used. Data represent mean \pm SD ($n = 3$).

7.3.5 Therapeutic activity of Nav-gal in xenografts and orthotopic models of NSCLC

In order to validate the efficiency of the prodrug **Nav-gal** in combination with senescence-inducing chemotherapy *in vivo*, we used a model whereby A549 cells were transplanted subcutaneously into the flanks of severe combined immunodeficient (SCID) mice. In a first approach, we aimed to assess the induction of senescence in tumour-bearing mice treated with cisplatin. Histological analyses of the tumours collected after treatment showed evidence of senescence induction upon cisplatin administration (as inferred from SA- β -Gal positivity) (Figure 5a). The effects of concomitant treatment with cisplatin and each senolytic were then investigated. Once tumours reached an average volume of 100 mm³, mice were treated with cisplatin and daily doses of Navitoclax and **Nav-gal**, alone or in combination, for 17 days (as shown in Figure 5b). Importantly, both drugs improved the tumour growth inhibition of cisplatin (Figure 5c). The combination of cisplatin with either Navitoclax or **Nav-gal** had comparable effects on tumour growth inhibition, but both showed statistically significant differences with control and monotherapy groups. In contrast, Navitoclax and **Nav-gal** had no appreciable effect on tumour growth when administered in the absence of cisplatin, indicating that their therapeutic activities require concomitant induction of senescence by cisplatin in this model system. Consistently, histological analyses of the tumours revealed that cisplatin treatment results in increased p21 positivity (correlating with Western blot analyses of cisplatin-treated cells *in vitro*, Figure S2B) and decreased Ki67 positivity, which together constitute a hallmark of senescent cells (Figure 5d,e). Treatment with cisplatin and either Navitoclax or **Nav-gal** exhibited reduced levels of p21 and Ki67 positivity, alongside a strong TUNEL signal, strongly suggesting that apoptosis of senescent cells facilitates the anti-tumour effect. Additionally, a therapeutic effect of both Navitoclax and **Nav-gal** in tumour growth was observed in a sequential treatment after one week of cisplatin administration, suggesting a potential application as adjuvant therapy for clearing senescent cells (Figure S4A,B). To obtain further evidence of the therapeutic potential of **Nav-gal** in combination with senescence-inducing

chemotherapy in a more physiological context, we used an orthotopic model of NSCLC. Here, wild-type C57BL/6J mice were transplanted (via tail vein injection) with a syngeneic luciferase-expressing KP lung adenocarcinoma cell line (L1475Luc).³¹ Once tumours were established in the lungs, baseline luciferase signals were obtained and mice were then treated for 10 days with cisplatin alone, cisplatin and **Nav-gal** in combination, or their vehicles in combination, using the experimental scheme shown in Figure S5A. Representative images of the luciferase signal at initial and end-points are shown in Figure S5B. Luciferase signal monitoring demonstrated that concomitant treatment of the mice with cisplatin and **Nav-gal** significantly decreased tumour burden (Figure S5C) compared with cisplatin monotherapy. Histological analysis of the lungs showed high burden of senescent cells only in cisplatin-treated mice (as evidenced by increased SA- β -Gal and p21 levels), and decreased SA- β -Gal and p21 levels and higher TUNEL staining in mice concomitantly treated with cisplatin and **Nav-gal**, indicating enhanced apoptosis of senescent cells (representative areas are shown in Figure S5D).

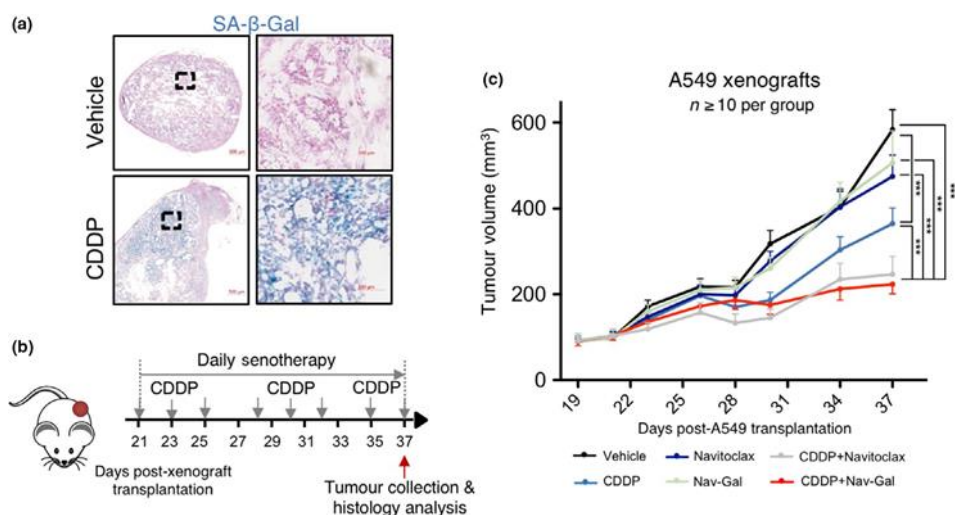


Figure 5 Concomitant treatment with the prodrug **Nav-gal** and cisplatin significantly inhibits tumour growth in a human lung cancer xenograft mouse model. (a) Representative images of A549 xenografts stained for SA- β -Gal activity (in blue) after treatment with cisplatin or vehicle. (b) Schematic representation of concomitant treatment on A549-xenograft-bearing mice. (c) Tumour volume of A549 xenografts in mice concomitantly treated with cisplatin and Navitoclax or **Nav-gal** (as described in (b)); $n \geq 10$ tumours per group. Data represent mean \pm SEM.

Taken together, these results demonstrate that the combination of senescence-inducing therapy with senotherapy is highly effective in inhibiting tumour growth *in vivo*, providing preclinical proof-of-principle of the therapeutic benefits of using **Nav-gal** as a potent prodrug with senolytic activity.

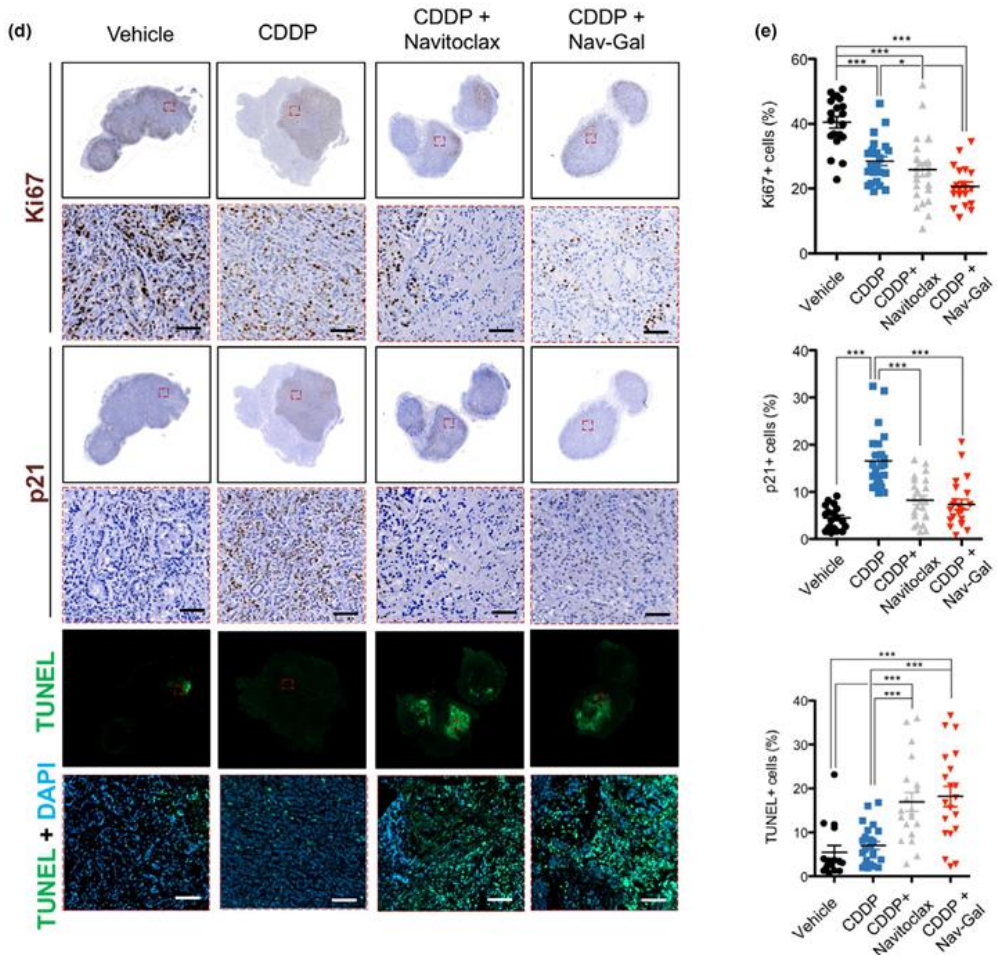


Figure 5. (d) Representative histological images of tumours at the end of concomitant treatment, stained for Ki67 and p21 expression, and labelled using TUNEL staining. Scale bar = 100 μ m. (e) Percentage of Ki67- (top), p21- (middle) and TUNEL-positive (bottom) cells in tumours from animals treated with vehicle, cisplatin, or cisplatin and Navitoclax or **Nav-gal** concomitantly ($n \geq 5$ tumours per group). For quantification, a total of 4 fields per tumour was analysed, covering most of the total tumour area. Two-way ANOVA followed by Bonferroni post-tests was performed to calculate the significance of the results; * $p < .05$; ** $p < .01$; *** $p < .001$.

7.3.6 Nav-gal has reduced platelet toxicity when compared with Navitoclax

Thrombocytopenia is a major dose-limiting, and clinically important, toxicity that is produced by Navitoclax in human patients.^{22,33} A potential benefit for galacto-conjugation of senolytic drugs is the reduction of their associated toxicities, and the potential widening of their therapeutic windows. To determine whether galacto-conjugation affected platelet toxicity, we performed *ex vivo* experiments with both human and murine blood samples where we exposed the whole blood to increasing concentrations of either Navitoclax or **Nav-gal**, using fluorescein-labelled annexin V to identify apoptotic platelets by flow cytometry³⁴ (Figure S6A,B). As observed in Figure 6a,b for human blood and in Figure 6c,d for mouse blood, when samples were exposed to the same concentrations of Navitoclax and **Nav-gal**, the proportion of platelets with annexin V signal was significantly higher after exposure to Navitoclax than with **Nav-gal**. This effect persists in both models, despite a significant difference in platelet sensitivity to BCL-2 family inhibition between each model. To determine whether **Nav-gal** also protected platelet levels at therapeutic doses *in vivo*, we first examined the platelet count of wild-type C57BL/6J treated daily with senotherapy for a total of 10 days (Figure 6e). As shown in Figure 6f, daily administration of Navitoclax resulted in severe thrombocytopenia after only 5 days of treatment, independently of the route of administration. Remarkably, **Nav-gal** treatment did not cause thrombocytopenia in the mice and led to platelet count levels comparable to those of vehicle-treated individuals, showing reduced platelet toxicity compared to Navitoclax. In order to validate our findings in the context of an *in vivo* cancer model, the platelet count was also assessed at end-points of the concomitant treatment of xenograft-bearing mice described in Figure 5b-d. Notably, as shown in Figure 6g,h, no significant additional thrombocytopenia was observed in the group treated with

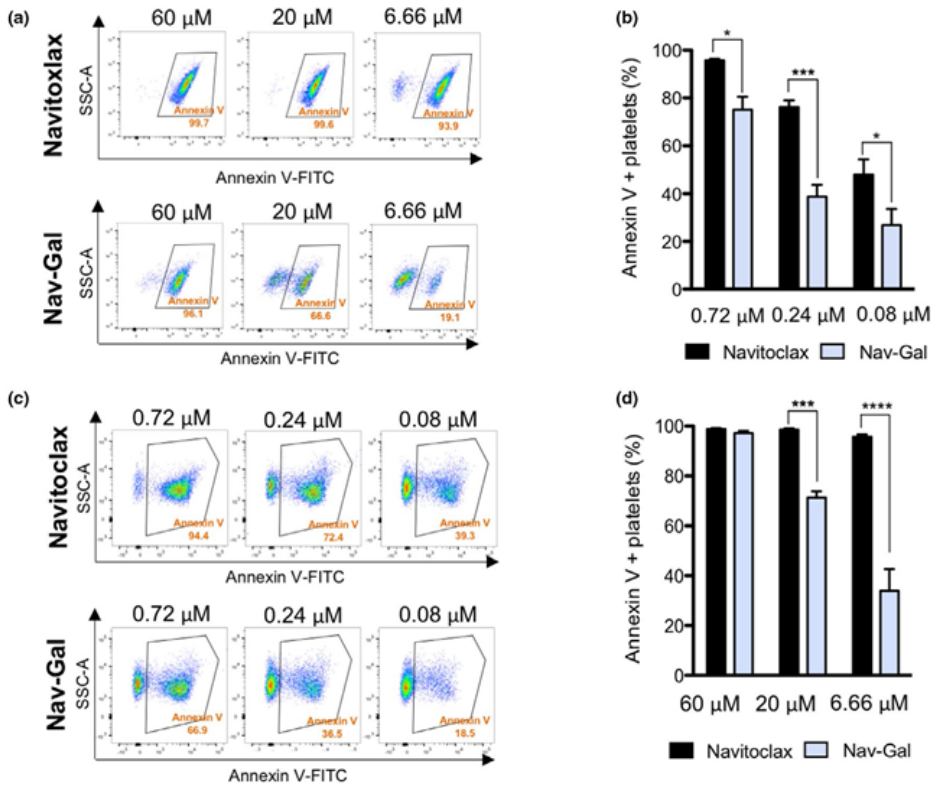


Figure 6 Nav-gal reduces thrombocytopenia in mice undergoing chemotherapeutic and senolytic treatment and reduces platelet apoptosis in mouse and human blood *ex vivo*, compared to Navitoclax. (a) Blood from healthy human volunteers was collected and treated *ex vivo* with 60, 20 and 6.66 μM Navitoclax or **Nav-gal** as described. Apoptosis was analysed after Annexin V-FITC antibody incubation by flow cytometry. Graphs show proportion of apoptotic platelets upon each treatment based on scatter signals and Annexin V expression signal after gating for CD41-positive cells. (b) Percentage of Annexin V-positive platelets in human blood after treatment with 60, 20 and 6.66 μM Navitoclax or **Nav-gal**. Bars represent mean \pm SD ($n = 3$). (c) Blood from wild-type C57BL/6J mice was collected and treated *ex vivo* with 0.72, 0.24 and 0.08 μM Navitoclax or **Nav-gal** as described. Apoptosis was analysed after Annexin V-FITC antibody incubation by flow cytometry. Graphs show proportion of apoptotic platelets upon each treatment based on scatter signals and Annexin V expression signal after gating for CD41-positive cells. (d) Percentage of Annexin V-positive platelets in mouse blood after treatment with 0.72, 0.24 and 0.08 μM Navitoclax or **Nav-gal**. Bars represent mean \pm SD ($n = 5$).

cisplatin and **Nav-gal** (cf. Navitoclax). We also found that **Nav-gal** reduced platelet toxicity, either in combination with cisplatin or as monotherapy, when administered in a sequential manner (Figure S4A–C), providing further evidence of platelet protection *in vivo*. These results confirm that the galacto-conjugation of Navitoclax to produce the **Nav-gal** prodrug serves as an effective strategy to decrease Navitoclax-driven thrombocytopenia at physiologically relevant concentrations capable of halting cancer growth. Altogether, we conclude that galacto-conjugated Navitoclax is effective in clearing senescent cells *in vivo* and can reduce its associated toxicities.

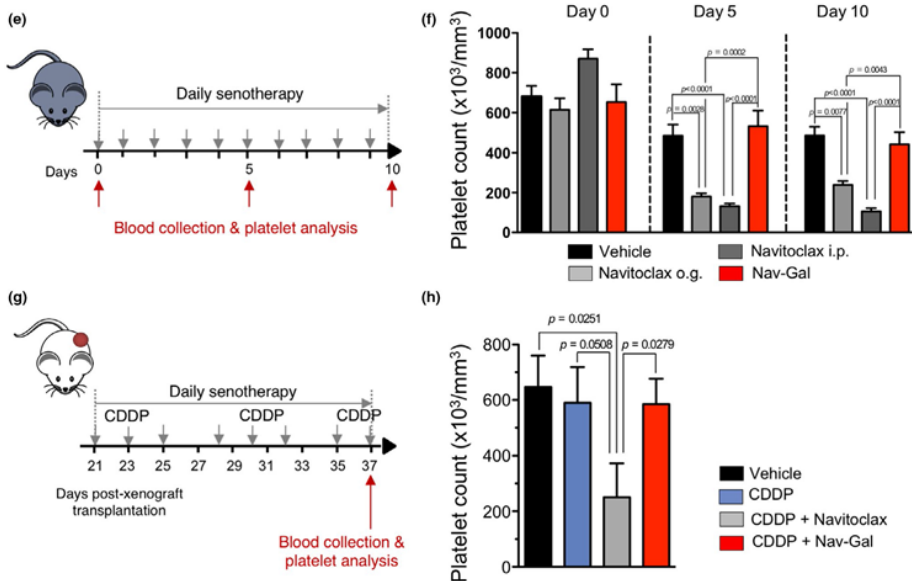


Figure 6. (e) Wild-type C57BL/6J mice were treated daily with Navitoclax by oral gavage (o.g.) (100 mg/kg body weight), with Navitoclax administered by i.p. injection (85 mg/kg body weight) or with **Nav-gal** (85 mg/kg body weight) for 10 consecutive days. Blood was collected on day 0, 5 and 10 by superficial vessel puncture and platelet count was analysed. (f) Platelet count on day 0, 5 and 10 during the treatment of wild-type C57BL/6J mice in each experimental condition as described in (e) (vehicle, $n = 4$; Navitoclax o.g., $n = 9$; Navitoclax i.p., $n = 8$; **Nav-gal**, $n = 8$). Bars represent mean \pm SEM. (g) SCID mice bearing A549-derived xenografts were treated with cisplatin (CDDP, 1.5 mg/kg body weight three times a week) and concomitant daily senotherapy (Navitoclax [100 mg/kg body weight] or **Nav-gal** [85 mg/kg body weight]) as shown in this schematic representation. Blood was collected after treatment by cardiac puncture and, platelet count was analysed. (h) Platelet count in each experimental condition described in (g) upon end of treatment *in vivo* (vehicle and CDDP, $n = 5$; CDDP + Navitoclax, $n = 4$; CDDP + **Nav-gal**, $n = 6$). Data represent mean \pm SEM. Two way ANOVA followed by Bonferroni post-tests or one-tailed t tests was performed to calculate the significance of the results; * $p < .05$; ** $p < .001$; *** $p < .0001$

7.4 Discussion

In the last decade, the use of novel genetically engineered mouse models has demonstrated that the selective elimination of senescent cells attenuates a number of age-related pathologies and promotes the healthspan and lifespan of mice.³⁵ These observations resulted in the development of senotherapies—therapies aimed at interfering with cellular senescence, either by killing senescent cells (senolytics) or by inhibiting the SASP (senomorphics or senostatics).¹² However, specifically targeting senescent cells still remains a considerable challenge in most cases, and senotherapies are not exempt from both on- and off-target toxicities, due to the activity of these agents in normal cells. Here, we report a versatile methodology for the generation of prodrugs that permits a more selective senolytic activity. We show that galactoconjugation of the BCL-2 family inhibitor Navitoclax allows therapeutically relevant activity in subcutaneous tumour xenografts and orthotopic mouse models of chemotherapy-induced senescence in the context of lung carcinoma. In addition, this strategy reduces Navitoclax-associated thrombocytopenia in treated mice, and platelet apoptosis in human and murine blood samples. Targeting cellular senescence by galactoconjugation relies on the high levels of lysosomal β -Gal (SA- β -Gal) activity present in multiple types of senescent cells. Although SA- β -Gal is an imperfect marker of senescence, diseased tissues are often positive for this marker, particularly when senescent cells accumulate and persist in damaged areas.^{23,36} To exploit the accumulated pathological SA- β -Gal activity, we previously used beads with a mesoporous silica core that were functionally capped with a homogeneous coating of galacto-oligosaccharides, thereby allowing the encapsulation of cytotoxic drugs, including doxorubicin and Navitoclax, as well as fluorescent tracers for the detection of senescent cells. This nanotechnology enabled preferential cargo release within senescent cells, and the efficacy of this approach

was validated in models of bleomycin-induced pulmonary fibrosis and palbociclib-treated melanoma and NSCLC tumours.²⁶ However, despite the emergent interest in the development of nanomedicine and the considerable technical success of an increasing number of nanotechnologies in preclinical models, only a small number of formulations have reached clinical translation. The current limitations stem from an incomplete understanding of nano-bio interactions, potential toxicities, and challenges regarding biodistribution, such as systemic trafficking, presence of physiological barriers, mechanisms of cellular uptake, pharmacokinetics/pharmacodynamics (PK/PD), and routes and timelines of elimination.³⁷ In order to simplify the delivery of drugs to the lysosome of senescent cells, we recently created an OFF-ON two-photon fluorescent probe conjugated with an acetylated galactose for tracking cellular senescence *in vivo*.²⁷ Acetylation is a widely used technique to markedly increase cellular permeabilization and uptake of *N*-acetylated amino sugars.²⁸ We show here that conjugation of Navitoclax with a β -Gal activity-driven, cleavable acetylated galactose results in an effective prodrug that enhances its selective senolytic activity (over the parent drug) in a variety of cell types and senescence triggered by different stimuli, suggesting a potentially universal approach for senescent cell targeting. This includes cisplatin-induced senescence in human (A549) and mouse (KP) lung cancer lines; human melanoma (SK-Mel-103) and mouse mammary gland (4T1) cancer cell lines responsive to palbociclib; doxorubicin-induced senescent colorectal carcinoma cells (HCT116); mouse lung fibroblasts (MLg cells) subjected to X-ray radiation and human lung fibroblasts undergoing oncogene-induced senescence (ER:Mek IMR90 cells). Since Navitoclax is a potent small-molecule inhibitor of BCL-2, BCL-XL, and BCL-W proteins that exerts its killing activity by inducing apoptosis,³⁸ we also tested whether this underlying mechanism of cell death is conserved for **Nav-gal**. Similarly to Navitoclax, we observed that **Nav-gal** induces the appearance of

annexin V-positive cells in two models of chemotherapy-induced senescence, namely cisplatin-induced senescent A549 lung cancer cells and palbociclib-induced senescent SK-Mel-103 melanoma cells, thereby indicating that senolysis by **Nav-gal** is driven by the implementation of the apoptotic programme. After validating the use of **Nav-gal** with senescent cancer cells in culture, we focused on two *in vivo* models of lung carcinogenesis subjected to senescence-inducing chemotherapy. We showed that simultaneous administration of **Nav-gal** with the standard-of-care senescence-inducing cisplatin (widely used in the management of NSCLC patients) resulted in reduced tumour burden in SCID mice bearing subcutaneous tumour xenografts comprised of human A549 lung cancer cells. Concomitant treatment with cisplatin and **Nav-gal** also reduced tumour burden in an orthotopic transplantation model using murine KP lung adenocarcinoma cells. **Nav-gal** administration showed a strong effect in reducing tumour growth during both sequential and concomitant treatment with cisplatin. Combination treatment suggests an additive/synergistic effect between cisplatin and **Nav-gal**, as observed in our clonogenic assays and further confirmed by the calculated coefficient of drug interaction (CDI). It is important to note that neither Navitoclax nor **Nav-gal** had any relevant impact on tumour burden in the absence of cisplatin in our murine models, strongly suggesting a therapeutic activity restricted to the induction of senescence or whenever tumours contain senescent areas, but not in fully proliferative tumours. These observations reinforce the concept of **Nav-gal** as a senolytic prodrug and, more generally, open up the possibility of using senotherapies as promising adjuncts to treat cancer in combination with senescence-inducing chemotherapies. The eradication of senescent cancer cells by **Nav-gal** may also prevent tumour progression by mitigating the senescent secretome (SASP) and its broad range of potential protumorigenic effects.⁶ In this regard, cancer therapies can induce senescence not only in cancer cells but also in

stromal cells, and this is also the case in lung cancer patients subjected to platinum- and taxane-based chemotherapy regimens.¹⁰ Stromal senescence appears to establish an immunosuppressive microenvironment that influences and promotes tumorigenesis³⁹ and can also be a fundamental driver of the metastatic niche.⁹ Future studies will examine the impact of **Nav-gal** on stromal senescence. Taken together, our data reinforce the concept that combination treatments comprised of senescence-inducing radio/chemotherapy and senolytics might result in potent approaches for precision cancer management in the near future. As with many targeted agents, Navitoclax presents clinically important and dose-limiting haematological toxicities in clinical trials, including thrombocytopenia,²² presenting particular challenges when given in combination with cytotoxic chemotherapies which also have dose-limiting haematological toxicities. For Navitoclax, this occurs because of the importance of BCL-XL in platelet survival, and the gradual reduction of its levels by Navitoclax promotes a change in the molecular clock that determines platelet lifespan leading to the pro-apoptotic activity of BAK.⁴⁰ In addition to thrombocytopenia, the first trial to evaluate Navitoclax in lymphoid malignancies resulted in grade III transaminitis and gastrointestinal bleed in a proportion of patients subjected to a continuous dosing schedule.³³ The modification of Navitoclax with an acetylated galactose may prevent the exposure of healthy (nonsenescent) cells to the inhibitory activity of BCL-2 family protein members and, thereby, reduce unwanted side effects. In support of this, our IC₅₀ experiments with A549 cells treated with cisplatin indicated that the enhanced senolytic index of **Nav-gal** when compared to Navitoclax is mainly due to reduced cytotoxicity in the absence of senescence induction, suggesting that the prodrug is not efficiently activated in nonsenescent A549 cells. Also, we noted that although the percentage of annexin V-positive senescent cancer cells at a high concentration of both Navitoclax and **Nav-gal** is

similar and results in the complete eradication of these cells, nonsenescent cancer cells were substantially more protected from the induction of apoptosis when exposed to **Nav-gal**, indicating enhanced selective sensitivity for **Nav-gal** for senescent cells. Importantly, we have observed that **Nav-gal** results in less thrombocytopenia (compared with Navitoclax) in daily-treated mice. We also show that **Nav-gal** reduces apoptosis in platelets, using both human and mouse blood samples. A recent study has shown that another Navitoclax derivative, namely DT2216, exerts anti-tumour activity by targeting BCL-XL to the VHL E3 ligase for proteolytic degradation.⁴¹ However, distinctly to **Nav-gal**, DT2216 has not been designed for targeting senescent cells, but for reducing thrombocytopenia (as platelets are characterized by poor VHL E3 ligase expression) while maintaining anti-cancer properties. In addition, DT2216 specifically targets BCL-XL, but not BCL-2 or BCL-W, which may also hinder its potential senolytic activity. In summary, we have synthesized a potent senolytic prodrug that can be used to kill multiple types of senescent cells. We propose galacto-conjugation as a versatile strategy that might be expanded to other cytotoxic agents and senolytic drugs to develop more specific, next-generation senolytics. As a proof-of-principle, we show that galacto-conjugated Navitoclax (**Nav-gal**) selectively kills a variety of human and murine cell types undergoing senescence by different stressors *in vitro* and that it has therapeutic efficacy in combination with cisplatin in murine NSCLC models. Importantly, we also demonstrate that galacto-conjugation of senolytics can reduce potential toxicities of the conjugated drug. The development of galacto-conjugated prodrugs has considerable promise for improving cancer treatment, as well as other human senescence-related disorders.

7.5 Experimental procedures

7.5.1 Synthesis, characterisation and hydrolysis reaction studies

For the synthesis of **Nav-gal** prodrug, 40 mg (0.04 mmol) of Navitoclax (Eurodiagnostico), 25 mg (0.06 mmol) of 2,3,4,6-tetra-O-acetyl- α -D-galactopyranosyl-bromide (Sigma) and 10.5 mg (0.07 mmol) of K_2CO_3 (Sigma) were mixed. Anhydrous acetonitrile (Sigma) was added, and the mixture was stirred at 70°C for 3 h under argon-enriched atmosphere. The solvent was eliminated under vacuum. The product was purified by flash chromatography on silica gel (Sigma), from hexane-ethylacetate (3:7 v/v; Scharlab) to hexane-ethylacetate (7:3 v/v) used as eluent. Purified **Nav-gal** was obtained as a yellow powder in 35% yield. For large stocks used in mouse experiments, the reactions were performed in different batches. Once the desired amount was obtained, all batches were pooled and purified on a single flash chromatography column as described above.

7.5.2 Characterisation of Nav-gal prodrug

Nav-gal was characterised by conventional techniques. For samples preparation, pure **Nav-gal** was dissolved in deuteriochloroform ($CDCl_3$; Sigma) and transferred to a Wilma NMR tube (Sigma). Samples were immediately analysed by proton nuclear magnetic resonance (1H -NMR), Carbon-13 nuclear magnetic resonance (^{13}C -NMR) and homonuclear bidimensional correlated spectroscopy (COSY NMR). NMR spectra were acquired with a Bruker FT-NMR Avance 400 (Ettlingen, Germany) at 300 K and analysed with MestReNova 6.0 software. Chemical shifts are expressed as δH (ppm) relative tetramethylsilane (TMS). Attenuated total reflectance (ATR) was performed in a Bruker Tensor 27 FT-IR (Ettlingen, Germany) at room temperature and analysed with OPUS Data Collection Program (V1.1).

Finally, high resolution mass spectrometry (HRMS) was recorded with an ABSciex TRIPLETOF T5600.

7.5.3 Hydrolysis reaction of Nav-gal studies

For hydrolysis reaction studies, aqueous solutions of Navitoclax and **Nav-gal** at a concentration of 10^{-5} M (pH 7) in 0.01% DMSO were prepared. Human β -Gal (Biotechne, R&D Systems) was then added to **Nav-gal** solutions to a final concentration of 8 ng/ μ l, and chromatograms were acquired after complete reaction ($\lambda_{\text{exc}} = 365$ nm) with a Waters 1525 binary HPLC pump equipped with a Waters 2990 diode array detector. Chromatograms were obtained using Empower 3 software. Conditions: KromasilC18 column, 0.9 ml/min, (H₂O (0.1% acetic acid): MeOH gradient elution: 50:50 3 min, 40:60 7 min, 30:70 10 min, 20:80 5 min, 10:90 3 min, 0:100 3 min. Data analysis was performed using OriginPro8 software.

7.5.4 Cells and reagents

The human lung carcinoma cell line A549 was obtained from the European Collection of Authenticated Cell Cultures (ECACC). SKMEL-103 (human melanoma), 4T1 (breast cancer), HCT116 (human colorectal carcinoma) and MLg (mouse lung fibroblastic) cell lines were obtained from the American Type Culture Collection (ATCC). The murine KP lung adenocarcinoma cell line L1475 was derived from Kras^{LSL-G12D/+};p53^{Fx/Fx} mice⁴² and transduced with MSCV-luciferase-hygromycin retrovirus, as previously described.³¹ A549, SK-MEL-103, 4T1 and L1475(luc) cell lines were maintained in DMEM, and supplemented with 10% FBS (Sigma). HCT116 cells were grown in McCoy's 5A medium (Thermo Fisher Scientific) supplemented with 10% FBS. MLg cells were cultured in DMEM-F-12 culture media (Sigma) supplemented with 2 mM l-Glutamine and 10% FBS. ER:Mek IMR90 cells were cultured in phenol red-free DMEM (Sigma) supplemented with 10% FBS, 2 mM l-Glutamine and 1 mM sodium pyruvate (Sigma). All cells were incubated in 20% O₂ and 5% CO₂ at 37°C. Cells were

routinely tested for Mycoplasma using the universal mycoplasma detection kit (ATCC) or by RNA-capture ELISA. For senescence induction, A549 cells were treated with 15 Mm of cisplatin (Stratech) for 10 days. SK-MEL-103 and 4T1 cells were treated with 5 μ M palbociclib (Eurodiagnostico) for 7 days. HCT116 cells were treated with 100 nM doxorubicin (Carbosynth) for 72 h. MLg cells were irradiated with 10 Gy and used for viability assays 10 days later. ER:Mek IMR90 cells were treated with 200 nM 4-hydroxytamoxifen for 72 h and used for viability assays 2 days later. For experiments with cells, cisplatin (Stratech) was reconstituted in sterile PBS; palbociclib (Eurodiagnostico), Navitoclax (Stratech) and **Nav-gal** were reconstituted in DMSO. For *in vivo* experiments, cisplatin was reconstituted in saline; Navitoclax was formulated in 10% ethanol, 30% polyethylene glycol 400 and 60% Phosal PG, and **Nav-gal** was reconstituted in DMSO and further diluted in saline.

7.5.5 GLB1 downregulation

For transient downregulation of GLB1, a total of 30,000 control or 50,000 senescent A549 and SK-MEL-103 cells were plated per well in a 24-well plate. The next day, cells were transfected with TriFECTa[®] Kit DsiRNA Duplex siRNAs (Integrated DNA Technologies) hs.Ri. GLB1.13.1 (siRNA1), hs.Ri.GLB1.13.3 (siRNA2) or scrambled siRNA, using Lipotectamine RNAiMAX Reagent (Thermo Fisher Scientific) as per manufacturer's instructions. After 48 h, RNA was extracted using the RNeasy Mini Kit (Qiagen) and cDNA was synthesized with the High-Capacity RNA-to-cDNA[™] Kit (Thermo Fisher Scientific). Gene expression of GLB1 and ACTB genes was measured by quantitative real-time PCR performed on a QuantStudio thermocycler (Applied Biosystems) following Luna[®] Universal qPCR Master Mix (New England Biolabs) protocol and amplification parameters, and using predesigned KiCqStart[®] SYBR[®] Green Primers H_GLB1_1 and H_ACTB_1 pairs (Sigma-Aldrich). Relative quantification was carried out using 2^{- $\Delta\Delta$ Ct} methodology.

7.5.6 Cell viability and apoptosis analysis

For A549, SK-MEL-103, 4T1, HCT116 and ER:Mek IMR90 cell lines, control and senescent cells were seeded in flat-bottom-clear 96-well plates at a density of 6,000–8,000 and 4,000–6,000 cells per well, respectively. The following day cells were treated with serial dilutions of **Nav-gal** or Navitoclax in 0.2% FBS-containing media. Viability was assessed 48 or 72 h later after two hours of incubation at 37°C with CellTiter-Glo® Luminescent Cell Viability Assay (Promega) or CellTiter-Blue® Cell Viability Reagent (Promega). Raw data were obtained by measuring luminescence in a VICTOR Multilabel Plate Reader (Pelkin Elmer) or fluorescence at an excitation/emission wavelength of 560 nm/590 nm in an Infinite 200 PRO Multimode Spectrophotometer (TECAN). For MLg cells, control and senescent cells were seeded in a 12-well plate at a density of 80,000 and 60,000 cells per well respectively, and cells were treated with three to five different increasing concentrations of **Nav-gal** or Navitoclax on the following day. After 72 h, viability was assessed with CellTiter-Blue® Cell Viability Reagent (Promega) as described above. To determine the induction of apoptosis after the treatment with Navitoclax and **Nav-gal**, 4,000 senescent and 6,000 nonsenescent A549 or SK-Mel-103 cells were seeded in 96-well plates. 24 h later, annexin V Fluorescent Reagent (Essen Bioscience) was added to the media, and after a first scan, the cells were treated with vehicle (DMSO), 11 µM Navitoclax or 11 µM **Nav-gal** for 48 h. Images were collected every 2 h with an Incucyte® S3 Live-Cell Analysis System microscope (Essen Bioscience) over time. A total of 2 pictures per well were analysed using the IncuCyte ZOOM™ software analyser, and total and annexin V-positive cells were counted using ImageJ software.

7.5.7 Clonogenic assay

For clonogenic potential analysis, 10,000 A549 cells were seeded per well in a 6-well plate and allowed to attach overnight. In a first approach (concomitant treatment), cells were then treated with increasing and concomitant concentrations of cisplatin and Navitoclax or **Nav-gal**. In a second approach (sequential treatment), cells were first treated with increasing concentrations of cisplatin for 7 days, and then Navitoclax or **Nav-gal** were added for 7 additional days. Fresh drug was added every 2–3 days, and 10 days later, colonies were washed with PBS and fixed with 4% PFA for 10 min. They were then permeabilized using ice-cold methanol for 20 min, and left to dry. Colonies were then stained with 0.5% crystal violet for 30 min, and excess was removed by thoroughly washing three times with deionised water. Colonies were imaged using a BioRad GelDoc XR+ machine (BioRad Technologies). To calculate mean clonogenic potential, staining of colonies was subsequently diluted in 10% acetic acid and optical density (OD) was measured at 595 nm using an Infinite 200 PRO Multimode Spectrophotometer (PECAN) microplate reader. The blank (10% acetic acid) was subtracted from each OD measurement, and the average value for each experimental condition was calculated and normalized against clonogenic potential value obtained in no-treatment condition. To analyse the synergistic effect of the concomitant treatment of cisplatin and the senolytics Navitoclax and **Nav-gal**, we calculated the co-coefficient of drug interaction (CDI) using the normalized clonogenic potential values of the individual and concomitant treatments at different concentrations. CDIs were calculated as ratios following the formula $CDI = (AB)/(A \times B)$, where AB is the clonogenic potential value of the concomitant treatment with the two drugs combined at a specific concentration, and A and B are the clonogenic potential values of the individual treatments of each drug at such concentration. Following this formula, a $CDI > 1$ indicates that

the drugs are antagonistic, a CDI = 1 indicates that the drugs are additive and a CDI < 1 indicates that the drugs are synergistic, with values closer to 0 indicating higher synergy between the drugs. This effect can depend on the ratio and molarity of drugs used, and for this reason, CDIs were calculated and plotted at different molar ratios of cisplatin and Navitoclax or **Nav-gal**.

7.5.8 Immunoblotting

Cell lysis was performed using RIPA buffer (Sigma) supplemented with phosphatase inhibitors (PhosSTOP™ EASYpak Phosphatase Inhibitors Cocktail, Roche) and protease inhibitors (Complete™ Protease Inhibitor Cocktail, Roche). Proteins were quantified and separated by SDS-PAGE and transferred to polyvinylidene difluoride (PVDF) membranes (Millipore) according to standard protocols. Membranes were immunoblotted with antibodies against p21 and p53 from Santa Cruz Biotechnology, and phospho-Rb (pRBS780) from Cell Signaling. After incubation with the primary antibody overnight, membranes were washed and incubated with secondary HRP conjugated AffiniPure antibodies (Jackson ImmunoResearch) for 1 h at room temperature and subsequently incubated with Enhanced Chemiluminescence Detection solution (Amersham). Membranes were placed on X-ray films and processed using a Xograph Compact X4 automatic processor.

7.5.9 Mouse experiments

All mice were treated in strict accordance with the local ethical committee (University of Cambridge Licence Review Committee) and the UK Home Office guidelines. For the orthotopic model experiment, 5–6 weeks old C57BL/6J mice were transplanted in the lungs with 3×10^5 syngeneic luciferase-expressing KP (L1475(luc)) lung tumour cells via tail-vein injection. All mice were maintained in

ventilated cages within a specific pathogen free animal facility. Luminescence values were recorded 5 days later after i.p. injection with D-luciferin (150 mg/kg body weight, PerkinElmer) using an IVIS Spectrum Zenogen machine (Caliper Life Sciences) and analysed with Living Image software, and then randomized into the different experimental groups. Mice were treated with either vehicle, 1 mg/kg CDDP (via i.p. injection) every 3 days and 85 mg/kg **Nav-gal** (via i.p. injection) for two consecutive days after each CDDP administration. Luminescence values were recorded again as described above on day 5 and 15, when treatment was finished, all mice were culled by anaesthetic overdose, and lungs were collected for subsequent histological analyses. To establish subcutaneous tumour xenografts, 5–7 weeks old SCID (CB17-Prkdcscid/J) females were injected subcutaneously with 4×10^6 A549 cells in each flank. Tumours were measured with callipers every 2–3 days, and the tumour volume was calculated with the formula $\text{length} \times \text{width}^2/2$. When tumour volume reached an average of 100 mm^3 , mice were randomised and assigned to one of the control or therapy groups. Therapy was initiated with either vehicle, 1.5 mg/kg cisplatin (CDDP, via intraperitoneal (i.p.) injection) three times per week, 100 mg/kg Navitoclax (via oral gavage) 5 days ON/2 days OFF, 85 mg/kg **Nav-gal** (via i.p. injection) 5 days ON/2 days OFF, or a combination of the mentioned drugs. Mice were culled by cervical dislocation after 3 weeks of treatment. For platelet toxicity analysis, wild-type C57BL/6J mice were treated daily with 100 mg/kg Navitoclax (via oral gavage), 85 mg/kg Navitoclax (via i.p. injection) or 85 mg/kg **Nav-gal** (via i.p. injection) for 10 consecutive days. To analyse platelet count in mice, blood was collected by cardiac puncture during isoflurane anaesthesia in xenograft experimental mice, and by superficial vessel puncture in wild-type C57BL/6J experimental mice. Blood was collected into anticoagulating Microvette® tubes (Sarstedt), and platelet levels were immediately measured using a Scil Vet abc Plus hematology analyser (Horiba).

7.5.10 Histology

SA- β -Gal staining was performed in frozen tissue sections using the Senescence β -Gal Staining kit (Cell Signaling), following the manufacturer instructions. Briefly, whole tissue was fixed at RT for 15 min with a 2% formaldehyde and 0.2% glutaraldehyde, washed and incubated for 6 h at 37°C with the staining solution containing X-gal in *N,N*-dimethylformamide (pH 6.0). Tissues were subsequently counterstained with nuclear fast red, dehydrated and mounted. For immunohistochemistry, 5 mm paraffin sections were deparaffinised and rehydrated, and slides were incubated with anti-p21 (Abcam) and Ki67 (Abcam) antibodies at 4°C overnight, or processed for TUNEL staining using the DeadEnd™ fluorometric TUNEL System (Promega) as per manufacturer's instructions. Immunohistological reaction was of p21, and Ki67 was developed using 3,3'-diaminobenzidine tetrahydrochloride (DAB), and nuclei counterstained with haematoxylin. For immunofluorescence, frozen tissue sections were either processed for TUNEL staining using the above mentioned kit or alternatively fixed in 4% PFA for 10 min, permeabilised with 0.5% Triton™ X-100 for 3 min and subsequently blocked with Normal Donkey Serum for 1 h at room temperature. They were then probed with anti-p21 (Abcam) and Ki67 (Abcam) antibodies at 4°C overnight. The following day, sections were incubated with Anti-Rat IgG 555 and Anti-Rabbit IgG 488 secondary antibodies (Cell Signaling Technologies), briefly incubated in DAPI-containing PBS, and mounted using Fluoromount-G™ Mounting Medium. Images were obtained using an AxioScan Slide Scanner (Zeiss) and processed with ZEN 2 Blue Edition software (Zeiss). Positive signal for p21, Ki67 and TUNEL was quantified with ImageJ.

7.5.11 Platelet apoptosis analysis

For human platelets apoptosis assay, blood from three healthy volunteers was extracted according to the UPV ethics procedures and processed essentially as shown in reference 34. For mouse platelet apoptosis assay, blood from five wild-type C57BL/6J mice was collected by cardiac puncture in accordance with the University of Cambridge ethical committee and the UK Home Office guidelines. Samples were collected in nonvacuum citrate tubes (DH medical material), and blood in control tubes was diluted in Tyrodes Buffer. Blood in treated samples was mixed with 2X drug solution (either Navitoclax or **Nav-gal**) in RPMI (10% FBS). Control and treated specimens were incubated for 5 h in 20% O₂ and 5% CO₂ at 37°C. Treated samples were diluted in Tyrodes Buffer, and then all specimens were mixed with Annexin Binding Buffer (Thermo Fisher Scientific) and incubated for 10 min with Annexin V-FITC (Immunostep) and CD-41-PE (Immunostep) conjugated antibodies. A23187 (Sigma), a calcium ionophore, was also added in parallel control samples to induce cell death and be used as a positive control. Samples were finally diluted in Annexin Binding Buffer (Thermo Fisher Scientific), and data were acquired using an FC500 MPL Flow Cytometer (Beckman-Coulter) for human samples and an LSR Fortessa cell analyser running the FACSDiva software (BD Biosciences) for mouse samples. FlowJo 10.3 software was used to analyse the results.

7.5.12 Statistical analysis

Statistical analyses were performed as described in the figure legend for each experiment. Statistical significance was determined by one- and two-way ANOVA, Student's t tests and Bonferroni post hoc tests using Prism 5 software (GraphPad)

as indicated. A p-value below .05 was considered significant and indicated with asterisk: * $p < .05$, ** $p < .01$ and *** $p < .005$.

7.6 Acknowledgments

The Munoz-Espin's laboratory is supported by the Cancer Research UK (CRUK) Cambridge Centre Early Detection Programme (RG86786), by a CRUK Programme Foundation Award (C62187/A29760), by a CRUK Early Detection OHSU Project Award (C62187/ A26989), by a Medical Research Council (MRC) New Investigator Research Grant (NIRG) (MR/R000530/1) and by a Royal Society Research Grant (RG160806). E.G.-G. is holder of a “La Caixa” Foundation Scholarship for postgraduate studies at European Universities. C.G.-L. holds a EPSRC Scholarship for postgraduate studies at University of Cambridge. R.M laboratory members thank the financial support from the Spanish Government (project RTI2018-100910-B-C41) and the Generalitat Valenciana (project PROMETEO 2018/024). B.L-T. is grateful to the Spanish Ministry of Economy for their PhD grants (FPU15/02707). A. L.-V. is grateful to Instituto de Salud Carlos III for her grant “IFI17/00039”, cofounded by European Regional Development Fund/European Social Fund “Investing in your future”. J. F.-B thanks to his postdoctoral fellowship (PAID-10-17). A.B. acknowledges the Spanish government for her Juan de Cierva Incorporation Grant and her Ayuda Torres Quevedo contract. We thank Prof T. Green and Dr S. Mendez-Ferrer (Wellcome-MRC Cambridge Stem Cell Institute) for the analyses on platelet counts. We also thank Prof T. Jacks (KrasLSL-G12D), Prof A. Berns (p53F_x), and the National Institutes of Health Mouse Repository for the mice used to derive KP cells.

7.7 Conflict of interests

R.M.-M. and M.S. are founders and advisors of Senolytic Therapeutics, Inc. C.P.M is an AstraZeneca employee. The remaining authors declare no competing interests.

7.8 Author contributions

E.G.-G., M.P.-R. and B.L.-T. performed most of the experiments and contributed to the experimental designs, data analysis, and discussion and writing. In particular, M.P.-R. and E.G.-G. performed the most of the *in vivo* experiments and some of the experiments with *in vitro* cultured cells, and B.L.-T. developed the prodrug and performed its synthesis, reaction studies together with J.F.-B., as well as the *ex vivo* analysis of platelet apoptosis with human blood samples and *in vitro* experiments with 4T1 cells. D.M. performed the *ex vivo* analysis of platelet apoptosis in mice and contributed to animal experiments, experimental designs, data analysis and discussion. J.R.W. carried out Incucyte Imaging System experiments, cell viability assays and contributed to data analysis. C.G.-L. helped with histological and SA- β -Gal analyses from tumour sections; H.O. performed cell viability assays and contributed to data analysis. Z.Z. helped with immunofluorescence analyses of orthotopically transplanted lungs; A. L.-V. performed some of the experiments with *in vitro* cultured cells and characterisation of cellular senescence in cell lines. M.R. performed IC50 experiments with SK-Mel-103 cells together with B.L.-T. L.F. helped with pharmacology analyses. C.P.M. generated KP reagents and provided guidance with *in vivo* work. M.S. provided expertise on cellular senescence, and contributed to the discussion. G.J.D provided translational and clinical oversight and contributed to writing. R.M.-M., A.B. and F.S. supervised the chemical synthesis of

the prodrug and contributed to data analysis and discussion. D.M.-E. designed and supervised the biological studies, analysed the data and wrote the manuscript. All authors revised and commented on the manuscript.

7.9 Data availability statement

The data that support the findings of this study are available from the corresponding author upon reasonable request.

7.10 References

1. V. Gorgoulis, P. D. Adams, A. Alimonti, D. C. Bennett, O. Bischof, C. Bishop, J. Campisi, M. Collado, K. Evangelou, G. Ferbeyre, J. Gil, E. Hara, V. Krizhanovsky, D. Jurk, A. B. Maier, M. Narita, L. Niedernhofer, J. F. Passos, P. D. Robbins, C. A. Schmitt, J. Sedivy, K. Vougas, T. von Zglinicki, D. Zhou, M. Serrano, M. Demaria, *Cell* **2019**, *179*, 813.
2. D. Muñoz-Espín, M. Serrano, *Nature Reviews Molecular Cell Biology* **2014**, *15*, 482.
3. B. G. Childs, M. Gluscevic, D. J. Baker, R. M. Laberge, D. Marquess, J. Dananberg, J. M. Van Deursen, Senescent cells: An emerging target for diseases of ageing. *Nature Reviews Drug Discovery* **2017**, *16*, 718–735.
4. D. McHugh, J. Gil, *The Journal of cell biology* **2018**, *217*, 65.
5. J. M. Gonzalez-Meljem, J. R. Apps, H. C. Fraser, J. P. Martinez-Barbera, *British journal of cancer* **2018**.
6. D. V Faget, Q. Ren, S. A. Stewart, *Nature reviews. Cancer* **2019**, *19*, 439.
7. S. Lee, C. A. Schmitt, *Nature cell biology* **2019**, *21*, 94.
8. M. Demaria, M. N. O’Leary, J. Chang, L. Shao, S. Liu, F. Alimirah, K. Koenig, C. Le, N. Mitin, A. M. Deal, S. Alston, E. C. Academia, S. Kilmarx, A. Valdovinos, B. Wang, A. de Bruin, B. K. Kennedy, S. Melov, D. Zhou, N. E. Sharpless, H. Muss, J. Campisi, *Cancer Discovery* **2017**, *7*, 165.
9. X. Luo, Y. Fu, A. J. Loza, B. Murali, K. M. Leahy, M. K. Ruhland, M. Gang, X. Su, A. Zamani, Y. Shi, K. J. Lavine, D. M. Ornitz, K. N. Weilbaecher, F. Long, D. V. Novack, R. Faccio, G. D. Longmore, S. A. Stewart, *Cell Reports* **2016**, *14*, 82.
10. R. S. Roberson, S. J. Kussick, E. Vallieres, S.-Y. J. Chen, D. Y. Wu, *Cancer research* **2005**, *65*, 2795.
11. B. Lozano-Torres, A. Estepa-Fernández, M. Rovira, M. Orzáez, M. Serrano, R. Martínez-Máñez, F. Sancenón, The chemistry of senescence. *Nature Reviews Chemistry* **2019**, *3*, 426–441.
12. M. Paez-Ribes, E. González-Gualda, G. J. Doherty, D. Muñoz-Espín, *EMBO molecular medicine* **2019**, e10234.
13. Y. Zhu, T. Tchkonja, H. Fuhrmann-Stroissnigg, H. M. Dai, Y. Y. Ling, M. B. Stout, T. Pirtskhalava, N. Giorgadze, K. O. Johnson, C. B. Giles, J. D. Wren, L. J. Niedernhofer, P. D. Robbins, J. L. Kirkland, *Aging Cell* **2016**, *15*, 428.

14. R. Yosef, N. Pilpel, R. Tokarsky-Amiel, A. Biran, Y. Ovadya, S. Cohen, E. Vadai, L. Dassa, E. Shahar, R. Condiotti, I. Ben-Porath, V. Krizhanovsky, *Nature Communications* **2016**, 7.
15. M. J. Yousefzadeh, Y. Zhu, S. J. McGowan, L. Angelini, H. Fuhrmann-Stroissnigg, M. Xu, Y. Y. Ling, K. I. Melos, T. Pirtskhalava, C. L. Inman, C. McGuckian, E. A. Wade, J. I. Kato, D. Grassi, M. Wentworth, C. E. Burd, E. A. Arriaga, W. L. Ladiges, T. Tchkonina, J. L. Kirkland, P. D. Robbins, L. J. Niedernhofer, *EBioMedicine* **2018**, 36, 18.
16. Y. Zhu, T. Tchkonina, T. Pirtskhalava, A. C. Gower, H. Ding, N. Giorgadze, A. K. Palmer, Y. Ikeno, G. B. Hubbard, M. Lenburg, S. P. O'Hara, N. F. LaRusso, J. D. Miller, C. M. Roos, G. C. Verzosa, N. K. LeBrasseur, J. D. Wren, J. N. Farr, S. Khosla, M. B. Stout, S. J. McGowan, H. Fuhrmann-Stroissnigg, A. U. Gurkar, J. Zhao, D. Colangelo, A. Dorronsoro, Y. Y. Ling, A. S. Barghouthy, D. C. Navarro, T. Sano, P. D. Robbins, L. J. Niedernhofer, J. L. Kirkland, *Aging cell* **2015**, 14, 644.
17. M. P. Baar, R. M. C. Brandt, D. A. Putavet, J. D. D. Klein, K. W. J. Derks, B. R. M. Bourgeois, S. Stryeck, Y. Rijksen, H. van Willigenburg, D. A. Feijtel, I. van der Pluijm, J. Essers, W. A. van Cappellen, W. F. van IJcken, A. B. Houtsmuller, J. Pothof, R. W. F. de Bruin, T. Madl, J. H. J. Hoeijmakers, J. Campisi, P. L. J. de Keizer, *Cell* **2017**, 169, 132.
18. H. Fuhrmann-Stroissnigg, Y. Y. Ling, J. Zhao, S. J. McGowan, Y. Zhu, R. W. Brooks, D. Grassi, S. Q. Gregg, J. L. Stripay, A. Dorronsoro, L. Corbo, P. Tang, C. Bukata, N. Ring, M. Giacca, X. Li, T. Tchkonina, J. L. Kirkland, L. J. Niedernhofer, P. D. Robbins, *Nature communications* **2017**, 8, 422.
19. Y. Wang, J. Chang, X. Liu, X. X. Zhang, S. Zhang, X. X. Zhang, D. Zhou, G. Zheng, *Aging* **2016**, 8, 2915.
20. A. Guerrero, N. Herranz, B. Sun, V. Wagner, S. Gallage, R. Guiho, K. Wolter, J. Pombo, E. E. Irvine, A. J. Innes, J. Birch, J. Glegola, S. Manshaei, D. Heide, G. Dharmalingam, J. Harbig, A. Olona, J. Behmoaras, D. Dauch, A. G. Uren, L. Zender, S. Vernia, J. P. Martínez-Barbera, M. Heikenwalder, D. J. Withers, J. Gil, *Nature Metabolism* **2019**.
21. F. Triana-Martínez, P. Picallos-Rabina, S. Da Silva-Álvarez, F. Pietrocola, S. Llanos, V. Rodilla, E. Soprano, P. Pedrosa, A. Ferreirós, M. Barradas, F. Hernández-González, M. Lalinde, N. Prats, C. Bernadó, P. González, M. Gómez, M. P. Ikonomopoulou, P. J. Fernández-Marcos, T. García-Caballero, P. Del Pino, J. Arribas, A. Vidal, M. González-Barcia, M. Serrano, M. I. Loza, E. Domínguez, M. Collado, *Nature communications* **2019**, 10, 4731.
22. S. Cang, C. Iragavarapu, J. Savooji, Y. Song, D. Liu, *Journal of hematology & oncology* **2015**, 8, 129.
23. A. Hernandez-Segura, J. Nehme, M. Demaria, *Trends in Cell Biology* **2018**, 28, 436.
24. G. P. Dimri, X. Lee, G. Basile, M. Acosta, G. Scott, C. Roskelley, E. E. Medrano, M. Linskens, I. Rubelj, O. Pereira-Smith, *Proceedings of the National Academy of Sciences of the United States of America* **1995**, 92, 9363.
25. A. Agostini, L. Mondragón, A. Bernardos, R. Martínez-Mañez, M. D. Marcos, F. Sancenón, J. Soto, A. Costero, C. Manguan-García, R. Perona, M. Moreno-Torres, R. Aparicio-Sanchis, J. R. Murguía, *Angewandte Chemie International Edition* **2012**, 51, 10556.
26. D. Muñoz-Espín, M. Rovira, I. Galiana, C. Giménez, B. Lozano-Torres, M. Paez-Ribes, S. Llanos, S. Chaib, M. Muñoz-Martín, A. C. Uceró, G. Garaulet, F. Mulero, S. G. Dann, T. VanArsdale, D. J. Shields, A. Bernardos, J. R. Murguía, R. Martínez-Mañez, M. Serrano, *EMBO molecular medicine* **2018**, e9355.
27. B. Lozano-Torres, I. Galiana, M. Rovira, E. Garrido, S. Chaib, A. Bernardos, D. Muñoz-Espín, M. Serrano, R. Martínez-Mañez, F. Sancenón, *Journal of the American Chemical Society* **2017**, 139, 8808.
28. S.-U. Lee, C. F. Li, C.-L. Mortales, J. Pawling, J. W. Dennis, A. Grigorian, M. Demetriou, *PLOS ONE* **2019**, 14, e0214253.

29. X. Liu, Y. Zhang, W. Huang, W. Tan, A. Zhang, *Bioorganic & Medicinal Chemistry* **2018**, *26*, 443.
30. J. Chang, Y. Wang, L. Shao, R.-M. Laberge, M. Demaria, J. Campisi, K. Janakiraman, N. E. Sharpless, S. Ding, W. Feng, Y. Luo, X. Wang, N. Aykin-Burns, K. Krager, U. Ponnappan, M. Hauer-Jensen, A. Meng, D. Zhou, *Nature Medicine* **2016**, *22*, 78.
31. F. K. Turrell, E. M. Kerr, M. Gao, H. Thorpe, G. J. Doherty, J. Cridge, D. Shorthouse, A. Speed, S. Samarajiwa, B. A. Hall, M. Griffiths, C. P. Martins, *Genes & development* **2017**, *31*, 1339.
32. Y. Zhao, J.-L. Gao, J.-W. Ji, M. Gao, Q.-S. Yin, Q.-L. Qiu, C. Wang, S.-Z. Chen, J. Xu, R.-S. Liang, Y.-Z. Cai, X.-F. Wang, *Journal of interventional ethnopharmacology* **2014**, *3*, 68.
33. W. H. Wilson, O. A. O'Connor, M. S. Czuczman, A. S. LaCasce, J. F. Gerecitano, J. P. Leonard, A. Tulpule, K. Dunleavy, H. Xiong, Y.-L. Chiu, Y. Cui, T. Busman, S. W. Elmore, S. H. Rosenberg, A. P. Krivoshik, S. H. Enschede, R. A. Humerickhouse, *The Lancet Oncology* **2010**, *11*, 1149.
34. M. Vogler, H. A. Hamali, X.-M. Sun, E. T. W. Bampton, D. Dinsdale, R. T. Snowden, M. J. S. Dyer, A. H. Goodall, G. M. Cohen, *Blood* **2011**, *117*, 7145.
35. D. J. Baker, B. G. Childs, M. Durik, M. E. Wijers, C. J. Sieben, J. Zhong, R. A. Saltness, K. B. Jeganathan, G. C. Verzosa, A. Pezeshki, K. Khazaie, J. D. Miller, J. M. Van Deursen, *Nature* **2016**, *530*, 184.
36. N. E. Sharpless, C. J. Sherr, *Nature Reviews Cancer* **2015**, *15*, 397.
37. J. Shi, P. W. Kantoff, R. Wooster, O. C. Farokhzad, *Nature reviews. Cancer* **2017**, *17*, 20.
38. C. Tse, A. R. Shoemaker, J. Adickes, M. G. Anderson, J. Chen, S. Jin, E. F. Johnson, K. C. Marsh, M. J. Mitten, P. Nimmer, L. Roberts, S. K. Tahir, Y. Xiao, X. Yang, H. Zhang, S. Fesik, S. H. Rosenberg, S. W. Elmore, *Cancer research* **2008**, *68*, 3421.
39. M. K. Ruhland, A. J. Loza, A.-H. Capietto, X. Luo, B. L. Knolhoff, K. C. Flanagan, B. A. Belt, E. Alspach, K. Leahy, J. Luo, A. Schaffer, J. R. Edwards, G. Longmore, R. Faccio, D. G. DeNardo, S. A. Stewart, *Nature communications* **2016**, *7*, 11762.
40. K. D. Mason, M. R. Carpinelli, J. I. Fletcher, J. E. Collinge, A. A. Hilton, S. Ellis, P. N. Kelly, P. G. Ekert, D. Metcalf, A. W. Roberts, D. C. S. Huang, B. T. Kile, *Cell* **2007**, *128*, 1173.
41. S. Khan, X. Zhang, D. Lv, Q. Zhang, Y. He, P. Zhang, X. Liu, D. Thummuri, Y. Yuan, J. S. Wiegand, J. Pei, W. Zhang, A. Sharma, C. R. McCurdy, V. M. Kuruvilla, N. Baran, A. A. Ferrando, Y.-M. Kim, A. Rogojina, P. J. Houghton, G. Huang, R. Hromas, M. Konopleva, G. Zheng, D. Zhou, *Nature medicine* **2019**, *25*, 1938.
42. E. L. Jackson, K. P. Olive, D. A. Tuveson, R. Bronson, D. Crowley, M. Brown, T. Jacks, *Cancer Research* **2005**, *65*, 10280.

7.11 Supporting Information

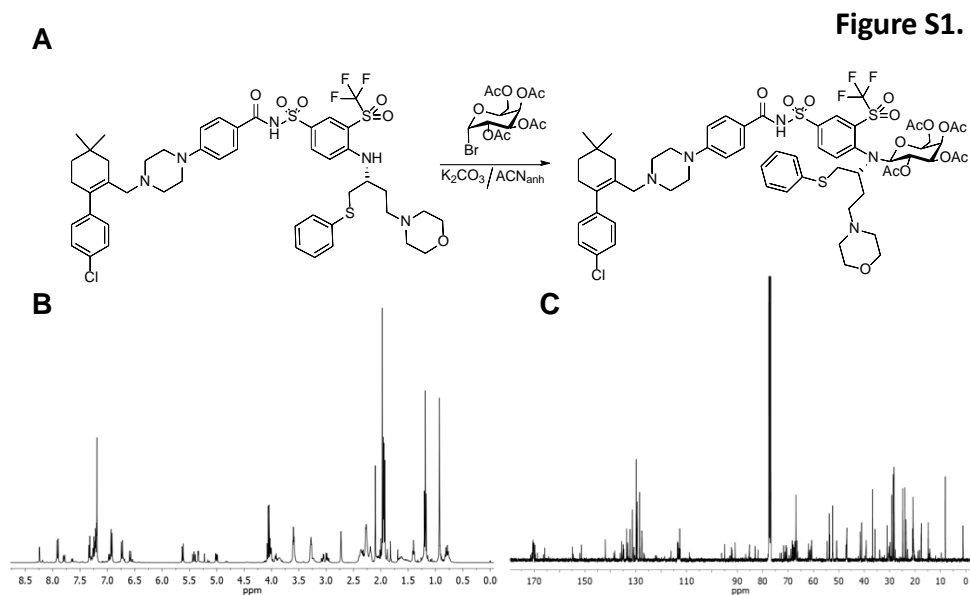


Figure S1. Molecular characterisation of pro-drug Nav-gal. (A) Schematic chemical structural representation of synthesis of Nav-gal prodrug. (B-C) Chemical shifts of the signals of proton (B) and carbon (C) atoms of Nav-gal observed in ^1H and ^{13}C NMR recorded in a 400MHz NMR spectrometer using deuterated chloroform (CDCl_3) as solvent. ^1H NMR (400 MHz, CDCl_3) δ = 8.25 (d, J =2.19Hz, 1H), 7.98 (d, J =9.18Hz, 1H), 7.86 (dd, J = 2.19, 9.18Hz, 1H), 7.41-7.26 (m, 5H), 7.03 (d, J =8.43,2H), 7.01 (d, J =8.43Hz,2H), 6.80 (d, J =9.4Hz, 2H), 6.65 (d, J =9.4Hz, 2H), 5.71 (d, J =8.24 Hz,1H), 5.48 (dd, J =10.37, 8.24 Hz, 1H), 5.41 (d, J =2.72 Hz, 1H), 5.07 (dd, J =3.41, 10.4 Hz, 1H), 4.09-4.06 (m, 1H), 4.00-3.94 (m, 2H), 3.80 (t, J =4.51 Hz, 4H), 3.28 (t, J =5.15 Hz, 4H), 3.10-2.92 (m, 3H), 2.73 (s, 2H), 2.43-2.14 (m, 12H), 2.04 (s, 3H), 2.02 (s, 3H), 2.01 (s, 3H), 1.99 (s,3H), 1.82 (s, 2H), 1.69-1.50 (m, 2H), 1.4 (m, 3H), 0.99 (s, 6H) ppm. (c) ^{13}C NMR (400 MHz, CDCl_3) δ =170.24, 170.48, 170.26, 170.05, 169.21, 154.90, 151.31, 141.97, 135.55, 134.93, 133.63, 132.22, 131.34, 131.30, 131.29, 131.15, 129.83, 129.49, 129.44, 129.41, 129.39, 128.46, 127.62, 127.52, 113.60, 113.38, 112.67, 94.76, 90.80, 71.72, 70.76, 68.64, 68.35, 66.92, 60.68, 54.59, 53.79, 53.74, 53.56, 52.42, 50.86, 50.95, 46.82, 41.64, 41.00, 39.22, 36.77, 35.79, 31.00, 29.83, 29.11, 28.58, 28.26.

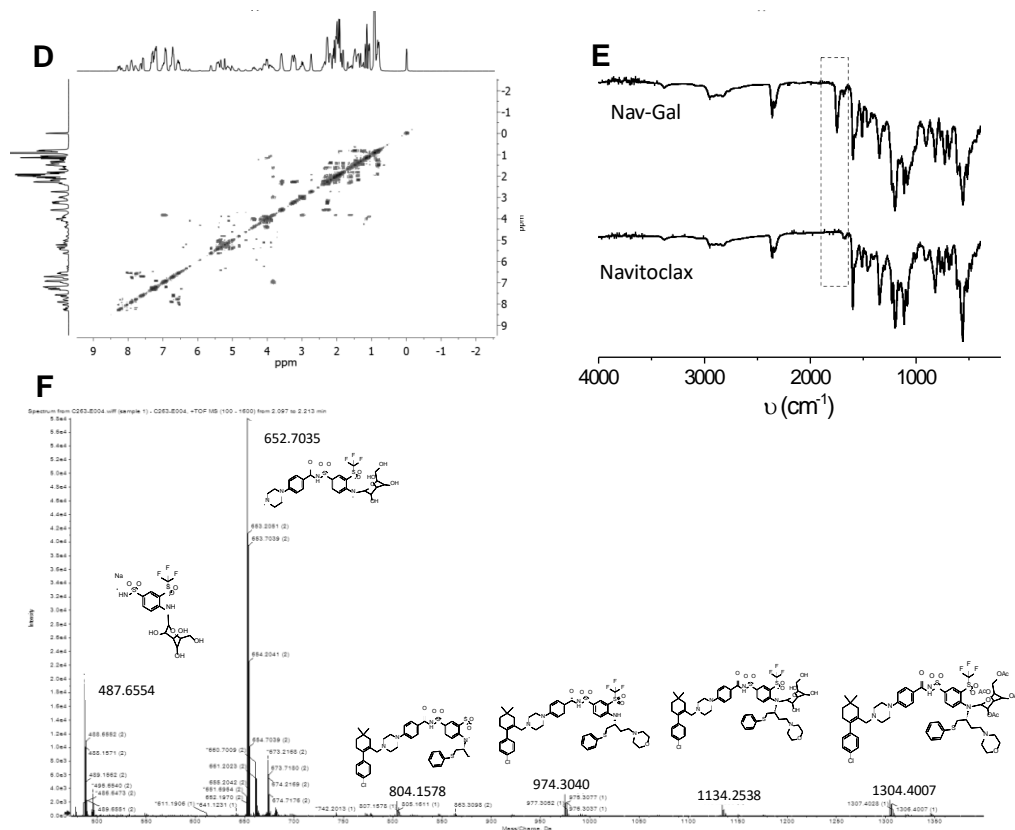


Figure S1. (D) Homonuclear bidimensional correlated spectroscopy ^1H - ^1H (2D) COSY NMR (400MHz, CDCl_3). Signals outside of the diagonal arises from the protons that are coupled together in neighbouring carbons. (E) Attenuated total reflectance (ATR) spectra of **Nav-gal** and Navitoclax compounds, the signal centered at ca. 1795 cm^{-1} are assigned to the C=O stretching vibration present in **Nav-gal** structure. (F) The high resolution mass spectra shows molecular fragments obtained after **Nav-gal** ionization corroborating the chemical structure of **Nav-gal**. HRMS-EI m/z : calculated:(M+H) = 1304.3979 m/z , measured:(M+H) = 1304.4001 m/z .

Figure S2.

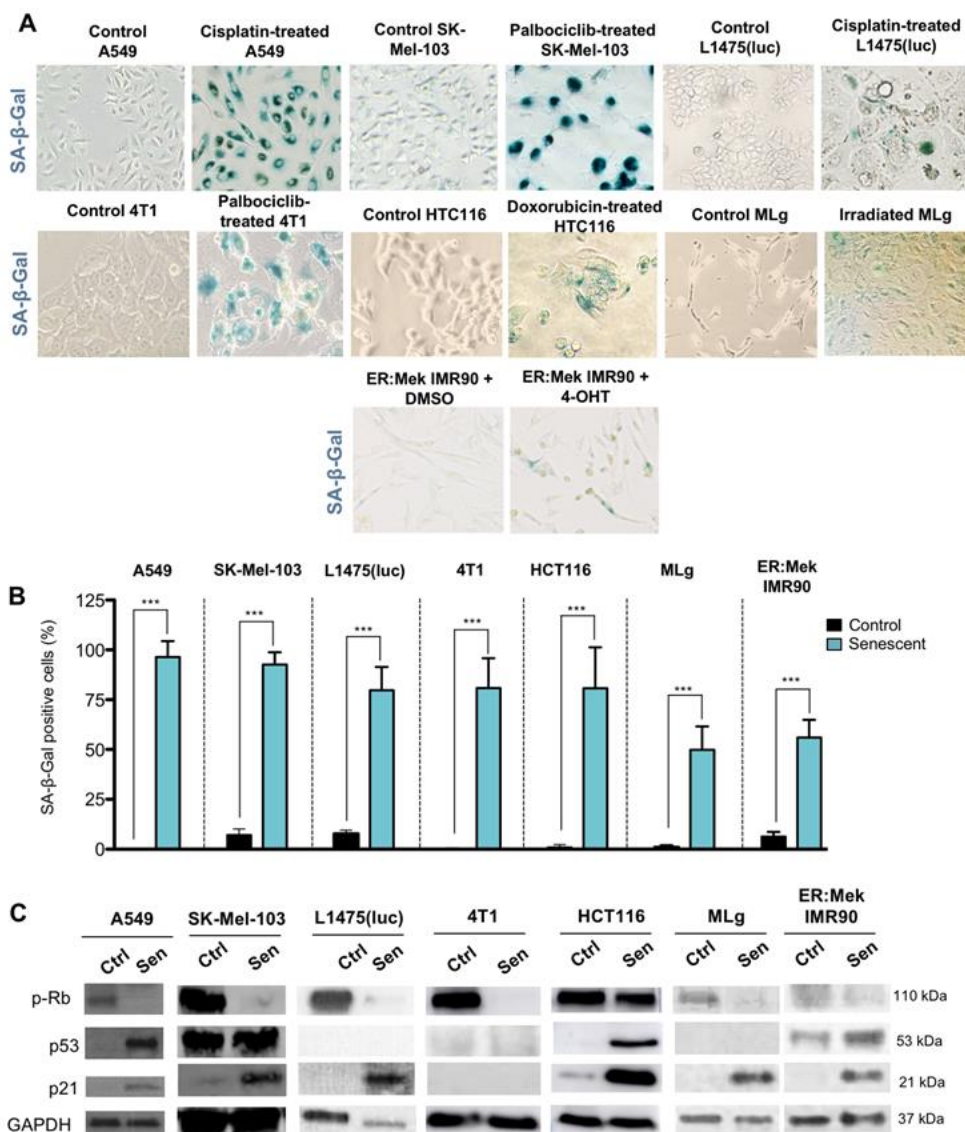


Figure S2. Assessment of the induction of cellular senescence in cell lines used for in vitro experiments. (A) Representative images of SA- β -gal staining of control and cisplatin-induced senescent A549 cells, palbociclib-induced senescent SK-Mel-103 cells, cisplatin-induced senescent KRasG12D/WT;p53^{-/-} lung cancer cells (L1475(luc)), palbociclib-induced 4T1 senescent cells, doxorubicin-induced senescent HCT116, irradiation-induced MLg fibroblastic cells and hydroxytamoxifen-treated ER:Mek IMR90 cells. (B) Quantification of SA- β -gal positive cells of control and senescent cells. (C) Western blot analysis of the expression of phospho-retinoblastoma (p-Rb), p53 and p21 in control and senescent cells.

Figure S3.

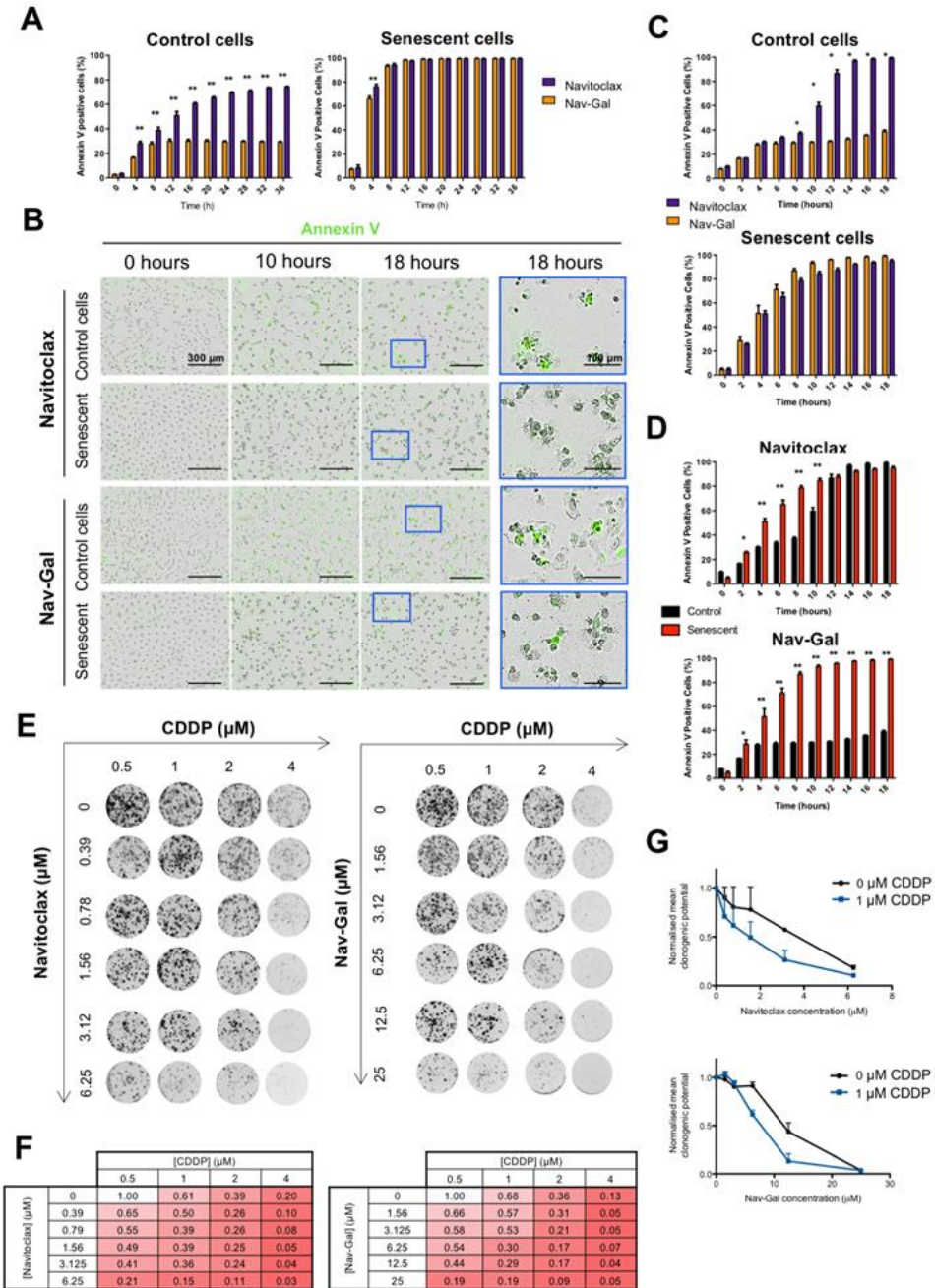


Figure S3. The galacto-conjugated pro-drug Nav-gal shows a lower induction of apoptosis of non-senescent melanoma SK-Mel-103 cells and lung cancer A549 cells, and significantly decreases clonogenic potential in combination with cisplatin. (A) Average percentage of Annexin V-positive 3

cells in control (left) or cisplatin (CDDP)-induced senescent A549 cells (right) exposed to Navitoclax (10 μ M) or **Nav-gal** (10 μ M) treatment over time. (B) Representative images of cell viability depicting staining for Annexin V (green) of control or palbociclib-induced senescent SK-Mel-103 cells, exposed to Navitoclax (10 μ M) or **Nav-gal** (10 μ M) treatment over time. Scale bar at lower magnification = 300 μ m. Scale bar at higher magnification = 100 μ m. (C) Average percentage of Annexin V-positive cells in control (top) or palbociclib-induced senescent SK-Mel-103 cells (bottom) exposed to Navitoclax (10 μ M) or **Nav-gal** (10 μ M) treatment overtime. (D) Same as in (C) but directly comparing the effect in control and senescent cells of Navitoclax (top) or **Nav-gal** (bottom) treatment. (E) Representative images of clonogenic survival of A549 cells exposed to increasing concentrations of CDDP for 7 days followed by the treatment of Navitoclax (left) or **Nav-gal** (right) as specified in axis for 7 days (sequential treatment). (F) Numerical heat-map representation of normalised mean clonogenic potential after 7 days of CDDP treatment followed by 7 days of senotherapy treatment navitoclax (left) or **Nav-gal** (right), where 1 = maximum clonogenic potential corresponding to CDDP 0.5 μ M condition (n=2). (G) Normalised mean clonogenic potential of A549 cells upon increasing concentrations of Navitoclax (left) or **Nav-gal** (right) as a single or combined treatment with CDDP. In (E) data represent mean \pm SEM (n=3), and in (A, C and D) data represent mean \pm SD (n=3), where for each biological repeat the percentage of Annexin V-positive cells was calculated in 3 independent technical repeats per experimental condition. Statistical significance was calculated using two-tailed Student's t-tests; *p < 0.05, **p < 0.001.

Figure S4.

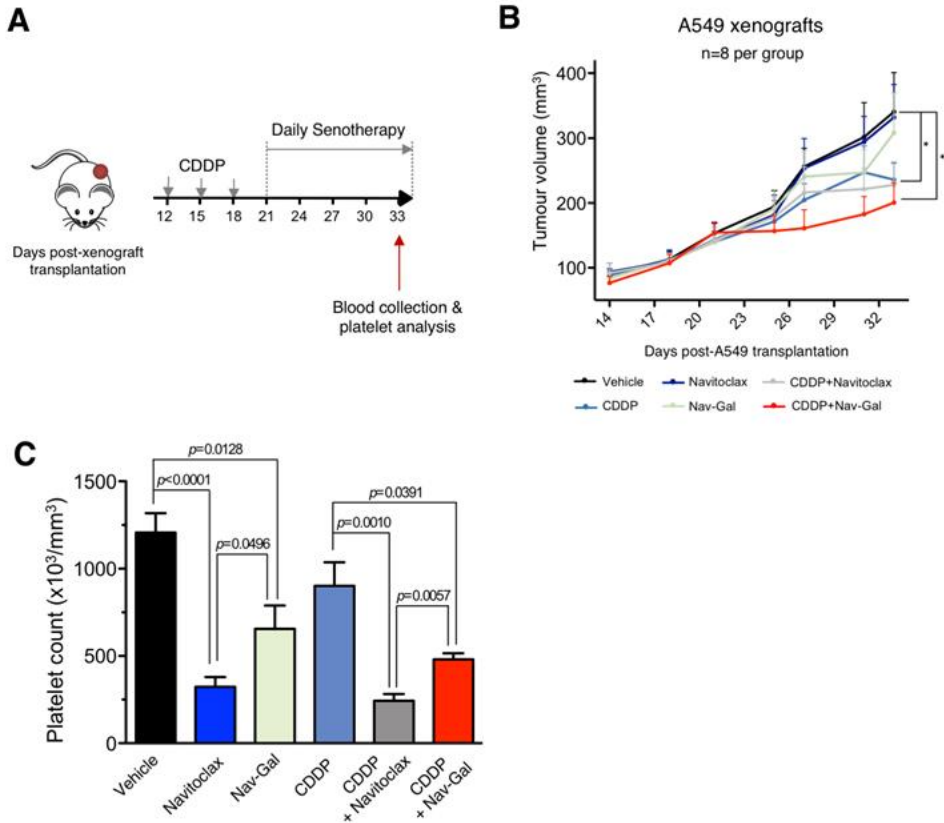


Figure S4. Sequential Nav-gal treatment after chemotherapy decreases tumour volume and platelet toxicity compared to Navitoclax. (A) A549-xenograft-bearing mice were first treated for a week with cisplatin (CDDP, 1.5 mg/kg three times a week) and then treated daily with Navitoclax (100 mg/kg body weight) or **Nav-gal** (85 mg/kg body weight) or their vehicles until end-point. Blood was then collected by cardiac puncture and the platelet count in each group was analysed. (B) Tumour volume of A549 xenografts in mice treated as described in (A) over time. (C) Platelet count in each experimental condition upon end of treatment in vivo (vehicle, Navitoclax, **Nav-gal** and CDDP + Navitoclax, n=5; CDDP and CDDP + **Nav-gal**, n=3). Data represent mean \pm SEM. Two-way ANOVA followed by Bonferroni post-tests or one-tailed t-tests were performed to calculate the significance of the results; * $p < 0.05$.

Figure S5.

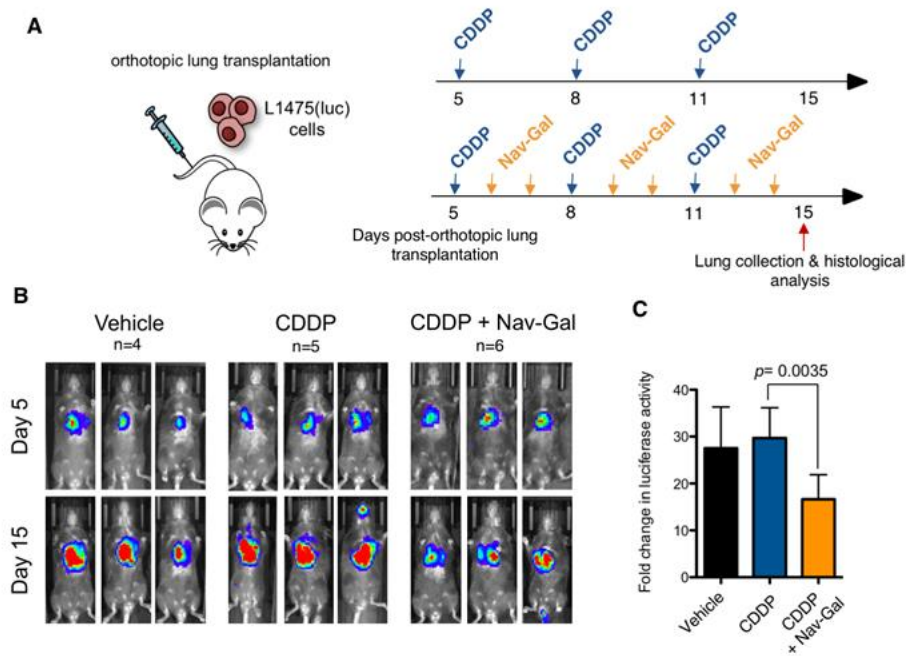


Figure S5. Concomitant treatment of lung tumours with pro-drug Nav-gal and cisplatin significantly decreases tumour burden in an orthotopic lung cancer mouse model. (A) Murine KP lung cancer cells were orthotopically transplanted in the lungs of C57BL/6J mice via tail-vein injection. After 5 days, animals were imaged and randomised into different groups following luciferase signal analysis, and subsequently treated with either vehicle (n=4), cisplatin (1 mg/kg body weight; n=5) or cisplatin and **Nav-gal** (85 mg/kg body weight; n=6) as shown in the schematic representation. Mice 4 were imaged at day 10 and 15 post-transplantation and lungs were collected at end-point for histological analysis. (B) Representative images of luciferase activity signal at day 5 (start of treatment) and 15 (end of treatment) of each experimental group are shown. (C) Fold-change of relative luciferase activity of each group over-time.

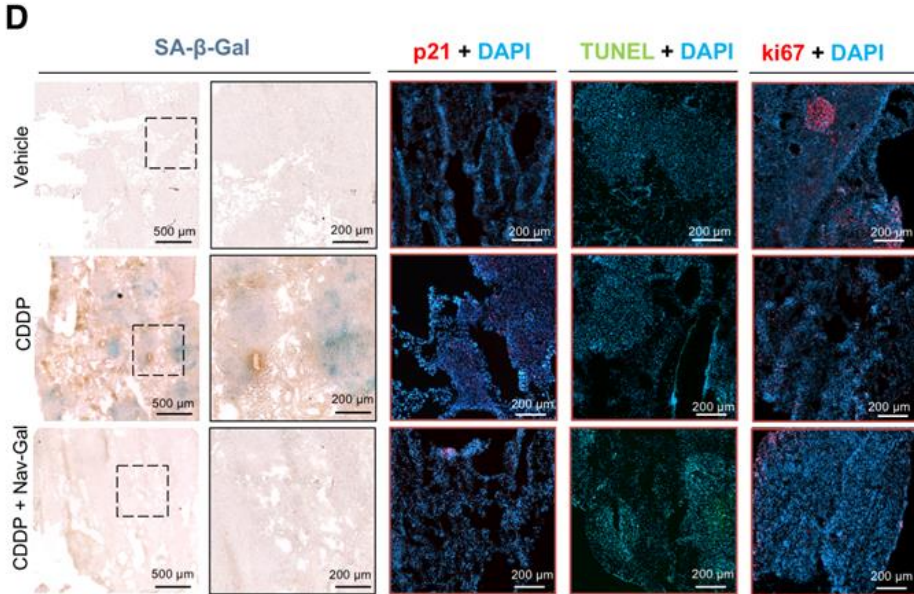


Figure S5. (D) Representative histological images of lung sections of each experimental group stained for SA-gal activity (in blue), p21 (red), TUNEL (green) and ki67 (red). Data in (C) represent mean \pm SEM, and statistical significance was calculated by one-way ANOVA followed by Bonferroni post-tests.

Figure S6.

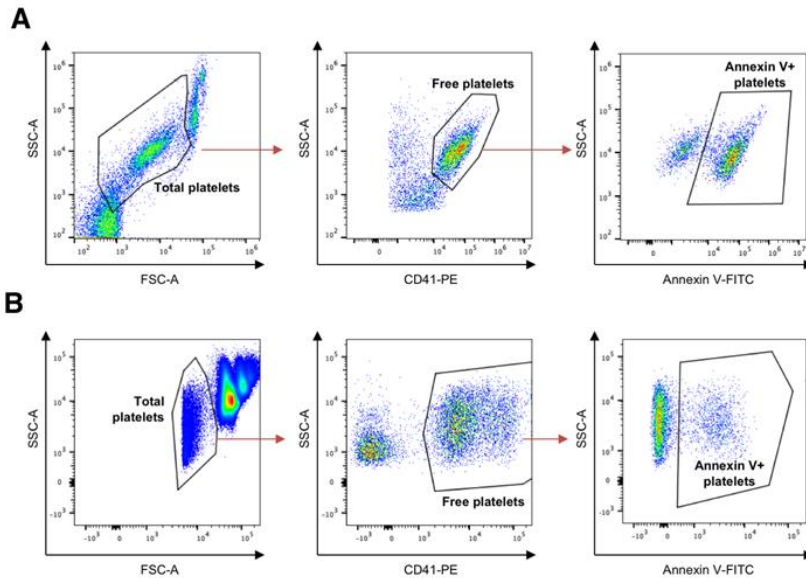


Figure S6. Gating strategy for the analysis of Annexin V-positive platelets (apoptotic platelets) in samples from (A) human and (B) mouse blood. Total platelet events were gated based on scatter signals (SSC-A vs FSC-A) and then free platelets were gated through CD41 expression. The percentage of apoptotic platelets was determined by analysing the Annexin V-positive population.

Chapter 8 | Conclusions and Perspectives

The function of cellular senescence is to prevent damaged or stressed cells from proliferating. However, normal ageing or certain conditions can cause senescent cells to accumulate in tissues, thereby promoting inflammation and tissue ageing. Research around senescence has expanded in recent years, particularly with respect to strategies to modulate senescence and to detect and eliminate senescent cells. A number of new advances in the field of senotherapeutics are expected in the following years. In terms of detection, both chromogenic and fluorogenic probes are especially appealing as simple systems to detect cellular senescence. However, one general drawback of existing probes is that, even in realistic *in vivo* models, the staining is visualized only after the animal is euthanized or probes are tested in animal models that were not directly related to senescence (using a *lacZ* gene transfection, which results in high levels of bacterial β -Gal expression in the cell cytoplasm, unlike the lysosomal β -Gal activity associated with senescent cells). When this thesis started, there were very few examples of non-invasive or less invasive probes to detect the presence of senescent cells in realistic *in vivo* models. Such probes would be highly desirable, as they would allow monitoring the fate of senescent cells in real time. If these probes were accessible, we envision advances in detection cellular senescence in combination with classical imaging techniques, such as computed tomography, magnetic resonance imaging and positron emission tomography. Beyond small molecules, there is a marked interest in the development of (bio)molecules or nanoparticles that selectively release tracers in senescent cells or nanoparticles that selectively “interact” with senescent cells. Development of new systems for detection would benefit both fundamental senescence research as well as applied research into monitoring the efficacy and mechanisms of senolytics. Selective probes are expected to help detecting senescent cells in aged or damaged tissues and to become suitable tools to monitor the action of senolytics in multiple, age-

related disorders and assess treatment response. One of the main questions in the senotherapeutics field is how to differentiate senolytic and senomorphic compounds in *in vivo* models. A detailed understanding of senescence will allow us to rationally develop new probes and come closer to answering this important question.

In this context, this PhD thesis has attempted to contribute to this field by designing three new probes, a nanodevice based on gated mesoporous silica nanoparticles for the detection of cellular senescence and a pro-drug to kill senescent cells. All probes and materials have been successfully tested *in vivo* in various models of cellular senescence.

At this respect, in the third chapter, a new molecular two-photon probe for the detection of cellular senescence *in vivo* is developed (**AHGa**). The probe consists of a naphthalimide fluorophore, with an L-histidine methyl ester linker and an acetylated galactose attached to one of the aromatic nitrogen atoms of L-histidine. Probe **AHGa** is hydrolyzed in senescent cells, resulting in enhanced fluorescent emission intensity. The probe presents greater selectivity *in vivo* against senescent SK-Mel-103 human melanoma cells (chemotherapeutically induced) than against control cells. Besides, *in vivo* detection of cellular senescence is assessed in xenografted mice with senescence inducing chemotherapy.

The fourth chapter describes another two-photon probe (**HeckGal**) containing a new fluorophore with higher excitation and emission wavelength (in the NIR zone) which presents great versatility and is able to detect senescent cells in different types of cell lines with different induction methods of senescence. Moreover, **HeckGal** detects senescent cells *in vivo* in palbociclib-treated orthotopic model of mouse breast cancer and in a mouse model of renal fibrosis.

As mentioned above, there is a real need for non-invasive and easily-readout probes for cellular senescence detection. We deal with this problem in the fifth chapter, through the design of a renally clearable probe. Specifically, cellular senescence is detected using a new cyanine-7-based diuretic probe containing sulfonic acid moieties (**Cy7Gal**) that is hydrolyzed in senescent cells into the highly emitting fluorophore **Cy7**. The burden of senescence is quantified *in vivo* by direct measurement of urine fluorescence in a palbociclib-treated orthotopic model of mouse breast cancer, in naturally aged mice and in mice with accelerated senescence. **Cy7Gal** is the first example able to detect cellular senescence *in vivo* in urine and may serve as a basis for the development of new molecular probes for the easy diagnosis of different diseases, as well as for the monitoring of therapeutic treatments of patients.

The sixth chapter is the last one devoted to cellular senescence detection. In this chapter, **NB**-loaded MSNs capped with a galactohexasaccharide is developed (**S3**). **NB** is highly emissive with a remarkable band at 672 nm, yet this fluorescence is quenched inside the pores of the **S3** nanoparticles (due to π -stacking interactions). On the other hand, the galactohexasaccharide cap in **S3** confers the nanoparticles specific selectivity for senescent cells, which overexpressed SA- β -Gal. This enzyme is able to hydrolyze the galactohexasaccharide cap with the subsequent release of **NB**, which results in a marked emission enhancement. **S3** optically detects cellular senescence *in vitro* in SK-Mel-103 and 4T1 senescent cells, and *in vivo* in a palbociclib-treated BALB/cByJ mice bearing breast cancer tumor.

Finally, chapter seven describes the preparation of the pro-drug **Nav-gal** by combining the well-known senolytic drug Navitoclax and a galactose unit. **Nav-gal** is not able to inhibit the antiapoptotic proteins of the BCL-2 family when linked to sugar. However, upon diffusion to the lysosome of senescent cells, SA- β -Gal

hydrolyzes the glycosidic bond in **Nav-gal**, yielding free navitoclax. **Nav-gal** is validated *in vitro* in different senescent cell lines and *in vivo* in a mouse lung cancer model. Moreover, thrombocytopenia is reduced with **Nav-gal** when compared with Navitoclax.

The development of probes, nanomaterials and prodrugs to target senescent cells *in vivo* is a promising strategy to detect and treat aging-related diseases. However, taking into the account that these systems are still in the initial stages of biomedicine applications, some drawbacks still need to be overcome and for instance the potential effects in the organism have to be completely analyzed. The benefit-to-risk ratio has to be studied and more research efforts are needed to finally use probes and senolytic drugs in clinical applications. Several new advances in the field of cellular senescence detection and treatment are expected in the near future. It is our hope that the results achieved in this PhD thesis open new research opportunities and inspire the development of new smart probes and pro-drugs for their application in the field of cellular senescence, as well as in other biomedical unresolved needs.